NATIONAL TECHNICAL UNIVERSITY OF ATHENS

School of Chemical Engineering

Department II: Process Analysis and Plant Design

Thermodynamics and Transport Phenomena Laboratory

Thermodynamic modelling and simulation of mercury distribution in natural gas

Ph.D. Thesis

by

Vasileios D. Koulocheris

Supervisor: Epaminondas Voutsas, Professor

Athens, March 2021

Thermodynamic modelling and simulation of mercury distribution in natural gas

A dissertation presented by

Vasileios D. Koulocheris

to

the School of Chemical Engineering

in partial fulfillment of the requirements for the degree of

Doctor of Philosophy

in

Chemical Engineering

Supervisor:	Epaminondas Voutsas, Professor
Supervising Committee:	Konstantinos Magoulas, Professor
	Sofia Stamataki, Professor

National Technical University of Athens

Athens, Greece

March 2021

The approval of this Ph.D. dissertation by the School of Chemical Engineering of the National Technical University of Athens does not imply the acceptance of the author's opinions (Law 5343/1932 Article 202 § 2).

Η έγκριση της διδακτορικής διατριβής από την Ανωτάτη Σχολή Χημικών Μηχανικών του Εθνικού Μετσόβιου Πολυτεχνείου δεν υποδηλώνει αποδοχή των απόψεων του συγγραφέα (Ν.5343/32 Άρθρο 202 § 2).

Abstract

Mercury and its species occur naturally in all fossil fuels, such as natural gas (NG), crude oil, and coal. The concentration of mercury in oil and gas varies depending on source, but it is usually of the order of a few parts per billion (ppb). However, even at these very low concentrations, mercury and its species can cause significant problems during oil & gas processing and, therefore, its levels in a plant must be monitored. Mercury is toxic to living organisms and, for this reason, strict regulations are in place regarding mercury emissions to the environment from industrial activities. In addition, mercury can cause catalyst poisoning and corrode the equipment through various mechanisms, such as Liquid Metal Embrittlement (LME)[1]. Indicative of the risk that Hg poses to process is the fact that until today about 10 industrial accidents have been recorded, which were caused by corrosion of equipment by mercury.

For the proper management of mercury in oil & gas treatment plants, it is necessary to know the distribution of mercury in the different phases, e.g. gas, liquid, aqueous, during drilling and topside treatment processes. Scientific research in this field is currently active. Although some thermodynamic models describing the distribution of elemental mercury in NG have already been proposed, there are still aspects of the issue that are not sufficiently covered in the literature. For example, although in the vapor and liquid streams of the NG processing plants various mercury forms other than elemental, such as HgS, $HgCl_2$, MeHg, Me_2Hg etc. have been identified, their distribution has not been described so far with any thermodynamic model. The existence of other forms of mercury apart from the elemental indicates that it may also participate in reactions during NG processing, which have not been investigated in the open literature nor have they been included in any model. The development of such a model becomes even more complicated if one takes into account the adsorption/chemisorption of mercury on piping and equipment walls, and also the great variation in pressure and temperature along the natural gas value chain.

The aim of the thesis is to develop a thermodynamic model that can accurately describe the simultaneous chemical & phase equilibria (CPE) of mercury in natural gas, and its application in the simulation of Hg distribution in natural gas processing plants. Towards this, the UMR-PRU EoS/G^E model is extended to mixtures of mercury with compressed gases (CO_2, N_2), hydrocarbons, water, and polar compounds that are often encountered during oil & gas processing, such as amines, glycols and alcohols. For comparison purposes, the widely used cubic EoS SRK and PR are also employed. To ensure that the models correctly predict the vapor pressure of pure mercury, different functions for their attractive term are examined. For UMR-PRU and PR the Mathias-Copeman α-function is proposed, while for SRK the α-function by Twu is employed. Pertinent α-function parameters are fitted to pure mercury experimental vapor pressure data with average absolute relative deviation (AARD) lower than 1%. Afterwards, model interaction parameters are fitted to experimental Hg solubility measurements. For the cubic EoS, generalized correlations for the binary interaction

parameters are developed for hydrocarbons, while for polar compounds temperature-dependent BIPs are determined. The overall results show that UMR-PRU yields the best results in binary hydrocarbon and polar mixtures of mercury, while it also yields the lowest deviations in most multicomponent hydrocarbon mixtures and in all polar multicomponent mixtures.

In order to study the possible reaction between mercury and hydrogen sulfide in natural gas ($Hg^0 + H_2S \Leftrightarrow \beta$-$HgS + H_2$), the UMR-PRU model is also extended to mixtures of hydrogen with compressed gases (CO_2, N_2), hydrocarbons, water, and polar compounds. For comparison, the PPR78 model is also employed. The ability of PR to predict pure hydrogen properties is checked, and the Soave expression for the attractive term is found to yield the best results, while also ensuring that the *α*-function is consistent. UMR-PRU model interaction parameters are then determined by fitting binary vapor-liquid equilibrium data for hydrogen binary mixtures. It is found that UMR-PRU shows a lower overall deviation in bubble point pressure (8.1%) than PPR78 (13.2%). Both models are also employed for predictions in multicomponent hydrogen mixtures with hydrocarbons and compressed gases, with UMR-PRU yielding the best results.

After successful model extension to mercury and hydrogen mixtures, UMR-PRU is employed for calculating mercury saturation concentration in typical hydrocarbon fluids. For this purpose, the multiphase flash algorithm that was developed in this work is employed, which can handle systems that contain up to four phases: vapor-liquid hydrocarbon-aqueous-mercury. The results show that mercury solubility in the various phases increases exponentially with temperature and generally increases in the order aqueous < vapor < liquid hydrocarbon phase. The effect of pressure on mercury solubility in the different phases is also examined, and results show a weak dependency in the liquid hydrocarbon and aqueous phases. On the other hand, Hg^0 solubility in the vapor phase is found to decrease with pressure, until a plateau is reached. Phase composition is found to play an important role and different behaviors can be observed, e.g. in fluids involved in early-stage separation processes from those that can be found in the condensate stabilization train of a gas processing plant.

The second point of focus in this work is the theoretical study of the reaction between elemental mercury and H_2S in natural gas, which could provide an explanation for the origin of β-HgS solid particles found in condensate tank sediments. Chemistry dictates that mercury has a high affinity for sulfur and its compounds, and H_2S is the most abundant sulfuric compound in natural gas, so a reaction between them is deemed reasonable. Both cases of vapor and liquid phase reaction are examined by calculating the pertinent equilibrium constants. Then, the simultaneous chemical & phase equilibria in the same fluids were solved by employing the Gibbs energy minimization algorithm developed in this work.

The UMR-PRU model is subsequently employed for simulating mercury distribution in an existing offshore natural gas processing platform. For comparison the SRK-Twu model is also used, and model results are compared to field measurements regarding mercury concentration in selected streams. For the purposes of this study, a simplified version of the

process is implemented in UniSim Design R460.2 and the distribution of mercury in the various streams is examined. The effect of the reaction between mercury and H_2S is also studied. Different scenarios are considered, based on the presumed amount of mercury in the plant feeds according to mass balance calculations. Mercury partitioning in the TEG dehydration & regeneration process, as well as in MEG regeneration are also examined in separate simulations. The results in the case of no reaction show that both models yield very good predictions regarding mercury concentrations in process gases, but overpredict Hg levels in condensate fluids. UMR-PRU is found to yield the most accurate results for Hg distribution in aqueous streams, as well as in the processes involved in TEG dehydration & regeneration, and MEG regeneration.

On the other hand, when the reaction is also included, it is found that the models yielded better results for Hg concentration in condensates, but deviate from the measurements in gas streams. In addition, UMR-PRU predicts an amount of produced solid β-HgS, which is closer to the expected value based on the field data. Considering the uncertainty of measurements concerning Hg concentration in liquid samples due to various experimental challenges, it is deemed that UMR-PRU yields the best overall results, while it is also capable of describing processes involving polar compounds, such as TEG dehydration & regeneration, where classical cubic EoS perform poorly.

Finally, the developed CPE algorithm is applied for the study of complex mixtures involving non-reactive and reactive azeotropes. Such mixtures are commonly encountered in the chemical and petroleum industry, and require advanced thermodynamic tools that can accurately predict their equilibria. Such tools are important in order to determine the feasibility of separation processes, such as reactive distillation. In this work, the CPE algorithm is applied for studying the MTBE synthesis from methanol and isobutene, as well as the synthesis of isopropyl acetate via esterification of acetic acid with isopropanol. The algorithm is coupled with classical activity coefficient models, UNIQUAC and NRTL, as well as with UMR-PRU. The results show that the CPE algorithm is very robust, and that thermodynamic models coupled with the algorithm can successfully describe the chemical & phase equilibria involved in these systems, providing important information about the feasibility of separation processes.

Περίληψη

Ο υδράργυρος και οι ενώσεις του αποτελούν φυσικό συστατικό των ορυκτών καυσίμων, όπως ο άνθρακας, το αργό πετρέλαιο και το φυσικό αέριο (ΦΑ). Η συγκέντρωση του υδραργύρου στο πετρέλαιο και το φυσικό αέριο ποικίλλει ανάλογα με την προέλευση, όμως συνήθως είναι της τάξης των μερικών μερών ανά δισεκατομμύριο (ppb). Εντούτοις, ακόμα και σε αυτές τις πολύ χαμηλές συγκεντρώσεις, ο υδράργυρος και οι ενώσεις του μπορούν να προκαλέσουν σημαντικά προβλήματα κατά την επεξεργασία πετρελαίου και φυσικού αερίου και γι' αυτό τα επίπεδα Hg σε μια μονάδα επεξεργασίας πρέπει να παρακολουθούνται. Ο υδράργυρος είναι τοξικός για τους ζωντανούς οργανισμούς και για το λόγο αυτό υφίστανται αυστηροί περιορισμοί στις εκπομπές Hg στο περιβάλλον από βιομηχανικές δραστηριότητες. Επιπλέον, ο υδράργυρος μπορεί να δηλητηριάσει τους καταλύτες και να προκαλέσει διάβρωση του εξοπλισμού μέσω διάφορων μηχανισμών. Ενδεικτικό της επικινδυνότητας του Hg είναι το γεγονός πως μέχρι σήμερα έχουν προκληθεί περίπου 10 βιομηχανικά ατυχήματα εξαιτίας διάβρωσης εξοπλισμού από υδράργυρο.

Για την ορθή διαχείριση του υδραργύρου σε μονάδες επεξεργασίας πετρελαίου και φυσικού αερίου, είναι απαραίτητη η γνώση της κατανομής του υδραργύρου στις διάφορες φάσεις, π.χ. αέρια, υγρή, υδατική, κατά την εξόρυξη και τις υπέργειες διεργασίες επεξεργασίας. Η επιστημονική έρευνα στο πεδίο αυτό βρίσκεται αυτή τη στιγμή σε εξέλιξη. Παρόλο που στο παρελθόν έχουν προταθεί κάποια θερμοδυναμικά μοντέλα που να περιγράφουν την κατανομή του στοιχειακού υδραργύρου στο ΦΑ, υπάρχουν ακόμα πτυχές του προβλήματος που δεν καλύπτονται επαρκώς από τη βιβλιογραφία. Για παράδειγμα, ενώ στα αέρια και υγρά ρεύματα που εντοπίζονται σε μονάδες επεξεργασίας ΦΑ έχουν βρεθεί διάφορες μορφές υδραργύρου εκτός της στοιχειακής, όπως HgS, $HgCl_2$, MeHg, Me_2Hg κλπ., η κατανομή τους δεν έχει περιγραφτεί έως τώρα με κάποιο θερμοδυναμικό μοντέλο. Η ύπαρξη και άλλων μορφών υδραργύρου πέραν της στοιχειακής υποδεικνύει ότι ο υδράργυρος πιθανώς συμμετέχει σε αντιδράσεις κατά την επεξεργασία του ΦΑ, οι οποίες δεν έχουν διερευνηθεί στην ανοικτή βιβλιογραφία, ούτε έχουν περιγραφτεί με κάποιο μοντέλο. Η ανάπτυξη τέτοιων μοντέλων γίνεται ακόμα πιο πολύπλοκη αν ληφθεί υπόψιν η προσρόφηση/χημειορόφηση του υδραργύρου στις σωληνώσεις και τον εξοπλισμό, καθώς και η μεγάλη διαφοροποίηση στις συνθήκες που επικρατούν κατά μήκος της αλυσίδας αξίας του ΦΑ.

Ο σκοπός της διατριβής είναι η ανάπτυξη ενός θερμοδυναμικού μοντέλου που να μπορεί να προβλέπει με ακρίβεια την ταυτόχρονη ισορροπία φάσεων και χημικών αντιδράσεων του υδραργύρου στο ΦΑ, και η εφαρμογή του για την προσομοίωση της κατανομής του Hg σε μονάδες επεξεργασίας ΦΑ. Για τον σκοπό αυτόν, το EoS/G^E μοντέλο UMR-PRU επεκτείνεται σε μείγματα του υδραργύρου με συμπιεσμένα αέρια (CO_2, N_2), υδρογονάνθρακες, νερό και πολικά συστατικά που χρησιμοποιούνται συχνά κατά την επεξεργασία ΦΑ, όπως αμίνες, γλυκόλες και αλκοόλες. Για σύγκριση, χρησιμοποιούνται επίσης και οι ευρέως διαδεδομένες κυβικές καταστατικές εξισώσεις (ΚΕ) SRK και PR. Για να διασφαλιστεί η ακριβής πρόβλεψη της τάσης ατμών του καθαρού Hg, εξετάζονται διάφορες συναρτήσεις για τον ελκτικό όρο των ΚΕ. Για τον ελκτικό όρο των UMR-PRU και PR προτείνεται η έκφραση των Mathias-

Copeman, ενώ για την SRK χρησιμοποιείται ο ελκτικός όρος του Twu. Οι σχετικές παράμετροι των ελκτικών όρων προσαρμόζονται σε πειραματικά δεδομένα τάσης ατμών του καθαρού Hg με μέση απόλυτη σχετική απόκλιση (AARD) μικρότερη από 1%. Έπειτα, οι παράμετροι αλληλεπίδρασης των μοντέλων προσαρμόζονται σε πειραματικά δεδομένα διαλυτότητας Hg. Για τις κυβικές ΚΕ αναπτύσσονται γενικευμένες συσχετίσεις για τις δυαδικές παραμέτρους αλληλεπίδρασης Hg με υδρογονάνθρακες, ενώ για τις παραμέτρους αλληλεπίδρασης Hg με πολικές ενώσεις αναπτύσσονται θερμοκρασιακά εξαρτημένες σχέσεις. Τα συνολικά αποτελέσματα δείχνουν ότι το UMR-PRU δίνει τα καλύτερα αποτελέσματα στα δυαδικά μείγματα Hg με υδρογονάνθρακες και στα πολικά μείγματα που περιέχουν υδράργυρο, ενώ επίσης οδηγεί στις χαμηλότερες αποκλίσεις στα περισσότερα πολυσυστατικά μείγματα με υδρογονάνθρακες και σε όλα τα πολικά πολυσυστατικά μείγματα.

Για τη μελέτη της πιθανής αντίδρασης ανάμεσα στον υδράργυρο και το υδρόθειο στο ΦΑ ($Hg^0 + H_2S \Leftrightarrow \beta$-$HgS + H_2$), το UMR-PRU επεκτείνεται και σε μείγματα υδρογόνου με συμπιεσμένα αέρια (CO_2, N_2), υδρογονάνθρακες, νερό και πολικά συστατικά. Για σύγκριση, χρησιμοποιείται επίσης το μοντέλο PPR78. Γίνεται έλεγχος της ικανότητας της PR για την πρόβλεψη των ιδιοτήτων του καθαρού υδρογόνου, από τον οποίο προκύπτει ότι ο ελκτικός όρος του Soave δίνει τα καλύτερα αποτελέσματα, ενώ ταυτόχρονα ικανοποιεί τα κριτήρια θερμοδυναμικής συνέπειας των ελκτικών όρων. Έπειτα, γίνεται προσαρμογή των παραμέτρων αλληλεπίδρασης του UMR-PRU σε δυαδικά πειραματικά δεδομένα ισορροπίας ατμού-υγρού. Προκύπτει ότι το UMR-PRU δίνει μικρότερη απόκλιση στις πιέσεις σημείου φυσαλίδας (8.1%) σε σχέση με την PPR78 (13.2%). Τα δύο μοντέλα χρησιμοποιούνται επίσης για προβλέψεις σε πολυσυστατικά μείγματα υδρογόνου με υδρογονάνθρακες και συμπιεσμένα αέρια, με το UMR-PRU να παρουσιάζει τις μικρότερες αποκλίσεις.

Μετά την επιτυχή επέκταση του μοντέλου σε μείγματα που περιέχουν υδράργυρο και υδρογόνο, το UMR-PRU εφαρμόζεται για τον υπολογισμό της συγκέντρωσης κορεσμού του υδραργύρου σε διάφορα τυπικά ρευστά ΦΑ. Για τον σκοπό αυτόν, χρησιμοποιείται ο αλγόριθμος πολυφασικής ισορροπίας που αναπτύχθηκε στην παρούσα διατριβή, ο οποίος μπορεί να διαχειριστεί συστήματα που περιλαμβάνουν έως 4 φάσεις: αέριο-υγροί υδρογονάνθρακες-υδατική-υδράργυρος. Τα αποτελέσματα δείχνουν ότι η διαλυτότητα του υδραργύρου στις διάφορες φάσεις αυξάνεται εκθετικά με τη θερμοκρασία και σε γενικές γραμμές ακολουθεί τη σειρά: υδατική < αέρια < υγρή υδρογονανθρακική. Διερευνάται επίσης η επίδραση της πίεσης στη διαλυτότητα Hg στις φάσεις, και τα αποτελέσματα δείχνουν μικρή εξάρτηση για την υγρή υδρογονανθρακική και την υδατική φάση. Αντίθετα, στην αέρια φάση η διαλυτότητα του υδραργύρου μειώνεται με την αύξηση της πίεσης, μέχρι να επιτευχθεί ένα πλατό. Η σύσταση της φάσης παίζει σημαντικό ρόλο και διαφορετική συμπεριφορά μπορεί να παρατηρηθεί, π.χ. στα ρευστά που εντοπίζονται σε πρωταρχικούς διαχωρισμούς ισορροπίας σε μια μονάδα με αυτά που βρίσκονται στη γραμμή σταθεροποίησης των συμπυκνωμάτων ΦΑ.

Το δεύτερο σημείο εστίασης αυτής της διατριβής είναι η θερμοδυναμική ανάλυση της αντίδρασης μεταξύ του στοιχειακού υδραργύρου και του υδρόθειου στο ΦΑ, η οποία θα μπορούσε να εξηγήσει την προέλευση των στερεών σωματιδίων β-HgS που εντοπίζονται σε ιζήματα δεξαμενών συμπυκνωμάτων ΦΑ. Η χημεία υποδεικνύει ότι ο υδράργυρος έχει υψηλή συνάφεια με το θείο και τις ενώσεις του, και καθώς το H_2S είναι η πιο συχνή ένωση θείου που απαντά στο ΦΑ, θα ήταν λογική μια αντίδραση ανάμεσα σε Hg και H_2S. Η αντίδραση μελετάται τόσο στην αέρια, όσο και στην υγρή υδρογονανθρακική φάση, υπολογίζοντας τις σχετικές σταθερές ισορροπίας της αντίδρασης. Έπειτα, επιλύεται η ταυτόχρονη ισορροπία φάσεων και χημικών αντιδράσεων με τη βοήθεια του αλγορίθμου ελαχιστοποίησης ενέργειας Gibbs που αναπτύσσεται στην παρούσα διατριβή.

Το μοντέλο UMR-PRU εφαρμόζεται ακολούθως για την προσομοίωση της κατανομής του υδραργύρου σε μια υπάρχουσα υπεράκτια πλατφόρμα επεξεργασίας ΦΑ. Για σύγκριση, χρησιμοποιείται και το μοντέλο SRK-Twu, και τα αποτελέσματα αντιπαραβάλλονται με πειραματικές μετρήσεις πεδίου σχετικά με την συγκέντρωση Hg σε διάφορα ρεύματα της μονάδας. Για τον σκοπό αυτόν, δημιουργείται μια απλοποιημένη προσομοίωση στο UniSim Design R460.2 και μελετάται η κατανομή του υδραργύρου στα διάφορα ρεύματα. Μελετάται επίσης η επίδραση της αντίδρασης μεταξύ Hg και H_2S στην κατανομή του υδραργύρου. Εξετάζονται διαφορετικά σενάρια για την ποσότητα του υδραργύρου στις εισόδους της μονάδας σύμφωνα με υπολογισμούς ισοζυγίων μάζας. Επίσης, μελετάται η κατανομή υδραργύρου στις διεργασίες αφύγρανσης ΦΑ με TEG και αναγέννησης, καθώς και στην ανάκτηση και αναγέννηση MEG. Τα αποτελέσματα στην περίπτωση χωρίς αντίδραση δείχνουν ότι και τα δύο μοντέλα προβλέπουν πολύ ικανοποιητικά τη συγκέντρωση Hg στα αέρια ρεύματα της μονάδας, όμως υπερεκτιμούν τη συγκέντρωση Hg στα συμπυκνώματα ΦΑ. Το UMR-PRU δίνει τα καλύτερα αποτελέσματα όσον αφορά συγκεντρώσεις Hg σε υδατικά ρεύματα, καθώς και στην κατανομή Hg στις διεργασίες που συμμετέχουν οι TEG, MEG.

Από την άλλη πλευρά, όταν περιλαμβάνεται και η αντίδραση, τα μοντέλα δίνουν καλύτερα αποτελέσματα στα συμπυκνώματα, όμως αποκλίνουν περισσότερο από τις μετρήσεις για τα αέρια ρεύματα. Επίσης, η προβλεπόμενη ποσότητα παραγόμενου στερεού β-HgS σύμφωνα με το UMR-PRU είναι πιο κοντά στην αναμενόμενη με βάση τις μετρήσεις πεδίου. Λαμβάνοντας υπόψιν τη μεγάλη αβεβαιότητα των μετρήσεων συγκέντρωσης Hg στα συμπυκνώματα ΦΑ εξαιτίας διάφορων πειραματικών προκλήσεων, το UMR-PRU θεωρείται ότι δίνει τα καλύτερα αποτελέσματα συνολικά, ενώ μπορεί να περιγράψει και τις διεργασίες στις οποίες συμμετέχουν πολικά συστατικά, όπως η αφύγρανση ΦΑ με TEG, όπου οι κλασσικές κυβικές ΚΕ αποτυγχάνουν.

Τέλος, ο αλγόριθμος ταυτόχρονης ισορροπίας φάσεων και χημικών αντιδράσεων εφαρμόζεται για τη μελέτη σύνθετων μειγμάτων που παρουσιάζουν αζεότροπα ή και αντιδρώντα αζεότροπα. Τέτοια μείγματα συναντώνται συχνά στη χημική και πετρελαϊκή βιομηχανία και απαιτούν προχωρημένα θερμοδυναμικά μοντέλα για την ακριβή πρόβλεψη της ισορροπίας. Τέτοια εργαλεία είναι σημαντικά για να καθοριστεί η εφικτότητα

διεργασιών διαχωρισμού, όπως η απόσταξη με αντίδραση (reactive distillation). Στην παρούσα διατριβή, ο αλγόριθμος εφαρμόζεται για τη μελέτη της σύνθεσης MTBE από μεθανόλη και ισοβουτυλένιο, καθώς και για τη σύνθεση ισοπροπυλεστέρα μέσω της εστεροποίησης οξικού οξέος με ισοπροπανόλη. Ο αλγόριθμος συνδυάζεται με τα κλασσικά μοντέλα συντελεστή ενεργότητας UNIQUAC και NRTL, καθώς και με το μοντέλο UMR-PRU. Τα αποτελέσματα δείχνουν ότι ο αλγόριθμος είναι εύρωστος και ότι τα θερμοδυναμικά μοντέλα σε συνδυασμό με τον αλγόριθμο μπορούν να περιγράψουν επιτυχώς την ταυτόχρονη ισορροπία φάσεων και χημικών αντιδράσεων στα συστήματα αυτά, προσφέροντας χρήσιμες πληροφορίες σχετικά με την εφικτότητα των διεργασιών διαχωρισμού.

Acknowledgements

Having now completed my PhD thesis, looking back I see a wonderful journey with ups and downs, fears and hopes, joys and sad moments, as all journeys are. This has been a lifetime dream of mine, and I am grateful that it came to fruition, while it also enabled me to travel in beautiful places, meet new people, and for a brief time work abroad. The recent pandemic outbreak has taught us that we should not take these for granted. I have also understood that the path towards the PhD thesis is not a sprint, but a marathon, which requires substantial psychological (and sometimes physical) resilience, courage, persistence, and of course support and guidance from others. To these people I am grateful and would like to express my thanks.

First of all, I would like to thank my supervisor, Professor Epaminondas Voutsas for entrusting me with such an interesting and challenging thesis, and for his continuous support, counsel and inspiration throughout these years. I would also like to thank the members of my supervising committee, Professor Konstantinos Magoulas and Professor Sofia Stamataki for their support during this project.

I would like to express my gratitude towards Equinor ASA, Norway (formerly known as Statoil) and Gassco for funding this PhD thesis. I would like to especially thank Dr. Eleni Panteli and Dr. Stathis Skouras, Principal Researchers at Equinor, for our excellent collaboration throughout these years. They both gave me insight into the petroleum industry and presented me with some of the challenges encountered in oil & gas processing. I am also grateful to them for giving me the opportunity to work with them in the Research & Technology Center of Equinor, in Trondheim, Norway as part of an internship. Apart from excellent engineers, they are also exceptional people, who welcomed me warmly in Norway and made my stay there enjoyable.

I would also like to express my gratitude to my colleagues at the Thermodynamics and Transport Laboratory, who served as a second family to me during my work there. I am indebted to Dr. Vicky Louli for her valuable advices and support. I would also like to thank senior staff members Dr. Georgia Pappa and Dr. Christos Boukouvalas for their help, and post-doc researcher Dr. Myrto Dardavila. I am also grateful to my once fellow PhD students, who now bear the Dr. title, namely Dr. Nefeli Novak, Dr. Eirini Petropoulou and Dr. Eleni Boli, for their support, advices, and help with algorithmic problems, especially during my early PhD days. I would also like to thank my current fellow PhD students, Anthi Plakia, Ioulia Georgiopoulou, Akis Tasios and Nikos Prinos, as well as the diploma thesis students with whom we collaborated closely, namely Verdiana Garofalo and Marina Panteli. All members of the lab, past and present, created a very friendly and inspirational work environment, which is rare to find, and I am glad to call them friends. I will always cherish the funny moments we shared in the lab, especially during the lunch breaks, which helped me go through the hardships of the PhD.

Last but not least, I would like to express my deepest gratitude to my family for their unceasing support, encouragement, counsel, and for the sacrifices they made for me to be able to achieve my dreams.

A large and important life chapter is hereby ended, but with eagerness and anticipation of what great might come next…

Athens, March 2021

Vassilis Koulocheris

Table of Contents

Abstract v
Περίληψη viii
Acknowledgements xii
Table of Contents xiii
List of Tables xviii
List of Figures xxi
Abbreviations xxv
1. Introduction 1
1.1 Motivation 1
1.2 Objectives 2
1.3 Thesis structure 3
2. Mercury: A toxic pollutant 5
2.1 The properties of mercury 5
2.2 Mercury related health and safety issues 6
2.3 Mercury in nature 8
2.4 Mercury in fossil fuels 11
2.5 Hg partitioning during NG processing 13
2.6 Mercury reactions in hydrocarbons 14
2.7 Analytical methods for Hg measurement 15
2.7.1 Overview 15
2.7.2 Analytical techniques 15
2.7.3 Challenges for experimenters 19
3. Natural gas processing 21
3.1 Introduction 21
3.2 The natural gas value chain 22
3.3 Basic processes 25
3.3.1 Inlet separation 26
3.3.2 Condensate stabilization 26
3.3.3 NGL recovery & fractionation 26
3.3.4 Acid gas removal 27
3.3.5 Water removal 27
3.3.6 Mercury removal 28

4. Phase & chemical equilibria 30
4.1 Thermodynamic equilibrium 30
4.2 Phase equilibrium 31
4.2.1 Vapor – liquid equilibrium 32
4.2.2 Liquid – liquid equilibrium 33
4.2.3 Solid solubility 33
4.3 Chemical reaction equilibrium 34
4.3.1 Gas phase reactions 36
4.3.2 Liquid phase reactions 36
4.4 Stability 37
5. Algorithms for chemical & phase equilibria 40
5.1 Phase equilibrium algorithms 40
5.1.1 Bubble point pressure calculation 41
5.1.2 Dew point temperature calculation 42
5.1.3 Two-phase PT flash algorithm 43
5.1.4 Multiphase PT flash algorithm 44
5.2 Simultaneous chemical & phase equilibrium algorithm 48
5.2.1 Working equations 48
5.2.2 Reference state chemical potential 50
5.2.3 Initialization 51
5.2.4 Procedure 52
6. Thermodynamic models 54
6.1 Equations of state 54
6.1.1 Virial equation of state 54
6.1.2 Cubic equations of state 55
6.2 *a*-functions 56
6.3 Activity coefficient models 57
6.3.1 The NRTL model 58
6.3.2 The UNIQUAC model 59
6.4 Advanced models 60
6.5 Mixing rules 60
6.5.1 Virial EoS for mixtures 61
6.5.2 The van der Waals one fluid theory 61

6.5.3 The Universal Mixing Rules 62
6.6 The UMR-PRU model 64
6.7 The PPR78 model 64
6.8 Thermodynamic models for mercury 65
7. Thermodynamic modelling of elemental mercury solubility in natural gas components 67
7.1 Introduction 67
7.2 Pure Hg^0 vapor pressure 67
7.3 Description of Hg^0 solubility in binary mixtures 68
7.3.1 Database with experimental Hg^0 solubilities & evaluation 68
7.3.2 Results & discussion 72
7.4 Prediction of Hg^0 solubility in multicomponent mixtures 81
7.5 Conclusions 85
8. Thermodynamic modelling of hydrogen vapor-liquid equilibrium with oil & gas components 87
8.1 Introduction 87
8.2 *α*-function consistency and pure H_2 property estimation 88
8.3 VLE description in binary mixtures of hydrogen 89
8.4 Prediction of hydrogen VLE in multicomponent systems 93
8.5 Conclusions 96
9. Mercury chemical & phase equilibria in natural gas 97
9.1 Introduction 97
9.2 Mercury solubility in typical natural gas and condensate mixtures 97
9.3 Mercury reaction with H_2S in natural gas and condensate mixtures 101
9.3.1 Thermodynamic analysis of the reaction 101
9.3.2 CPE calculations in typical natural gas and condensate fluids 104
9.4 Conclusions 107
10. Simulation of mercury distribution in an offshore natural gas processing plant 109
10.1 Introduction 109
10.2 Process description 109
10.3 Simulation of mercury distribution in the overall process 110
10.3.1 Mercury mass balance calculations 113
10.3.2 Description of the studied scenarios 115
10.3.3 Simulation of Hg distribution in the overall process without reaction 116

10.3.4 Investigation of the effect of fluid characterization 123
10.3.5 Simulation of Hg distribution with reaction 125
10.4 Simulation of Hg distribution in TEG dehydration & regeneration process 137
10.4.1 Process description 137
10.4.2 Mercury mass balance calculations 138
10.4.3 Simulation of Hg distribution 139
10.5 Mercury distribution in MEG regeneration process 143
10.5.1 Process description 143
10.5.2 Simulation of Hg distribution 144
10.6 Validation of the simulation 146
10.6.1 Fluid compositions 146
10.6.2 Stream flowrates 149
10.6.3 H_2S and CO_2 in process gases 150
10.7 Conclusions 151
11. Phase and chemical equilibrium in systems involving non-reactive and reactive azeotropes 155
11.1 Introduction 155
11.2 Thermodynamic modelling 156
11.3 Cyclohexane synthesis 157
11.4 MTBE synthesis 158
11.5 Acetic acid/isopropanol esterification 165
11.6 Conclusions 170
12. Conclusions & future work 171
12.1 Conclusions 171
12.2 Future work 174
References 175
Appendix A: The Hayden-O' Connell method 189
Appendix B: Model parameters 193
Appendix C: Database with experimental data 198
Appendix D: Simulation data 201
Appendix E: Publications 204
Appendix References 205

List of Tables

Table 2.1. Melting points, boiling points and solubilities of the most common Hg compounds [2, 6]. 6
Table 2.2. Analytical techniques for the determination of the concentration of Hg & its species [23]. 16
Table 2.3 Analytical methods for Hg speciation in hydrocarbon matrices [24]. 18
Table 2.4. Effect of container material on loss rate of Hg species [27]. 20
Table 3.1. Natural gas composition depending on origin (% mole) [29]. 21
Table 3.2. Specifications for rich gas transport (offshore to onshore) [31]. 24
Table 3.3. Specifications for sales gas transport [31]. 24
Table 4.1. Equilibrium criteria for a closed system [35]. 30
Table 5.1. Different types of equilibrium calculations based on input and output variables. 40
Table 6.1. Expressions for ac and b parameters of cubic EoS. 56
Table 6.2. α-functions employed in this work. 56
Table 6.3. Consistency criteria for alpha functions of cubic EoS [55]. 57
Table 7.1. Calculated parameters of pure Hg^0 for Twu and Mathias-Copeman α-functions employed in SRK and PR EoS, respectively, and corresponding deviations in vapor pressure. 68
Table 7.2. UNIFAC interaction parameters between mercury and other groups determined in this work for UMR-PRU model. 72
Table 7.3. Regressed coefficients estimating binary interaction parameters between Hg^0 and hydrocarbons heavier than ethane via Eq. 7.2 for SRK-Twu and PR-MC models. 73
Table 7.4. Optimum and generalized k_{ij} values for SRK-Twu and PR-MC along with their corresponding deviations in Hg^0 mole fraction compared with deviations yielded by the UMR-PRU model. 74
Table 7.5. Estimated k_{ij} values between Hg^0 and polar compounds for SRK-Twu and PR-MC models along with pertinent deviations in Hg^0 mole fraction compared with deviations yielded by the UMR-PRU model. 75
Table 7.6. Prediction results in experimental data sets excluded from the correlation database (APPENDIX) with SRK-Twu, PR-MC, and UMR-PRU. Generalized k_{ij}'s employed for SRK-Twu and PR-MC. 76
Table 7.7. Database with experimental Hg^0 solubilities in hydrocarbon mixtures. 82
Table 7.8. Database with experimental Hg^0 solubilities in polar mixtures. 82
Table 7.9. Compositions (% mol) of multicomponent systems examined in this work. 82
Table 7.10. Model prediction results in multicomponent hydrocarbon mixtures. Generalized k_{ij}'s employed for SRK-Twu and PR-MC. 83
Table 7.11. UNIFAC interaction parameters determined in this work between water/polar components to be used in LLE calculations for mercury systems with UMR-PRU model. 85

Table 7.12. Model prediction results in polar mixtures. Temperature-dependent k_{ij}'s employed for SRK-Twu and PR-MC.....85
Table 8.1. Correlation and prediction results for pure hydrogen properties with PR EoS and different *α*-functions.....89
Table 8.2. UNIFAC interaction parameters between hydrogen and other groups determined in this work for UMR-PRU model.....90
Table 8.3. VLE results with UMR-PRU and PPR-78 models.....90
Table 8.4. Experimental data and prediction results regarding hydrogen mixtures with UMR-PRU and PPR78 models.....95
Table 9.1. Molar composition (%) and C_{7+} fraction properties of the fluids studied in this work.....98
Table 9.2. Thermodynamic properties of reaction (Eq. 9.1) components at 298.15 K and 1 atm.....102
Table 9.3. Constants A and B used in Eq. 9.4 for calculating the equilibrium constant of the reaction between Hg^0 and H_2S.....103
Table 10.1. Process conditions according to real process information.....112
Table 10.2. Estimated elemental (Hg^0) and total (THg) mercury mass flowrates at plant outlets, based on field campaign measurements and actual process data (flowrates).....113
Table 10.3. Estimated elemental (Hg^0) and total (THg) mercury mass flowrates at test separator (10-001) outlets, based on field campaign measurements and actual process data (flowrates).....114
Table 10.4. Estimated elemental (Hg^0) and total (THg) mercury mass flowrates at the stabilizer (10-008), based on field campaign measurements and actual process data (flowrates).....115
Table 10.5. Scenarios for studying mercury distribution in the offshore NG processing platform.....116
Table 10.6. Elemental mercury concentration in selected plant streams as calculated with UMR-PRU and SRK-Twu.....117
Table 10.7. Distribution of elemental mercury as % of total amount entering each separator according to scenario 3.....120
Table 10.8. Mercury concentration in selected plant streams as calculated with UMR-PRU and TTPL characterization method [69] (no Hg reaction considered).....124
Table 10.9. Hg^0 distribution as % of total amount entering each separator according to scenario 3.....124
Table 10.10. Elemental mercury concentration in selected plant streams as calculated with SRK-Twu and UMR-PRU with scenario 3 and liquid phase reaction (K_{eq} from data by Robie et al. [127]).....128
Table 10.11. Distribution of elemental mercury as percent of total amount entering each separator according to scenario 3 with liquid phase reaction (K_{eq} from data by Robie et al. [127]).....130

Table 10.12. Conversion percent and produced HgS amount at each separator as calculated with SRK-Twu and UMR-PRU according to scenario 3 (K_{eq} from data by Robie et al. [127]). 134
Table 10.13. Conversion percent and produced HgS amount at each separator as calculated with SRK-Twu according to scenario 3 and the three different equilibrium constants calculated in Chapter 9 (Table 9.3).....135
Table 10.14. Estimated elemental mercury mass flowrates at glycol contactor A (30-101), based on field campaign measurements and actual process data (flowrates). 138
Table 10.15. Estimated elemental mercury mass flowrates at glycol contactor B (30-201), based on field campaign measurements and actual process data (flowrates). 138
Table 10.16. Hg^0 concentration in TEG dehydration and regeneration process streams as calculated with UMR-PRU and SRK-Twu.....142
Table 10.17. TEG dehydration and regeneration process parameters. 142
Table 10.18. Hg^0 mass balance in glycol flash drum (30-111) as calculated from field campaign measurements and UMR-PRU simulation flowrates. 143
Table 10.19. Hg^0 concentration in MEG regeneration process streams as calculated with SRK-Twu and UMR-PRU. 146
Table 10.20. Flowrates (MSm^3/d) of plant gas streams as calculated with SRK-Twu and UMR-PRU. 149
Table 10.21. Flowrates (Sm^3/d) of plant condensate streams as calculated with SRK-Twu and UMR-PRU. 149
Table 10.22. Flowrates (Sm^3/d) of plant water streams as calculated with SRK-Twu and UMR-PRU. 150
Table 10.23. H_2S and CO_2 concentrations in selected plant streams as calculated with UMR-PRU and SRK-Twu.....151
Table 11.1. CPE results in mole fractions for the cyclohexane synthesis system at 500 K and 30 atm with Peng-Robinson EoS (k_{ij} = 0, K_{eq} = 184.93). 158
Table 11.2. VLE results for binary and ternary mixtures involved in MTBE synthesis. 159
Table 11.3. Parameters used in Eq. 11.4 for the calculation of the equilibrium constant of the MTBE synthesis reaction in the vapor and liquid phase. 160
Table 11.4. CPE results for vapor phase MTBE synthesis: deviations from molecular simulation data by Lísal et al. [159] (5 data points).....160
Table 11.5. CPE results for liquid phase MTBE synthesis: deviations ($AADx^a$) from experimental data by Izquierdo et al.[143] (17 data points). 160
Table 11.6. VLE and LLE results for mixtures involved in acetic acid/isopropanol esterification. 166
Table 11.7. Calculated and experimental reactive azeotrope composition in the acetic acid/isopropanol esterification system at 1 atm. 169

List of Figures

Figure 1.1. Mercuriferous belts and hot spots globally [4]. 2
Figure 2.1. Left image: A ruptured heat exchanger inlet nozzle due to mercury corrosion [11]; right image: Mercury-induced liquid metal embrittlement on a brazed aluminum heat exchanger [12]. 8
Figure 2.2. The global mercury cycle [5]....9
Figure 3.1. The natural gas value chain [31]....23
Figure 3.2. A typical PFD of an offshore gas processing plant [31]. 25
Figure 3.3. Block flow diagram of a typical onshore gas processing plant [31]. 26
Figure 3.4. Parallel mercury removal units (fixed-bed reactors) at a Thai gas plant [10]. 29
Figure 4.1. Gibbs energy of mixing for binary mixture CH_4/H_2S at 190 K and 45.6 bar [35]...38
Figure 4.2. Tangent plane distance plot for binary mixture CH_4/H_2S at 190 K and 45.6 bar at z_1=0.2 [35]. 39
Figure 5.1. Flowchart of bubble point pressure (BPP) algorithm. 42
Figure 5.2. Flowchart of dew point temperature (DPT) algorithm. 43
Figure 5.3. Two-phase PT flash algorithm. 44
Figure 5.4. Multiphase PT flash algorithm flowchart. 46
Figure 5.5. Excess Gibbs energy of mixing for CH_4/H_2S binary mixture at 190 K and 40.5 bar [35]. 47
Figure 5.6. Simultaneous chemical & phase equilibrium algorithm flowchart. 53
Figure 7.1. Vapor pressure of elemental mercury vs. temperature as calculated with PR-MC and SRK-Twu against pseudo-experimental data by DIPPR [85]. 68
Figure 7.2. Elemental mercury solubility in paraffinic, naphthenic and aromatic hydrocarbons vs carbon number at 293.15 K [86, 90]. 70
Figure 7.3. Elemental mercury solubility in polar compounds vs. temperature. (△): methanol; (□): MEG; (o): TEG. Blue markers: data from Gallup et al. [3]; red markers: data from Clever et al. [86]; green markers: data from Li et al. [89]. 70
Figure 7.4. Elemental mercury solubility in water vs. temperature. (o): data from Clever et al. [86]; (x): data from Gallup et al. [3]. 71
Figure 7.5. Hg^0 solubility in CO_2 at 243.15, 258.15, 268.15, 273.15, 278.15, 283.15, 288.15, 293.15, 298.15, 303.15 and 323.15 K as calculated with UMR-PRU, SRK-Twu, and PR-MC models. (O): exp. data from Chapoy et al. [84]; (△): exp. data from Yamada et al. [91]. 76
Figure 7.6. Hg^0 solubility in nitrogen as calculated with UMR-PRU, SRK-Twu, and PR-MC models. Exp. data from Chapoy et al. [84]. (Exp. data uncertainties not visible above 258.15 K.) 77
Figure 7.7. Hg^0 solubility in methane at 243.15, 258.15, 263.15, 268.15, 273.15, 278.15, 283.15, 288.15, 293.15, 298.15, 303.15 and 323.15 K as calculated with UMR-PRU, SRK-Twu, and PR-MC models. (O): exp. data from Chapoy et al. [84]; (△): exp. data from Yamada et al. [91]. (Exp. data uncertainties not visible above 243.15 K.) 77

Figure 7.8. Hg^0 solubility in ethane at 244.15, 258.15, 268.15, 273.15, 278.15, 283.15, 288.15, 293.15, 298.15, 303.15 and 323.15 K as calculated with UMR-PRU, SRK-Twu, and PR-MC models. (O): exp. data from Chapoy et al. [84]; (△): exp. data from Yamada et al. [91]. 78
Figure 7.9. Hg^0 solubility in (a) propane, (b) n-pentane, (c) n-octane, (d) n-dodecane, (e) 2,2-dimethyl butane, and (f) cyclohexane vs. temperature. Generalized k_{ij}'s employed for SRK-Twu and PR-MC. 79
Figure 7.10. Hg^0 solubility in (a) toluene, (b) o-xylene, (c) water, (d) methanol, (e) MEG, and (f) TEG vs. temperature. Generalized k_{ij}'s used for hydrocarbon solvents and temperature-dependent k_{ij}'s used for polar solvents with SRK-Twu and PR-MC. 80
Figure 7.11. Hg^0 solubility in mixtures 1-3 as calculated with UMR-PRU, SRK-Twu and PR-MC models against exp. data by Chapoy et al. [79] at 4 isotherms: (●): 243.15 K; (▲): 273.15 K; (■): 298.15 K; (**X**): 323.15 K; solid red line: UMR-PRU; black dashed line: SRK-Twu; black dotted line: PR-MC. (Exp. data uncertainties not visible above 243.15 K.).....84
Figure 8.1. Isothermal dew and bubble point curves for 6 binary mixtures with UMR-PRU: (a) H_2 (1) – CO_2 (2), (b) H_2 (1) – CH_4 (2), (c) H_2 (1) – C_2H_6 (2), (d) H_2 (1) – C3 (2), (e) H_2 (1) – cyC6 (2), (f) H_2 (1) – benzene (2). (**x**): experimental bubble points, (**+**): experimental dew points, (o)**:** experimental critical points, solid lines: model results. 92
Figure 8.2. Isothermal dew and bubble point curves for 2 binary mixtures with UMR-PRU: (a) H_2 (1) – nC16 (2), (b) H_2 (1) – iC4 (2). (**x**): experimental bubble points, (**+**): experimental dew points, solid lines: model results. 93
Figure 8.3. Experimental points and VLE results for 5 ternary mixtures of hydrogen: (a) $H_2/CH_4/C_2H_6$ at 144.26 K and 68.95 bar, (b) H_2/CH_4/C3 at 199.82 K and 34.47 bar, (c) $H_2/N_2/CH_4$ at 120 K and 100 bar, (d) $H_2/CO_2/CH_4$ at 258.15 K and 68.95 bar, (e) H_2/CO_2/nC5 at 273.15 K and 68.95 bar. (▲): exp. mole fractions in liquid phase; (●): exp. mole fractions in vapor phase; dashed lines: exp. tie lines; solid red lines: UMR-PRU model predictions. 94
Figure 9.1. Mercury solubility vs. temperature at constant pressure with UMR-PRU. Blue line: vapor phase; Orange line: liquid phase; Green line: aqueous phase. 99
Figure 9.2. Mercury solubility vs. pressure at constant temperature with UMR-PRU. Blue line: vapor phase; Orange line: liquid phase; Green line: aqueous phase. 100
Figure 9.3. Equilibrium constant for $Hg^0 + H_2S$ reaction as function of temperature. Solid lines: vapor phase reaction; Dashed lines: liquid phase reaction. 103
Figure 9.4. Conversion of elemental mercury to β-HgS vs. temperature for Fluid 1 at 50 bar with different reaction equilibrium constants: (a) vapor phase reaction, (b) liquid phase reaction. Solid lines: UMR-PRU model predictions; Dashed line: maximum temperature at which an aqueous phase is present. 104
Figure 9.5. Conversion of elemental mercury to β-HgS vs. temperature for Fluid 4 at 45 bar with different reaction equilibrium constants: (a) vapor phase reaction, (b) liquid phase reaction. Solid lines: UMR-PRU model predictions; Dashed line: maximum temperature at which an aqueous phase is present. 105

Figure 9.6. Conversion of elemental mercury to *β*-HgS vs. temperature for Fluid 4 at different pressures: (a) vapor phase reaction (K_{eq}=KG2), (b) liquid phase reaction (K_{eq}=KL1). Solid lines: UMR-PRU model predictions; Dashed line: maximum temperature at which an aqueous phase is present.....106
Figure 9.7. Initial overall Hg^0 concentration that is required for saturation of Fluid 4 vs. temperature assuming liquid phase reaction with different equilibrium constants (45 bar). 107
Figure 10.1. Process flow diagram of the simplified simulation of the offshore NG processing platform. 111
Figure 10.2. Elemental mercury distribution in plant outlets as percentage of total Hg^0 exiting the plant. The distribution is estimated based on the field campaign measurements and actual process data (flowrates). 114
Figure 10.3. Hg^0 concentration in selected plant streams as calculated with UMR-PRU and SRK-Twu according to scenario 3 against field measurements. 118
Figure 10.4. Distribution of elemental mercury with UMR-PRU and SRK-Twu as % of total amount entering each separator according to scenario 3. 119
Figure 10.5. Elemental mercury distribution in plant outlets as percentage of total Hg^0 entering the plant. Calculations based on scenario 3 with SRK-Twu. 122
Figure 10.6. Elemental mercury distribution in plant outlets as percentage of total Hg^0 entering the plant. Calculations based on scenario 3 with UMR-PRU. 123
Figure 10.7. Elemental mercury distribution in plant outlets as percentage of total Hg^0 entering the plant. Calculations based on scenario 3 with UMR-PRU and TTPL characterization method [69]. 125
Figure 10.8. Attaching a reaction set to a fluid package in UniSim.....126
Figure 10.9. Inserting components and stoichiometric coefficients for a reaction in UniSim. 126
Figure 10.10. Defining calculation basis, reaction phase and equilibrium constant in UniSim. 127
Figure 10.11. Elemental mercury concentration in selected plant streams as calculated with UMR-PRU and SRK-Twu according to scenario 3 with liquid phase reaction (K_{eq} from data by Robie et al. [127]). UMR-PRU results annotated with (*) are not fully representative, because stabilizer (10-008) is solved as isothermal.....131
Figure 10.12. Distribution of elemental mercury with UMR-PRU and SRK-Twu as percent of total amount entering each separator according to scenario 3 with liquid phase reaction (K_{eq} from data by Robie et al. [127]).....132
Figure 10.13. Elemental mercury distribution in plant outlets as % of total Hg^0 entering the plant. Calculations based on scenario 3 with SRK-Twu and assuming liquid phase reaction (K_{eq} from data by Robie et al. [127]).....136

Figure 10.14. Elemental mercury distribution in plant outlets as % of total Hg^0 entering the plant. Calculations based on scenario 3 with UMR-PRU and assuming liquid phase reaction (K_{eq} from data by Robie et al. [127]). 136
Figure 10.15. Elemental mercury distribution in plant outlets as % of THg exiting the plant. The distribution is estimated based on the field campaign measurements and actual process data (flowrates) (K_{eq} from data by Robie et al. [127]). 137
Figure 10.16. PFD of simplified TEG dehydration & regeneration unit (Train A) in UniSim. 140
Figure 10.17. PFD of simplified MEG regeneration unit in UniSim. 145
Figure 10.18. Measured and calculated composition of stabilizer (10-008) inlet. 147
Figure 10.19. Measured and calculated composition of stabilizer (10-008) vapor outlet....147
Figure 10.20. Measured and calculated composition of amine contactor (20-103) inlet. ...148
Figure 10.21. Measured and calculated composition of export gas. 148
Figure 11.1. T-X-Y diagram for isobutene in MTBE synthesis system at 5 bar together with molecular simulation data points from Lísal et al. [159]. (O): transformed mole fractions in liquid phase; (△): transformed mole fractions in vapor phase; (■): pseudo-reactive azeotrope; solid lines: UMR-UNIQUAC predictions. K_{eq} from Lísal et al. [159]. 162
Figure 11.2. X-Y diagram for isobutene and methanol in MTBE synthesis system at 5 bar together with molecular simulation data points from Lísal et al. [159]. (O): transformed mole fractions of methanol; (△): transformed mole fractions of isobutene; solid line: UMR-UNIQUAC predictions for isobutene; dashed line: UMR-UNIQUAC predictions for methanol. K_{eq} from Lísal et al. [159].....162
Figure 11.3. Residue curves in transformed compositions as predicted with UMR-UNIFAC for the MTBE synthesis system with n-butane present as inert at 1 atm. K_{eq} from Tejero et al. [160]. 164
Figure 11.4 Residue curves in transformed compositions as predicted with UMR-UNIFAC for the MTBE synthesis system with n-butane present as inert at 7 atm. K_{eq} from Tejero et al. [160]. 164
Figure 11.5. Residue curves in transformed compositions as predicted with virial/UNIQUAC for the acetic acid/isopropanol esterification system at 1 atm (K_{eq} = 8.7). The temperatures shown are those predicted by the model.....168
Figure 11.6. Residue curves in transformed compositions as predicted with UMR-UNIQUAC for the acetic acid/isopropanol esterification system at 1 atm (K_{eq} = 8.7). The temperatures shown are those predicted by the model.....168

Abbreviations

AAD	Average Absolute Deviation
AARD	Average Absolute Relative Deviation
BBP	Bubble Point Pressure
BIP	Binary Interaction Parameter
CAPE	Computer Aided Process Engineering
CAPEX	Capital Expenditure
CN	Carbon Number
CPA	Cubic Plus Association
CPE	Simultaneous Chemical and Phase Equilibria
EoS	Equation(s) of State
EoS/G^E	Equation(s) of State coupled with excess Gibbs energy models through advanced mixing rules
HSE	Health, Safety, and Environment
IP	Interaction Parameter
LLE	Liquid-Liquid Equilibrium
LNG	Liquefied Natural Gas
MC	Mathias-Copeman α-function of cubic equations of state
MRU	Mercury Removal Unit
MW	Molecular Weight
NG	Natural Gas
NGL	Natural Gas Liquids
NRTL	Non-Random Two-Liquid activity coefficient model
OPEX	Operating Expenditure
PFD	Process Flow Diagram
PPR78	Predictive Peng-Robinson 1978 equation of state
PR	Peng-Robinson equation of state
PR-MC	Peng-Robinson equation of state coupled with Mathias-Copeman α-function
SAFT	Statistical Associating Fluid Theory
SRK	Soave-Redlich-Kwong equation of state
SRK-Twu	Soave-Redlich-Kwong equation of state coupled with Twu α-function
THg	Total mercury
TTPL	Thermodynamics and Transport Phenomena Laboratory
UMR	Universal Mixing Rules
UMR-PRU	Universal Mixing Rules combined with PR EoS and UNIFAC
UNIFAC	UNIQUAC functional group activity coefficient model
UNIQUAC	UNIversal QUAsi-Chemical activity coefficient model
vdW1f	Van der Waals one fluid mixing rules
VLE	Vapor-Liquid Equilibrium
VLLE	Vapor-Liquid-Liquid Equilibrium

1. Introduction

1.1 Motivation

Mercury and its species occur naturally in all fossil fuels, such as natural gas (NG), crude oil, and coal. The concentration of mercury in oil and gas varies depending on source, but it is usually of the order of a few parts per billion (ppb) [2]. Despite this, mercury and its species can cause significant problems during oil & gas processing and, therefore, its levels in a plant must be monitored. Mercury is toxic to living organisms and, for this reason, strict regulations are in place regarding mercury emissions to the environment from industrial activities. In addition, mercury can cause catalyst poisoning and corrode the equipment through various mechanisms, such as Liquid Metal Embrittlement (LME) [1]. Indicative of the risk Hg poses to process is the fact that until today about 10 industrial accidents have been recorded, which were caused by corrosion of equipment by mercury [3].

In the past, hydrocarbons with elevated mercury concentration were linked with a limited number of reservoirs around the world [3]. A depiction of mercuriferous belts and hot spots globally is presented in Figure 1.1. For this reason, additional measures for mercury management were taken only in plants that processed oil & gas originating from these locations. In fact, due to this need for utilization of special processes for the removal of mercury, hydrocarbons with increased Hg concentration are sold in the global market at significantly lower prices [3]. In recent years, deeper drillings have led to the production of hydrocarbons with increased mercury concentrations even in areas where previously this phenomenon had not been observed [3]. Consequently, the implementation of measures for the effective management of Hg becomes necessary in an increasing number of oil and gas processing plants.

For the proper management of mercury in oil & gas treatment plants to become possible, it is necessary to know the distribution of mercury in the different phases during drilling and topside treatment processes. Scientific research in this field is currently active. Although some thermodynamic models describing the distribution of elemental mercury in NG have already been proposed, there are still aspects of the issue that are not sufficiently covered in the literature. For example, although in the vapor and liquid streams of the NG processing plants various mercury forms other than elemental, such as HgS, $HgCl_2$, MeHg, Me_2Hg etc. have been identified, their distribution has not been described so far with any thermodynamic model. The existence of other forms of mercury apart from the elemental indicates that it may also participate in reactions during NG processing, which have not been investigated in the open literature nor have they been included in any Hg behavior prediction model. The development of such a model becomes even more complicated if one takes into account the adsorption/chemisorption of mercury on piping and equipment walls, and also the great variation in pressure and temperature along the natural gas value chain.

Another point that needs to be highlighted is the difficulty encountered during the determination of the amount of elemental mercury and its compounds in different systems via various analytical methods. It has been observed that the measurements can be affected by the material of sample vessels, the presence of oxygen, reagent impurities etc. [2]. This, combined with the often confidential nature of the oil industry data, make challenging the search for reliable data regarding the distribution and concentrations of mercury and its compounds in oil and gas processing plants.

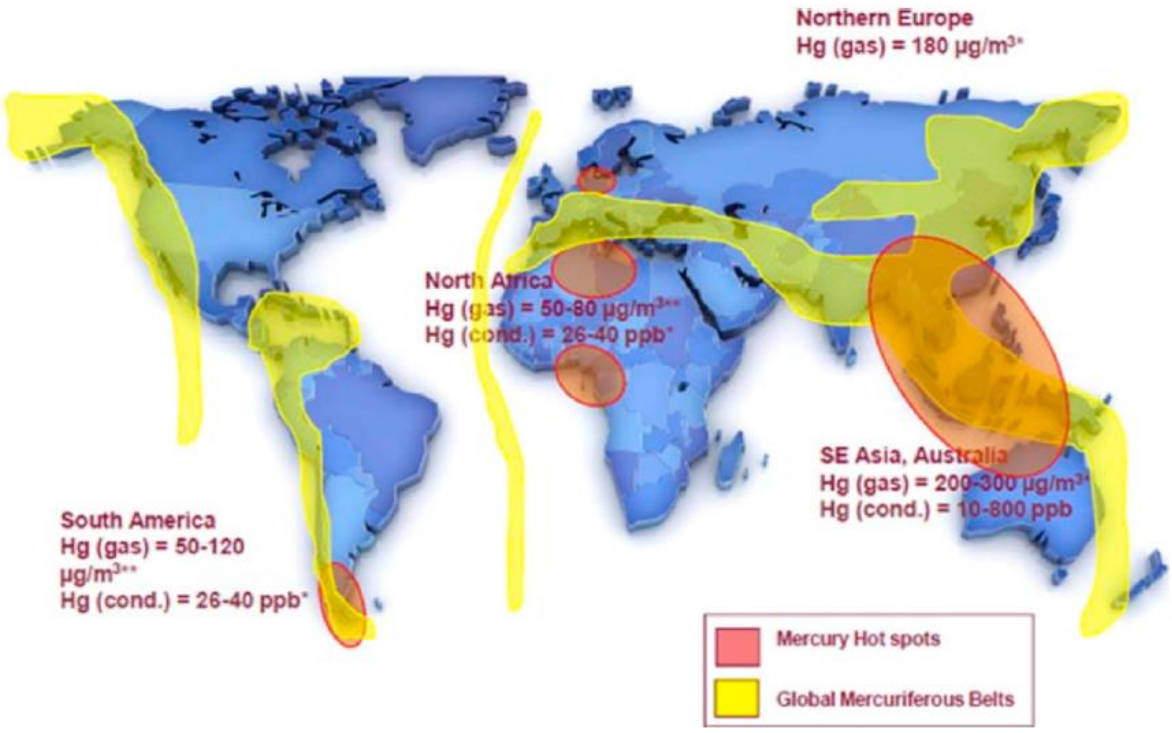

Figure 1.1. Mercuriferous belts and hot spots globally [4].

1.2 Objectives

The aim of this thesis is to develop a thermodynamic model that can accurately describe the simultaneous chemical & phase equilibria (CPE) of mercury in natural gas, and its application in the simulation of Hg distribution in a natural gas processing plant. The objectives of this thesis are:

- Assessment and development of widely used equations of state for describing the phase & chemical equilibria of mercury in natural gas.
- Thermodynamic study of possible reactions between mercury and sulfur compounds present in natural gas, which can lead to solid HgS formation.
- Development of algorithms for performing multiphase flash and simultaneous chemical & phase equilibria calculations.

- Implementation of the developed thermodynamic models in simulating mercury distribution in an existing natural gas processing plant.

1.3 Thesis structure

The structure of the thesis is as follows:

In Chapter 2, a literature review on mercury is conducted, and information is provided regarding its physical and chemical properties, its environmental cycle, its occurrence and partitioning in oil & gas, as well as the analytical methods for determining its concentration in various matrices.

In Chapter 3, the basic elements of natural gas processing are outlined. The key points and typical flow diagrams of processes, such as inlet separation, condensate stabilization, NGL fractionation and removal processes of contaminants are provided.

In Chapter 4, the theoretical background behind thermodynamic equilibrium is given with the pertinent mathematical formalism. The conditions and different types of equilibrium are also explained.

In Chapter 5, the algorithms for solving the different types of equilibria are outlined. The working equations and flowcharts for classical calculations in binary systems, such as bubble and dew point calculations or flash are provided. Furthermore, the multiphase flash and simultaneous chemical & phase equilibria algorithms are developed.

In Chapter 6, the thermodynamic models employed in this work are presented in detail. These include the virial equation of state, the widely used Soave-Redlich-Kwong and Peng-Robinson cubic equations of state, the UMR-PRU EoS/G^E model, the PPR-78 model, as well as the UNIQUAC and NRTL activity coefficient models. Different formulations for a-functions of cubic equations of state are also presented, along with consistency criteria.

In Chapters 7 and 8, the UMR-PRU model is extended to mixtures involving mercury and hydrogen, respectively. The mixtures of interest are gases (CO_2, N_2), hydrocarbons, and polar components that are commonly used for natural gas processing, such as glycols and amines. The performance of UMR-PRU is compared with that of other popular models, such as SRK, PR and PPR-78.

In Chapter 9, the developed multiphase flash algorithm is employed for calculating the saturation concentration of mercury in typical natural gas mixtures. These calculations are of high interest for NG processing applications in order to avoid mercury dropout which can cause health, safety and environmental issues. In this chapter, the possible equilibrium reaction between mercury and hydrogen sulfide in natural gas is studied. The equilibrium constant of the reaction is calculated, and the developed simultaneous chemical & phase

equilibria algorithm is employed for calculating the produced HgS amount in typical natural gas mixtures.

In Chapter 10, the UMR-PRU model is employed for simulating the distribution of mercury in an existing natural gas processing plant. The simulation is implemented in UniSim Design, and Hg partitioning in all the involved processes are studied. A simulation is also performed by taking into account mercury reaction with H_2S. The results of UMR-PRU are compared with field measurements, as well as with calculations with the SRK equation of state.

In Chapter 11, the developed simultaneous chemical & phase equilibria algorithm is employed for calculations in complex mixtures involving reactive and non-reactive azeotropes. The purpose of this chapter is to further validate the algorithm, and to check the performance of UMR-PRU as a predictive tool.

Finally, in Chapter 12 the main conclusions of this thesis are summarized, and suggestions for future work are provided.

2. Mercury: A toxic pollutant

2.1 The properties of mercury

Mercury has been known since the antiquity, when it was used for medical purposes as it was considered to prolong life and help maintain good health, as well as making jewelry, ointments, etc. In modern times, until its toxic properties were made known, mercury was used in the manufacture of thermometers, manometers, lamps, batteries, dental alloys, antiseptics, antiparasitics etc. but its use is gradually limited and is expected to be eliminated in the future [5].

Mercury (Hg) is a chemical element with atomic number 80 and atomic mass of 200.59 g/mol. Despite the fact that it is categorized as a heavy metal, mercury has very low melting and boiling points (-38.83°C and 356.7 °C respectively), resulting in being the only metal, which is in liquid form under ambient conditions [6]. Another peculiar property of mercury is its high vapor pressure in relation to its atomic weight. These odd characteristics of Hg can be explained by its particular electron configuration, which imparts properties similar to noble gases, such as weak bonds and relative chemical inertia [7].

In nature, mercury occurs in three oxidative states: 0 (referred to as elemental or metallic mercury, Hg^0), +1 (mercury (I), mercurous) and +2 (mercury (II), mercuric). It is immune to all non-oxidizing acids, but reacts with oxidizing acids, such as concentrated H_2SO_4, HNO_3 and others. Also, it reacts readily with halogens and non-metals, such as sulfur, phosphorus and others, and dissolves other metals (e.g., Au, Ag, Cu, Zn, Al) to form amalgams. An exception is iron, which does not form an amalgam with Hg and is therefore often used as a manufacturing material for mercury storage containers [7]. It is also known that mercury is oxidized and methylated by sulfur-reducing bacteria.

Knowledge of the solubility of mercury is important for understanding its distribution in the different phases during oil & gas processing. Elemental mercury is soluble in hydrocarbons and water. In general, Hg^0 solubility in hydrocarbons increases exponentially with temperature and becomes higher as the molecular weight increases. The solubility of elemental mercury is higher in straight chain hydrocarbons than in branched or olefinic, while in aromatic hydrocarbons it is higher than in alkanes. Regarding polar solvents, which are frequently used in NG processing, Hg^0 solubility follows the general order alcohols> TEG> MEG> amines> water [3]. These observations are further discussed in Chapter 7. When the concentration of Hg^0 in a fluid exceeds its solubility, it can be precipitated as pure liquid (or solid) elemental mercury.

Mercuric sulfide (HgS) is the most common source of mercury in nature. It is found in solid form under ambient conditions, it decomposes above 560°C, and is practically insoluble in water and hydrocarbons. Mercury sulfide occurs naturally in three crystalline forms: a) α-HgS,

also known as cinnabar, which has a red color, triangular crystal structure and is the most widespread form, b) β-HgS (metacinnabar), which has a black color, cubic crystal structure and is formed at low temperatures, and c) γ-HgS (hypercinnabar), which has hexagonal crystal structure and is formed at high temperatures [8].

Some basic properties of the most common Hg compounds are summarized in Table 2.1.

Table 2.1. Melting points, boiling points and solubilities of the most common Hg compounds [2, 6].

Formula	Name	Melting Point (°C)	Boiling Point (°C)	Solubility in H_2O @25°C (ppmw)	Solubility in oil @25°C (ppmw)	Solubility in glycol @25°C (ppmw)
Hg^0	Elemental mercury	-38.8	357	0.05	2	<1
$HgCl_2$	Mercuric chloride	277	302	70,000	>10	>50
$HgSO_4$	Mercuric sulfate	300 (decomp.)		30	N/A[a]	N/A
HgO	Mercuric oxide	500 (decomp.)		50	low	N/A
HgS	Mercuric sulfide	560 (decomp.)		0.01	<0.01	<0.01
HgSe	Mercuric selenide	800 (decomp.)		$-\log K_{sp}=100$	N/A	N/A
$(CH_3)_2Hg$	Dimethylmercury	-42	96	<1	N/A	N/A
$(C_2H_5)_2Hg$	Diethylmercury	-45	170	<1	N/A	N/A
CH_3HgCl	Methylmercury chloride	170 (decomp.)		>10,000	1,000	>1,000

[a] N/A: Not Available

2.2 Mercury related health and safety issues

Mercury is known to be toxic to living organisms and is characterized by the US Environmental Protection Agency (EPA) as a neurotoxin. This property makes it a source of risk not only for the health of workers during production, equipment maintenance, and decommissioning, but also for the general population, through its emission to the environment during oil & gas processing or combustion. Its effect on health depends on many factors, such as the form of mercury, its quantity, the person's age and health status, the route of entry to the body (e.g. through inhalation, ingestion, skin contact) etc. [4].

Short term exposure to high concentrations of mercury vapors can cause damage to the nervous, digestive, respiratory and nasal systems and cause symptoms, such as cough, difficulty in breathing, chest pain, inflammation of the lungs, and even death. Organic mercury compounds, such as methylmercury and dimethylmercury, are also particularly toxic. The symptoms due to long term exposure even to low concentrations of mercury are mainly related to nervous system damage, manifested as lack of muscle coordination, loss of memory, trembling limbs etc. [9]. In Norway, the permissible exposure limit to mercury is 20

µg/m^3 (8-hour time weighted average), while in Malaysia the total inorganic mercury limit in blood is 15 µg/L, according to government guidelines [4].

Mercury also has the ability to corrode the equipment via different mechanisms. Through the formation of amalgams, Hg^0 corrodes the equipment either because the amalgams are more brittle than the pure metal, or due to amalgam reaction with the free water present in the produced hydrocarbons [4, 9]. An example of the latter is when mercury amalgamates with aluminum in the presence of moisture, and the amalgam reacts further with water to produce hydrogen and free Hg, resulting in the corrosion process being repeated until all Al is oxidized [4]:

$$Hg + Al \Rightarrow HgAl \qquad \text{Eq. 2.1}$$

$$HgAl + 6H_2O \Rightarrow Al_2O_3 \cdot 3H_2O + H_2 + Hg \qquad \text{Eq. 2.2}$$

Another mercury corrosion mechanism is that of Liquid Metal Embrittlement (LME), which occurs when liquid mercury comes in contact with other metals. LME involves the adsorption of Hg atoms on stressed surfaces and crack tips along grain boundaries, which causes the interatomic bonds of the substrate to weaken [4]. Cracks initiated by LME can propagate rapidly, particularly near welds [4, 10]. In the case of aluminum, LME can occur if the protective oxide layer (Al_2O_3) is damaged, e.g. through corrosion, abrasion or differential thermal expansion.

Mercury corrosion is a matter of concern in LNG production plants, which commonly use aluminum heat exchangers. Due to the very low process temperatures, mercury can easily drop out as a separate pure liquid or solid phase. Any solid mercury deposits can be converted to liquid or gas when temperature increases, e.g. during plant shutdown or maintenance. For this reason, protective measures should be taken by the personnel to avoid contact with mercury during these operations. Two examples of mercury-induced industrial accidents are 1973 in Skikda, Algeria, where the corrosion of a cryogenic heat exchanger by mercury led to an explosion, and 2004 in Moomba, Australia, where an explosion also occurred due to corrosion of a nozzle by Hg [9]. Some examples of equipment corrosion by mercury are presented in Figure 2.1.

Figure 2.1. Left image: A ruptured heat exchanger inlet nozzle due to mercury corrosion [11]; right image: Mercury-induced liquid metal embrittlement on a brazed aluminum heat exchanger [12].

Mercury can also adsorb on carbon/stainless steel surfaces and complex into the scale/metal grain boundaries [4]. In the presence of hydrogen sulfide, which is commonly found in oil and gas, mercury can react with the iron oxide present on the pipe surface and form a mercury-rich layer [1, 2]. Thus, it is apparent that proper management of mercury in oil & gas processing plants is of paramount importance.

2.3 Mercury in nature

Mercury occurs naturally in the soil in the form of rocks, in the atmosphere mainly as Hg^0, and in the waters in the form of inorganic salts and organic compounds (mainly methylmercury). Mercury has the ability to circulate between these reservoirs, by partaking in its own biogeochemical cycle, which involves transformations through physical, chemical and biological activities as shown in Figure 2.2 [5].

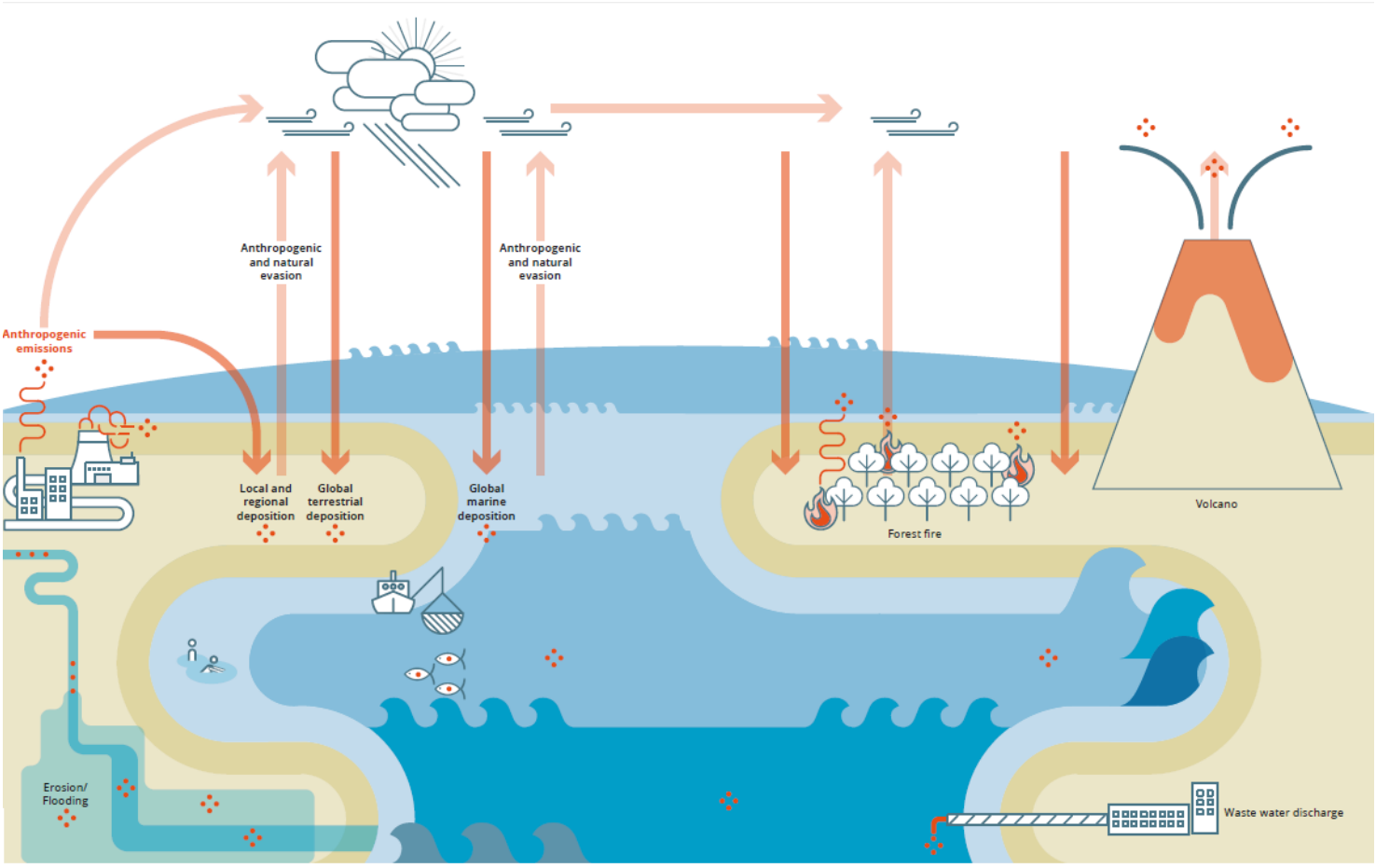

Figure 2.2. The global mercury cycle [5].

The release of Hg into the biosphere is due to both natural and anthropogenic factors. Natural sources include volcanic activity, soil erosion, natural fires, and the dissolution of mercury in the waters. Anthropogenic mercury sources include vinyl chloride manufacture, artisanal gold mining, cement production, oil refining, waste management, metal processing and burning of fuel (coal, wood etc.) [5]. In the past several consumer products used to include mercury, e.g. batteries, lamps, thermometers, dental fillings, computer monitors etc., so their disposal led to mercury release in the environment. However, in the recent decades, mercury use in consumer products has been prohibited in most countries.

The atmosphere is the main vehicle by which mercury is transported around the globe and deposited on land and water. Through the atmosphere mercury can travel and deposit in areas far from industrial activity. Nonetheless, mercury in the atmosphere and soil poses less risks to human and animal health than in water. The aquatic environment is more important because it can act as a long-term storage of mercury, in which Hg can be converted into the much more toxic methylmercury by bacteria. Mercury has an estimated lifetime of 30 years in the upper ocean, while it can remain for centuries in deeper ocean. It is also estimated that

up to 350,000 tn of Hg are stored in oceans worldwide, of which about 2/3 are due to human activities [5].

Methylmercury tends to accumulate in aquatic organisms in a process called bioaccumulation. As predatory animals feed on prey that have already accumulated mercury, Hg concentrations increase when moving up the food chain. This process is known as biomagnification and is found to be more significant in colder waters. To minimize mercury intake by humans, the EU has placed a limit on Hg content of fish for consumption, which is specified as 0.5 mg/kg for most fish species and 1 mg/kg for predatory species such as tuna and swordfish [5].

The estimated global annual release of Hg in the atmosphere from all sources is estimated to be between 2500 tn [5] and 5000 tn [2], with the main sources being small-scale gold mining and coal combustion. In the US, during the period of 1994-95 it was estimated by the EPA that the Hg emissions to the environment were 140 tn, of which 125 tn came from the combustion of coal, waste and petroleum with a distribution of 50/40/10 percent respectively. Nevertheless, the estimates of Hg emissions from oil combustion are questionable due to the lack of data on the concentration of mercury in crude oil and its products [2]. In 2010, the Hg emissions to air were estimated to be about 90 tn in the EU and 50 tn in North America [5], with the main sources being electricity generation and industrial activities. Future projections show that, at best, mercury emissions will stabilize around current levels.

One of the most characteristic examples of mercury health impacts was the incident that occurred in Minamata, Japan during the 1950s when animals and humans showed symptoms of an unknown neurological disease. It was later found that the disease was caused by mercury poisoning due to the contamination of the Minamata Bay by a local factory producing acetic acid, acetaldehyde and other chemicals. The factory was releasing several hundred tonnes of mercury-contaminated effluent over many years into the bay, which was a major local source of food. The Minamata disease -as it would be later called- affected thousands of people and caused the death of hundreds [5].

In 2013 the “Minamata Convention on Mercury” was adopted internationally and has been since signed by 98 parties. The treaty was symbolically named after the Minamata incident and its objective is to ‘protect human health and the environment from anthropogenic emissions and releases of mercury and mercury compounds’. The key focus areas of the convention include the monitoring of mercury use and emissions, the improvement of knowledge about mercury, and the reduction of mercury use and release to the environment [5].

In the EU, the requirements of the Minamata Convention were largely addressed by existing legislation. However, in 2017 further measures were introduced, which banned all new uses

of mercury, set deadlines for ceasing all industrial uses of mercury, and imposed rigorous waste management provisions [5]. In the US, the Environmental Protection Agency issued the first national standards to reduce mercury and other toxic air pollutant emissions from coal- and oil-fired power plants in 2011. These are known as Mercury and Air Toxics Standards (MATS) and set air pollution limits that must be met by facilities [13].

2.4 Mercury in fossil fuels

Mercury and its compounds are a natural component of hydrocarbons of geological origin, such as coal, natural gas and crude oil. The concentration of mercury in crude oil varies considerably depending on its origin. Typically, crude varieties processed in the US contain from 1 to 1000 ppb Hg (by mass), with the mean value close to 5 ppb [2].

Although the geological mechanisms that explain the existence of Hg in crude oil and natural gas have not been thoroughly explored, the most likely explanation is the release of mercury from the Earth's crust through geological forces (pressure and temperature) and its migration in gaseous form in the pockets where crude oil and NG are accumulated [2].

The reservoirs with high concentrations of mercury usually have an increased carbon dioxide content and a reduced content of hydrogen sulfide and mercaptans, but this does not necessarily mean that they are low in sulfur [3]. The increased CO_2 concentration is due to the gradual thermal decomposition of carbonate source rocks commonly found in such deposits. On the other hand, the reduced H_2S and mercaptans content is due to their gradual reaction with elemental mercury to produce β-HgS. In sweeter reservoirs, elemental mercury and its compounds are found in all phases (gas, crude oil, gas condensates and water), while in sour reservoirs Hg is almost entirely in the form of β-HgS [3].

In un-drilled reservoirs one can assume that the solubility of elemental mercury in the various phases is that dictated by the vapor-liquid-liquid equilibrium. During the drilling process, mercury emerges on the surface along with oil and is probably redistributed to the various phases due to temperature and pressure changes. The cooling of the fluids as they migrate to the surface can cause the condensation of Hg^0 in the form of droplets, which are then adsorbed on particles of sand, clays and waxes [3].

The determination of the forms in which mercury can be found in oil and gas is critical to developing methods of managing it. Scientific research in this field is still ongoing, but some methods have already been proposed to categorize Hg forms in oil and gas. A first attempt was made by Wilhelm et al., who proposed the following distinction of mercury forms [2]:

1. Dissolved elemental mercury (Hg^0): Elemental mercury has a solubility in liquid hydrocarbons of some ppm. It can adsorb on metal surfaces (e.g. pipes, vessels) and suspended particles of waxes, clays and sand. Due to the adsorption and the reactions in

which Hg^0 partakes, its measured concentration decreases as the distance from the oil and/or gas well increases.

2. Dissolved organic mercury (RHgR and RHgX, where R = CH_3, C_2H_5 etc. and X = Cl^- or other inorganic anion): Compounds of this type are soluble in crude oil and natural gas condensates. Similarly with Hg^0, they exhibit adsorption tendencies, but due to the difference in boiling points and solubility relative to Hg^0, they are distributed differently in the various distillation fractions. This category includes dialkylmercury (e.g. dimethylmercury, diethylmercury) and monomethylmercury halides (or other inorganic ions).

3. Inorganic mercury salts ($Hg^{2+}X$ or $Hg^{2+}X_2$, where X = inorganic ion): Inorganic salts of Hg are soluble in crude oil and natural gas condensates, but are preferably distributed to the aqueous phase during early separations. Typically, mercury chlorides are about 10 times more soluble than elemental mercury in organic solvents. Compounds of this category may also be suspended in oil or adsorbed on suspended particles.

4. Complexed mercury (HgK or HgK_2, where K = organic acid, porphyrin or thiol): The existence of such compounds in produced hydrocarbons is not fully confirmed and depends mainly on the composition of the fluid in question.

5. Suspended mercury compounds: In this category fall HgS and HgSe compounds, which are insoluble in water and hydrocarbons, but can be found in the form of very small, suspended solid particles.

6. Suspended adsorbed mercury: This category includes inorganic and organic compounds of Hg, which are not dissolved but are adsorbed on inert particles (e.g. sand, waxes). They can usually be easily removed by physical separation methods, such as filtration or centrifugation.

Another categorization is based on the solubility of the forms of mercury. “Dissolved” or “soluble” Hg is that which can pass through a filter with arbitrary pore size (usually 0.2-0.8 μm, ideally 0.45 μm), otherwise it is characterized as “insoluble”. The latter is also called “particulate Hg” and is comprised mainly of β-HgS. A disadvantage of this method is the fact that particulate Hg with size smaller that the pore size of the filter can be falsely characterized as dissolved. In fact, some researchers suggest that there is no true “dissolved” Hg in oil, rather small β-HgS particles [3].

In natural gas, mercury is found almost entirely in its elemental form and at concentrations much lower than saturation, indicating the absence of liquid mercury phase in most reservoirs. In gas condensates, the dominant form of mercury is again the elemental (>50% of total Hg, THg), but there are also Hg compounds, such as suspended HgS and dissolved $HgCl_2$ (10-50% of THg), as well as traces (<1% THg) of dimethyl-mercury and possibly traces of

CH_3HgCl [2]. Finally, in high pH amine solutions, mercury is found in the form of HgS_2H^-, whereas in glycol dehydrators the predominant forms of mercury are of the $Hg(SR)_2$ type [3].

It should be noted that the presence of dialkylmercury (RHgR) compounds in produced hydrocarbons is questionable according to some researchers due to the absence of monoalkylmercury compounds in crude oil samples that would be expected to be similarly abundant with RHgR. The presence of RHgR compounds is usually inferred during analytical measurements when the amount of THg is not equal to the sum of the quantities of individual mercury forms that were determined separately. Although dialkylmercury compounds have been measured directly in some cases, the concentrations were very small and could be attributed to analytical errors [2]. Therefore, the dominant forms of mercury in gas condensate are believed to be Hg^0, $HgCl_2$ and suspended HgS particles [2, 14].

2.5 Hg partitioning during NG processing

Case studies on gas processing plants [14-17] have shown that roughly 80% of elemental mercury is distributed in the export gas, with the remaining 20% following the export condensate. Ezzeldin et al. [14] have also shown that a large portion of Hg is emitted to the environment through gas vents from regeneration processes. However, mercury distribution in a plant is dependent on processing conditions and should be studied on a case-by-case basis.

In polar substances, which are frequently used in the gas processing stages (e.g. sweetening, dehydration etc.), Hg^0 partitioning is expected to follow the general solubility order: alcohols> TEG> MEG> amines> water [3]. As a consequence of this, the presence of common hydrate inhibitors (MEG and methanol) in the aqueous phase can significantly increase its concentration in Hg relative to pure water.

Sabri et al. [18] studied the partitioning of mercury during MEG regeneration process and found that Hg^{2+} (in the form of $HgCl_2$) is unstable in MEG due to the presence of salts and organic species. Three different MEG solutions were examined: laboratory grade MEG, salted laboratory MEG, and MEG from a gas processing plant. The samples were spiked with $HgCl_2$ and then heated at 170°C under atmospheric pressure in order to simulate the plant scale regeneration process. The study results showed that 90% of spiked Hg^{2+} remained in the laboratory grade sample, with the rest migrating to the gas phase as elemental mercury. Interestingly, in the salted lab sample 80% of Hg^{2+} converted to Hg^0 and migrated to the gas phase, indicating the work of reductive mechanisms attributed to the presence of ions in the solution. In the industrial sample, it was found that 50% of Hg^{2+} left the sample as Hg^0. Another observation made during this study, was the precipitation of insoluble solid particles (“tar-like residue”) that contained mercury, which was postulated to be dependent on pH.

As has been already mentioned, inorganic Hg salts which are soluble in crude oil and natural gas condensates are preferably distributed to the aqueous phase during early separations. On the other hand, suspended mercury compounds such as HgS are insoluble in oil and water and must be removed early-on through physical methods (e.g. filtration).

2.6 Mercury reactions in hydrocarbons

While the reactions of mercury in natural waters have been thoroughly investigated by the scientific community for health and environmental reasons, very few information is available in the open literature regarding its reactions in oil and natural gas systems.

Oil & gas processing can potentially cause the transformation of mercury into other forms. Theoretically, high temperature processes (e.g. hydrotreatment) can convert mercury compounds into elemental mercury. On the other hand, there are no known reductive mechanisms that justify the conversion of inorganic or organic mercury compounds into Hg^0 [2].

An explanation for solid metacinnabar (β-HgS) found in tank sediments [2, 3, 17] could be the reaction of Hg^0 with elemental sulfur or sulfuric compounds in NG. After reviewing the relevant literature, it is not clear whether mercury reacts with S or H_2S to form HgS. The phase in which the reactions occur is also unknown. However, if it is assumed that they take place in the gas phase, both reactions have a negative ΔG^o value [19, 20], which suggests that both are feasible under ambient conditions:

$$Hg + S \Leftrightarrow \beta\text{-}HgS,\ \Delta G^o = -47.7\ kJ/mol \qquad \text{Eq. 2.3}$$

$$Hg + H_2S \Leftrightarrow \beta\text{-}HgS + H_2,\ \Delta G^o = -14.3\ kJ/mol \qquad \text{Eq. 2.4}$$

It should be noted that in the article by Gallup et al. [3], a Hg^0 reaction with mercaptans is also mentioned.

According to Gallup et al. [3], the existence of mercury forms of the type HgS_2H^- and $Hg(SR)_2$ in high pH amine solutions and glycols is due to reactions of oxidant traces in gas with H_2S, mercaptans and other species. Depending on the temperature at which the regeneration takes place, these Hg compounds may decompose. These compounds can also continue to react, leading to formation of Hg-rich sludges containing 100s of ppm Hg. In these sludges, mercury is found mostly in the form of β-HgS.

Furthermore, it has been proven that elemental mercury reacts with $HgCl_2$ to form Hg_2Cl_2, which is insoluble in hydrocarbons and precipitates, according to the following reaction:

$$Hg^0 + HgCl_2 \Rightarrow Hg_2Cl_2 \downarrow \quad \text{Eq. 2.5}$$

It has been measured that this reaction has a half-life of 10 days at ambient temperature [21], however the origin of $HgCl_2$ in natural gas systems is unclear. A reasonable explanation would be the reaction of mercury compounds with chloride salts (e.g. NaCl, KCl, $CaCl_2$ etc.) which are known to be present in reservoir brines, but this requires further investigation.

Finally, the following mechanism has been proposed for the adsorption of mercury on steel pipes [1]:

$$H_2S + Fe_2O_3 \Rightarrow 2FeO + S + H_2O \quad \text{Eq. 2.6}$$

$$Hg + S \Leftrightarrow HgS \quad \text{Eq. 2.7}$$

Unfortunately, no equilibrium or kinetic constants are available in the literature for the reactions of Hg in hydrocarbon systems.

2.7 Analytical methods for Hg measurement

2.7.1 Overview

Experience has shown that the accurate determination of total mercury and the speciation of Hg compounds require sophisticated sampling techniques and rigorous analytical procedures [22]. This is due to the presence of several Hg species in crude oil and gas condensate samples that are rarely accounted for in routine measurements, as well as the various problems that can arise during the analytical methods. As will be discussed later, measurements can be affected by the material of sample containers (Hg can adsorb on surfaces), by the presence of oxygen, by the purity of the reagents used etc. [2].

Analytical techniques in hydrocarbon matrices vary depending on sampling method, species conversion/separation (e.g. digestion, extraction, filtration, vaporization etc.), and detection method. While total mercury (THg) measurements in liquid and gaseous hydrocarbons have been well-established and proven to be accurate, the methods for quantitative speciation of Hg compounds are more recent and less verified [22].

2.7.2 Analytical techniques

Through the years, numerous analytical techniques for the determination of the concentration of Hg and its species in various matrices have been used. Clevenger et al. [23] have reviewed the vast majority of these techniques and have tabulated them together with the measured form of Hg, the Limit of Detection (LOD) both as concentration and absolute

value, the Relative Standard Deviation (RSD), the Linear Dynamic Range (LDR; defined as the concentration range for which the signal is linear with concentration), and possible interferences. The methods are summarized in Table 2.2.

The most common methods for total Hg measurement are cold vapor atomic absorption spectrometry (CVAAS) and cold vapor atomic fluorescence spectrometry (CVAFS), with the latter having a lower LOD. Other methods include inductively coupled plasma (ICP) or microwave induced plasma (MIP) followed by mass spectrometry (MS) or atomic emission spectrometry (AES) detection. For the examination of crude oils, neutron activation analysis (NAA) methods have also been used. NAA, ICP/MIP and MS/AES do not require digestion of the sample (thus minimizing some of the potential errors) and all report detection limits less than 0.1 ng/g [22].

For the speciation of Hg compounds, gas chromatography (GC) or high-performance liquid chromatography (HPLC) is usually employed coupled with the aforementioned detection methods, with the most common method being GC-ICP-MS. The Hg mass balance is usually described as:

$$\text{Total Hg} = Hg^0 + (RHgR + HgK) + (HgCl_2 + RHgCl) + \text{suspended Hg} \qquad \text{Eq. 2.8}$$

Some analytical methods that have been used for Hg speciation in hydrocarbon matrices are summarized in Table 2.3.

Table 2.2. Analytical techniques for the determination of the concentration of Hg & its species [23].

Method	Hg form	LOD (conc., abs.)	RSD	LDR	Interferences
CV-AAS	Hg^0	0.02 ppb, 0.1 ng	2%	0-30 ppb	N/A
CV-AAS, preconcentration	Hg^0	0.042 ppt, 0.084 ng	10%	N/A	N/A
ETA-AAS, preconcentration	Hg^0	0.1 ppt, 5 pg	2.7%	3 orders of magnitude	N/A
Speciation with AAS	Hg^{2+} CH_3Hg^+	0.4 ppt, 0.4 ng 0.03 ppt, 0.03 ng	18% 25%	>3 orders of magnitude	1-octanol butyltetrahy-drofuran
CV-AFS	Hg^0	0.001 ppt, N/A	3%	N/A	N/A
CV-AFS, preconcentration	Hg^0	0.1 ppt, 4.5 pg	5%	5 orders of magnitude	N/A
ETA-LEAFS	Hg^0	1.4 ppt, 14 fg	3%	7 orders of magnitude	N/A
ICP-AFS	Hg^0	40 ppt, N/A	N/A	N/A	N/A
Speciation with AFS, preconcentration	Hg^0 $(CH_3)_2Hg$ $(C_2H_5)_2Hg$	N/A, 0.3 pg N/A, 0.3 pg N/A, 0.4 pg	N/A N/A N/A	N/A N/A	N/A N/A

	CH_3HgCl CH_3CH_2HgCl	N/A, 2.0 pg N/A, 3.1 pg	N/A N/A		
MIP-AES	Hg^0	0.01 ppt, 0.5 pg	4.5%	>4 orders of magnitude	N/A
ICP-AES	Hg^0	50 ppt, 5 ng	2.3%	N/A	Au, Pd, Pt, Sb
DCP-AES, preconcentration	Hg^0	50 ppt, 50 pg	1.6%	3 orders of magnitude	Se^{4+}, S^{2-}, I^-
Ring discharge AES, preconcentration	Hg^0	<0.5 ppt, N/A	1%	3 orders of magnitude	Matrix effects
Speciation with AES	Hg^{2+} CH_3Hg^+	0.28 ppb, 280 ng 0.04 ppb, 40 ng	N/A N/A	N/A	humic substances
PAS	Hg^{2+}	3 ppt, N/A	6%	>2 orders of magnitude	Ag^+, Au^{3+}, Cu^{2+}
METAL	Hg^0	3 ppq, N/A	N/A	8 orders of magnitude	N, O, NH_3, sample matrix
MIOR	Hg^0	N/A, 10 pg	N/A	N/A	N/A
XRFS, preconcentration	Hg^0	60 ppt, 1.8 ng	N/A	N/A	N/A
MPIS	Hg^0	0.22 ppb, 220 fg	N/A	N/A	N/A
LIBS	Hg^0	5 ppb, N/A	N/A	N/A	N/A
FANES	Hg^0	2 ppt, 20 pg	6%	3 orders of magnitude	N/A
ICP-MS	Hg^0	0.08 ppt, 8 pg	2.7%	>3 orders of magnitude	N/A
Speciation with ICP-MS, preconcentration	CH_3Hg^+	0.02 ppb, 1 pg	4%	>3 orders of magnitude	N/A
Enzyme inhibition spectrometry	Hg^{2+}	0.1 ppt, N/A	7%	4 orders of magnitude	Bi^{3+}, Cd^{2+}
Enzyme inhibition fluorimetry	Hg^{2+}	2 ppb, N/A	N/A	N/A	Ag^+
IDA, preconcentration	Hg^{2+}	20 ppb, 0.2 µg	4.16%	N/A	MoO_4^{2-}, $S_2O_3^{2-}$, SO_3^{2-}, Ce^{4+}, Sb^{3+}, Bi^{3+}, I^-
Au film sensor	Hg^0	N/A, 0.05 ng	N/A	>3 orders of magnitude	H_2S
ASV	Hg^{2+}	0.2 ppt, N/A	3.3%	0.3-2.4 ppt	N/A
PSA	Hg^{2+}	0.5 ppb, N/A	2.5%	5-30 ppb	Rh^{3+}, Pb^{2+}
CSP	Hg^{2+}	0.1 ppb, 1 ng	4%	3 orders of magnitude	Fe^{3+}, NO_x, CO_2
DPV	$HgCl_4^{2-}$	2 ppt, N/A	N/A	3 orders of magnitude	Cu^{2+}, SO_4^{2-}

VSA	Hg^{2+}	0.6 ppb, N/A	2.6%	2 orders of magnitude	N/A
Enzyme inhibition conductimetry	Hg^{2+}	20 ppb, N/A	2.9%	N/A	Ag^{2+}
Electrochemical biosensor	Hg^{2+} CH_3Hg^+ $C_2H_5Hg^+$	1 ppb, N/A 2 ppb, N/A 2 ppb, N/A	≤4%	2-10 ppb	N/A

*ETA-LEAFS: electrothermal atomization two-step laser enhanced AFS, DCP-AES: dc discharge He plasma AES, PAS: photoacoustic spectroscopy, METAL: metastable energy transfer for atomic luminescence, MIOR: magnetically induced optical rotation, XRFS: X-ray fluorescence spectroscopy, MPIS: double resonance multiphoton ionization spectroscopy, LIBS: time-resolved laser-induced breakdown spectroscopy, FANES: furnace atomic nonthermal excitation spectroscopy, IDA: isotope dilution analysis, ASV: anodic stripping voltammetry, PSA: potentiometric stripping analysis, CSP: current stripping chronopotentiometry, DPV: differential pulse voltammetry, VSA: voltammetric stripping analysis

Table 2.3 Analytical methods for Hg speciation in hydrocarbon matrices [24].

Method[a]	**Matrix**	**Hg^0**	**DAHg**[b]	**Hg^{2+}**	**HgS**	**CH_3Hg**	**other**
HPLC-CVAA operational	gas condensate	X		X		X	
CGC-MIP-AES	gas condensate		X			X	(Hg^0 + Hg^{2+})
GC-MIP-AES GC-FAPES			X				
GC-ICP-MS	crude oil gas condensate naphtha	X	X	X			
GC-ICP-MS	condensate	X	X				
operational	crude oil gas condensate	X		X		X	suspended Hg
GC-CVAF	crude oil	X		X	X		Hg adsorbed to particulate

[a]AES: atomic emission spectroscopy, FAPES: furnace atomization plasma emission spectroscopy, CGC: capillary gas chromatography, HPLC: high performance liquid chromatography, CVAA: cold vapor atomic absorption, ICP: inductively coupled plasma, CVAF: cold vapor atomic fluorescence, MIP: microwave induced plasma, GC: gas chromatography, MS: mass spectroscopy; [b] DAHg: dialkylmercury

THg concentration is usually determined by oxidative extraction. Suspended mercury is quantitatively determined by measuring total mercury of an agitated sample followed by measuring total mercury of a filtered portion of the agitated sample. Ionic and monoalkyl forms ($HgCl_2$ + RHgCl) are determined by non-oxidative extraction of filtered samples using dilute acids. Hg^0 is determined by sparging and collecting the volatile component on a trap (usually made of Au). The sum of the concentrations of dialkylmercury and complexed mercury often is estimated from the discrepancy in the mass balance [22].

It should be noted that some analysts do not explicitly state the sampling procedures or analytical processing steps, and for this reason some data regarding Hg^0 concentration are suspected to include a contribution from suspended forms of Hg. Furthermore, oxidation of Hg^0 due to sample contact with air or presence of trace oxidants in the reagents can alter the distribution of Hg species. Finally, in old publications it is often difficult to discern if the reported concentrations refer to elemental or total mercury.

2.7.3 Challenges for experimenters

As has been previously mentioned, experimenters face some challenges when conducting Hg measurements in samples. First of all, mercury and some of its species are volatile and migrate to the gas phase when a vessel is depressurized to ambient conditions, leading to a loss of Hg from the sample.

Experience has also shown that the sample container material can play an important role in Hg measurement, because of the adsorption of Hg and its species on container walls. It has been found that acidification of samples stored in glass containers with nitric acid leads to an increased measured THg concentration compared to non-acidified samples. Bloom [25] found that the speciation of a sample is affected by the container, concluding that Hg^{2+} and Hg^0 are unstable in all commonly used shipping containers, while Ezzeldin et al. [14] conclude that the acidification effect is more significant than that of the container material in non-polar matrices. Bloom and Gallup [26] suggest that the best solution for analyzing crude oil samples in borosilicate glass vials is to analyze the bulk fluid and then include any adsorbed species by following a washing procedure. The effect of container material on the loss rate of Hg species is shown in Table 2.4.

Another serious problem is the interconversion of Hg species in the samples. Bloom and Gallup [26] have found that Hg^0 reacts not only with hydrocarbon solvent impurities, but also with the solvent itself, leading to increased measured Hg^0 solubility. Elemental mercury in samples can also be oxidized to ionic forms by coming in contact with air, water or trace oxidants in the reagents, and for this reason a small amount of $SnCl_2$ solution is usually added in the samples to reduce any oxidized compounds. According to Wilhelm [2], high concentrations of inorganic mercury in crude oil and gas condensate samples could be an artifact of sampling, sample aging and analytical method.

Table 2.4. Effect of container material on loss rate of Hg species [27].

Sample	Hg species	Hg conc.	Analytical method[a]	Container material[b]	Hg loss
Distilled water	Hg^{2+}	25 µg/l	FAAS	PE	75% after 150h
				PVC	90% after 150h
				soft glass	85% after 350h
Distilled water	Hg^{2+}	1 µg/l	CVAAS	LPEIII	97% after 8d
				LPEVI	26% after 8d
				CPE	52% after 8d
				PP	81% after 8d
Deionized water	Hg^{2+}	4 µg/l	CVAAS	PE	87% after 12d
				Pyrex	86% after 20d
Deionized water	CH_3HgCl	8 µg/l	CVAAS	PE	80% after 12d
				Teflon	stable for months
				glass	40% after 12d
Potable water	Hg^{2+}	1 µg/l	CVAFS	PET	40% after 10d
				glass	
Distilled water	Hg^{2+}	0.1-10 µg/l	CVAAS	glass	stable for 5mo
				PE	stable for 10d

[a]FAAS: flame atomic absorption spectroscopy, CVAAS: cold vapor atomic absorption spectroscopy, CVAFS: cold vapor atomic fluorescence spectroscopy; [b] PE: polyethylene, PVC: polyvinyl chloride, LPE: linear polyethylene, CPE: conventional polyethylene, PP: polypropylene, PET: poly(ethylene terephthalate)

3. Natural gas processing

3.1 Introduction

Natural gas (NG) is widely used as a fuel for the production of electricity in the primary energy sector, for powering automobiles, as well as for heating and other domestic uses by households. Natural gas is also used as a raw material in manufacturing, e.g. for the production of ethylene, ammonia, hydrogen etc. It is considered to be one of the most environmentally friendly fossil fuels, since its combustion produces a negligible amount of sulfur dioxide (SO_2), and lower nitrous oxide (NO_x) and carbon dioxide (CO_2) emissions as compared to coal or oil.

Natural gas had been discovered in the Middle East since ancient times. It was noticed that burning springs were formed when lightning ignited natural gas seeping from the ground. In regions, such as Persia, Greece, and India temples were built around this “eternal fire”. The use of natural gas as an energy source dates back to 900 BC in China, and the first known natural gas well was drilled by the Chinese in 211 BC. In Europe, natural gas was discovered in 1659 in Great Britain, but was not commercialized until 1790. In the US, the first natural gas well was developed in 1821 [28].

Natural gas occurs in rock reservoirs in Earth’s crust either by itself or in conjunction with or dissolved in crude oil and/or water. Its formation is attributed to the degradation of organic matter that had been accumulated in the past millions of years through various mechanisms. Natural gas consists mainly of light hydrocarbons, such as methane, ethane, propane, and butane, but can also contain heavier hydrocarbons, carbon dioxide, nitrogen and sulfur compounds, such as hydrogen sulfide. Trace quantities of argon, hydrogen, helium, selenium and heavy metals, such as mercury and arsenic can also be present. Depending on origin, the composition of natural gas can vary significantly, as shown in Table 3.1.

Table 3.1. Natural gas composition depending on origin (% mole) [29].

	Alberta, Canada	Colorado, USA	Kansas, USA	Bach Ho Field, Vietnam	Miskar field, Tunisia	New Mexico, USA	Texas, USA
He	0	0	0.45	0	0	0	1.8
N_2	3.2	26.1	14.7	0.2	16.9	0.7	25.6
CO_2	1.7	42.7	0	0.1	13.6	0.8	0
H_2S	3.3	0	0	0	0.1	0	0
CH_4	77.1	30.0	72.9	70.9	63.9	96.9	65.8
C2	6.6	0.6	6.3	13.4	3.3	1.3	3.8
C3	3.1	0.3	3.7	7.5	1.0	0.2	1.7
C4	2.0	0.2	1.4	4.0	0.5	0.05	0.8
C5+	3.0	0.3	0.6	2.6	0.6	0.02	0.5

In the past, due to the practical difficulties in handling and transport of gases, natural gas was regarded as an unwanted byproduct of oil drilling, and was left to vent to the atmosphere or

burned. The technological advancements during the 20th century which allowed for the transportation and storage of natural gas led to an increase in its usage as an energy source. Particularly after the oil crisis in the 1970s, natural gas gained momentum and its role in the energy sector became increasingly important. Until today, the consumption of natural gas shows an increasing trend with time, with its share in the worldwide primary energy sector being 24.2% in 2019 [30].

In recent years, worldwide efforts to mitigate global warming are intensified as governments set increasing goals for the use of renewable energy in electricity generation. Toward this, coal- and oil-fired power plants are being gradually phased-out in most regions due to their high CO_2 emissions. Since renewable energy from solar and wind is intermittent, natural gas can provide a stable base load of electric power, with much lower CO_2 emissions. Therefore, natural gas is expected to play an important role in this transition, and to gradually replace the share of oil and coal in the power sector.

3.2 The natural gas value chain

The natural gas value chain involves all the steps from exploration and drilling to gas reaching the final consumer. It is usually divided in three parts: upstream, midstream, and downstream. The upstream part involves exploration, drilling, production and offshore processing. The midstream part involves onshore processing to achieve sales gas specifications, and the downstream part involves storage, metering and distribution of gas to the final consumers. A schematic of the natural gas value chain is shown in Figure 3.1.

The most common terms that are used in the industry to describe the different types of gas are:

- *Wet gas*: a gas that is saturated with water as it comes out of the wellhead
- *Dry gas*: a gas that has been dehydrated to reach transport specifications (usually 30 ppm mol)
- *Sour gas*: a gas that is rich in acid gases, such as CO_2 and H_2S
- *Sweet gas*: a gas that has been treated to remove acid gases
- *Rich gas*: a gas that is rich in heavy hydrocarbons and requires further processing
- *Sales gas*: a gas that fulfills all specifications and is ready for sale to the market
- *Natural gas liquids* (NGL): ethane and heavier hydrocarbons (C2+)
- *Condensate*: heavier liquids from integrated gas/oil production (C6+)
- *Liquified Natural Gas* (LNG): natural gas that has been liquified by cooling to -162°C at 1 bar

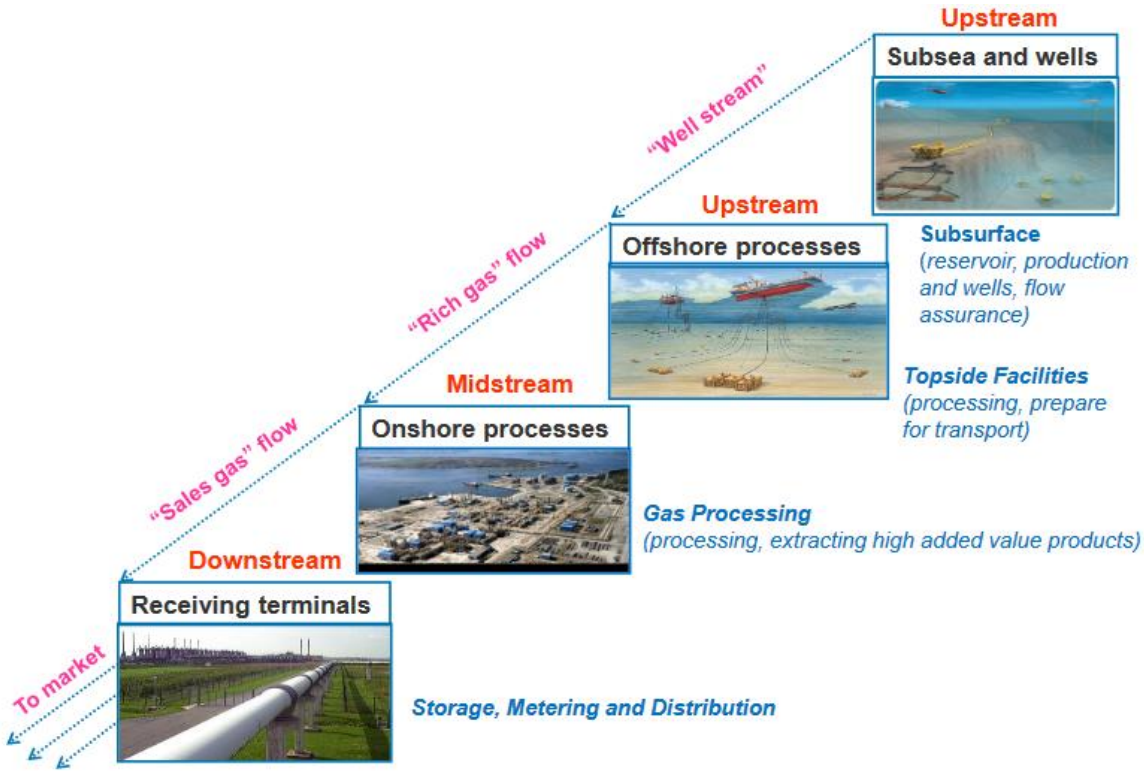

Figure 3.1. The natural gas value chain [31]

The raw natural gas that is extracted from the reservoirs must be processed so that it can be transported safely and efficiently either for further processing or for use by consumers. Final customers also set limits for its calorific value and contaminant levels. The specifications set by pipeline operators and end users often determine:

- minimum, maximum, and nominal delivery pressure
- water dew point or content
- maximum condensable hydrocarbon content or hydrocarbon dew point
- minimum heating value
- contaminant levels
- maximum delivery temperature

Condensation of hydrocarbons or water during transportation is unwanted, since they can lead to mechanical problems in compressors. Water can also corrode the piping, especially in the presence of acid gases, such as H_2S and CO_2. At low temperatures and high pressures, water can lead to formation of hydrates, which can disrupt flow or even block the pipeline. Hydrates are stable structures that are formed between water and small molecules, such as CO_2 or methane.

In the case of offshore fields, natural gas undergoes a first treatment either in subsea templates or topside on platforms or floating vessels. Due to space and weight limitations, expensive labor and utilities, and safety issues, the processes that are conducted offshore are the minimum possible to achieve the specifications for transport to an onshore processing facility (Table 3.2). There, the gas is processed further to achieve sales gas specifications (Table 3.3), while valuable NGL products are recovered and separated.

Table 3.2. Specifications for rich gas transport (offshore to onshore) [31].

Designation and units	Specification
Max operating pressure (barg)	210
Min operating pressure (barg)	112
Max operating temperature (°C)	60
Min operating temperature (°C)	-10
Max cricondenbar pressure (barg)	105
Max cricondentherm temperature (°C)	40
Max water dew point (°C at 69 barg)	-18
Max carbon dioxide (%mol)	2
Max hydrogen sulfide and COS (ppmv)	2
Max O_2 (ppmv)	2
Max daily average methanol content (ppmv)	2.5
Max peak methanol content (ppmv)	20
Max daily average glycol content (L/MSm^3)	8

Table 3.3. Specifications for sales gas transport [31].

Designation and units	Specification
Hydrocarbon dew point (°C at 50 barg)	< -10
Water dew point (°C at 69 barg)	-18
Max carbon dioxide (%mol)	2.5
Max oxygen (ppmv)	2
Max hydrogen sulfide and COS (mg/Nm^3)	5
Max mercaptans (mg/Nm^3)	6
Maximum sulfur (mg/Nm^3)	30
Gross calorific value (MJ/Sm^3)	38.1 - 43.7
Gross calorific value (MJ/Nm^3)	40.2 - 46.0
Gross calorific value (kWh/Nm^3)	11.17 - 12.78
Wobbe index (MJ/Sm^3)	48.3 - 52.8
Wobbe index (MJ/Nm^3)	51.0 - 55.7
Wobbe index (kWh/Nm^3)	14.17 - 15.47

3.3 Basic processes

The objective of gas processing either offshore or onshore is to separate natural gas from condensate, acid gases, water and any other contaminants. For this purpose, several processes are employed as shown in Figure 3.2 and Figure 3.3. The basic separation processes that are used are flash separations or distillations (inlet separation, condensate stabilization, NGL extraction, NGL fractionation) and absorption (dehydration, sweetening). Depending on raw gas composition and process needs, adsorption processes may also be required to remove additional water or acid gases.

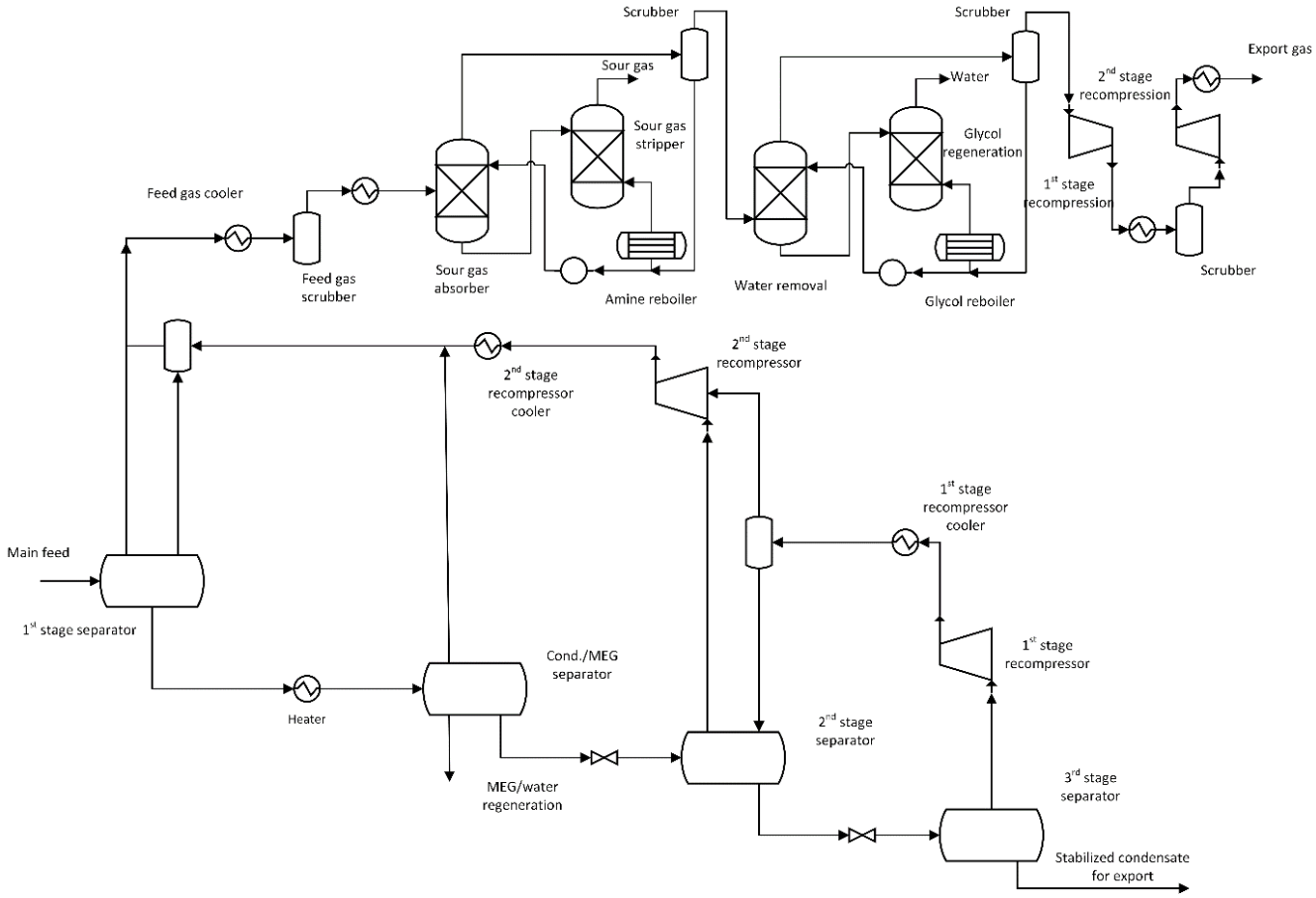

Figure 3.2. A typical PFD of an offshore gas processing plant [31].

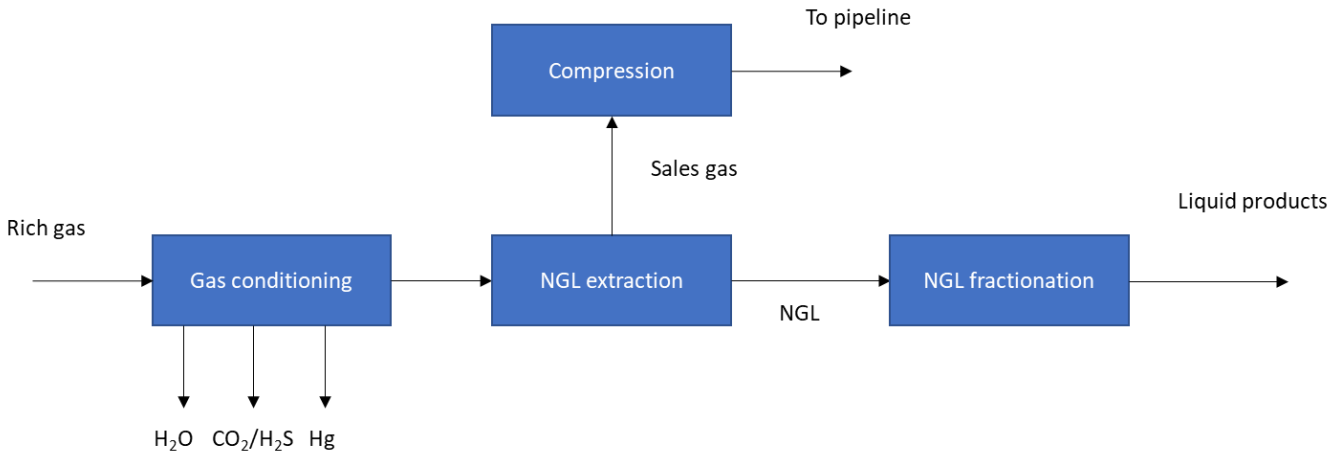

Figure 3.3. Block flow diagram of a typical onshore gas processing plant [31].

3.3.1 Inlet separation

Raw gas coming out of the reservoir is initially separated from water and heavier hydrocarbons in 3-phase flash drums ("inlet separators"). To achieve good separation between gas and liquid phases and to maximize hydrocarbon liquid recovery, usually two or more separation stages with decreasing pressures are required. The water produced from inlet separators is usually discharged. In cases where a hydrate inhibitor, i.e. MEG, has been injected in the reservoir fluid, the aqueous phase is further processed to regenerate the inhibitor. The condensates produced from inlet separators are led to the condensate stabilization process. Finally, the gases from inlet separation are mixed with gases produced in other processes, and undergo treatment to remove acid gases and water.

3.3.2 Condensate stabilization

The condensate produced during inlet separation, as well as any condensates from other processes must be stabilized before transportation. Stabilization involves the removal of the C1-C4 fraction from the condensate and is necessary for safety purposes, as well as for the maximization of gas recovery. For this purpose, one or more flash separators with decreasing pressure and/or increasing temperature are used, or in some cases distillation columns are employed. The aim of these processes is to satisfy the vapor pressure specification (True vapor pressure or Reid vapor pressure) for the stabilized condensate, which will allow its safe storage under ambient conditions. The stabilized condensate can be sold as is or it can be further processed onshore in refineries to separate it to its constituents.

3.3.3 NGL recovery & fractionation

The rich gas that is transported to onshore processing facilities usually contains a substantial amount of NGL (C2+ fraction), which can be recovered and separated into high added value

liquid products (C2, C3, iC4, nC4 and C5+). NGL recovery is achieved by letting the gas expand either by passing through a valve or an expander, during which the gas is cooled. The use of an expander is preferential since it achieves lower temperatures and the produced shaft work can be used in other processes, e.g. combination with a compressor. For the fractionation of NGL a series of distillation columns is employed. The number of columns depends on the number of products to be separated, e.g. for separating C2, C3, iC4, nC4 and C5+ four columns are required in total.

3.3.4 Acid gas removal

Most natural gases contain non-negligible amounts of acid gases (CO_2 and H_2S), which must be removed to achieve sales gas specifications. Acid gases can corrode equipment and piping, especially in the presence of free water in the gas. H_2S is also unwanted because it is toxic and can react with other natural gas components, while CO_2 reduces the heating value of natural gas. Typical specifications for natural gas are less than 5 ppmv H_2S [28] and less than 2-2.5 mol% CO_2 [31].

Acid gas removal from natural gas (also known as “sweetening”) is usually based on the processes of absorption or adsorption. Absorption processes either involve only physical dissolution of acid gases to a solvent or also chemical reaction between solvent and H_2S/CO_2. The most popular absorbents are aqueous amine solutions (monoethanolamine, diethanolamine, methyl-diethanolamine), which absorb acid gases with simultaneous reaction. The absorption usually takes place in a column (“contactor”), in which the sour gas and amine solution pass countercurrently. The amine that exits the contactor is called “rich amine” because it is rich in acid components, and can be regenerated and recycled back to the contactor. The regeneration part usually involves a flash separator, in which any hydrocarbons contained in the rich amine are vented, and a distillation column (“stripper”) which separates the acid gases from the amine.

Adsorption processes are employed when removal of acid gases at trace levels is required. The most popular adsorbents are metal oxides (iron or zinc oxide), which react with H_2S or mercaptans to form metal sulfide compounds. With this method, H_2S concentrations in gas below 0.1 ppmv can be achieved. Adsorption processes are typically non-regenerative and pose some technical problems such as hydrocarbon loss through condensation and increased weight, which prohibits its use offshore.

3.3.5 Water removal

Water occurs naturally in reservoirs and natural gas is usually saturated in water as it comes from the wellhead. In addition, some water can be absorbed from natural gas during processes that use aqueous solutions, such as sweetening. Water must be removed from natural gas to avoid flow problems, such as hydrate formation and slug flow. In addition, water reduces the heating value of gas and increases its volume. The presence of water in combination with acid gases can also lead to pipeline corrosion.

Water removal from reservoir fluids is initially carried out at the inlet separators, where most of the water is recovered. However, the produced gas still contains an amount of water, and further processing is required. The removal of water from natural gas (also known as "dehydration") can be achieved through absorption, adsorption or refrigeration. Glycol absorption is the most common method, during which the gas is passed countercurrently with a liquid glycol in an absorption column ("contactor"). The most widely used glycols are monoethylene glycol (MEG), diethylene glycol (DEG) and triethylene glycol (TEG). The glycol that exits the contactor is called "rich glycol" because it is rich in water, and can be regenerated and recycled back to the contactor. The regeneration part usually involves a flash separator, in which any hydrocarbons contained in the rich glycol are vented, and a stripping column which separates the water from the glycol.

Adsorption processes are employed when extreme water removal (up to 0.1 ppm) is required, e.g. before cryogenic processes involved in deep NGL recovery or LNG production. The most common adsorbents are molecular sieves (zeolites), activated alumina, and silica gel (SiO_2). Most adsorbents can be regenerated by heating, so usually two beds are employed: one bed is used for dehydration while the other is regenerated.

3.3.6 Mercury removal

In order to mitigate the risks imposed by mercury, it is typically removed from natural gas with the help of mercury removal units (MRUs). This is usually done at onshore gas processing plants, since MRUs are large and heavy, which prohibits their use offshore in most cases [2]. The specification for Hg concentration after treatment is usually 10 ng/Sm^3 for gases and 1 ng/g for liquid streams [4].

MRUs are usually fixed-bed reactors, which contain sorbents that are comprised of an inert substrate bonded with a mercury-reactive component. The substrates selectively adsorb Hg compounds, but do not react with them directly. The most common substrates are activated carbon, alumina or zeolites. The role of the mercury-scavenging component is usually played by sulfur or a noble metal, such as silver. As mercury passes through the sorbent, it reacts with the sulfur or amalgamates with the silver present in the substrate, and forms a mercury compound that is retained by the sorbent bed.

The most widely used sorbents are sulfur-impregnated activated carbon, metal sulfides or silver-impregnated molecular sieves. During the last 5 years, various researchers have proposed novel sorbents for mercury removal, such as deep eutectic solvents [32], carbon supported ionic liquids [33] and regenerable α-MnO_2 nanotubes [34]. Desirable properties of Hg sorbents used for natural gas treatment are: high sorption capacity, reusability, large pore volume, high dispersion of active phase on the substrate with large surface area, crushing strength and attrition resistance in order to facilitate low and stable pressure drop with plug flow, no channeling and no powder formation [4]. Additionally, sorbent pore size should be

carefully selected so that the substrate selectively adsorbs mercury and not heavy hydrocarbons [2].

Figure 3.4. Parallel mercury removal units (fixed-bed reactors) at a Thai gas plant [10].

Sulfur-impregnated activated carbon was for many years prevalent in gas processing plants, but has been gradually replaced by metal sulfides [10]. The reason behind this is the extensive micro-porous nature of activated carbon, which causes capillary condensation of the treated gas, especially when operating close to the dew point. In addition, the sulfur impregnated in the carbon can easily dissolve in liquid hydrocarbons or wet gas (i.e. gases that contain a considerable amount water), thus contaminating the gas and rendering the sorbent useless [2, 10].

Carbon-based and metallic sorbents are non-regenerable, as opposed to molecular sieves, which are regenerable. Molecular sieves can also be used in a combined process, where both mercury and water are removed from gas [2, 10]. Towards this, an already installed dehydration unit can be employed by loading an amount of silver-impregnated molecular sieves in addition to the ones already used for dehydration. Consequently, plants adopting this technology have minimal CAPEX costs as no additional units are required. In the regeneration cycle the molecular sieve is heated and mercury is released as vapor. The regen gas is then treated with a conventional non-regenerative method or an Hg condensation system is employed [2].

4. Phase & chemical equilibria

4.1 Thermodynamic equilibrium

Phase and chemical equilibrium calculations are paramount in chemical engineering, since they are widely applied in the design, operation, and optimization of many industrial processes, such as distillation, absorption, extraction, chemical synthesis etc. Such calculations are based on the assumption that the studied system has reached thermodynamic equilibrium, i.e. the macroscopic properties of the system are constant with time.

As a consequence of the 2nd law of thermodynamics, a system reaches thermodynamic equilibrium when its entropy, S, reaches its maximum value. Therefore, at equilibrium:

$$dS = 0 \qquad \text{Eq. 4.1}$$

For a closed system that does not react and is not under the influence of magnetic or electrical field, it can be derived that at equilibrium:

$$dS = \frac{1}{T}dU + \frac{P}{T}dV - \sum_i \frac{\mu_i}{T}dn_i = 0 \qquad \text{Eq. 4.2}$$

where *T* is the temperature, *U* is the internal energy, *P* is the pressure, *V* is the volume, μ_i is the chemical potential of component i, and n_i are the moles of component i. It should be noted that in Eq. 4.2 the kinetic and potential energies have been ignored because they are not involved in common applications.

From Eq. 4.2 it is identified that three types of equilibrium must be simultaneously satisfied to achieve thermodynamic equilibrium: 1) thermal equilibrium (*T* uniform across the system), 2) mechanical equilibrium (*P* uniform across the system), and 3) diffusive equilibrium (μ_i uniform across the system). It should be noted that the term "diffusive equilibrium" encompasses both the concepts of phase equilibrium and chemical reaction equilibrium.

Other state functions, such as Gibbs energy (*G)*, enthalpy (*H*), Helmholtz energy (*A*) etc. can also be used as an equilibrium condition, with the proper choice of independent variables as shown in Table 4.1. For usual practical applications it is convenient to choose readily available independent variables, such as temperature, pressure, volume or number of moles.

Table 4.1. Equilibrium criteria for a closed system [35].

Independent variables	State function to be minimized
S, *V*, **n**	*U*
U, *S*, **n** or *A*, *T*, **n**	*V*
S, *P*, **n**	*H*
T, *P*, **n**	*G*
T, *V*, **n**	*A*
H, *P*, **n** or *U*, *V*, **n**	*-S*

4.2 Phase equilibrium

At equilibrium under constant *T* and *P* it is true that:

$$(dG)_{T,P} = \sum_i \mu_i dn_i = 0 \qquad \text{Eq. 4.3}$$

which must apply for any **n**. Therefore, it is derived that μ_i must be equal for each component in all phases. The chemical potential can be calculated from one of the following expressions:

$$\mu_i = \left(\frac{\partial U}{\partial n_i}\right)_{S,V} = \left(\frac{\partial H}{\partial n_i}\right)_{S,P} = \left(\frac{\partial A}{\partial n_i}\right)_{T,V} = \left(\frac{\partial G}{\partial n_i}\right)_{T,P} \qquad \text{Eq. 4.4}$$

Due to the requirement for integration of Eq. 4.2, the chemical potential can only be calculated in relation to some reference state. In addition, absolute values of state functions like internal energy or entropy are required, which are unknown. To overcome these problems, the concept of fugacity, *f*, has been introduced, which takes the place of μ in calculations. Fugacity is defined as the isothermal change in the chemical potential of a substance in any system:

$$\mu_2 - \mu_1 = \mu(P_2, T) - \mu(P_1, T) = RT \ln\left(\frac{f_2}{f_1}\right) \qquad \text{Eq. 4.5}$$

where *R* is the universal gas constant.

The ratio of the fugacity of a pure component at pressure P divided by the same pressure is defined as the fugacity coefficient:

$$\phi = \frac{f}{P} \qquad \text{Eq. 4.6}$$

As pressure approaches zero, the state of the pure component approaches that of an ideal gas and the fugacity coefficient approaches unity:

$$\lim_{P\to 0} \phi = \lim_{P\to 0} \frac{f}{P} = 1 \qquad \text{Eq. 4.7}$$

When two or more phases ($I, II, \ldots, N_P$) are at equilibrium, the fugacity of each component, *i*, must be equal among all phases:

$$f_i^I = f_i^{II} = \cdots = f_i^{N_P} \qquad \text{Eq. 4.8}$$

The fugacity can be calculated from PVT experimental data or estimated via thermodynamic models as will be discussed in Chapter 6.

4.2.1 Vapor – liquid equilibrium

Depending on conditions and system complexity, two approaches can be followed for describing the vapor-liquid equilibrium (VLE) of mixtures. The first approach is to employ an activity coefficient model for describing liquid phase non-ideality and an equation of state (EoS) for the vapor phase. This approach is known as γ-ϕ and is usually applied at low pressures for polar mixtures that are not adequately described by common EoS with classical mixing rules. The other approach is to employ an EoS for describing both phases, and is referred to as ϕ-ϕ.

In both approaches, the vapor phase fugacity is expressed as:

$$\hat{f}_i^v = y_i \hat{\phi}_i^v P \qquad \text{Eq. 4.9}$$

where y_i is the mole fraction of component i in the vapor phase, $\hat{\phi}_i^v$ is the fugacity coefficient of component i in the vapor phase, and *P* is the pressure.

The liquid phase fugacity with the γ-ϕ approach is calculated from:

$$\hat{f}_i^l = x_i \gamma_i P_i^s \phi_i^s \exp\left(\frac{v_i (P - P_i^s)}{RT}\right) \qquad \text{Eq. 4.10}$$

where x_i is the mole fraction of component i in the liquid phase, γ_i is the activity coefficient, P_i^s is the vapor pressure, ϕ_i^s is the fugacity coefficient of the saturated pure liquid at temperature *T,* and v_i is the average molar volume of pure liquid i at temperature *T* from the vapor pressure to the system pressure *P.* The exponential term is also known as the Poynting effect, (*Pe*$_i$), and represents the effect of pressure on liquid phase fugacity.

By setting Eq. 4.9 equal to Eq. 4.10 we get:

$$y_i F_i P = x_i \gamma_i P_i^s \qquad \text{Eq. 4.11}$$

where

$$F_i = \frac{\hat{\phi}_i^v}{\hat{\phi}_i^s (Pe_i)} \qquad \text{Eq. 4.12}$$

At low pressures F_i can be approximated to be unity. Therefore, for solving VLE with the γ-ϕ method the activity coefficients and vapor pressures of the components are required. The first are usually taken from an activity coefficient model, while the latter can be calculated via the Antoine equation or any other correlation.

The liquid phase fugacity with the ϕ-ϕ approach is calculated from:

$$\hat{f}_i^l = x_i \hat{\phi}_i^l P \qquad \text{Eq. 4.13}$$

In this case, both $\hat{\phi}_i^v$ and $\hat{\phi}_i^l$ are calculated with an equation of state. The advantage of the ϕ-ϕ method is that both phases are treated with the same thermodynamic model, so no inconsistencies can occur. In addition, the system can be fully described, since an EoS can be used to calculate all its properties, such as volume, vapor pressure, enthalpy, heat capacity, speed of sound, surface tension etc. On the other hand, the γ-ϕ method is rather simpler and can be successfully employed for VLE calculations for polar mixtures at low pressures, in which classical EoS yield poor results.

4.2.2 Liquid – liquid equilibrium

Similarly with VLE, liquid-liquid equilibrium (LLE) can be solved with the γ-γ or the ϕ-ϕ method. Starting from the equifugacity criterion (Eq. 4.8) and by using Eq. 4.10 the γ-γ method is derived:

$$x_i^I \gamma_i^I = x_i^{II} \gamma_i^{II} \qquad \text{Eq. 4.14}$$

where I and II are the liquid phases at equilibrium.

Of special interest in this work is the case of LLE in binary mixtures, in which a component is at infinite dilution in the liquid phase that is rich in the other component. For example, if phase I is rich in component 1, then $\lim_{x_1 \to 1} \gamma_1^I = 1$ and Eq. 4.14 becomes:

$$\gamma_2^{II} = \frac{1}{x_2^{II}} \qquad \text{Eq. 4.15}$$

Finally, the ϕ-ϕ method is derived by combining Eq. 4.8 with Eq. 4.13:

$$x_i^I \hat{\phi}_i^{l,I} = x_i^{II} \hat{\phi}_i^{l,II} \qquad \text{Eq. 4.16}$$

4.2.3 Solid solubility

When a pure solid is in equilibrium with a fluid phase, its fugacity, f_s^{solid}, can be calculated with an activity coefficient model or an equation of state. If an Eos is used, the equilibrium relation is:

$$f_s^{solid}(T,P) = x_s \hat{\phi}_s P \qquad \text{Eq. 4.17}$$

where x_s is the solubility of the solid in the fluid phase, and $\hat{\phi}_s$ is the fugacity coefficient of the solid in the fluid phase.

The fugacity of the pure solid is usually calculated with respect to a reference fugacity, such as the solid vapor pressure or the fugacity of a hypothetical subcooled liquid (SCL) phase [36]. In this work, the latter is chosen:

$$f_s^{solid}(T,P) = f_s^{SCL}(T,P)\exp\left\{\left[\frac{\Delta h_s^m}{RT_s^m}\left(1-\frac{T_s^m}{T}\right)\right]+\frac{\left(V_s^{solid}-V_s^{SCL}\right)[P-P_s^{sub}(T)]}{RT}\right\} \quad \text{Eq. 4.18}$$

where $f_s^{SCL}(T,P)$ is the fugacity of the hypothetical pure subcooled liquid (SCL) phase, V_s^{solid} is the pure solid molar volume, V_s^{SCL} is the molar volume of the SCL phase, $P_s^{sub}(T)$ is the sublimation pressure, T_s^m is the melting temperature, and Δh_{Hg}^m is the enthalpy of melting.

The fugacity of the hypothetical subcooled liquid can be approximated to be equal to that of the saturated liquid. The sublimation pressure can be calculated from the integrated Clausius-Clapeyron equation:

$$\ln P_s^{sub}(T) = \ln P^s(T_s^{sub}) + \frac{\Delta h_s^{sub}}{RT_s^{sub}}\left(1-\frac{T_s^{sub}}{T}\right) \quad \text{Eq. 4.19}$$

where T_s^{sub} is the sublimation temperature, and Δh_s^{sub} the enthalpy of sublimation. However, the second term inside the exponential in Eq. 4.18 usually takes negligible values and can be omitted.

4.3 Chemical reaction equilibrium

In general, a reaction between N_C components can be expressed as:

$$\nu_1 A_1 + \nu_2 A_2 + \cdots + \nu_{N_c} A_{N_c} = 0 \quad \text{Eq. 4.20}$$

or more concisely for N_R reactions:

$$\sum_{i=1}^{N_C} A_i \nu_{ir} = 0\,, r = 1, \ldots, N_R \quad \text{Eq. 4.21}$$

where ν_i is the stoichiometric coefficient and A_i represents a chemical formula. The convention used in this work is that $\nu_i < 0$ for reactants and $\nu_i > 0$ products. The stoichiometric coefficients can be combined in the stoichiometric matrix $\mathbf{N}$, with N_C rows and N_R columns.

Another useful matrix is the formula matrix, **A**, which contains the number of elements that form each chemical formula A_i. For a system with N_E elements and N_C components the formula matrix is of size $N_E \times N_C$. The formula and stoichiometric matrices must satisfy:

$$\mathbf{AN} = \mathbf{0} \qquad \text{Eq. 4.22}$$

If the complete set of linearly independent reactions is known beforehand, and, therefore **N** is given, a formula matrix **A** can be found from this relation. Conversely, if **A** is given, a compatible stoichiometric matrix can be found from the same equation. In both cases, the resulting matrices are non-unique.

An important quantity for determining how much a reaction has progressed is the extent of the reaction, which is defined as the change in the number of moles of reactants or products in proportion to their respective stoichiometric numbers:

$$d\xi = \frac{dn_1}{\nu_1} = \frac{dn_2}{\nu_2} = \cdots = \frac{dn_{N_c}}{\nu_{N_c}} \qquad \text{Eq. 4.23}$$

Therefore:

$$dn_i = \nu_i d\xi \qquad \text{Eq. 4.24}$$

The criterion for chemical equilibrium is the same as that for phase equilibrium, namely that entropy must reach its maximum value, or equivalently Gibbs energy attains its minimum. By combining Eq. 4.3 with Eq. 4.24 we have:

$$\sum_i \nu_i \mu_i = 0 \qquad \text{Eq. 4.25}$$

From the relationship between chemical potential and Gibbs energy (Eq. 4.4), the definition of fugacity (Eq. 4.5) and Eq. 4.25 it can be derived that at chemical equilibrium:

$$\ln \prod_i \left(\hat{f}_i / f_i^o\right)^{\nu_i} = \frac{-\sum_i \nu_i \mu_i^o}{RT} = \frac{-\sum_i \nu_i G_i^o}{RT} = \frac{-\Delta G_r^o}{RT} \qquad \text{Eq. 4.26}$$

where ΔG_r^o is the Gibbs energy of the reaction, and exponent "o" denotes any property at the standard state of each component. The exponential form of Eq. 4.26 is defined as the equilibrium constant of the reaction:

$$K_{eq} = \prod_i \left(\hat{f}_i / f_i^o\right)^{\nu_i} \qquad \text{Eq. 4.27}$$

The chemical equilibrium constant is a function of temperature only and its temperature dependence is given by the van' t Hoff equation:

$$\frac{d \ln K_{eq}}{dT} = \frac{\Delta H_r^o}{RT^2} \qquad \text{Eq. 4.28}$$

where ΔH_r^o is the standard enthalpy change of the reaction. Standard property changes of a reaction can be calculated from the respective property changes of formation or combustion of the components that participate in the reaction. For the general property M:

$$\Delta M_r^o = \sum_i \nu_i M_i^o \qquad \text{Eq. 4.29}$$

From Eq. 4.28 it is evident that when a reaction is exothermic ($\Delta H_r^o < 0$) the equilibrium constant decreases as temperature increases, but when a reaction is endothermic ($\Delta H_r^o > 0$) its equilibrium constant increases as temperature increases. If ΔH_r^o is assumed to be temperature-independent, integration of Eq. 4.28 from T_1 to T_2 leads to:

$$\ln \frac{K_{eq}(T_2)}{K_{eq}(T_1)} = -\frac{\Delta H_r^o}{R}\left(\frac{1}{T_2} - \frac{1}{T_1}\right) \qquad \text{Eq. 4.30}$$

4.3.1 Gas phase reactions

For gases, usually the standard state fugacity, f_i^o, is taken to be equal to the standard pressure of 1 bar or 1 atm. Therefore, Eq. 4.27 becomes:

$$K_{eq} = \prod_i \left(y_i \hat{\phi}_i P\right)^{\nu_i} = K_\phi K_y P^{\Sigma \nu_i} \qquad \text{Eq. 4.31}$$

where $K_\phi = \prod_i \hat{\phi}_i^{\nu_i}$ and $K_y = \prod_i y_i^{\nu_i}$.

K_ϕ depends on temperature, pressure and composition, so solving Eq. 4.31 requires an iterative procedure. At sufficiently low pressures or high temperatures, the problem is simplified since ideal gas behavior can be assumed, so $\phi_i = K_\phi = 1$.

Based on this simplification, it is deduced that when the reaction is exothermic, K_y decreases as *T* increases at constant *P*, so the reaction shifts toward the reactants. Conversely, if the reaction is endothermic, K_y increases as *T* increases and reaction equilibrium shifts toward products. In addition, it is shown that when the total stoichiometric coefficient $\nu = \sum \nu_i$ is negative, an increase in *P* at constant *T* causes an increase in K_y, implying an equilibrium shift toward the products. If ν is positive, K_y decreases as *P* increases, and the equilibrium shifts toward reactants.

4.3.2 Liquid phase reactions

For liquids, usually the standard state fugacity, f_i^o, is taken to be equal to the fugacity of the pure component at 1 bar or 1 atm. Therefore, the ratio $\hat{f}_i / f_i^o$ becomes:

$$\frac{\hat{f}_i}{f_i^o} = x_i \gamma_i \frac{f_i(P)}{f_i^o(1)} \qquad \text{Eq. 4.32}$$

where $f_i(P)$ and $f_i^o(1)$ are the fugacities of the pure liquid *i* at the temperature of the system and pressure *P* and 1 bar, respectively. At low pressures f_i/f_i^o is often taken as unity. At high pressures it can be evaluated from:

$$\frac{f_i(P)}{f_i^o(1)} = \exp\left[\frac{V_i(P-1)}{RT}\right] \qquad \text{Eq. 4.33}$$

Eq. 4.27 for liquid phase reactions becomes:

$$K_{eq} = \prod_i \left(x_i \gamma_i \frac{f_i}{f_i^o}\right)^{\nu_i} = K_x K_\gamma K_f \qquad \text{Eq. 4.34}$$

where $K_x = \prod_i x_i^{\nu_i}$, $K_\gamma = \prod_i \gamma_i^{\nu_i}$ and $K_f = \prod_i \left\{\exp\left[\frac{V_i(P-1)}{RT}\right]\right\}^{\nu_i}$.

At low pressures $K_f = 1$, and for ideal solutions $K_\gamma = 1$.

4.4 Stability

The equifugacity criterion is a necessary but not sufficient condition for equilibrium. The necessary and sufficient condition is that the Gibbs energy of a system reaches its global minimum at constant *T* and *P*. Other criteria based on other state functions can also be employed as presented in Table 4.1, but Gibbs energy independent variables are convenient for practical applications. If the number of phases in a system is unknown beforehand, and a solution that satisfies the equifugacity criterion has been found, it should be investigated whether the formation or disappearance of a phase can cause a further reduction in the Gibbs energy of the system. This procedure is known as stability analysis and regarding this several methods have been proposed throughout the years. In this work, the tangent plane distance (TPD) method proposed by Michelsen [35, 37] is used.

To test if a phase with composition $\mathbf{z}$ is stable, it is assumed that an infinitesimal amount ϵ of a new phase with composition $\mathbf{w}$ is formed. The resulting change in the Gibbs energy of the system is:

$$\Delta G = \epsilon \sum_{i=1}^{N_C} w_i(\mu_i(\mathbf{w}) - \mu_i(\mathbf{z})) \qquad \text{Eq. 4.35}$$

If the resulting change in the Gibbs energy of the system is non-negative, i.e. Gibbs energy remains constant or increases, then the original phase is stable. This is known as the tangent plane condition of Gibbs:

$$\sum_{i=1}^{N_C} w_i(\mu_i(\mathbf{w}) - \mu_i(\mathbf{z})) \geq 0 \qquad \text{Eq. 4.36}$$

For example, the Gibbs energy of mixing for the binary mixture CH_4/H_2S is plotted against composition in Figure 4.1. At composition z_1=0.2, the tangent of the Gibbs energy of mixing intersects with the curve, which means that the mixture is unstable. The mixture is stable only for compositions outside the range defined by the two minima, which correspond to the equilibrium compositions of the liquid and vapor phase.

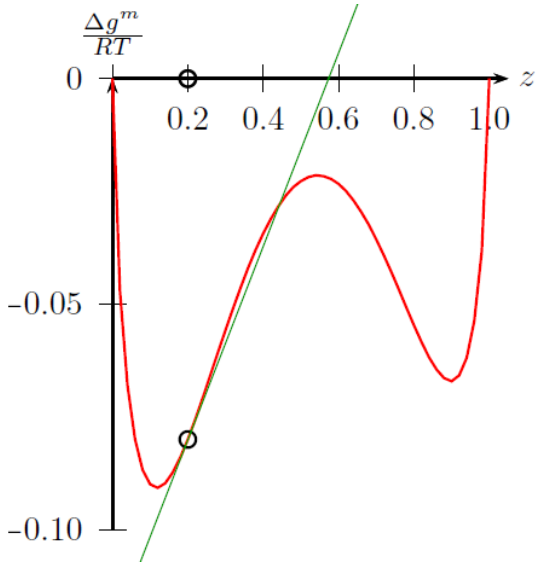

Figure 4.1. Gibbs energy of mixing for binary mixture CH_4/H_2S at 190 K and 45.6 bar [35].

Michelsen proposed an alternative formulation of the tangent plane condition by using the distance of the tangent from the Gibbs energy of mixing:

$$TPD(\mathbf{w}) = \sum_{i=1}^{N_C} w_i(\ln \hat{f}_i(\mathbf{w}) - \ln \hat{f}_i(\mathbf{z})) \qquad \text{Eq. 4.37}$$

which should be non-negative for any composition $\mathbf{w}$ for a mixture to be stable. In Figure 4.2 the tangent plane distance curve corresponding to the mixture of Figure 4.1 is shown. The mixture is unstable since the tpd curve takes negative values at z_1>0.42.

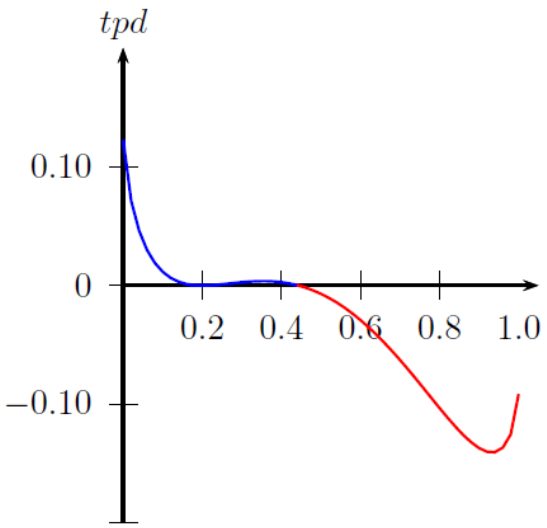

Figure 4.2. Tangent plane distance plot for binary mixture CH_4/H_2S at 190 K and 45.6 bar at z_1=0.2 [35].

If mole numbers, $\mathbf{W}$, are chosen as variables instead of mole fractions, then Eq. 4.37 becomes:

$$tm(\mathbf{W}) = 1 + \sum_{i=1}^{N_c} W_i\left[\ln W_i + \ln \hat{\phi}_i\,(\mathbf{W}) - \ln z_i - \ln \hat{\phi}_i(\mathbf{z}) - 1\right] \qquad \text{Eq. 4.38}$$

Instability can be determined by minimizing $tm(\mathbf{W})$. At the minimum we have:

$$\frac{\partial tm}{\partial W_i} = \ln W_i + \ln \hat{\phi}_i\,(\mathbf{W}) - \ln z_i - \ln \hat{\phi}_i(\mathbf{z}) = 0 \qquad \text{Eq. 4.39}$$

For finding the minima, a successive substitution method is usually employed. If a negative tm is found, a phase split will occur and mole fractions of the trial phase can be found from:

$$w_i = \frac{W_i}{\sum_{j=1}^{N_C} W_j} \qquad \text{Eq. 4.40}$$

It should be noted that in a system with more than one phases any phase can be used to test system stability, since at equilibrium the chemical potential (or fugacity) of each component is the same in all phases. However, in multiphase systems special care needs to be taken when selecting initial estimates for the trial phase composition, as will be discussed in Chapter 5.

5. Algorithms for chemical & phase equilibria

5.1 Phase equilibrium algorithms

For fully describing a system at equilibrium, the number of variables that must be known is dictated by the Gibbs phase rule:

$$F = N_C - N_R - N_P - SC + 2 \quad \text{Eq. 5.1}$$

where N_C is the number of components, N_R is the number of independent reactions, N_P is the number of phases, SC is the number of equations arising from special conditions, and the number two represents temperature *T* and pressure *P*. Thus, for a two-phase non-reactive binary mixture, it is derived that two intensive variables are required to fully describe the system. For the calculation of the phase equilibria of such a mixture, three different types of calculation exist depending on the known and unknown variables: bubble point, dew point and flash calculation. If *T* is the temperature, *P* the pressure, *x* the liquid phase composition and *y* the vapor composition, the different combinations of known and unknown variables are summarized in Table 5.1.

Table 5.1. Different types of equilibrium calculations based on input and output variables.

Calculation	Input	Output
Bubble point pressure (BPP)	*T, x*	*P, y*
Bubble point temperature (BPT)	*P, x*	*T, y*
Dew point pressure (DPP)	*T, y*	*P, x*
Dew point temperature (DPT)	*P, y*	*T, x*
Flash	*T, P*	*x, y*

The algorithms used in this work are based on those proposed by Michelsen [35]. In general, the algorithms for solving vapor-liquid equilibrium are based on the equifugacity criterion, the material balance for each component, and the requirement for mole fractions in the liquid and the vapor phase to sum to unity:

$$x_i \hat{\phi}_i^l P = y_i \hat{\phi}_i^v P \quad \text{Eq. 5.2}$$

$$\beta y_i + (1-\beta) x_i = z_i \quad \text{Eq. 5.3}$$

$$\sum_{i=1}^{N_C} (y_i - x_i) = 0 \quad \text{Eq. 5.4}$$

where β is the vapor phase fraction, i.e. the total moles in the vapor phase divided with the total moles of the system, and z_i is the mol fraction of component i in the feed. The above set of equations can be reformulated if equilibrium factors, K_i, are introduced:

$$K_i = \frac{y_i}{x_i} \qquad \text{Eq. 5.5}$$

Substituting this into the material balance equation yields:

$$x_i = \frac{z_i}{1 - \beta + \beta K_i} \qquad \text{Eq. 5.6}$$

$$y_i = \frac{K_i z_i}{1 - \beta + \beta K_i} \qquad \text{Eq. 5.7}$$

Substituting K_i in the equifugacity criterion yields:

$$K_i = \frac{\hat{\phi}_i^l}{\hat{\phi}_i^v} \qquad \text{Eq. 5.8}$$

Finally, the summation of mole fractions relation becomes:

$$\sum_{i=1}^{N_C} (y_i - x_i) = \sum_{i=1}^{N_C} \frac{z_i (K_i - 1)}{1 - \beta + \beta K_i} = 0 \qquad \text{Eq. 5.9}$$

5.1.1 Bubble point pressure calculation

The flowchart of the algorithm for determining bubble point pressure is given in Figure 5.1. The inputs to the algorithm are temperature, liquid phase composition, and an initial guess for pressure. The vapor fraction is set to zero. The outputs of the algorithm are the pressure and vapor phase composition. In the case of hydrocarbon systems, initial values for K_i can be estimated from Wilson's approximation:

$$\ln K_i = \ln\left(\frac{P_{c_i}}{P}\right) + 5.373(1 + \omega_i)\left(1 - \frac{T_{c_i}}{T}\right) \qquad \text{Eq. 5.10}$$

where T_{c_i}, P_{c_i} and ω_i are the critical temperature, critical pressure and acentric factor of component i.

The algorithm incorporates a nested loop scheme. In the inner loop the fugacity coefficients are kept constant and Eq. 5.9 is solved for *P* with Newton's method, while in the outer loop the fugacity coefficients are updated based on the new *P,* and new K_i are calculated from Eq. 5.8. Liquid and vapor phase compositions are calculated from Eq. 5.6 and Eq. 5.7. Inner loop convergence is achieved when $|P^{new} - P^{old}|$ is below a certain tolerance. Outer loop convergence is achieved when the differences $|K_i^{new} - K_i^{old}|$ and $\left|\hat{\phi}_i^l x_i - \hat{\phi}_i^v y_i\right|$ are below tolerance.

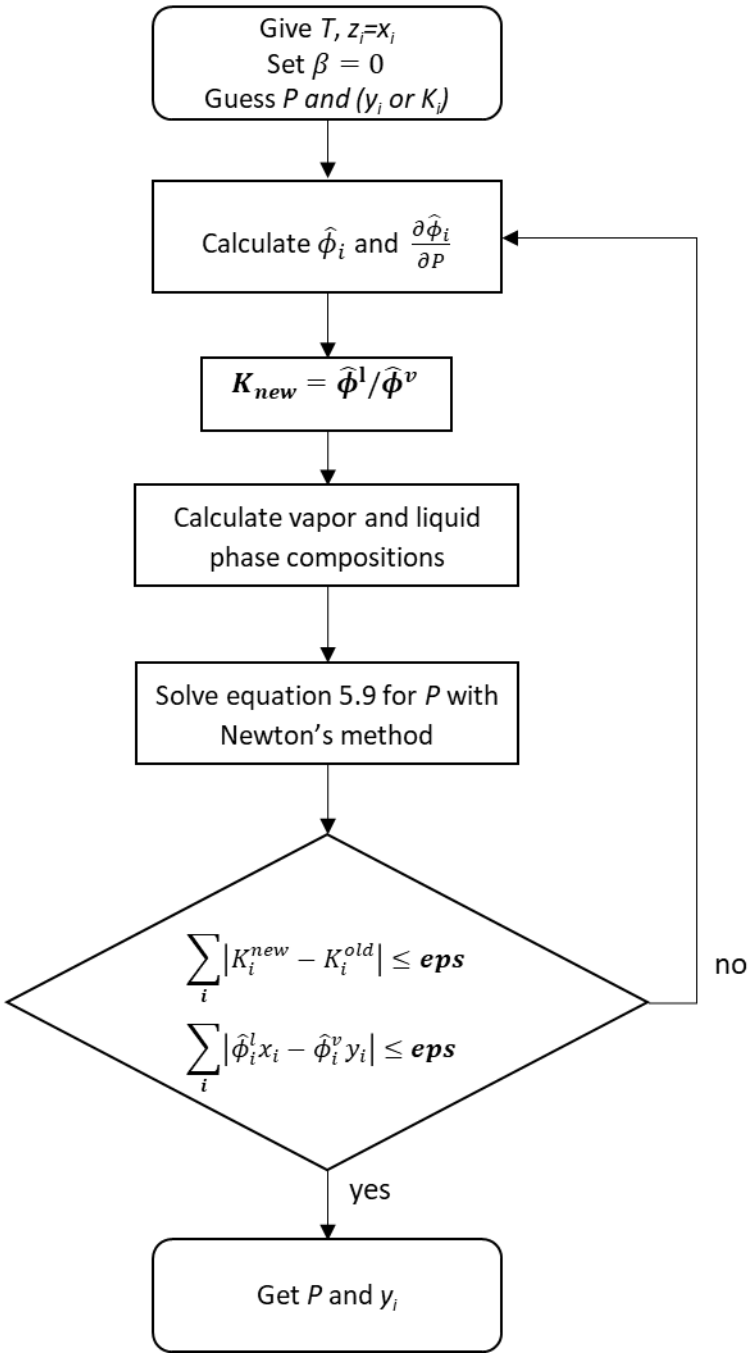

Figure 5.1. Flowchart of bubble point pressure (BPP) algorithm.

5.1.2 Dew point temperature calculation

The dew point temperature algorithm is similar to the BPP algorithm described above. Again, a nested loop scheme is employed, only now pressure and vapor phase composition are inputs, and temperature and liquid phase composition are outputs. The vapor fraction is set to one. The same nested loop scheme is employed, but now Eq. 5.9 is solved for *T* with Newton's method. The flowchart of the algorithm is presented in Figure 5.2.

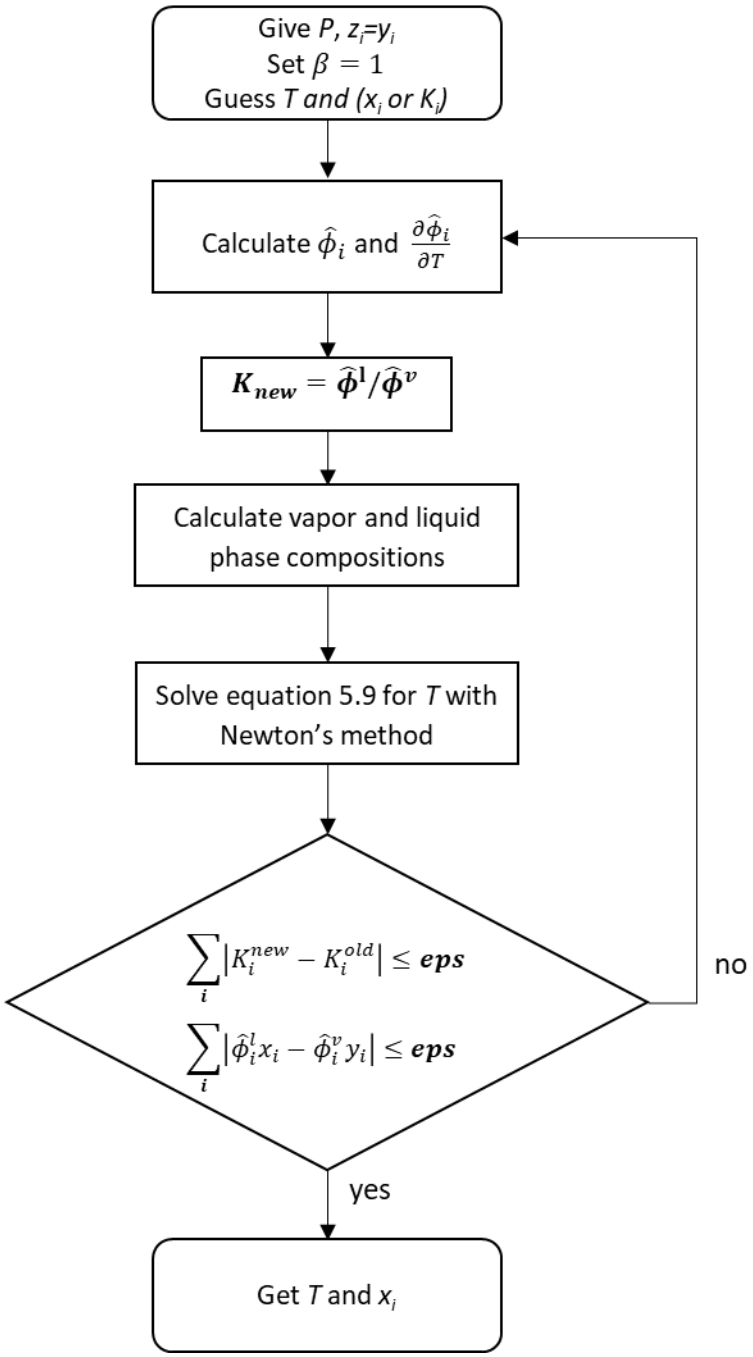

Figure 5.2. Flowchart of dew point temperature (DPT) algorithm.

5.1.3 Two-phase PT flash algorithm

The classical two-phase pressure-temperature (PT) flash has temperature, pressure and feed composition as inputs, and vapor fraction and vapor and liquid compositions as outputs. Once again, a nested loop scheme is employed. In the inner loop fugacity coefficients are kept constant and Eq. 5.9 is solved for β with Newton's method. Afterward, new compositions are calculated from Eq. 5.6 and Eq. 5.7. In the outer loop the fugacity coefficients are updated

based on the new compositions, and new K_i are found. Usually, $\beta = 0.5$ is selected as initial value. The flowchart of the algorithm is presented in Figure 5.3.

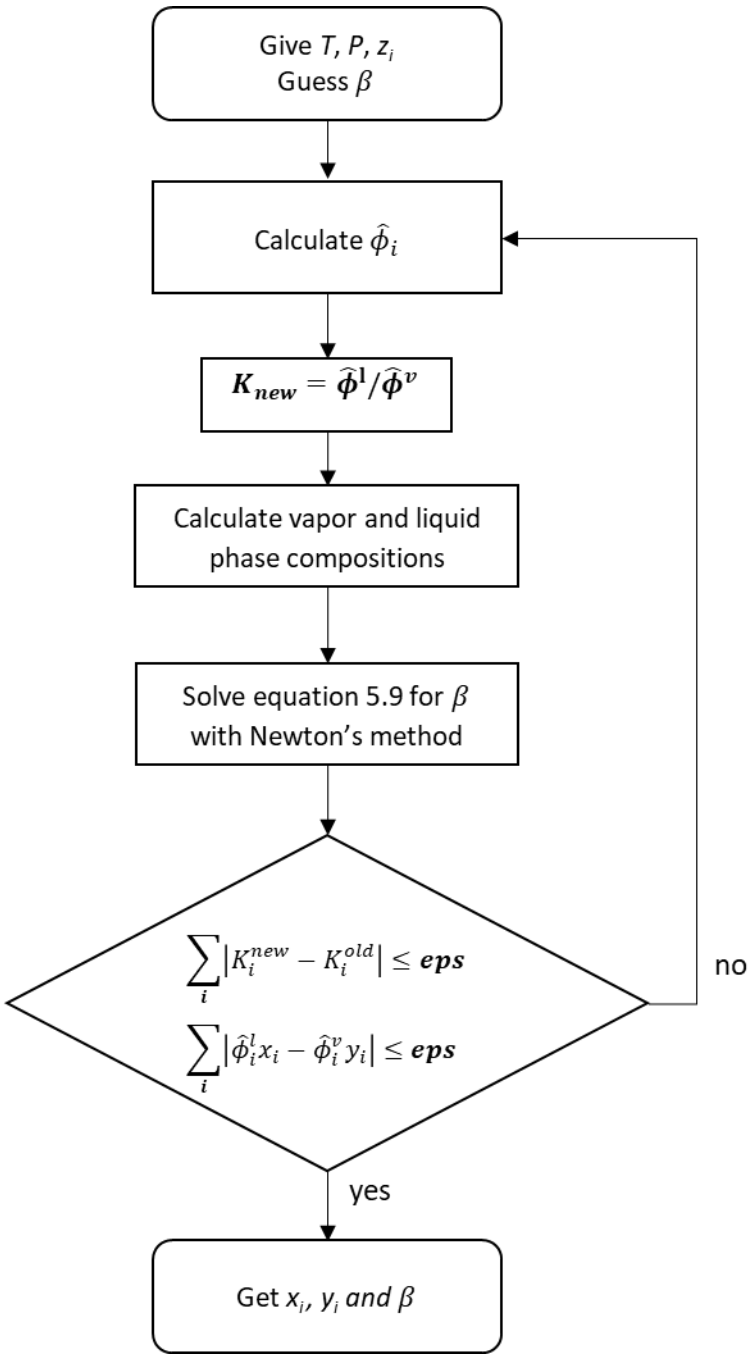

Figure 5.3. Two-phase PT flash algorithm.

5.1.4 Multiphase PT flash algorithm

Flash calculations in systems with more than two phases are more complex than the simple two-phase PT flash, especially in cases when no information is available beforehand for the total number of phases present at equilibrium. The algorithm implemented in this work is based on the method proposed by Michelsen [35, 38], which is essentially a reformulation of

the equations arising from the equilibrium condition. The working equations for a system with N_C components and N_P phases are:

$$Q(\boldsymbol{\beta}) = \sum_{j=1}^{N_P} \beta_j - \sum_{i=1}^{N_C} z_i \ln E_i \qquad \text{Eq. 5.11}$$

$$E_i = \sum_{k=1}^{N_P} \frac{\beta_k}{\hat{\phi}_{ik}} \qquad \text{Eq. 5.12}$$

$$g_j = \frac{\partial Q}{\partial \beta_j} = 1 - \sum_{i=1}^{N_C} \frac{z_i}{E_i} \frac{1}{\hat{\phi}_{ij}} \qquad \text{Eq. 5.13}$$

$$H_{jk} = \frac{\partial g_j}{\partial \beta_k} = \sum_{i=1}^{N_C} \frac{z_i}{E_i^2 \hat{\phi}_{ij} \hat{\phi}_{ik}} \qquad \text{Eq. 5.14}$$

Function Q is minimized with Newton's method, subject to the constraint $\beta_j \geq 0$:

$$\mathbf{H}\Delta\boldsymbol{\beta} + \mathbf{g} = \mathbf{0} \qquad \text{Eq. 5.15}$$

At the solution, the mole fractions in each phase are calculated from:

$$y_{ij} = \frac{z_i}{E_i} \frac{1}{\hat{\phi}_{ij}} \qquad \text{Eq. 5.16}$$

For solving the multiphase flash a nested loop scheme is employed, in which the set of Eq. 5.11 - Eq. 5.16 is solved in the inner loop by assuming composition-independent fugacity coefficients, and the fugacities of the components are updated in the outer loop based on the newly found compositions. After the successive substitution scheme has converged, it is necessary to perform stability analysis to check whether an additional phase can further reduce the Gibbs energy of the system. In this work, the tangent plane distance (TPD) criterion proposed by Michelsen [35, 37] is employed. During the calculations in the inner loop it may be necessary to de- or re-activate phases. The rather complex solution procedure is described in more detail in the book by Michelsen and Mollerup [35]. A flowchart of the algorithm is presented in Figure 5.4.

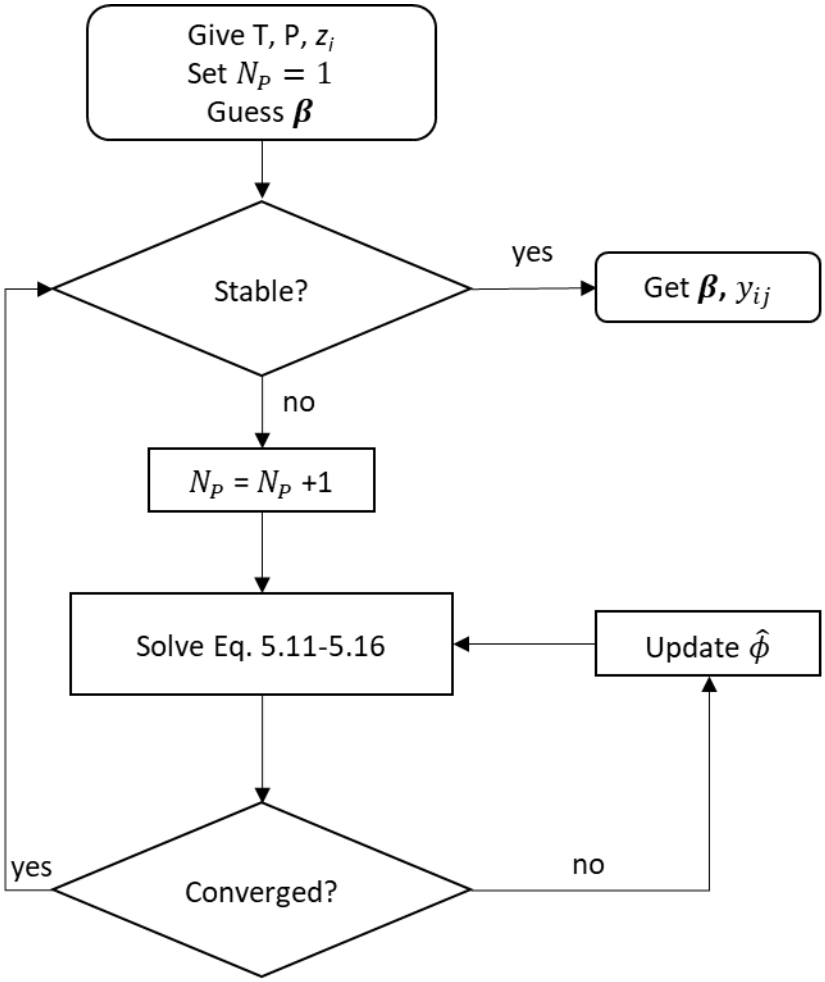

Figure 5.4. Multiphase PT flash algorithm flowchart.

The most challenging problem associated with multiphase flash is the stability analysis. More specifically, the difficulty lies in the decision of how many and which trial phases to introduce to the system during the stability analysis. In classical two-phase flash algorithms, two trial phases are sufficient: one “vapor-like” and one “liquid-like”. However, in multiphase problems Michelsen and Mollerup [35] suggest that at least N_C+1 trial phases are required for a complete screening in the absence of a priori knowledge. One of these corresponds to the search for a vapor phase and the rest N_C trial phases correspond to liquid phases rich in the respective components. However, problems can arise in finding all the minima when multiple liquid phases are present. An example of this is a “shielded” liquid phase, as shown in Figure 5.5. A flash calculation for this mixture is likely to yield a vapor-liquid equilibrium, which blocks access to a liquid-liquid equilibrium solution.

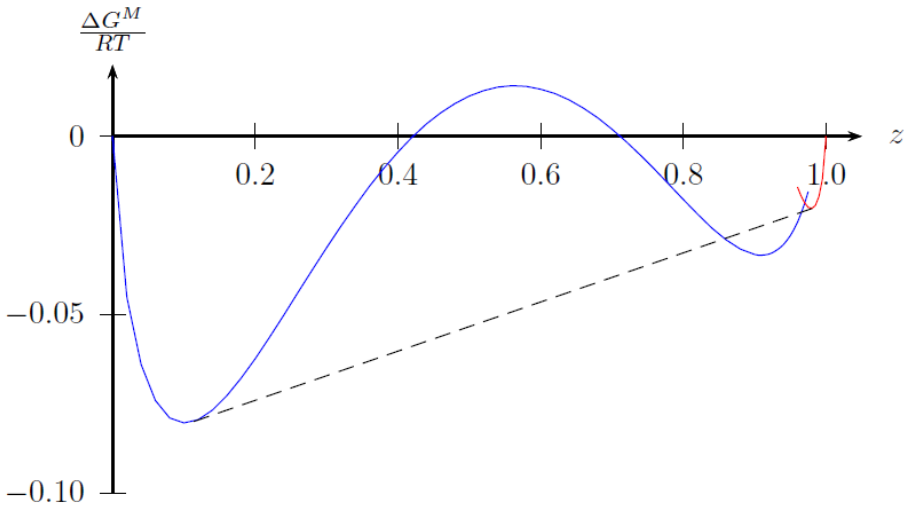

Figure 5.5. Excess Gibbs energy of mixing for CH_4/H_2S binary mixture at 190 K and 40.5 bar [35].

An exhaustive stability analysis for a mixture containing many components requires substantial computational effort. This problem can be overcome if the approximate compositions and maximum number of the potential phases are known in advance. Fortunately, this is the case in common hydrocarbon fluids, which may also contain water and/or mercury. In these mixtures it is reasonable to assume that at most four phases can be present under the usual processing conditions: vapor-liquid hydrocarbon-aqueous-mercury. For the purposes of this work, in addition to checking for a vapor- and a liquid-like phase, the formation of a pure water and a pure mercury phase is tested.

Since the solubility of other components in liquid mercury is practically zero, a free-mercury phase assumption can be used to accelerate the solution procedure, similarly with the free-water approach proposed by other researchers [39]. According to this, when a liquid mercury phase is found to be formed during the stability analysis, other components are not allowed to exist in this phase. The fugacity of mercury in this phase is equal to that of the saturated pure liquid Hg at the given temperature and pressure, while the fugacity of the other components in this phase is set to an arbitrary high value. Thus, computational time is saved by avoiding explicit calculation of the fugacity coefficients of the other components in the mercury phase.

In cases when the temperature is lower than the melting point of mercury, the free-mercury phase will be solid. In this case, the fugacity of pure solid mercury is calculated as described in Section 4.2.3.

5.2 Simultaneous chemical & phase equilibrium algorithm

5.2.1 Working equations

For solving the simultaneous chemical and phase equilibria (CPE) in a system, several algorithms have been proposed throughout the years. To tackle the problem, either the equations arising from equilibrium are simultaneously solved or the Gibbs energy of the system is minimized under material balance constraints [40]. Regarding the latter, two approaches can be identified: the stoichiometric and the non-stoichiometric method. The stoichiometric method utilizes the extents of the reactions and is best fit for systems with few reactions and without trace components. The non-stoichiometric method employs Lagrange multipliers and involves a rather intricate set of working equations, but it is more suitable for systems with multiple reactions and phases. In this work, the non-stoichiometric method of Gibbs energy minimization with Lagrange multipliers [41, 42] is employed.

The principle behind Gibbs minimization algorithms is that a system reaches equilibrium under constant temperature and pressure when its Gibbs energy reaches its global minimum. Therefore, the aim of the algorithm is to minimize the Gibbs energy of the mixture, subject to two constraints: mass of elements must be conserved, and component mole numbers must be non-negative. One of the most widely used constrained minimization methods is that of Lagrange multipliers, which utilizes the Lagrangian function:

$$\mathcal{L}(x, y, \lambda) = f(x, y) - \lambda \cdot g(x, y) \qquad \text{Eq. 5.17}$$

where $\mathcal{L}(x, y, \lambda)$ is the Lagrange function, $f(x, y)$ is the function to be minimized, λ is the Lagrange multiplier, and $g(x, y)$ is the constraint.

Due to the reactions, the material balance in CPE systems cannot be expressed in terms of component mole numbers. In the non-stoichiometric formulation, “elements” are chosen as basis for the material balance. Elements represent building blocks of components and can be chemical elements, groups of atoms or sometimes components themselves. Assuming a system with N_R linearly independent reactions, N_C components, and N_P phases, the number of elements (N_E) that must be selected is $N_E = N_C - N_R$.

The constrained minimization of the Gibbs energy can be expressed as:

$$\min_{\boldsymbol{n}} G(T,P,\boldsymbol{n}) = \min_{n_{ik}} \sum_{k=1}^{N_P}\sum_{i=1}^{N_C} n_{ik}\mu_{ik}(T,P,\boldsymbol{n}_k)$$

$$\text{subject to: } \sum_{k=1}^{N_P}\sum_{i=1}^{N_C} A_{ji}n_{ik} = b_j\,, \qquad j = 1,\dots,N_E \qquad \text{Eq. 5.18}$$

$$n_{ik} \geq 0, \qquad i = 1,\dots,N_C \quad k = 1,\dots,N_P$$

where G is the Gibbs energy, n_{ik} the moles of component i in phase k, μ_{ik} the chemical potential of component i in phase k, A_{ji} the number of element j in the chemical formula of component i, and b_j the total mole numbers of element j.

For convenience, the reduced Gibbs energy (G/RT) can be minimized since its minimum coincides with that of the Gibbs energy at constant temperature. Thus, the Lagrangian function becomes:

$$\mathcal{L}(\boldsymbol{n},\lambda) = \sum_{k=1}^{N_P}\sum_{i=1}^{N_C}\frac{n_{ik}\mu_{ik}}{RT} - \sum_{j=1}^{N_E}\lambda_j\left(\sum_{k=1}^{N_P}\sum_{i=1}^{N_C} A_{ji}n_{ik} - b_j\right) \qquad \text{Eq. 5.19}$$

It should be noted that the solution is a minimum of the Gibbs energy and not a minimum of the Lagrangian, but a saddle point. Consequently, derivatives with respect to mole numbers and Lagrange multipliers must satisfy:

$$\frac{\partial\mathcal{L}}{\partial n_{ik}} = \frac{\mu_{ik}}{RT} - \sum_{j=1}^{N_E} A_{ji}\lambda_j = 0\,, \qquad i = 1,\dots,N_C \quad k = 1,\dots,N_P \qquad \text{Eq. 5.20}$$

$$\frac{\partial\mathcal{L}}{\partial\lambda_j} = -\sum_{k=1}^{N_P}\sum_{i=1}^{N_C} A_{ji}n_{ik} + b_j = 0, \qquad j = 1,\dots,N_E \qquad \text{Eq. 5.21}$$

By introducing mole fractions and phase amounts, Eq. 5.21 becomes:

$$F_j^A = \sum_{k=1}^{N_P} n_{t,k}\sum_{i=1}^{N_C} A_{ji}x_{ik} - b_j = 0, \qquad j = 1,\dots,N_E \qquad \text{Eq. 5.22}$$

The second working equation arises from the condition that mole fractions in each phase must sum to unity:

$$F_k^B = \sum_{i=1}^{N_C} x_{ik} - 1 = 0, \qquad k = 1,\dots,N_P \qquad \text{Eq. 5.23}$$

The working equations of the algorithm are Eq. 5.22 and Eq. 5.23. For convenience, we define:

$$\mathbf{F}(\lambda, \boldsymbol{n}_t) = \begin{bmatrix} \boldsymbol{F}^A \\ \boldsymbol{F}^B \end{bmatrix} \quad \text{Eq. 5.24}$$

The mole fractions can be expressed as a function of the Lagrange multipliers by replacing the chemical potential with fugacity in Eq. 5.20:

$$\ln x_{ik} = \sum_{j=1}^{N_E} A_{ji}\lambda_j - \frac{\mu_{ik}^o}{RT} - \ln \frac{\hat{f}_{ik}}{f_{ik}^o} \quad \text{Eq. 5.25}$$

where μ_{ik}^o is the reference state chemical potential of component i in phase k, $\hat{f}_{ik}$ the fugacity of component i in phase k, and f_{ik}^o the reference state fugacity of component i in phase k.

Therefore, we have a system of $N_E + N_P$ equations with N_E Lagrange multipliers and N_P phase amounts as the unknowns. This system can be solved with Newton's method:

$$\mathbf{J}\begin{bmatrix} \Delta\lambda \\ \Delta\boldsymbol{n}_t \end{bmatrix} = -\mathbf{F} \quad \text{Eq. 5.26}$$

where $\mathbf{J}$ is the Jacobian matrix of $\mathbf{F}$. Assuming constant fugacity coefficients, the Jacobian is calculated as:

$$\mathbf{J}(\lambda, \boldsymbol{n}_t) = \begin{bmatrix} \boldsymbol{J^A} & \boldsymbol{J^B} \\ \boldsymbol{J^C} & \boldsymbol{J^D} \end{bmatrix} \quad \text{Eq. 5.27}$$

where:

$$J_{jq}^A = \frac{\partial F_j^A}{\partial \lambda_q} = \sum_{k=1}^{N_P} n_{t,k} \sum_{i=1}^{N_C} A_{ji}A_{qi}x_{ik}\,, \qquad j = 1, \dots, N_E \;\; q = 1, \dots, N_E \quad \text{Eq. 5.28}$$

$$J_{jq}^B = \frac{\partial F_j^A}{\partial n_{t,q}} = \sum_{i=1}^{N_C} A_{ji}x_{iq}\,, \qquad j = 1, \dots, N_E \;\; q = 1, \dots, N_P \quad \text{Eq. 5.29}$$

$$J_{kq}^C = \frac{\partial F_k^B}{\partial \lambda_q} = \sum_{i=1}^{N_C} A_{qi}x_{ik} = J_{qk}^B, \qquad k = 1, \dots, N_P \;\; q = 1, \dots, N_E \quad \text{Eq. 5.30}$$

$$J_{kq}^D = \frac{\partial F_k^B}{\partial n_{t,q}} = 0, \qquad k = 1, \dots, N_P \;\; q = 1, \dots, N_P \quad \text{Eq. 5.31}$$

5.2.2 Reference state chemical potential

From Eq. 5.25 it is apparent that in order to calculate component mole fractions, the reference state chemical potential is required. This can be sometimes found in tables at

specific temperatures and pressures, but when no information is available it can be calculated via the chemical equilibrium constant, as other researchers have suggested [42, 43]:

$$K_{rk}^{eq} = \exp\left(-\frac{\Delta G_{rk}^{o}}{RT}\right) = \exp\left(-\sum_{i=1}^{N_C}\frac{\nu_{ir}\mu_{ik}^{o}}{RT}\right) \quad \text{Eq. 5.32}$$

where K_{rk}^{eq} is the chemical equilibrium constant of reaction r in phase k and ΔG_{rk}^{o} the reference state Gibbs energy of reaction r in phase k, which can be calculated from the Gibbs energy of formation of the components that participate in the reaction.

Although N_C reference chemical potentials are required, there are only N_R chemical equilibrium constants. To overcome this problem, N_R reference components are selected, which must participate in at least one reaction, and we define:

$$\mu_{ik}^{o} = \begin{cases} \hat{\mu}_{ik}, & i \in reference\ components \\ 0, & i \notin reference\ components \end{cases} \quad \text{Eq. 5.33}$$

It should be noted that absolute values of μ_{ik}^{o} do not affect the calculations as long as Eq. 5.32 is satisfied. Therefore, in order to find the reduced reference state chemical potential of the reference components ($\hat{\mu}_{ik}/RT$), the following system is solved:

$$\frac{1}{RT}\widehat{\mathbf{N}}^{\mathbf{T}}\widehat{\boldsymbol{\mu}}_{\boldsymbol{k}} = \begin{bmatrix} -\ln K_{1k}^{eq} \\ \vdots \\ -\ln K_{rk}^{eq} \end{bmatrix} \quad \text{Eq. 5.34}$$

where $\widehat{\mathbf{N}}$ is the stoichiometric matrix of the reference components. When all phases share the same reference state, $\mu_{ik}^{o} = \mu_{iq}^{o}\big|_{q\neq k}$.

5.2.3 Initialization

In order to ensure algorithm convergence, good initial values for both independent variables (λ and n_t) are required. The final total mole number is relatively easy to guess and Tsanas et al. [42] comment that it has minimal impact on convergence. On the other hand, the Lagrange multipliers are not so intuitive and initial values are difficult to guess. To overcome this problem, a subset of the system of working equations is solved by assuming n_t and minimizing without constraints the following function, while keeping n_t constant:

$$Q(\lambda) = \sum_{k=1}^{N_P} n_{t,k}\left(\sum_{i=1}^{N_C} x_{ik} - 1\right) - \sum_{j=1}^{N_E}\lambda_j b_j \quad \text{Eq. 5.35}$$

This unconstrained minimization is carried out with Newton's method, by solving:

$$\nabla^2 Q \Delta\lambda = -\nabla Q \qquad \text{Eq. 5.36}$$

or equivalently:

$$\mathbf{J}^A \Delta\boldsymbol{\lambda} = -\mathbf{F}^{\mathbf{A}} \qquad \text{Eq. 5.37}$$

It can be proven that $\mathbf{J}^A$ is always positive definite, so it is guaranteed that the method will ultimately converge[42]. The calculated Lagrange multipliers and the guessed total mole numbers will serve as initial estimates for the full Newton's method (Eq. 5.26).

5.2.4 Procedure

Initially, the temperature, pressure and molar feed are given, and the number of phases is set to 1. Then, the total number of moles at equilibrium is guessed and initialization is carried out as described in the previous section by assuming a single ideal phase. Afterwards, a nested loop scheme is employed: in the inner loop the fugacity coefficients are kept constant and the Lagrange multipliers, phase amounts, compositions etc. are calculated. Inner loop convergence is achieved when the error is less than 10^{-10}. The error at iteration q ≥ 1 is:

$$error^{(q)} = \sqrt{\sum_{j=1}^{N_E} \left[\lambda_j^{(q)} - \lambda_j^{(q-1)}\right]^2 + \sum_{k=1}^{N_P} \left[n_{t,k}^{(q)} - n_{t,k}^{(q-1)}\right]^2} \qquad \text{Eq. 5.38}$$

After the inner loop has converged, new fugacity coefficients are calculated in the outer loop from the newly found compositions. In this work, it is assumed that the outer loop has converged when the maximum difference between the compositions at two consecutive iterations is less than 10^{-10}.

After outer loop convergence, stability analysis is performed in order to check if an additional phase can lower the Gibbs energy of the system, as described in Section 4.4. If the system resulting from the nested loop is found to be stable, then the algorithm has reached a solution. Otherwise, N_P is increased by one and the calculations in the nested loop are restarted. The stability analysis provides the initial estimates for the composition of the additional phase. A flowchart of the algorithm is presented in Figure 5.6.

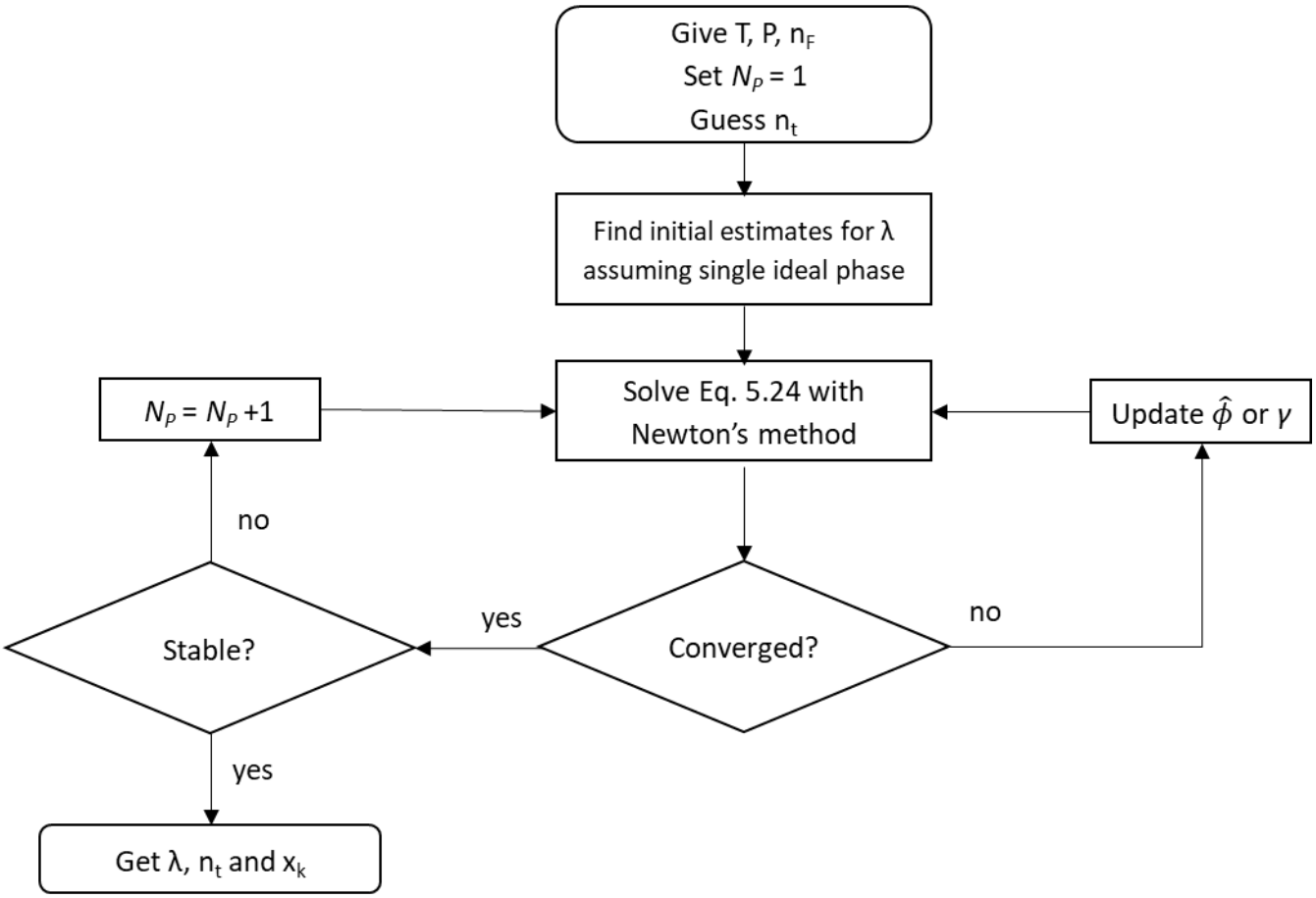

Figure 5.6. Simultaneous chemical & phase equilibrium algorithm flowchart.

6. Thermodynamic models

6.1 Equations of state

Equations of state (EoS) are algebraic relations between temperature (*T*), pressure (*P*) and volume (*V*), which are used for calculating the properties of pure components or mixtures. These relations are either derived from theory or can be semi-theoretical or even empirical. EoS are important tools for scientific and engineering applications, since they can predict the properties of a variety of mixtures at a diverse temperature and pressure range without the need for experimental data. Equations of state are also used for calculating all types of fluid-fluid equilibrium.

One of the earliest and simplest equations of state is the ideal gas law (*PV=nRT*), which was developed in 1834 by Clapeyron. As the name suggests, the ideal gas law is applicable only to gases, and considers gas molecules as point particles of zero volume, which do not interact with each other. Over the years more complex EoS were developed, which could be applied to a wider range of mixtures, conditions and phases.

6.1.1 Virial equation of state

The virial EoS is derived from the series expansion of the compressibility factor (*z=pV/RT*) with respect to pressure or inverse volume:

$$z = 1 + \frac{B}{V} + \frac{C}{V^2} + \cdots \qquad \text{Eq. 6.1}$$

$$z = 1 + B'P + C'P^2 + \cdots \qquad \text{Eq. 6.2}$$

where coefficients B, C, … (or B', C', …) are called second, third, … virial coefficients and depend only on temperature. The virial coefficients can also be related to molecular interactions through statistical mechanics. For example, coefficient B represents the molecular interactions between 2 molecules, coefficient C between 3 molecules etc.

The virial expansion is not rigorous at high pressures and does not yield satisfactory results for dense fluids and liquids, and for this reason it is only applied to gases and usually truncated at the second or third term. The virial coefficients can either be calculated by experimental PVT data or via empirical relations, such as those proposed by Tsonopoulos [44] or Hayden and O'Connell [45]. Estimation of virial coefficients through relations derived from statistical mechanics is also possible but not practical due to their increased mathematical complexity.

In this work, the virial EoS is used for describing vapor phase non-ideality in systems involving organic acids. The EoS is truncated at the second term and the Hayden-O'Connell [45] method is employed for estimating the second virial coefficient. The Hayden-O'Connell method takes into account the dimerization of carboxylic acids by relating the dimerization equilibrium

constant to the estimated B according to the chemical theory. The method is presented in detail in Appendix A.

6.1.2 Cubic equations of state

Cubic equations of state are among the most popular EoS finding extensive application in the petroleum and chemical industry [46]. They are named as such because they can be re-written as a cubic function of volume. The first cubic EoS was developed by van der Waals in 1873, who introduced two correction factors to the ideal gas law: the attractive parameter *a* and the repulsive parameter *b*. Parameter *a* accounts for the attractive forces between molecules, which cause a reduction in the observed pressure, while parameter *b* accounts for the volume occupied by all other molecules, which causes a reduction in the available volume for a molecule. The vdW EoS was a major breakthrough in thermodynamics due to its simplicity, the physical significance of its parameters, its ability to describe both vapor and liquid phases, and its good qualitative description of many experimental data [47].

Since the introduction of the vdW, several other cubic EoS have been proposed, with the most widely used today being Soave-Redlich-Kwong (SRK) [48] and Peng-Robinson (PR) [49]. Both models are essentially extensions of the vdW EoS that were introduced to improve the results for pure component vapor pressures and saturated liquid volumes. The main difference between SRK and PR is that the latter yields slightly better results for the volumetric properties. Despite SRK and PR being introduced almost 50 years ago, they are still widely used and considered as standard and proven methods by the industry due to their simplicity and good performance in many systems at a wide temperature and pressure range. However, cubic EoS do not yield satisfactory results in mixtures with molecules of very different sizes or in mixtures that contain polar and/or associating components.

Cubic equations of state can be written in generalized form as:

$$P = \frac{RT}{v-b} - \frac{a_c \cdot a(T)}{(v+\delta_1 b)(v+\delta_2 b)} \qquad \text{Eq. 6.3}$$

where *P* is the pressure, *T* is the temperature, v is the molar volume, *R* is the universal gas constant, a is the attractive parameter, b is the repulsive parameter, and δ_1, δ_2 are EoS specific constants. The SRK EoS is derived by setting $\delta_1 = 1$ and $\delta_2 = 0$, while the PR EoS is retrieved by setting $\delta_1 = 1 + \sqrt{2}$ and $\delta_2 = 1 - \sqrt{2}$. At the critical point, the EoS must satisfy that $\frac{\partial P}{\partial v}$ and $\frac{\partial^2 P}{\partial v^2}$ are equal to zero, which means that a_c and b are functions of critical temperature (T_c) and pressure (P_c). The a_c and b parameters for SRK and PR are presented in Table 6.1.

Table 6.1. Expressions for a_c and b parameters of cubic EoS.

EoS	a_c	b
SRK	$0.42748\frac{R^2T_c^2}{P_c}$	$0.08664\frac{RT_c}{P_c}$
PR	$0.45724\frac{R^2T_c^2}{P_c}$	$0.07780\frac{RT_c}{P_c}$

6.2 *α*-functions

To improve cubic EoS predictions of pure component properties, different expressions for the attractive term, $a(T)$, have been proposed over the years. Alpha functions are usually polynomial or exponential, with the most popular being those of Soave [48], Mathias and Copeman [50], Stryjek and Vera [51], Twu [52, 53] and Boston and Mathias [54]. The *α*-functions employed in this work are presented in Table 6.2.

Table 6.2. *α*-functions employed in this work.

***α*-function**	**Formula**		**Ref.**
Soave	$[1+m(1-T_r^{0.5})]^2$ $m_{SRK}=0.480+1.574\omega-0.176\omega^2$ $m_{PR}=0.37464+1.54226\omega-0.26992\omega^2$	Eq. 6.4	[48]
Mathias-Copeman	$[1+c_1(1-T_r^{0.5})+c_2(1-T_r^{0.5})^2+c_3(1-T_r^{0.5})^3]^2, \quad T_r \le 1$ $[1+c_1(1-T_r^{0.5})]^2, \quad T_r > 1$	Eq. 6.5	[50]
Twu	$T_r^{N(M-1)}\exp[L(1-T_r^{NM})]$	Eq. 6.6	[52]

The parameters of the *α*-functions are usually fitted to pure component vapor pressures and are extrapolated to the supercritical region. To accurately describe the properties in both the sub- and supercritical domain, some researchers use different functions below and above the critical temperature or include supercritical properties in the fitting procedure. However, the parameters of *α*-functions must be carefully selected so that the functions are consistent [55, 56]. An inconsistent *α*-function could lead to inaccurate predictions in mixtures with at least one supercritical component and/or improper variations of pure component supercritical properties with respect to temperature.

More specifically, α-functions are consistent when they are of class C^2, i.e. their 1st and 2nd derivatives with respect to temperature exist and are continuous. Moreover, the α-functions must be positive, monotonically decreasing ($d\alpha/dT \le 0$), convex ($d^2\alpha/dT^2 \ge 0$) and satisfy $d^3\alpha/dT^3 \le 0$ for any temperature. A summary of the consistency criteria together with their physical interpretations are presented in Table 6.3 [55].

Table 6.3. Consistency criteria for alpha functions of cubic EoS [55].

Criterion	Interpretation
a continuous	The a-function represents the strength of attraction forces with temperature, so it should be continuous.
$\lim_{T\to\infty} a(T) \neq \infty$	The a-function should reach a finite value at the infinite temperature limit.
$a(T) \geq 0$	The pressure of the system must decrease as attraction forces increase, so the second term of the EoS must always be negative.
$\frac{da}{dT} \leq 0$	Attraction forces decrease with temperature, as kinetic energy increases and molecules are driven further apart.
$\frac{d^2a}{dT^2} \geq 0$	If the second derivative of $a(T)$ with respect to temperature becomes zero, a cross in the c_v vs T isobars is observed, which does not agree with experimental data for any known substance.
$\frac{d^3a}{dT^3} \leq 0$	This criterion needs to be satisfied to avoid non-physical c_p changes with temperature.

6.3 Activity coefficient models

For modelling the vapor-liquid equilibrium of polar mixtures at low pressures, activity coefficient models are commonly used. These models provide a relationship for the activity coefficient of a component in a mixture as a function of *T*, *P* and composition. Activity coefficient models are also known as "excess Gibbs energy models", since the two are correlated:

$$RT \ln \gamma_i = \bar{G}_i^E = \left(\frac{\partial N G^E}{\partial N_i}\right)_{T,P,N_{j\neq i}} \qquad \text{Eq. 6.7}$$

where γ_i is the activity coefficient of component i, $\bar{G}_i^E$ is the partial molar excess Gibbs energy of component i, G^E is the excess Gibbs energy of mixing, N is the total number of moles in the system and N_i are the moles of component i. Excess properties, such as G^E, represent the difference between the properties of the real mixture and the properties of the hypothetical ideal mixture at the same conditions. Excess Gibbs energy is related to other excess properties:

$$G^E = H^E - TS^E = U^E + PV^E - TS^E \qquad \text{Eq. 6.8}$$

where H^E, S^E, U^E and V^E are the excess enthalpy, entropy, internal energy and volume of mixing. Therefore, mixing is affected by 3 factors: 1) an energetic (enthalpic), due to the

difference between molecular forces among molecules of the same and different kind, 2) an entropic, due to the difference between shape and size among molecules, and 3) the volume difference between the real mixture and the hypothetical ideal mixture due to both 1) and 2).

The excess Gibbs energy models are distinguished into two main categories: 1) *Wohl*-type models, which are purely empirical and find limited use today, and 2) local composition models, such as Wilson [57], NRTL [58] and UNIQUAC [59], which are semi-empirical. The latter has been used as a basis for the development of the UNIFAC group contribution model [60].

Local composition models are based on the two-liquid theory, according to which in a binary liquid mixture there are two types of "cells" on a molecular level: one that is created by molecules of component 1 surrounding a molecule of component 2 and one that is created by molecules of component 2 surrounding a molecule of component 1. Therefore, the local concentration around a molecule is different from the concentration in the bulk fluid. Due to the differences between the molecular forces among molecules of the same and different kind, the energetic parameters of local composition models are asymmetric.

Activity coefficient models are widely used in complex mixtures involving polar and/or associating compounds, where cubic EoS perform poorly. However, in contrast with EoS, activity coefficient models can only be applied to liquid phases and, for this reason, must be used in conjunction with another model in the case of vapor-liquid equilibrium calculations. Activity coefficient models are also incapable of estimating mixture properties other than G^E or γ_i. In this work, the NRTL, UNIQUAC and UNIFAC activity coefficient models are employed for performing chemical and phase equilibrium calculations in azeotropic mixtures.

6.3.1 The NRTL model

The Non-Random Two-Liquid (NRTL) activity coefficient model was proposed by Renon and Prausnitz [58] and is a modification of the Wilson equation [57]. Renon and Prausnitz introduced a "non-randomness" parameter, a_{ij}, to the equation for local mole fractions by Wilson to improve results in strongly non-ideal systems and to extend application in immiscible mixtures. According to NRTL, the activity coefficient of component i in a mixture is given by the following equations:

$$\ln \gamma_i = \frac{\sum x_j \tau_{ji} G_{ji}}{\sum x_k G_{ki}} + \sum \frac{x_j G_{ij}}{\sum x_k G_{kj}} \left(\tau_{ij} - \frac{\sum x_m G_{mj} \tau_{mj}}{\sum x_k G_{kj}} \right) \qquad \text{Eq. 6.9}$$

$$\tau_{ij} = \frac{g_{ij} - g_{jj}}{RT} = \frac{\Delta g_{ij}}{RT} = A_{ij} + \frac{B_{ij}}{T} \quad (X) \qquad \text{Eq. 6.10}$$

$$G_{ij} = \exp\left(-a_{ij}\tau_{ij}\right) \quad \text{Eq. 6.11}$$

where x_j is the mole fraction of component j, τ_{ij} is the energy parameter, G_{ij} is the Gibbs energy, g_{ij} is the residual Gibbs energy, $a_{ij} = a_{ji}$ is the non-randomness parameter, and A_{ij}, B_{ij} are binary interaction parameters.

6.3.2 The UNIQUAC model

The Universal Quasi-Chemical (UNIQUAC) activity coefficient model was developed by Abrams and Prausnitz [59] by combining Guggenheim's quasi-chemical theory [61] with the local composition theory. Except for molecular interactions, the theory also takes into account the contribution of molecule size to mixing. For a multicomponent mixture, the activity coefficient of component i is given by:

$$\ln \gamma_i = \ln \gamma_i^{comb} + \ln \gamma_i^{res} \quad \text{Eq. 6.12}$$

where γ_i^{comb} is the combinatorial (entropic) term that reflects the differences in molecular shape and size, and γ_i^{res} is the residual (enthalpic) term that represents the differences between intermolecular forces. γ_i^{comb} and γ_i^{res} are calculated as follows:

$$\ln \gamma_i^{comb} = \ln \frac{\Phi_i}{x_i} + \frac{z}{2} q_i \ln \frac{\Theta_i}{\Phi_i} + l_i - \frac{\Phi_i}{x_i} \sum x_j l_j \quad \text{Eq. 6.13}$$

$$\ln \gamma_i^{res} = -q_i \ln \left(\sum \Theta_j \tau_{ji} \right) + q_i - q_i \sum \frac{\Theta_j \tau_{ij}}{\sum \Theta_k \tau_{kj}} \quad \text{Eq. 6.14}$$

$$\Theta_i = \frac{q_i x_i}{\sum q_j x_j} \quad \text{Eq. 6.15}$$

$$\Phi_i = \frac{r_i x_i}{\sum r_j x_j} \quad \text{Eq. 6.16}$$

$$\tau_{ij} = \exp \frac{-\left(u_{ij} - u_{jj}\right)}{RT} = \exp \frac{-\Delta u_{ij}}{RT} = \exp \left(A_{ij} + \frac{B_{ij}}{T} \right) \quad \text{Eq. 6.17}$$

$$l_j = \frac{z}{2}\left(r_j - q_j\right) - \left(r_j - 1\right) \quad \text{Eq. 6.18}$$

where x_i is the mole fraction of component i, Θ_i and Φ_i are the area and volume fraction occupied by component i ,respectively, q_i and r_i are area and size parameters, z is the coordination number (equal to 10), τ_{ij} is the energy parameter, and A_{ij}, B_{ij} are binary interaction parameters (asymmetric).

6.4 Advanced models

To overcome the limitations of cubic EoS encountered in polar and/or associating mixtures, more complex models have been developed. A first approach at tackling the problem was the combination of a cubic EoS with an activity coefficient model through appropriate mixing rules. These models are named EoS/G^E and are derived by equating the excess Gibbs energy of the EoS with that of an activity coefficient model, such as NRTL, UNIQUAC etc.:

$$\left(\frac{G^E}{RT}\right)^{EoS}_{T,P_{ref},x} = \left(\frac{G^E}{RT}\right)^{act.\ coeff.\ model}_{T,P_{ref},x} \qquad \text{Eq. 6.19}$$

This equality is valid at a specific pressure, P_{ref}, which is usually either zero or infinite. The resulting models provide "the best of both worlds": they can be used both for low and high pressures, for all kinds of phase equilibria, even in complex mixtures involving size asymmetric or polar components.

Another approach at improving cubic EoS performance in associating mixtures was the addition of an extra term to the SRK (and later PR) that accounts for the association between components. The resulting model was named Cubic Plus Association (CPA) [62] and its association term was derived from the perturbation theory by Wertheim [63]. CPA has been shown to yield improved results in mixtures where classical cubic EoS perform poorly.

Beyond cubic EoS, more complex models have been developed, which are based on chemical, quasi-chemical or perturbation theories. These models contain different terms accounting for the various physical interactions, e.g. attractive, repulsive, chain and association term. The most popular among these theories is the Statistical Associating Fluid Theory (SAFT), which originated from the perturbation theory by Wertheim [63].

SAFT was put in EoS form by Chapman et al. [64] and until today several variations of the model have been developed, of which the most widely used is PC-SAFT [65]. SAFT takes into account attractive, repulsive, chain and association effects and its parameters have physical meaning. SAFT-type models have been proven to yield very good results in difficult systems, such associating mixtures, polymers, pharmaceuticals etc., but until today they have not been widely adopted by the industry due to their complexity, time-consuming solution procedure and increased number of parameters.

6.5 Mixing rules

To extend equations of state from pure components to mixtures, appropriate relations are used, which are called mixing rules. To describe mixture properties, it is necessary to include composition dependence in the EoS variables, which means that the EoS becomes an algebraic relation between *P*, *V*, *T* and composition. Throughout the years, several mixing rules have been proposed, but only those employed in this work are presented here.

6.5.1 Virial EoS for mixtures

When applied to mixtures, the virial EoS has the same formulation as presented in Eq. 6.1-Eq. 6.2 except the coefficients are now a function of both temperature and composition. The composition dependence of virial coefficients is rigorous:

$$B = \sum_i \sum_j x_i x_j B_{ij} \qquad \text{Eq. 6.20}$$

$$\mathrm{C} = \sum_i \sum_j \sum_k x_i x_j x_k C_{ijk} \qquad \text{Eq. 6.21}$$

where x_i, x_j, x_k are the molar fractions of components i, j and k in the mixture, and B_{ii} and C_{ii} are the pure component EoS parameters for component i. Cross coefficients ($B_{ij}, i \neq j$) are calculated with the same methods as those for pure components. It is assumed that coefficients are symmetric, i.e. $B_{ij} = B_{ji}$.

6.5.2 The van der Waals one fluid theory

The most widely used EoS mixing rules are those derived from the van der Waals one fluid theory (vdW1f). According to the one fluid theory, a mixture of specified composition has the same properties and property variations with *T* and *P* as some pure component with appropriate parameter values. For cubic EoS, such as SRK and PR, the mixing rules are written as:

$$a = \sum_i \sum_j x_i x_j a_{ij} \qquad \text{Eq. 6.22}$$

$$b = \sum_i \sum_j x_i x_j b_{ij} \qquad \text{Eq. 6.23}$$

where x_i, x_j are the molar fractions of components i and j in the mixture, and a_{ii} and b_{ii} are the pure component EoS parameters for component i. Cross parameters ($i \neq j$) are calculated from the following combining rules:

$$a_{\mathrm{ij}} = \left(1 - \mathrm{k_{ij}}\right)\sqrt{a_i a_j} \qquad \text{Eq. 6.24}$$

$$b_{ij} = \frac{b_i + b_j}{2} \qquad \text{Eq. 6.25}$$

where parameter $\mathrm{k_{ij}}$ is known as binary interaction coefficient. Parameter $\mathrm{k_{ij}}$ is often included in combining rules to improve EoS results and is usually estimated by regressing experimental binary VLE or LLE data.

6.5.3 The Universal Mixing Rules

The Universal Mixing Rules (UMR) were proposed by Voutsas et al. [66] and are a modification of the MHV1 [67] zero pressure mixing rules. The motivation was to develop a mixing rule that is applicable to all kinds of system asymmetries, hence the adjective "universal". These mixing rules are derived from equating the excess Gibbs energy of a cubic EoS with that calculated from original UNIFAC [60]. For the cohesion parameter of the EoS, the Staverman-Guggenheim part of the combinatorial and residual term of UNIFAC is employed. The Flory-Huggins term of the combinatorial part of UNIFAC is omitted because it was found to lead to poor results in asymmetric mixtures. For the covolume parameter of the cubic EoS, a quadratic composition-dependent mixing rule is used with an appropriate combining rule for the cross parameter. The equations involved are the following:

$$\frac{a}{bRT} = \frac{1}{A}\frac{G_{AC}^{E,SG} + G_{AC}^{E,res}}{RT} + \sum_i x_i \frac{a_i}{b_i RT} \qquad \text{Eq. 6.26}$$

$$b = \sum_i \sum_j x_i x_j b_{ij} \qquad \text{Eq. 6.27}$$

$$b_{ij} = \left(\frac{b_i^{1/2} + b_j^{1/2}}{2}\right)^2 \qquad \text{Eq. 6.28}$$

$$\frac{G_{AC}^{E,SG}}{RT} = 5\sum_i x_i q_i \ln\left(\frac{\theta_i}{\varphi_i}\right) \qquad \text{Eq. 6.29}$$

$$\frac{G_{AC}^{E,res}}{RT} = \sum_i x_i v_k^i \ln\left(\frac{\Gamma_k}{\Gamma_k^i}\right) \qquad \text{Eq. 6.30}$$

$$ln\Gamma_k = Q_k\left[1 - \ln\left(\sum_m \theta_m \Psi_{mk}\right) - \sum_m \frac{\theta_m \Psi_{mk}}{\sum_n \theta_n \Psi_{nm}}\right] \qquad \text{Eq. 6.31}$$

For component i:

$$\varphi_i = \frac{x_i r_i}{\sum_j x_j r_j} \qquad \text{Eq. 6.32}$$

$$\theta_i = \frac{x_i q_i}{\sum_j x_j q_j} \qquad \text{Eq. 6.33}$$

For UNIFAC group m:

$$\theta_m = \frac{Q_m X_m}{\sum_n Q_n X_n} \quad \text{Eq. 6.34}$$

$$X_m = \frac{\sum_j v_m^{(j)} x_j}{\sum_j \sum_n v_n^{(j)} x_j} \quad \text{Eq. 6.35}$$

$$\Psi_{nm} = \exp\left[-\frac{A_{nm} + B_{nm}(T - 298.15) + C_{nm}(T - 298.15)^2}{T}\right] \quad \text{Eq. 6.36}$$

where:

A: constant depending on the coupled EoS (for PR A = -0.53)

R: universal gas constant

T: temperature

v: molar volume

r_i: relative van der Waals volume of component i

q_i: relative van der Waals surface area of component i

φ_i: segment fraction of component i

θ_i: surface area fraction of component i

Q_k: relative van der Waals area of sub-group k

x: mole fraction

X_m: mole fraction of group m

$G_{AC}^{E,SG}$, $G_{AC}^{E,res}$: the Staverman-Guggenheim terms for the combinatorial and residual parts of the excess Gibbs energy (G^E) respectively

Γ_k: the residual activity coefficient of group k in solution

A_{nm}, B_{nm}, C_{nm}: the UNIFAC (or UNIQUAC) interaction parameters between groups (or components in the case of UNIQUAC) n and m, taken from tables or calculated by fitting experimental VLE or LLE data

6.6 The UMR-PRU model

The UMR-PRU model was originally proposed by Voutsas et al. [66] and belongs to the category of EoS/G^E models. It combines the Peng-Robinson EoS (Eq. 6.3) with original UNIFAC [60] (or UNIQUAC) through the Universal Mixing Rules discussed above. The abbreviation stands for Universal-Mixing-Rules-Peng-Robinson-UNIFAC. UMR-PRU employs the Soave expression (Eq. 6.4) for the attractive term of PR, except for polar components and mercury, for which the Mathias-Copeman (Eq. 6.5) expression is used with parameters presented in Appendix B. The UMR-PRU model has been proven to yield accurate results in a variety of mixtures including natural gas [66, 68-70], polar and associating mixtures [71, 72], and aqueous alkanolamine solutions [73, 74].

The UNIFAC interaction parameters (IPs) employed by UMR-PRU are retrieved from Hansen et al. [75], while the interaction parameters of gas groups have been calculated by fitting binary VLE data in the work of Louli et al. [68]. The interaction parameters between polar components (water, MEG, TEG, methanol) and gases have been estimated in the work of Petropoulou et al. [71, 72], while IPs between amines (MEA, MDEA), acid gases (CO_2, H_2S) and hydrocarbons have been calculated by Plakia et al. [73, 74]. In this work, UMR-PRU is extended to hydrocarbon mixtures containing mercury or hydrogen, as presented in Chapters 7 and 8. The UNIFAC group volume (R_k) and area parameters (Q_k), and UNIFAC IPs employed in this work for UMR-PRU are presented in Appendix B.

6.7 The PPR78 model

The Predictive-Peng-Robinson-78 (PPR78) model was developed by Jaubert and Mutelet [76] and is based on the modified Peng-Robinson EoS, which was proposed in 1978 [77]. The modification lies in the Soave-type α-function (Eq. 6.4), which employs different constants depending on the acentric factor:

$$m_{PR78} = \begin{cases} 0.37464 + 1.54226\omega - 0.26992\omega^2, & \omega \leq 0.491 \\ 0.379642 + 1.48503\omega - 0.164423\omega^2 + 0.016666\omega^3, & \omega > 0.491 \end{cases} \quad \text{Eq. 6.37}$$

This formulation was chosen to improve vapor pressure predictions for heavy hydrocarbons as compared to those with Eq. 6.4.

PPR78 utilizes the vdw1f mixing rules with temperature-dependent binary interaction parameters (k_{ij}) estimated though a group-contribution method:

$$k_{ij}(T) = \frac{-\frac{1}{2}\left[\sum_{k=1}^{N_g}\sum_{l=1}^{N_g}(\alpha_{ik}-\alpha_{jk})(\alpha_{il}-a_{jl})A_{kl}\cdot\left(\frac{298.15}{T}\right)^{\left(\frac{B_{kl}}{A_{kl}}-1\right)}\right]-\left[\frac{\sqrt{a_i(T)}}{b_i}-\frac{\sqrt{a_j(T)}}{b_j}\right]^2}{2\sqrt{a_i(T)\cdot a_j(T)}/(b_i\cdot b_j)} \quad \text{Eq. 6.38}$$

where N_g is the number of different groups, α_{ik} is the occurrence of group k in molecule i divided by the total number of groups present in molecule i, and $A_{kl} = A_{lk}$ and $B_{kl} = B_{lk}$ $(k \neq l)$ are constant group parameters fitted to binary data $(A_{kk} = B_{kk} = 0)$. All group parameters calculated so far for the PPR78 model are reported by Qian et al. [78]. PPR78 parameters between mercury and other groups have also been recently estimated by Chapoy et al. [79]

6.8 Thermodynamic models for mercury

One of the challenges for any model that attempts to accurately describe the partitioning of mercury in natural gas systems is the correct prediction of its vapor pressure, which is abnormally high for its atomic weight. For this reason, when a cubic EoS is employed, an advanced temperature dependence for the attractive term is employed or an adjusted to experimental vapor pressure data acentric factor is adopted for Hg^0.

The majority of the thermodynamic models that have been proposed so far in the literature regarding prediction of Hg^0 phase behavior in hydrocarbon systems is based on the widely used Soave-Redlich-Kwong EoS [48]. Edmonds et al. [80] proposed the use of a modified version of SRK coupled with Infochem's proprietary mixing rule for modelling the partitioning of mercury and some of its compounds between gas and condensate phases, as well as liquid mercury dropout. The authors fitted model parameters to pure component vapor pressure data and utilized binary interaction parameters (k_{ij}) fitted to experimental solubility data.

Khalifa et al. [81] proposed the use of SRK coupled with a group contribution method for estimating the binary interaction parameters in order to predict the solubility of mercury in normal alkanes, aromatics, water and alcohols. The authors also used an adjusted acentric factor for Hg, which was fitted to pure component vapor pressure data. Polishuk et al. [82, 83] implemented a SAFT-type model (CP-PC-SAFT) attached by a universal k_{ij} value in order to predict phase behavior of metallic mercury in liquid and compressed gaseous hydrocarbons.

More recently, Chapoy et al. [84] employed the SRK and PR-78 [77] EoS coupled with the Mathias-Copeman *α*-function for mercury. The authors regressed MC parameters for mercury on vapor pressure data separately for SRK and PR-78, and fitted temperature-dependent binary interaction parameters (k_{ij}) to experimental mercury solubility data. In a later work, Chapoy et al. [79] employed the PPR78 [76] EoS for calculating the phase equilibria of mercury in synthetic natural gas mixtures. Once again, the Mathias-Copeman *α*-function was

employed for mercury, and PPR78 model parameters were fitted to experimental mercury solubility data.

In this work, the SRK, PR, and UMR-PRU thermodynamic models are employed for describing mercury phase equilibria in natural gas systems. Different *α*-functions are explored for SRK and PR, and binary interaction parameters are estimated by regressing experimental solubility data.

7. Thermodynamic modelling of elemental mercury solubility in natural gas components

7.1 Introduction

In this chapter, the UMR-PRU model is extended to mixtures that contain elemental mercury, and is employed for predicting Hg^0 solubility in binary and multicomponent systems involving hydrocarbons, compressed gases, water, amines, alcohols, and glycols. A comparison is also made between UMR-PRU and the two most widely used cubic EoS, SRK [48] and PR [49]. Toward this, the capability of the models to predict pure mercury vapor pressure is improved by employing advanced attractive terms. Interaction parameters for all models are also estimated by regressing experimental Hg^0 solubility data, and the models are employed for predictions in multicomponent systems.

7.2 Pure Hg^0 vapor pressure

One of the challenges for any thermodynamic model that attempts to accurately describe the partitioning of Hg^0 in natural gas systems is the correct prediction of its vapor pressure, which is abnormally high for its atomic weight. For this reason, when a cubic EoS is employed, usually an advanced temperature dependence for the attractive term is selected, or an adjusted acentric factor is adopted for mercury if the classical Soave expression (Eq. 6.4) is used. In this work, two alternatives to Soave's original expression for the attractive term are compared: for SRK the expression by Twu [52] is employed (Eq. 6.6), and the model is referred as SRK-Twu, while for PR the expression proposed by Mathias and Copeman [50] is used (Eq. 6.5), and the model is referred as PR-MC. The Mathias-Copeman alpha function is also used by the UMR-PRU model for mercury and polar compounds.

For determining the pertinent alpha function parameters for mercury (c_1, c_2, c_3 for MC and L, M, N for Twu), 129 pseudo-experimental data points at a temperature range of 238.15 K – 1508.15 K were generated using the equation provided by DIPPR [85]. In the case of mercury, it is not necessary to check the alpha functions with the resulting parameters for consistency (Section 6.2), since mercury is not found in supercritical state at common processing conditions. In Table 7.1 the regressed attractive term parameters for Hg^0 are presented, along with the pertinent average absolute relative deviation (AARD) in vapor pressure. In Figure 7.1 the vapor pressure of elemental mercury versus temperature as calculated with SRK-Twu and PR-MC is plotted against the pseudo-experimental data. The results with the UMR-PRU model are omitted from the chart since UMR-PRU reverts to PR-MC for pure components. It is observed that SRK-Twu and PR-MC can accurately predict the vapor pressure of pure elemental mercury, with an AARD in vapor pressure of less than 1%. For comparison, calculations with the Soave expression for both EoS (ω_{Hg} = -0.1652 [85]) showed an AARD greater than 6%.

Table 7.1. Calculated parameters of pure Hg^0 for Twu and Mathias-Copeman *α*-functions employed in SRK and PR EoS, respectively, and corresponding deviations in vapor pressure.

SRK-Twu			PR-MC		
		AARD%[a] in P^s			AARD% in P^s
L	0.09245		C1	0.1491	
M	0.9784	0.57	C2	-0.1652	0.40
N	2.244		C3	0.1447	

[a] $AARD\% = 100/NDP \sum_{i=1}^{NDP} abs(P_{exp}^s - P_{calc}^s)/P_{exp}^s$, where P^s is the vapor pressure of pure Hg^0 and NDP is the number of experimental data points

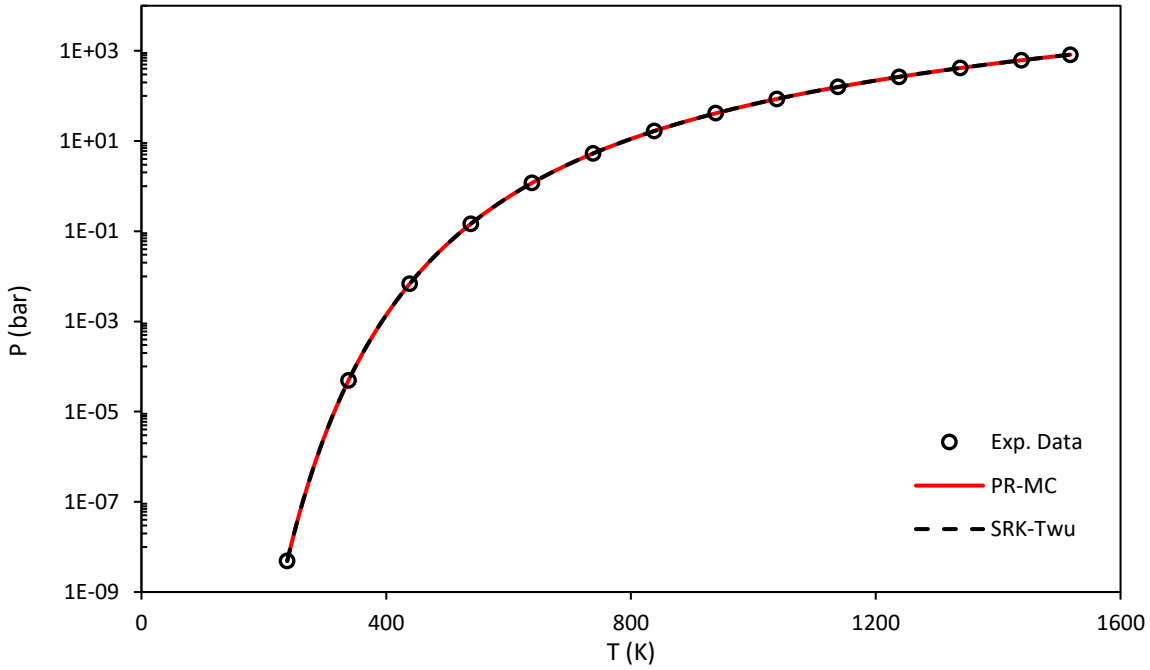

Figure 7.1. Vapor pressure of elemental mercury vs. temperature as calculated with PR-MC and SRK-Twu against pseudo-experimental data by DIPPR [85].

7.3 Description of Hg^0 solubility in binary mixtures

7.3.1 Database with experimental Hg^0 solubilities & evaluation

For the development of thermodynamic models that can accurately describe the solubility of elemental mercury in natural gas, reliable wide-range experimental data for binary Hg mixtures are required. The solvents of interest are hydrocarbons, gases (CO_2, N_2), water, and polar compounds used during NG processing, such as amines (MEA, MDEA), glycols (MEG, TEG) and alcohols (MeOH, EtOH etc.). For this purpose, a review of the literature was conducted, and the experimental measurements were compiled in a database, which is presented in Appendix C.

The main source of experimental data in the open literature is IUPAC's Solubility Data Series [86], which is mainly a compilation of liquid-liquid equilibrium measurements from different experimenters until 1987. Analyzing the results, the editors calculated new smoothed values for the solubility of mercury in the various compounds, which are designated as recommended by IUPAC. Despite its age, this source provides reliable data for various solvents at a satisfactory temperature range.

More recently, Miedaner et al. [87] presented some Hg^0 solubility measurements in hydrocarbons at high temperatures. Marsh et al. [88] and Gallup et al. [3] published studies on elemental mercury solubility in liquid hydrocarbons and polar solvents (i.e. water, alcohols, MEG, TEG) respectively, both covering a wide temperature range. Li et al. [89] also measured Hg^0 solubility in methanol, MEG, and TEG. Some Hg^0 solubility data in hydrocarbons are also available in the Gas Processors Association (GPA) research report RR-224 [90]. The most recently available data in the open literature are those of Yamada et al. [91] and Chapoy et al. [79, 84], who have measured Hg^0 solubility in CO_2, N_2, CH_4, C_2H_6, propane and mixtures thereof. Finally, proprietary Hg^0 solubility data in hydrocarbons, hydrocarbon mixtures and polar compounds have been kindly provided by Equinor [92, 93] for the purposes of this work.

In order to assess the available experimental data, mercury solubility in hydrocarbons is plotted as a function of carbon number at a constant temperature in Figure 7.2. For this purpose, the data by IUPAC [86] and GPA report [90] are employed. It is observed that mercury solubility increases roughly linearly with carbon number. It is also shown that the presence of side alkyl groups affects mercury solubility in paraffins and naphthenes. This may be explained by steric hindrance effects associated with branching: the surrounding ligands cause a "congestion", which makes mercury dissolution in the bulk fluid more difficult.

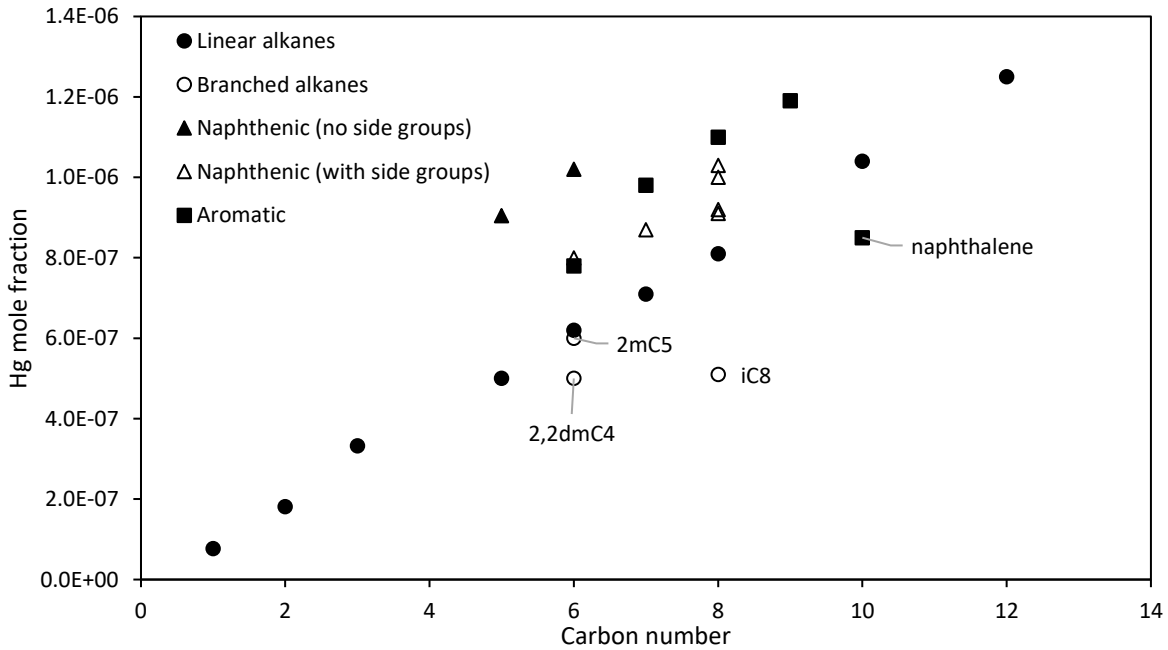

Figure 7.2. Elemental mercury solubility in paraffinic, naphthenic and aromatic hydrocarbons vs carbon number at 293.15 K [86, 90].

Notably, iso-octane appears to dissolve less mercury than 2-methylpentane, which may be due to its increased number of branched alkyl groups. In addition, it is observed that mercury solubility in naphthalene is lower than in other aromatics with less carbon atoms. This may be attributed to the increased rigidity of the fused aromatic rings that reduces their solubilization capacity as compared to non-fused aromatics. In general, mercury solubility appears to follow the order: naphthenics with no side groups > aromatics > naphthenics with side groups > linear alkanes > branched alkanes. The vast majority of the available experimental data conforms to the observed trends, and is, therefore, regarded as accurate.

The solubility of mercury in polar solvents other than water is plotted against temperature in Figure 7.3. Although solubilization capacity depends on many factors, such as solvent molecular weight, dipole moment, strength of intermolecular forces etc., by comparing polar solvents with similar molecular weights it appears that at constant temperature mercury solubility per molar basis increases in the order glycols < amines < alcohols. In addition, in Figure 7.3 it is observed that the various literature sources are in agreement. The only exception is the measurements by Li et al. [89] for MEG, which at the temperature range 253-313 K appear to be biased high, since they show a higher or roughly equal solubility in MEG as compared to methanol. For this reason, these data are excluded from the database that will be used for model correlation.

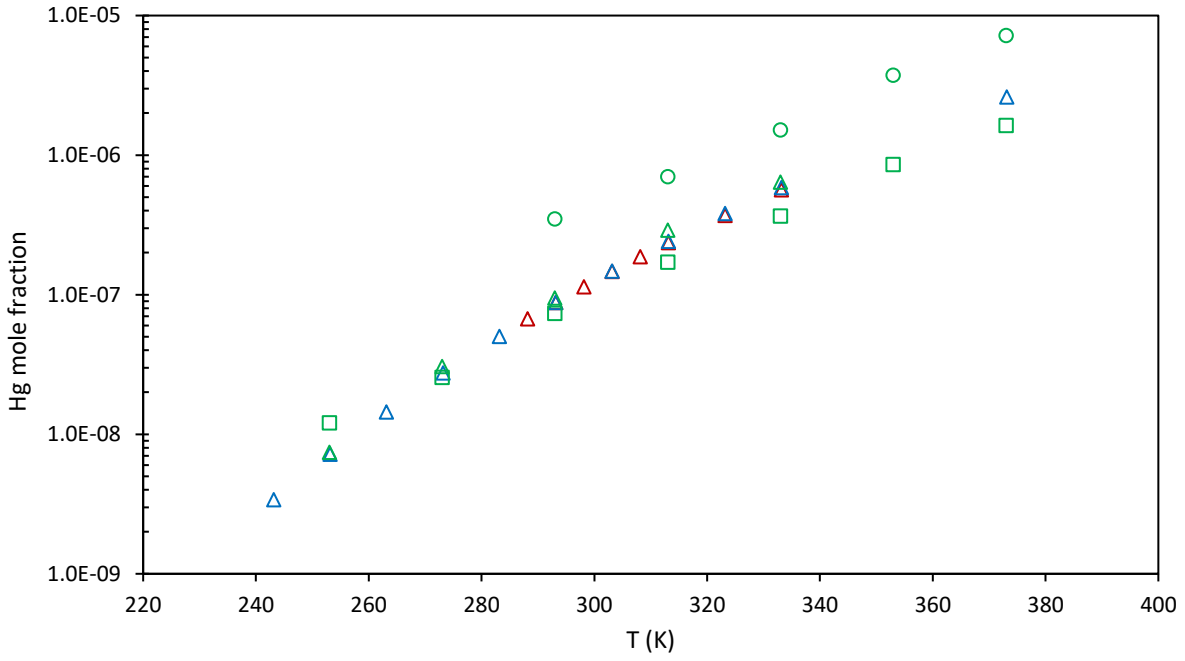

Figure 7.3. Elemental mercury solubility in polar compounds vs. temperature. (△): methanol; (□): MEG; (o): TEG. Blue markers: data from Gallup et al. [3]; red markers: data from Clever et al. [86]; green markers: data from Li et al. [89].

Regarding mercury solubility in water, there is a plethora of available experimental data in IUPAC's Solubility Data Series that show significant scatter, as shown in Figure 7.4. This may be attributed to the very low solubility of Hg^0 in water, which increases measurement uncertainty, especially if one takes into consideration the numerous experimental problems that have been already discussed. By examining the data, one can observe that the smoothed data by IUPAC (orange points) and the measurements by Gallup et al. [3] follow the same trend. This fact coupled with the credibility of the aforementioned sources constitute these data as the most reliable.

Overall, the data from different references for the majority of solvents were found to be in good agreement, with the following exceptions: 1) in n-octane the highest temperature measurement by Marsh et al. [88] at 413.15 K is in disagreement with the trend exhibited by the Miedaner et al. data (Figure 7.9), 2) for toluene the data by Miedaner et al. [87] appear to be biased low (Figure 7.10), 3) the data by Li et al. [89] for MEG appear biased high as already discussed. Therefore, these data points were excluded from the correlation database.

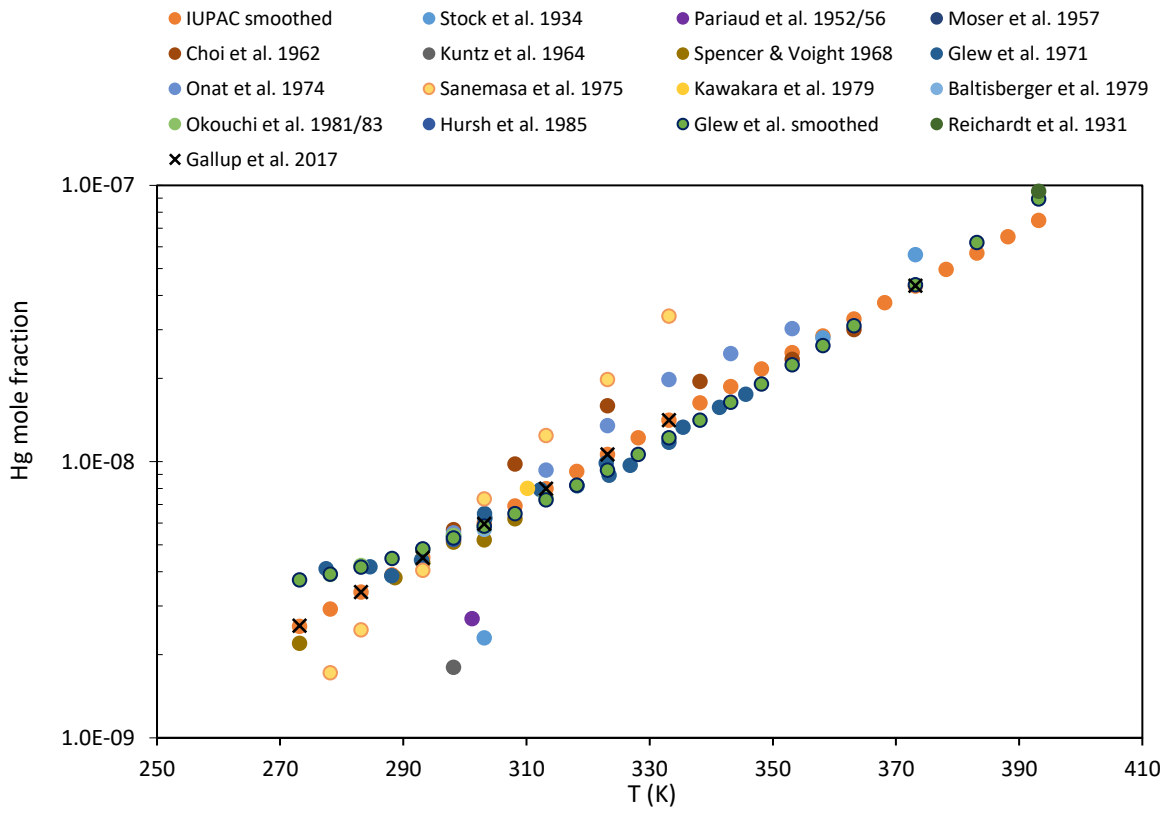

Figure 7.4. Elemental mercury solubility in water vs. temperature. (o): data from Clever et al. [86]; (x): data from Gallup et al. [3].

7.3.2 Results & discussion

Having ensured that the vapor pressure of Hg^0 is correctly predicted by the models, the next step is their parameterization for mixtures that contain elemental mercury. To this end, for SRK-Twu and PR-MC binary interaction parameters (k_{ij}) are estimated by fitting experimental Hg^0 solubility data, while for UMR-PRU new temperature-dependent UNIFAC interaction parameters are calculated following the same methodology. The objective function that was minimized during the regression was:

$$F_{obj} = \sum \left(\frac{S_{i,exp} - S_{i.calc}}{S_{i,exp}} \cdot 100 \right)^2 \qquad \text{Eq. 7.1}$$

where $S_{i,exp}$ and $S_{i.calc}$ are the experimental and calculated solubilities of elemental mercury in mole fraction basis, in each solvent, respectively.

For the extension of the UMR-PRU model in systems that contain mercury, Hg^0 was considered a separate UNIFAC group. The C_{nm} UNIFAC parameter (Eq. 6.36) was set to 0 for all binaries. During the fitting procedure it was observed that the solubility of mercury could not be correlated satisfactorily for linear, branched alkanes and cycloalkanes simultaneously, with the same binary interaction parameter (BIP). Therefore, the branched alkyl group and the cyclo-alkyl group were treated as separate UNIFAC groups, which in this work will be referred to as "bCH_2" and "cCH_2" respectively. The UNIFAC BIPs between groups CH_2, bCH_2 and cCH_2 were set equal to zero. The UNIFAC group-volume (R_K) and area (Q_K) parameters used in UMR-PRU are presented in Appendix B. Finally, the pure component critical temperatures, pressures and acentric factors necessary for all examined models were retrieved from the DIPPR data compilation [85]. The estimated UNIFAC group interaction parameters for the UMR-PRU model are presented in Table 7.2.

Table 7.2. UNIFAC interaction parameters between mercury and other groups determined in this work for UMR-PRU model.

m	n	A_{mn} (K)	B_{mn} (-)	C_{mn} (K^{-1})	A_{nm} (K)	B_{nm} (-)	C_{nm} (K^{-})
Hg	CO_2	681.17	4.5484	0	237.93	-1.4951	0
Hg	N_2	418.60	6.2324	0	308.81	-1.8667	0
Hg	CH_4	393.82	-0.0931	0	306.29	0.1852	0
Hg	C_2H_6	-80.36	0.5104	0	579.48	-0.6852	0
Hg	CH_2	947.05	4.9112	0	200.84	-0.9092	0
Hg	bCH_2	253.49	0.4966	0	362.76	-0.1603	0
Hg	cCH_2	733.53	3.1005	0	198.74	-0.9496	0
Hg	ACH	392.95	0.1600	0	245.11	-0.4325	0
Hg	$ACCH_2$	281.25	0.1781	0	295.44	1.0930	0
Hg	H_2O	-194.37	0.4464	0	534.35	-0.9257	0
Hg	MeOH	21.18	-0.1532	0	478.01	0.3878	0

Hg	OH	973.93	3.346	0	203.34	-0.2067	0
Hg	MEG	-9.01	-0.1574	0	535.30	0.4901	0
Hg	TEG	-34.38	1.0532	0	536.25	-0.5657	0
Hg	MEA	-52.59	1.6500	0	562.95	-1.7985	0
Hg	MDEA	14.72	0.8337	0	483.64	-0.5336	0

For prediction purposes, the binary interaction parameters of PR-MC and SRK-Twu that were fitted to experimental data for hydrocarbons heavier than ethane ("optimum k_{ij}'s") were used to develop generalized correlations of the form:

$$k_{ij} = A \cdot T_b + B \cdot MW + C \qquad \text{Eq. 7.2}$$

where T_b is the normal boiling point (in K) and MW is the molecular weight of the hydrocarbon, respectively. This form of correlation was chosen in order to enable distinction between isomers. Separate correlations for paraffinic, naphthenic, and aromatic hydrocarbons were deemed necessary, since mercury solubility in them shows different behavior as discussed in Section 7.3.1. Such correlations are very important for process simulation purposes, e.g. when pseudo-components are defined to characterize the heavy end fraction of natural gases and oils, where the only available information is the MW and T_b. The A, B and C coefficients for the two models are presented in Table 7.3. The optimum and generalized k_{ij}'s, as well as model deviations are presented in Table 7.4.

Table 7.3. Regressed coefficients estimating binary interaction parameters between Hg^0 and hydrocarbons heavier than ethane via Eq. 7.2 for SRK-Twu and PR-MC models.

Model	Hydrocarbon type	A	B	C
SRK-Twu	Paraffinic	-0.00041	-0.00025	0.17611
	Naphthenic	0.00140	-0.00452	-0.06382
	Aromatic	0.00313	-0.00693	-0.48925
PR-MC	Paraffinic	-0.00041	-0.00038	0.17513
	Naphthenic	0.00117	-0.00432	-0.00973
	Aromatic	0.00296	-0.00666	-0.46288

To obtain better correlation results in polar solvents, where cubic EoS with classical mixing rules are known to perform poorly, temperature-dependent k_{ij}'s were also estimated between all Hg^0/polar solvent binaries for SRK-Twu and PR-MC. The resulting parameters are presented in Table 7.5 along with deviations of all examined models from the experimental data.

Model prediction results in the experimental data sets that were excluded from the correlation database are presented in Table 7.6. Some representative results regarding calculated Hg^0 solubilities in various solvents are shown in Figure 7.5 through Figure 7.10.

Table 7.4. Optimum and generalized k_{ij} values for SRK-Twu and PR-MC along with their corresponding deviations in Hg^0 mole fraction compared with deviations yielded by the UMR-PRU model.

Solvent	SRK-Twu				PR-MC				UMR-PRU
	Optimum k_{ij}	AARD%[a]	Generalized k_{ij}	AARD%	Optimum k_{ij}	AARD%	Generalized k_{ij}	AARD%	AARD%
CO_2	0.3690	8.25	-	-	0.3651	7.89	-	-	5.87
N_2	-0.0168	9.52	-	-	0.0580	9.04	-	-	7.90
CH_4	0.0549	6.87	-	-	0.0913	6.95	-	-	5.49
C_2H_6	0.0867	6.13	-	-	0.0877	6.11	-	-	4.84
C3	0.0576	7.73	0.0712	9.65	0.0533	7.49	0.0644	8.78	3.75
nC5	0.0355	13.35	0.0324	14.42	0.0256	12.01	0.0220	13.28	9.90
nC6	0.0250	2.08	0.0156	6.22	0.0099	1.23	0.0034	4.60	5.63
nC7	0.0042	0.38	-0.0001	2.83	-0.0117	0.59	-0.0140	1.85	5.47
nC8	-0.0116	16.83	-0.0147	16.92	-0.0293	14.94	-0.0305	14.94	8.37
nC10	-0.0599	13.07	-0.0414	14.02	-0.0802	12.33	-0.0608	13.73	11.67
nC12	-0.0689	25.83	-0.0656	25.75	-0.0923	22.60	-0.0887	22.54	16.61
nC20	-0.1561	19.42	-0.1457	20.48	-0.1854	18.06	-0.1832	18.31	20.31
nC28	-0.2046	3.25	-0.2094	3.91	-0.2606	3.35	-0.2613	3.44	18.64
iC4	0.0415	0.84	0.0553	8.63	0.0351	1.11	0.0468	7.37	4.37
2-m-C5	0.0166	4.81	0.0190	5.33	0.0048	4.46	0.0068	4.93	5.18
2,2-dm-C4	0.0319	9.77	0.0233	11.39	0.0187	9.24	0.0111	10.74	8.54
2,2,4-tm-C5	0.0246	5.68	-0.0039	22.80	0.0083	4.62	-0.0197	22.75	3.22
cyC5	0.0644	3.68	0.0711	6.97	0.0576	3.98	0.0646	8.61	9.23
m-cyC5	0.0442	13.54	0.0394	15.69	0.0341	12.21	0.0305	13.64	12.08
cyC6	0.0522	11.48	0.0518	11.53	0.0422	10.80	0.0409	10.96	11.41
m-cyC6	0.0266	3.37	0.0168	7.68	0.0152	2.83	0.0040	8.62	3.42
cis-1,2-dm-cyC6	-0.0237	4.58	-0.0062	10.97	-0.0392	4.20	-0.0228	10.31	3.76
cis-1,4-dm-cyC6	-0.0238	3.24	-0.0138	6.53	-0.0393	2.89	-0.0292	6.45	2.26
trans-1,2-dm-cyC6	-0.0094	4.04	-0.0151	4.76	-0.0249	3.66	-0.0302	4.44	9.39
trans-1,4-dm-cyC6	-0.0124	3.76	-0.0208	6.12	-0.0273	3.43	-0.0350	5.53	9.34
cyC8	0.0283	2.77	0.0231	3.88	0.0060	2.44	0.0016	3.36	13.62

benzene	0.1184	3.39	0.0746	41.34	0.1079	2.40	0.0621	45.88	3.48
ethylbenzene	0.0099	5.52	0.0558	24.50	-0.0059	6.00	0.0414	24.73	26.42
1,2,4-tm-benzene	0.0266	13.51	0.0624	20.30	0.0071	13.25	0.0461	22.38	8.64
isopropyl benzene	0.0143	2.59	0.0093	4.43	-0.0017	2.11	-0.0041	2.78	11.77
t-butyl benzene	-0.0022	1.96	-0.0356	27.38	-0.0111	1.24	-0.0481	31.57	5.98
toluene	0.0723	10.10	0.0730	10.08	0.0583	9.25	0.0591	9.23	4.75
o-xylene	0.0608	3.00	0.0815	16.11	0.0467	3.43	0.0657	15.36	6.18
m-xylene	0.0533	11.66	0.0649	13.87	0.0369	11.19	0.0500	13.71	6.98
naphthalene	0.1916	6.99	0.1592	15.96	0.1708	6.75	0.1368	17.45	6.96
Overall		**7.64**		**13.09**		**7.20**		**12.61**	**6.89**

[a] $AARD\% = \frac{100}{NDP}\sum_{i=1}^{NDP} abs(S_{exp}^{Hg} - S_{calc}^{Hg})/S_{exp}^{Hg}$, where *S* is mole fraction of Hg^0 and NDP is the number of experimental data.

Table 7.5. Estimated k_{ij} values between Hg^0 and polar compounds for SRK-Twu and PR-MC models along with pertinent deviations in Hg^0 mole fraction compared with deviations yielded by the UMR-PRU model.

Solvent	SRK-Twu				PR-MC				UMR-PRU
	T-indep. k_{ij}[a]	AARD%[b]	T-dep. k_{ij}[c]	AARD%	T-indep. k_{ij}	AARD%	T-dep. k_{ij}	AARD%	AARD%
Water	0.8269	81.51	0.002460*T-0.088416	1.63	0.8135	80.97	0.002422*T-0.084172	2.01	3.06
Methanol	0.4520	33.17	0.000925*T+0.173418	3.50	0.4349	30.16	0.000816*T+0.189436	4.72	2.33
Ethanol	0.3671	21.15	0.001592*T-0.112608	1.00	0.3544	20.67	0.001565*T-0.117875	1.10	4.09
Propanol	0.2888	18.65	0.001346*T-0.102508	5.29	0.2787	17.38	0.001266*T-0.088412	5.01	6.90
MEG	0.5117	29.99	0.001035*T+0.193241	4.07	0.4998	28.12	0.000986*T+0.196180	4.02	3.49
TEG	0.3071	32.61	0.001693*T-0.220924	3.29	0.2801	32.95	0.001778*T-0.276395	3.65	2.51
MEA	0.4387	2.79	0.000305*T+0.336695	0.90	0.4151	2.38	0.000264*T+0.333385	0.90	0.77
MDEA	0.3306	6.93	0.000491*T+0.184129	1.99	0.2812	9.33	0.000782*T+0.04945	1.89	2.19
Overall		**34.37**		**2.83**		**33.37**		**3.21**	**2.92**

[a] Temperature-independent k_{ij}; [b] $AARD\% = \frac{100}{NDP}\sum_{i=1}^{NDP} abs(S_{exp}^{Hg} - S_{calc}^{Hg})/S_{exp}^{Hg}$, where *S* is mole fraction of Hg^0 and NDP is the number of experimental data; [c] Temperature-dependent k_{ij} (T in K).

Table 7.6. Prediction results in experimental data sets excluded from the correlation database (Appendix C) with SRK-Twu, PR-MC, and UMR-PRU. Generalized k_{ij}'s employed for SRK-Twu and PR-MC.

Solvent	AARD%[a]		
	SRK-Twu	PR-MC	UMR-PRU
CO_2	8.80	7.92	7.84
N_2	7.39	7.96	6.36
CH_4	2.50	2.39	5.27
nC5	15.10	20.69	26.12
nC6	8.76	7.63	6.29
methanol	5.37	5.51	4.51
MEG	20.43	19.92	20.29
TEG	9.54	10.13	9.53
Overall	**7.42**	**7.95**	**9.45**

[a] $AARD\% = \frac{100}{NDP}\sum_{i=1}^{NDP} abs(S_{exp}^{Hg} - S_{calc}^{Hg})/S_{exp}^{Hg}$, where S is mole fraction of Hg^0 and NDP is the number of experimental data.

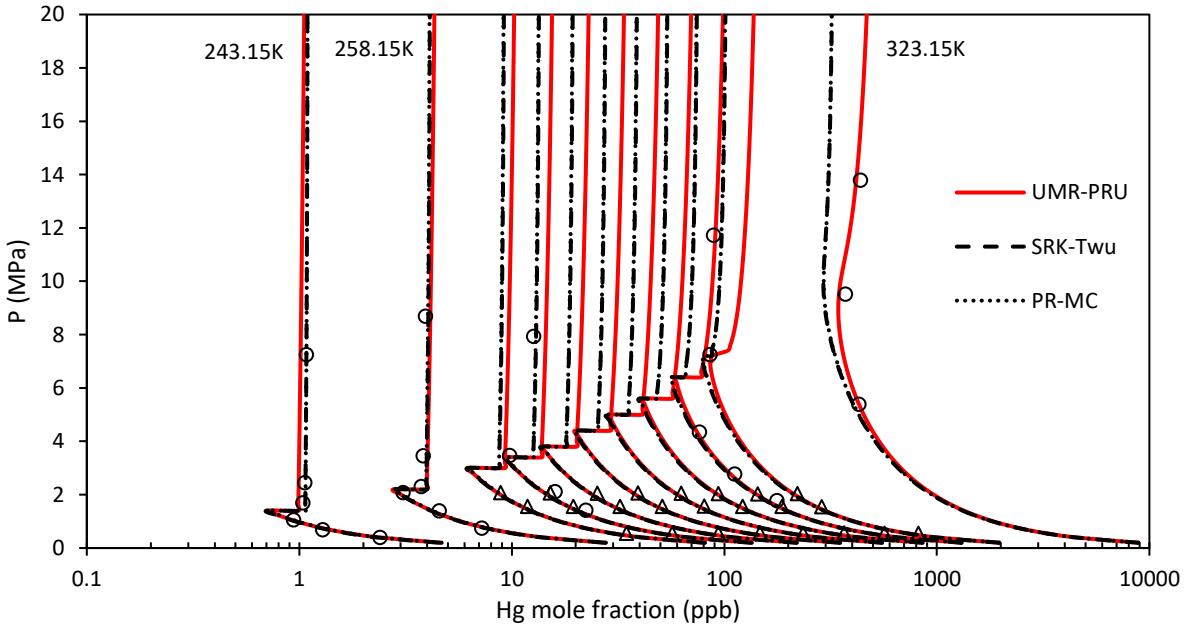

Figure 7.5. Hg^0 solubility in CO_2 at 243.15, 258.15, 268.15, 273.15, 278.15, 283.15, 288.15, 293.15, 298.15, 303.15 and 323.15 K as calculated with UMR-PRU, SRK-Twu, and PR-MC models. (O): exp. data from Chapoy et al. [84]; (△): exp. data from Yamada et al. [91].

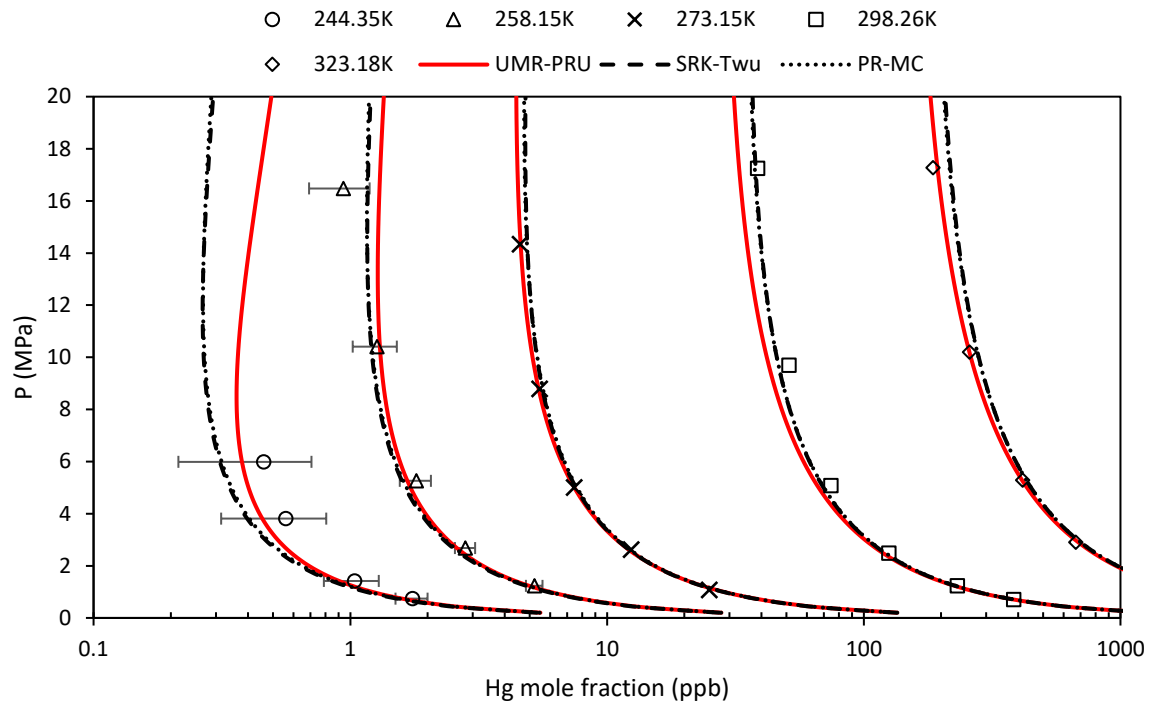

Figure 7.6. Hg^0 solubility in nitrogen as calculated with UMR-PRU, SRK-Twu, and PR-MC models. Exp. data from Chapoy et al. [84]. (Exp. data uncertainties not visible above 258.15 K.)

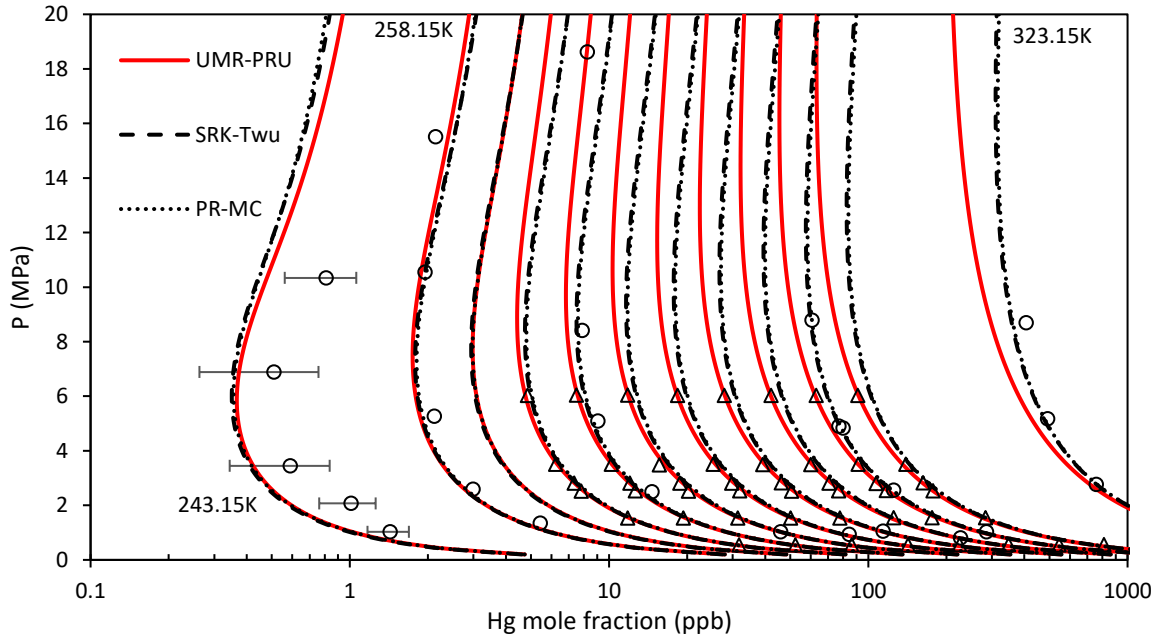

Figure 7.7. Hg^0 solubility in methane at 243.15, 258.15, 263.15, 268.15, 273.15, 278.15, 283.15, 288.15, 293.15, 298.15, 303.15 and 323.15 K as calculated with UMR-PRU, SRK-Twu, and PR-MC models. (O): exp. data from Chapoy et al. [84]; (△): exp. data from Yamada et al. [91]. (Exp. data uncertainties not visible above 243.15 K.)

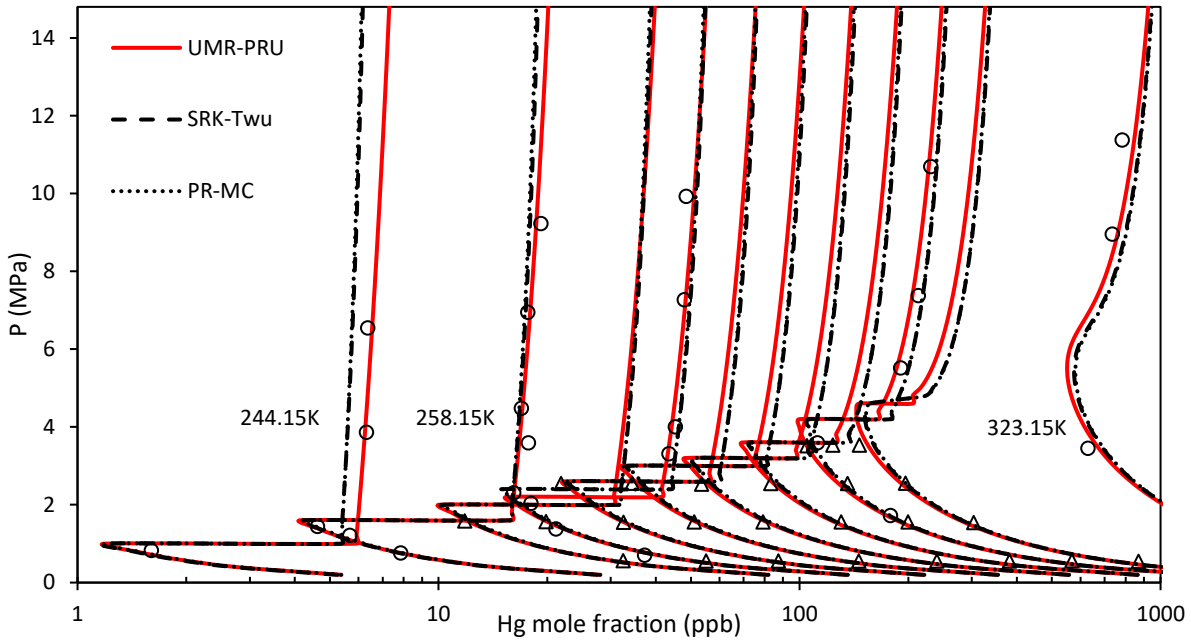

Figure 7.8. Hg^0 solubility in ethane at 244.15, 258.15, 268.15, 273.15, 278.15, 283.15, 288.15, 293.15, 298.15, 303.15 and 323.15 K as calculated with UMR-PRU, SRK-Twu, and PR-MC models. (O): exp. data from Chapoy et al. [84]; (△): exp. data from Yamada et al. [91].

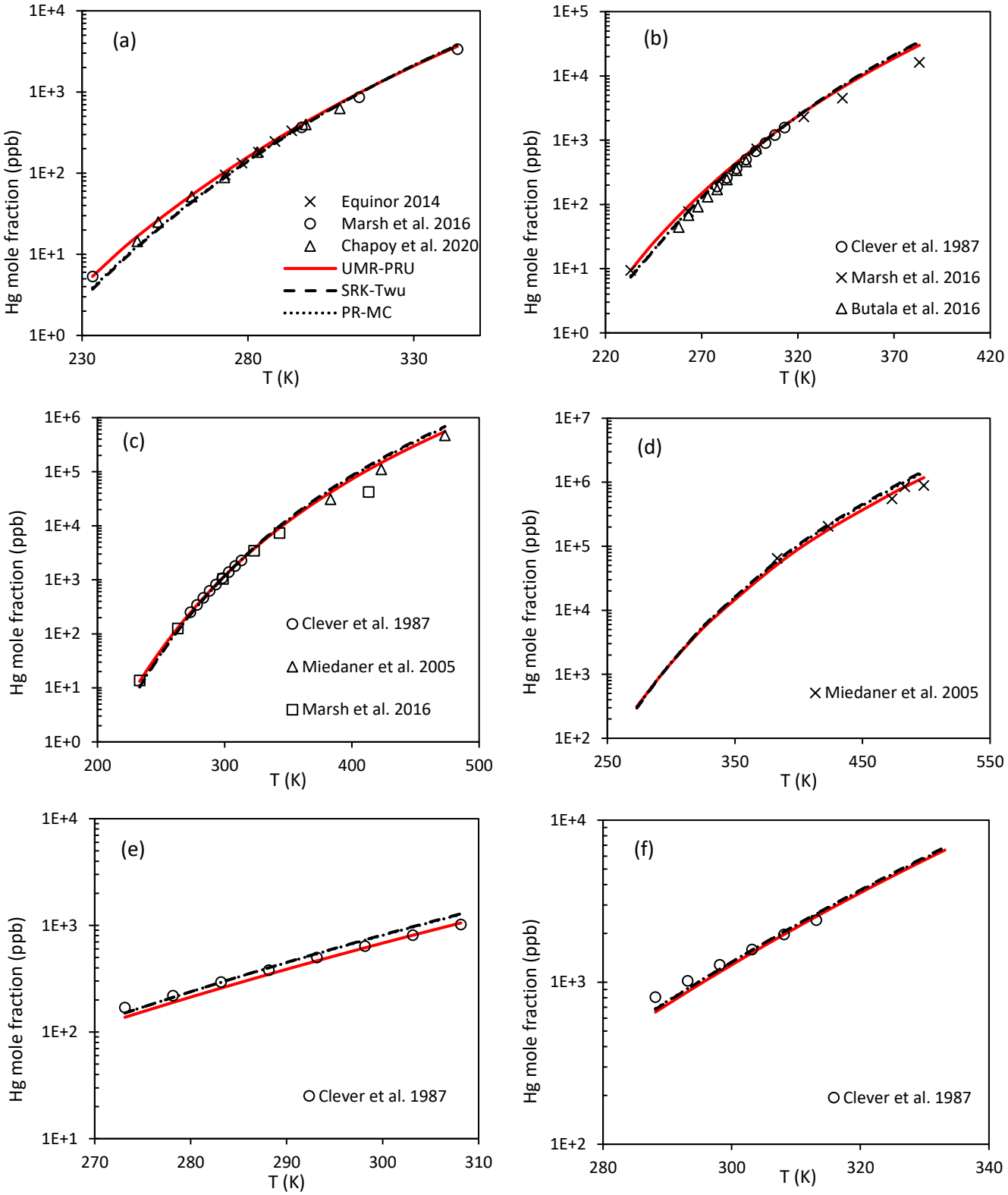

Figure 7.9. Hg^0 solubility in (a) propane, (b) n-pentane, (c) n-octane, (d) n-dodecane, (e) 2,2-dimethyl butane, and (f) cyclohexane vs. temperature. Generalized k_{ij}'s employed for SRK-Twu and PR-MC.

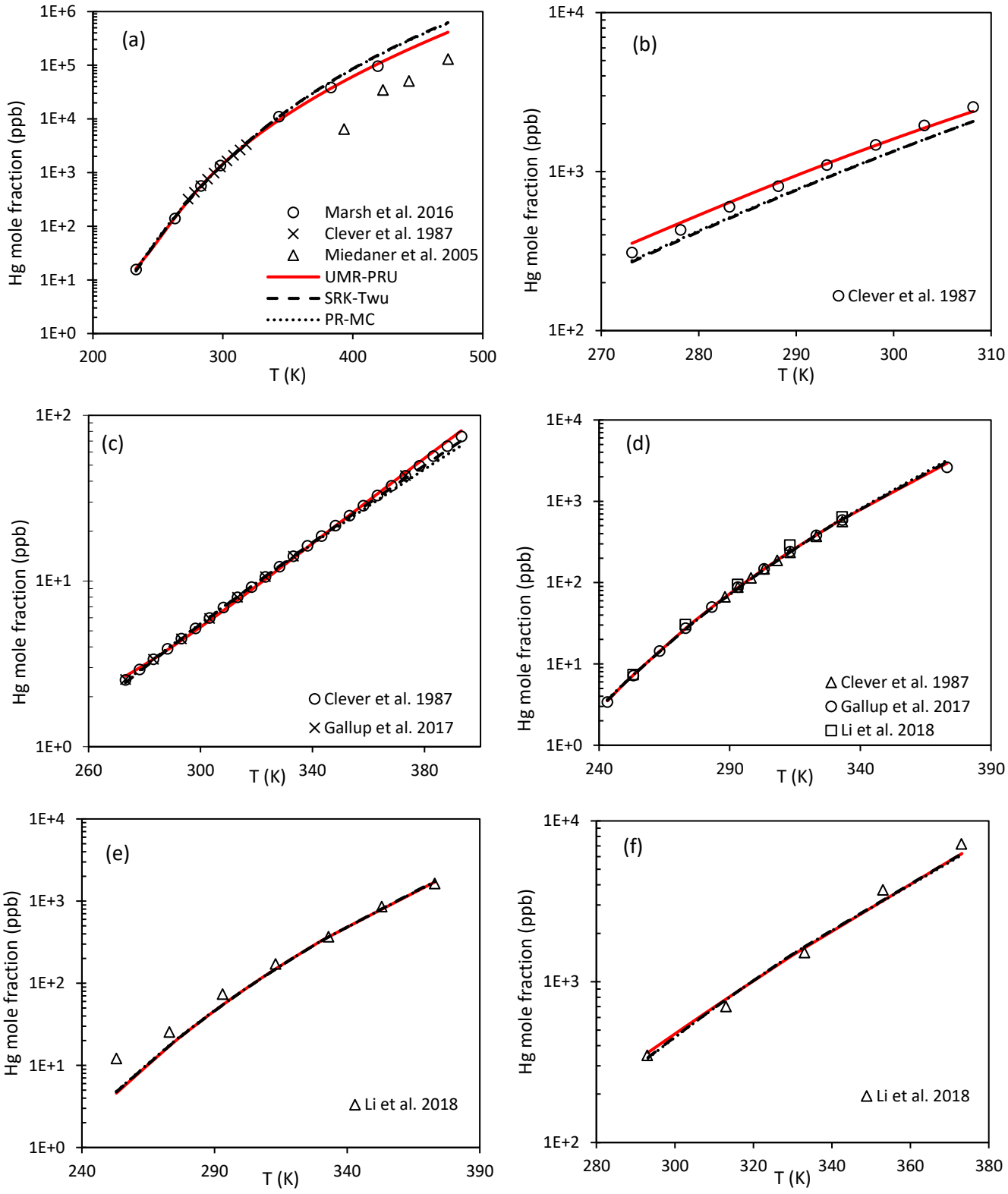

Figure 7.10. Hg^0 solubility in (a) toluene, (b) o-xylene, (c) water, (d) methanol, (e) MEG, and (f) TEG vs. temperature. Generalized k_{ij}'s used for hydrocarbon solvents and temperature-dependent k_{ij}'s used for polar solvents with SRK-Twu and PR-MC.

Overall, it is observed that UMR-PRU, as well as SRK-Twu and PR-MC with optimum binary interaction parameters, can accurately describe the solubility of elemental mercury in CO_2, N_2, and hydrocarbons. SRK-Twu and PR-MC yield very similar results, indicating that both attractive term formulations can be successfully employed for calculations in the systems of interest. Nevertheless, UMR-PRU yields the lowest AARD as compared to those of SRK-Twu and PR-MC, even when optimum k_{ij} values are used for the latter. This confirms the advantage of using advanced mixing rules such as UMR over the traditional vdW1f.

When generalized BIPs are used for SRK-Twu and PR-MC, the two models yield fairly good results regarding Hg^0 solubility in the aforementioned compounds. However, worse results are obtained in mixtures of Hg^0 with branched alkanes and aromatics. Despite using different generalized correlations for paraffinic, naphthenic and aromatic hydrocarbons, it appears that the k_{ij}'s for the latter are difficult to generalize with MW and T_b. This indicates that mercury solubility in aromatic hydrocarbons may also depend on other factors, such as molecule size and conformation.

Regarding Hg^0 solubility in polar solvents, it is shown that the SRK-Twu and PR-MC EoS with traditional vdW1f mixing rules yield unsatisfactory correlation results when a temperature-independent k_{ij} is employed. The correlation results are improved significantly when a linear temperature dependence is attached to the binary interaction parameter. SRK-Twu also appears to have a slight advantage over PR-MC in these mixtures. On the other hand, UMR-PRU yields very low deviations from experimental data, with an AARD similar or lower than those of the other models with temperature-dependent k_{ij}'s.

Finally, regarding model predictions in systems excluded from the correlation database, it is shown that all models yield similar results. The highest deviations are observed in n-pentane and MEG, where the experimental data from the various sources exhibit slightly different trends with temperature (Figure 7.9).

7.4 Prediction of Hg^0 solubility in multicomponent mixtures

The final step is model evaluation based on their capability to predict the solubility of elemental mercury in multicomponent mixtures, which are of high interest for oil & gas processes. Toward this, a literature review is conducted and relevant experimental data are compiled in a database.

Marsh et al. [88] have measured the solubility of mercury in two hydrocarbon mixtures, but the data cannot be used for model validation since there is no information on the phase type and density of the fluids. Chapoy et al. [79] have measured Hg^0 solubility in three synthetic natural gas mixtures at a wide temperature and pressure range. The GPA research report RR-224 [90] also contains some measurements for Hg^0 solubility in liquid propane/iso-butane mixture. Finally, Equinor has kindly provided measurements for elemental mercury solubility in liquid hydrocarbon mixtures, as well as mixtures of polar compounds (methanol, MEG, TEG,

MDEA) with water. All the available experimental data are summarized in Table 7.7 through Table 7.9.

Table 7.7. Database with experimental Hg^0 solubilities in hydrocarbon mixtures.

Solvent	Ref.	Type	T range (K)	P range (bar)	NDP[a]
Mix 1	[79]	VLE	243.15-323.14	6.8-160.6	19
Mix 2	[79]	VLE/LLE	243.16-323.15	7.3-155.4	15
Mix 3	[79]	VLE/LLE	243.16-323.15	6.6-137.9	14
Mix 4	[92]	SC	263.15-293.15	27.6-69.0	8
Mix 5	[93]	LLE	293.15-313.15	1.0	3
Mix 6	[93]	LLE	293.15-333.15	1.0	3
Mix 7	[93]	LLE	293.15-333.15	1.0	3
Mix 8	[93]	LLE	293.15-333.15	1.0	3
Mix 9	[90]	LLE	253.15-278.15	33.9-69.0	10

[a]NDP: number of experimental data points

Table 7.8. Database with experimental Hg^0 solubilities in polar mixtures.

Solvent	Ref.	Type	T range (K)	P range (bar)	Water content (% wt.)	NDP[a]
MeOH + H_2O	[93]	LLE	283.15-313.15	1.0	5-30	9
MEG + H_2O	[93]	LLE	283.15-313.15	1.0	5-40	16
TEG + H_2O	[93]	LLE	293.15-313.15	1.0	1-10	12
MDEA + H_2O	[93]	LLE	303.15-323.15	1.0	40	3

[a]NDP: number of experimental data points

Table 7.9. Compositions (% mol) of multicomponent systems examined in this work.

Component	Mix 1	Mix 2	Mix 3	Mix 4	Mix 5	Mix 6	Mix 7	Mix 8	Mix 9
CO_2	0.7710	8.7212	69.3500	2.1600	-	-	-	-	-
N_2	0.3900	0.4695	3.0760	1.0300	-	-	-	-	-
CH_4	89.2400	74.9060	26.2840	88.1000	-	-	-	-	-
C_2H_6	6.5160	10.3970	0.9310	6.2000	-	-	-	-	-
C3	2.2550	3.9420	0.2889	2.5100	-	-	-	-	59.4000
iC4	0.3170	0.5769	-	-	-	-	-	-	40.6000
nC4	0.4410	0.9871	0.0719	-	-	-	-	-	-
iC5	0.0442	-	-	-	-	-	-	-	-
nC5	0.0299	-	-	-	-	-	-	-	-
nC6	-	-	-	-	60.0000	50.0000	50.0000	20.0000	-
nC8	-	-	-	-	30.0000	-	-	-	-
nC12	-	-	-	-	10.0000	-	-	-	-
cyC6	-	-	-	-	-	50.0000	-	55.0000	-
toluene	-	-	-	-	-	-	50.0000	25.0000	-

The deviations of model predictions from experimental Hg^0 solubilities in multicomponent hydrocarbon mixtures are presented in Table 7.10 and in polar mixtures in Table 7.12. Some representative results in hydrocarbon mixtures are shown in Figure 7.11. It should be noted that for the calculations with SRK-Twu and PR-MC, the binary interaction parameters between components other than mercury were retrieved from Aspen HYSYS v8.8 software.

Regarding model results in hydrocarbon mixtures, it appears that in mixtures 1-3, UMR-PRU yields much higher deviations than the other models. However, this is mainly due to the high deviations in the lowest isotherm of 243.15 K, where measurement uncertainties are non-negligible. Nonetheless, UMR-PRU predictions below 100 bar are within the range of measurement uncertainty. If the lowest isotherm is excluded from the analysis of mixtures 1-3, the overall AARD of model predictions in them become 8.1%, 7.8% and 10.8% with SRK-Twu, PR-MC and UMR-PRU model, respectively. Therefore, all three models yield satisfactory results in these mixtures. In mixtures 4-5, all models yield similar results, with UMR-PRU being the most accurate. On the other hand, in mixtures 6-7 all models yield high deviations and appear to overpredict Hg^0 solubility at the highest measured temperature of 333.15 K. Finally, in mix 9 the models again yield comparable results, with PR-MC being the most accurate.

Table 7.10. Model prediction results in multicomponent hydrocarbon mixtures. Generalized k_{ij}'s employed for SRK-Twu and PR-MC.

Solvent	AARD%		
	SRK-Twu	PR-MC	UMR-PRU
Mix 1	9.18	8.93	17.09
Mix 2	9.54	8.87	22.91
Mix 3	11.11	10.29	15.29
Mix 4	8.92	8.20	7.64
Mix 5	10.19	9.41	7.82
Mix 6	25.69	23.97	22.64
Mix 7	17.24	16.05	14.96
Mix 8	17.35	16.09	4.53
Mix 9	9.58	7.91	12.71
Overall	**10.92**	**10.10**	**15.65**

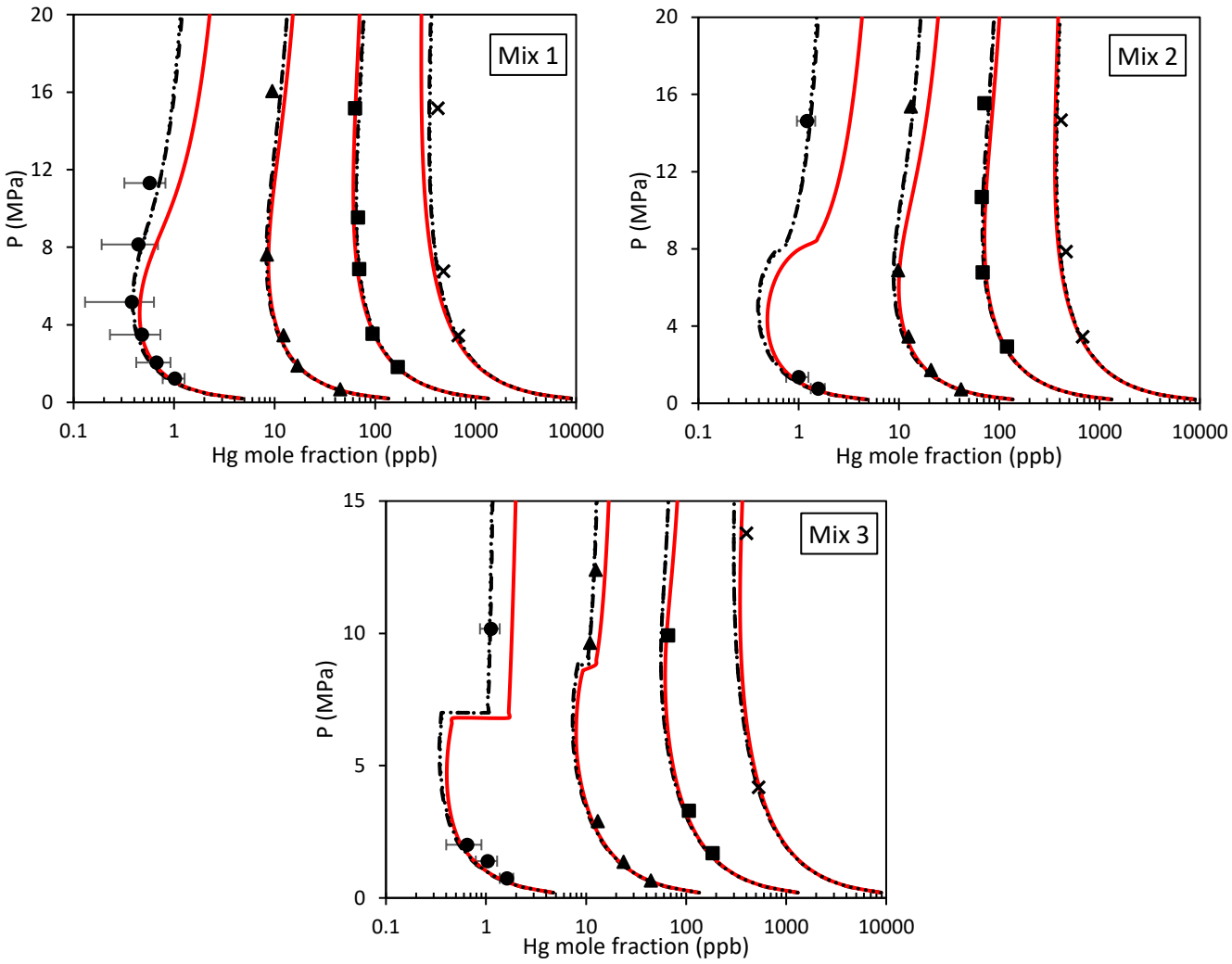

Figure 7.11. Hg^0 solubility in mixtures 1-3 as calculated with UMR-PRU, SRK-Twu and PR-MC models against exp. data by Chapoy et al. [79] at 4 isotherms: (●): 243.15 K; (▲): 273.15 K; (■): 298.15 K; (**X**): 323.15 K; solid red line: UMR-PRU; black dashed line: SRK-Twu; black dotted line: PR-MC. (Exp. data uncertainties not visible above 243.15 K.)

Regarding polar mixtures, preliminary calculations with UMR-PRU showed that it was challenging to find appropriate UNIFAC interaction parameters that can simultaneously describe well both the binary mixtures of polar components with mercury, as well as the ternary mixtures with water. In these mixtures, besides polar component/mercury and water/mercury interactions, polar component/water interactions also play an important role. The existing UMR-PRU parameters between polar components/water have been estimated in previous works [71-73] based on vapor-liquid equilibrium data. Since the examined mixtures in this work concern liquid-liquid equilibrium, it was decided to simultaneously fit the Hg/polar component and water/polar component parameters both to binary and ternary mixtures, based on the experimental data presented in Appendix C and Table 7.8, respectively. The resulting water/polar solvent parameters are recommended for use only in mercury systems that are in liquid-liquid equilibrium and are presented in Table 7.11.

Table 7.11. UNIFAC interaction parameters determined in this work between water/polar components to be used in LLE calculations for mercury systems with UMR-PRU model.

m	n	A_{mn} (K)	B_{mn} (-)	C_{mn} (K^{-1})	A_{nm} (K)	B_{nm} (-)	C_{nm} (K^{-})
MeOH	H_2O	-249.29	0	0	230.24	0	0
MEG	H_2O	-193.14	0	0	20.46	0	0
TEG	H_2O	-81.29	0	0	-163.39	0	0
MDEA	H_2O	-78.90	0	0	-989.76	0	0

Table 7.12. Model prediction results in polar mixtures. Temperature-dependent k_{ij}'s employed for SRK-Twu and PR-MC.

Solvent	AARD%		
	SRK-Twu	PR-MC	UMR-PRU
MeOH + H_2O	17.24	12.26	4.08
MEG + H_2O	32.15	32.87	4.07
TEG + H_2O	19.30	19.25	5.36
MDEA + H_2O	12.26	22.35	2.78
Overall	**23.45**	**23.36**	**4.36**

The results of the examined models in ternary mercury mixtures are presented in Table 7.12. It is known that the addition of water in a polar solvent reduces Hg^0 solubility. Although this effect is qualitatively described by the cubic EoS, even with temperature-dependent k_{ij}'s, SRK-Twu and PR-MC yield unsatisfactory results, with an AARD greater than 20%. Conversely, UMR-PRU yields very low deviations from experimental data. This confirms the superiority of advanced mixing rules, such as UMR, over the traditional vdW1f.

7.5 Conclusions

In this chapter, the UMR-PRU model has been successfully extended to mixtures of mercury with gases (CO_2, N_2), hydrocarbons, water, alcohols, glycols and amines. For comparison, the widely used cubic EoS SRK and PR were also employed with modified attractive terms, in order to correctly describe the vapor pressure of pure mercury. More specifically, SRK was coupled with the *α*-function proposed by Twu, while the Mathias-Copeman function was used for PR and for mercury and polar compounds with UMR-PRU. The pertinent *α*-function parameters were determined by fitting experimental Hg^0 vapor pressure data, and very low deviations were achieved (<1%).

Subsequently, interaction parameters were determined for all models by fitting experimental Hg^0 solubility data. For UMR-PRU, three new UNIFAC groups were introduced –Hg^0, bCH_2 and cCH_2– and temperature dependent interaction parameters between the groups involved in the studied systems were estimated. For SRK-Twu and PR-MC generalized correlations for predicting the k_{ij} values between mercury and hydrocarbons heavier than ethane were developed based on the hydrocarbon type (paraffinic, naphthenic, aromatic), and their molecular weight and boiling point. In addition, temperature-dependent k_{ij}'s were estimated

for SRK-Twu and PR-MC between mercury and polar solvents, such as water, alcohols, glycols and amines. Overall model results in binary mixtures were very satisfactory, with UMR-PRU being the most accurate.

Finally, all models were employed for predicting Hg^0 solubility in multicomponent hydrocarbon systems, as well as in ternary mixtures with water. In hydrocarbon mixtures, all models yielded similar results with satisfactory deviations, while in polar mixtures UMR-PRU yielded the best results. This confirms the superiority of advanced mixing rules, such as UMR, over the traditional vdW1f. Therefore, it is concluded that UMR-PRU is a powerful tool for modelling mercury phase behavior in mixtures involved in oil & gas processing.

8. Thermodynamic modelling of hydrogen vapor-liquid equilibrium with oil & gas components

8.1 Introduction

A main point of focus of this work is the study of the theoretical reaction between elemental mercury and hydrogen sulfide present in natural gas, which leads to formation of solid mercury sulfide:

$$Hg + H_2S \Leftrightarrow \beta\text{-}HgS + H_2 \qquad \text{Eq. 8.1}$$

Hydrogen is also a product of this reaction, so in order to study the simultaneous chemical & phase equilibria of Hg^0 in natural gas with UMR-PRU it is necessary to extend the model in mixtures of hydrogen with NG components.

Besides this, a thermodynamic model that can accurately describe hydrogen phase equilibrium in oil & gas components is useful for various applications. Hydrogen finds extensive use in the petroleum industry in processes such as hydrodesulfurization, hydrocracking etc. These processes are of great economic importance, since they transform heavy oil into more valuable light components, and allow stricter sulfur content specifications to be met. In the last decades, hydrogen has also been proposed as a replacement for fossil fuels in the energy sector. The combustion of hydrogen produces no greenhouse gases (e.g. CO2) or toxic pollutants, and can be used for electricity production, to power automobiles or for domestic uses. In recent years, the proposal for the replacement of a substantial amount of natural gas by hydrogen in the existing natural gas grid is advocated. In the future, hydrogen is expected to play an important role in achieving a “zero-emissions” society [94].

Hydrogen is the lightest and most abundant chemical element in nature. At ambient conditions, it is found in the form of a colorless, odorless, tasteless, non-toxic, highly combustible diatomic gas (H_2). Because of its very small molecule size, hydrogen is characterized as a quantum fluid, which means that its physical properties can be fully described only if quantum effects are also considered [95]. Furthermore, H_2 is found in supercritical state at common process conditions (T_c = 33.18 K, P_c = 13.13 bar [85]), making accurate vapor-liquid equilibrium (VLE) description in mixtures even more challenging.

For describing the VLE of hydrogen/hydrocarbon systems, the Grayson-Streed method [96] has been traditionally used by the petroleum industry. This method was proposed in 1963 as an improvement to the classical Chao-Seader method [97] specifically for such mixtures and it involves the calculation of the distribution coefficient ($K_i=y_i/x_i$) using three different models. The Grayson-Streed method has the advantage of being predictive, but it fails to accurately describe the solubility of hydrogen in heavy hydrocarbons.

One of the first attempts at describing the vapor-liquid equilibria of hydrogen/hydrocarbon mixtures solely with a cubic equation of state (EoS) was that of Graboski and Daubert [98] in 1979. These authors employed the SRK EoS but introduced another attractive term temperature dependency specifically for hydrogen, which they fitted to binary VLE data, thus eliminating the need for binary interaction parameters (k_{ij}). A few years later, Moysan et al. [99, 100] developed generalized correlations for predicting the k_{ij} between hydrogen and other substances to be used with the SRK and PR EoS combined with classical van der Waals one fluid mixing rules.

Since these early works, a multitude of thermodynamic models has been proposed in the literature regarding VLE description of hydrogen/hydrocarbon systems, ranging from classical cubic equations of state to SAFT-type or even quantum-mechanical models. In order to overcome the aforementioned challenges, many authors employ a modified attractive term (α) for the cubic EoS [101-107] or utilize more advanced mixing rules [102, 104, 108-110]. More recently, Qian et al. [111] employed a group contribution method for predicting the binary interaction parameters of the PPR78 EoS. Some authors have also used variations of the SAFT EoS for predicting hydrogen phase equilibria in hydrocarbon systems [112-114]. Lastly, Lei et al. [115] employed COSMO-RS for modelling the solubility of hydrogen in diesel.

In this work, the UMR-PRU model is extended to mixtures of hydrogen with hydrocarbons, gases (N_2, CO_2, H_2S), and polar compounds (water, methanol, MEG, TEG) and is employed for VLE predictions in binary and multicomponent H_2 mixtures. The performance of UMR-PRU is also compared with that of another predictive model, namely PPR78.

8.2 *a*-function consistency and pure H_2 property estimation

The first step in the extension of UMR-PRU to mixtures containing hydrogen is to check the capability of the PR EoS to describe pure H_2 properties. Both the Soave (Eq. 6.4) and Mathias-Copeman (Eq. 6.5) expressions for the attractive term of PR are evaluated for calculating hydrogen properties at sub- and supercritical conditions. It must also be ensured that the selected *a*-function is consistent, according to the mathematical criteria discussed in Section 6.2.

Le Guennec et al. [55, 56] found that Soave's expression is consistent until very high temperatures (> 1500 K) only when [m(m+1)] > 0. In the case of hydrogen, which has an acentric factor equal to -0.215 [85], this requirement is satisfied. On the other hand, the study by Le Guennec et al. showed that the Mathias-Copeman *a*-function is inconsistent due to the utilization of different expressions for the sub- and supercritical domain. However, if the cubic expression of MC is maintained both at sub- and supercritical temperatures, a set of c_1, c_2, c_3 parameters can be found, for which the α-function satisfies the consistency criteria at least until an arbitrary high temperature.

For evaluating the Soave and Mathias-Copeman *a*-functions, 100 experimental data regarding H_2 vapor pressure were generated from the DIPPR data compilation [85] at temperatures

from the triple to the critical point, and 230 enthalpy (H) and 230 isobaric heat capacity (C_p) experimental data points were generated from the NIST database [116] at temperatures from 300 K to 750 K and pressures from 15 bar to 500 bar. It should be noted that the generated data for C_p and H concern the supercritical region, while the vapor pressure concerns the subcritical region. Different fitting methods for the MC parameters were explored by regressing pure H_2 vapor pressure or both vapor pressure and enthalpy while imposing consistency constraints on the parameters. The criteria employed in this work ensured that the alpha function is consistent at least until 1000 K, a temperature which is higher than those encountered in common oil & gas industrial processes. The regressed parameters were also tested in predicting the isobaric heat capacity of pure H_2 at supercritical conditions. The results of the MC parameter fitting are summarized in Table 8.1 and are compared with the respective results obtained with Soave's expression.

Table 8.1. Correlation and prediction results for pure hydrogen properties with PR EoS and different *α*-functions.

Alpha function	Regressed property	AARDP^s%[a]	AARDH%	AARDC$_p$%
Mathias-Copeman	P^s	3.01	1.83	0.37
Mathias-Copeman	P^s + H	3.06	1.76	0.22
Soave	-	3.16	1.68	0.18

[a] $AARD\% = 100/ND \sum_{i=1}^{ND} \left|X_i^{exp} - X_i^{calc}\right| / X_i^{exp}$, where ND is the number of experimental data points and X the studied property (P^s for vapor pressure, H for enthalpy and C_p for isobaric heat capacity)

It is shown that when consistency criteria are enforced on the MC parameters, similar results are obtained regardless of the temperature region of regression. These results are also similar with the ones yielded by Soave's α-function. In other words, even though the MC expression is more complex, in the case of hydrogen this α-function provides no advantage against the classical Soave expression when consistency constraints are imposed on its parameters. Therefore, due to the simplicity of the Soave expression and its slightly better results for the supercritical properties, it was decided that this α-function will be employed for hydrogen in UMR-PRU.

8.3 VLE description in binary mixtures of hydrogen

For extending UMR-PRU to mixtures containing hydrogen, a literature review was conducted regarding pertinent binary VLE experimental data. A plethora of experimental measurements was found in the open literature, with the main sources being the Chemistry Data Series by DECHEMA [117] and Solubility Data Series by IUPAC [118]. In total, 3807 experimental bubble and 2309 dew points were collected. The database is presented in detail in Appendix C.

Following the previous work on UMR-PRU model extension for mercury, the cyclo-alkyl main group "cCH_2" was maintained. The UNIFAC binary interaction parameters employed in UMR-

PRU were estimated through bubble point pressure (BBP) regression, with the minimized objective function being:

$$F_{obj} = \frac{1}{ND}\sum_{i=1}^{ND}\left(\frac{\left|P_i^{exp} - P_i^{calc}\right|}{P_i^{exp}} \cdot 100\right) \quad \text{Eq. 8.2}$$

For the groups participating in components, for which the experimental data spanned a temperature range less than 100 K, the C_{nm} UNIFAC parameter (Eq. 6.36) was set equal to 0. The estimated UNIFAC group interaction parameters for the UMR-PRU model are presented in Table 8.2 and the deviations of model calculations from the experimental data are presented in Table 8.3. For comparison, results with PPR-78 are also included in the same table. Some typical isothermal phase diagrams for binary systems with UMR-PRU are presented in Figure 8.1 and Figure 8.2.

Table 8.2. UNIFAC interaction parameters between hydrogen and other groups determined in this work for UMR-PRU model.

m	n	A_{mn} (K)	B_{mn} (-)	C_{mn} (K^{-1})	A_{nm} (K)	B_{nm} (-)	C_{nm} (K^{-1})
CO_2	H_2	521.47	0.783	0	-53.53	-3.276	0
N_2	H_2	-86.71	-1.009	0	-19.32	-0.220	0
H_2S	H_2	-29.37	-8.694	0	-107.19	-7.431	0
CH_4	H_2	387.15	1.291	8.35E-04	-82.98	-0.121	3.02E-03
C_2H_6	H_2	517.10	4.375	1.59E-02	-185.68	-2.540	-3.16E-03
CH_2	H_2	-8.51	-0.934	2.38E-03	186.74	-0.711	-6.85E-04
cCH_2	H_2	322.35	-3.218	2.13E-03	-89.31	1.945	8.57E-04
ACH	H_2	328.04	-3.016	8.15E-04	8.32	1.879	-1.08E-03
$ACCH_3$	H_2	83.44	-4.348	9.50E-03	233.79	10.954	-1.37E-02
H_2O	H_2	1251.53	7.474	-1.99E-02	520.94	6.421	-4.48E-02
MeOH	H_2	371.45	-4.112	2.85E-02	234.28	26.433	3.26E-01
MEG	H_2	419.94	-1.103	0	232.72	0.852	0
TEG	H_2	443.90	-0.885	0	305.47	-1.018	0

Table 8.3. VLE results with UMR-PRU and PPR-78 models.

H_2 with	UMR-PRU		PPR78	
	AARDP%	AADy [a]	AARDP%	AADy
CO_2	6.8	3.30	15.5	3.62
N_2	9.7	2.20	10.7	1.44
H_2S	12.2	-	12.1	-
CH_4	4.1	1.87	12.9	1.73
C_2H_6	10.2	1.09	37.1	1.28
C3	8.1	1.20	8.5	1.32
nC4	9.9	1.10	12.3	1.87
nC5	10.1	0.01	17.5	1.53
nC6	10.3	1.27	14.3	1.68

nC7	9.5	2.35	10.9	2.66
nC8	4.1	0.91	12.2	3.50
nC10	7.6	1.81	8.5	2.92
nC12	11.9	-	2.7	-
nC14	9.9	-	4.8	-
nC16	15.3	0.46	6.0	0.45
nC20	24.9	0.11	14.5	0.04
iC4	17.9	5.56	13.8	5.26
2,3-dm-C4	7.2	-	11.0	-
iC8	7.5	0.95	13.9	1.51
cyC6	6.1	0.20	5.7	0.25
m-cyC6	1.9	-	20.5	-
b-cyC6	9.4	0.75	11.8	3.01
benzene	5.5	1.07	4.1	0.78
toluene	9.9	2.50	9.2	2.96
m-xylene	9.0	2.03	8.5	2.32
p-xylene	5.3	-	9.5	-
e-benzene	6.8	-	2.5	-
1,2,4-tm-benzene	2.8	-	16.7	-
1,3,5-tm-benzene	13.9	-	13.5	-
isopropylbenzene	6.8	-	6.0	-
diphenylmethane	5.5	0.57	10.3	0.94
naphthalene	11.7	-	5.5	-
1-m-naphthalene	3.7	0.64	3.3	1.61
phenanthrene	18.7	0.06	12.8	0.05
tetralin	4.2	2.37	3.7	2.35
H_2O	6.4	2.98	11.0	1.31
MeOH	8.8	0.30	-	-
MEG	0.5	-	-	-
TEG	2.4	-	-	-
Overall [b]	**8.1**	**1.64**	**13.2**	**1.81**

[a] $AADy = 100/ND \sum_{i=1}^{ND} \left| y_i^{exp} - y_i^{calc} \right|$, where ND is the number of experimental data points and y the mole fraction of hydrogen in the vapor phase; [b] Excluding MeOH, MEG and TEG.

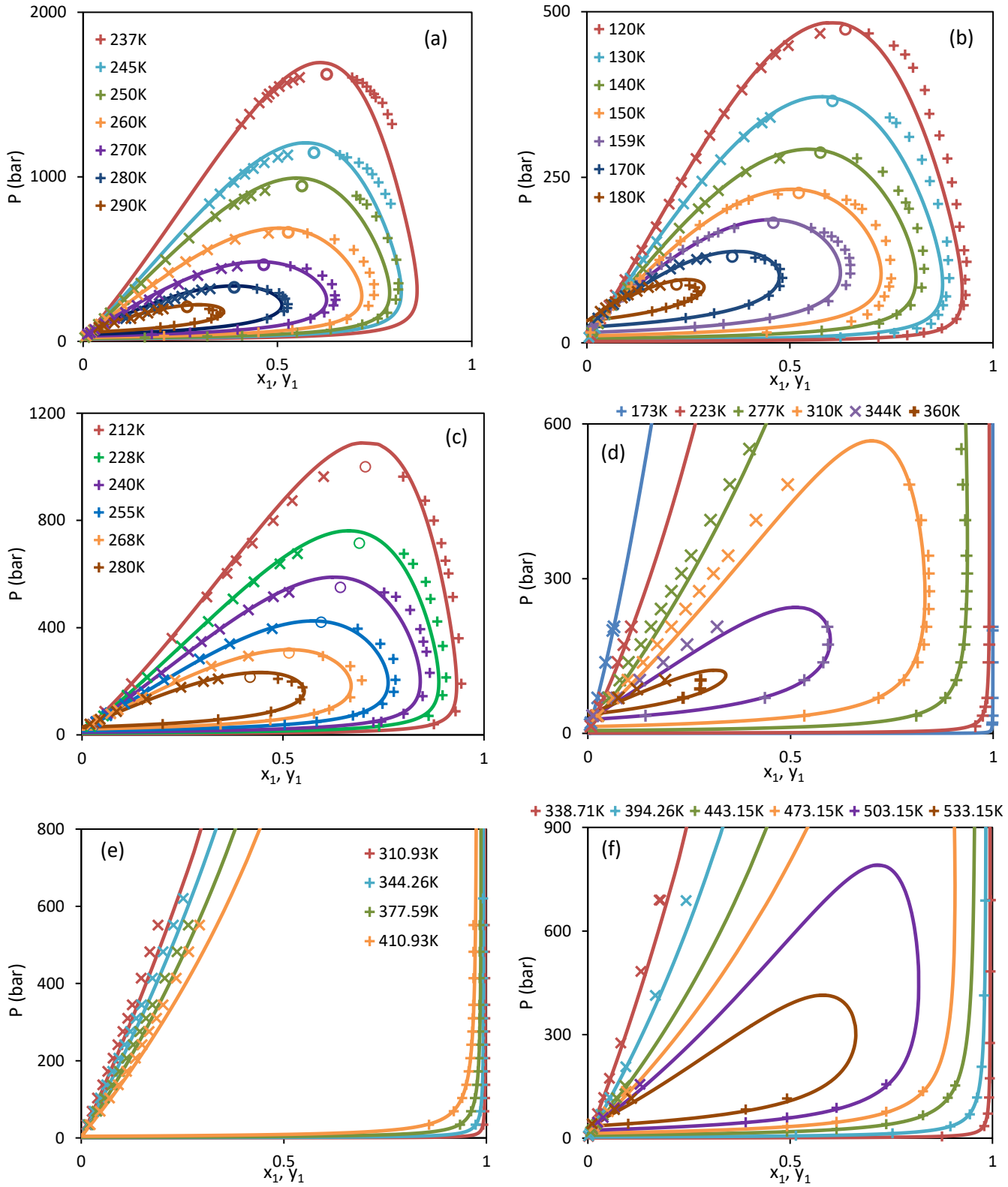

Figure 8.1. Isothermal dew and bubble point curves for 6 binary mixtures with UMR-PRU: (a) H_2 (1) – CO_2 (2), (b) H_2 (1) – CH_4 (2), (c) H_2 (1) – C_2H_6 (2), (d) H_2 (1) – C3 (2), (e) H_2 (1) – cyC6 (2), (f) H_2 (1) – benzene (2). (**x**): experimental bubble points, (**+**): experimental dew points, (o)**:** experimental critical points, solid lines: model results.

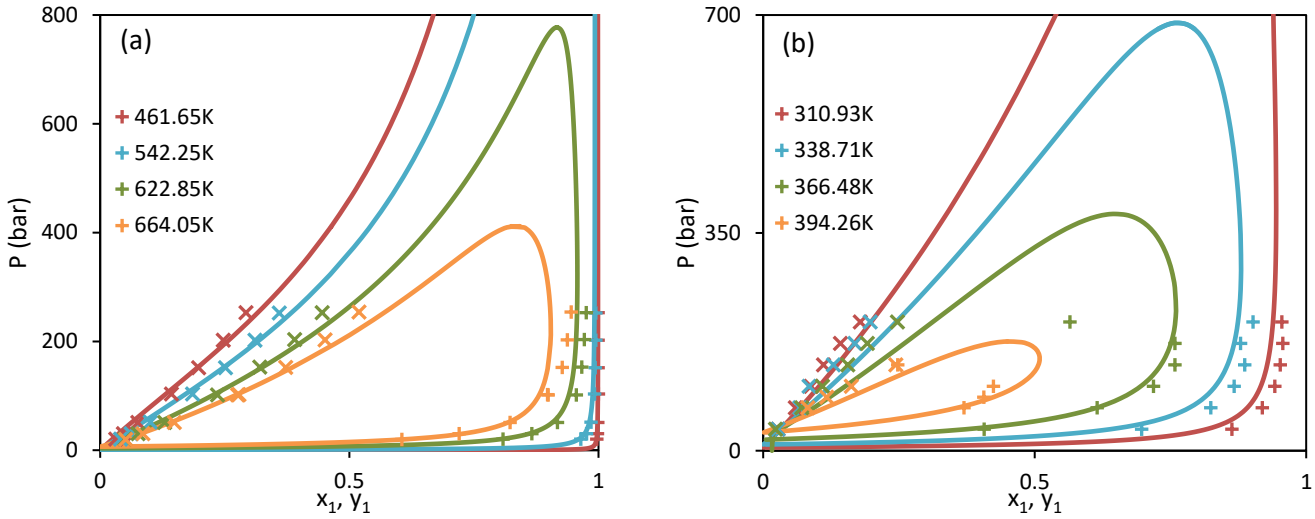

Figure 8.2. Isothermal dew and bubble point curves for 2 binary mixtures with UMR-PRU: (a) H_2 (1) – nC16 (2), (b) H_2 (1) – iC4 (2). (**x**): experimental bubble points, (**+**): experimental dew points, solid lines: model results.

The overall deviations reveal that UMR-PRU is capable of accurately describing the VLE of hydrogen binary mixtures, yielding better overall results than PPR78 both in BBP and vapor phase composition. Regarding gas components (CO_2, N_2, CH_4, C_2H_6), light normal alkanes up to n-decane and branched alkanes, it is observed that UMR-PRU yields better results than PPR78. Notably, in the case of ethane PPR78 yields an abnormally high AARD% in bubble point pressure, which according to Qian et al. [111] can be attributed to the compromise between VLE data and critical point restitution during PPR78 parameter regression. On the other hand, in heavy alkanes PPR78 appears to be more accurate than UMR-PRU. Concerning naphthenic hydrocarbons, UMR-PRU yields slightly better results than PPR78, while in aromatic hydrocarbons PPR78 has a slight advantage. Finally, UMR-PRU yields very satisfactory results in H_2 mixtures with polar compounds such as methanol, MEG and TEG. Such calculations cannot be performed with PPR78, as the model has not been extended to include the relevant groups.

8.4 Prediction of hydrogen VLE in multicomponent systems

The final step is model evaluation based on its capability to predict the VLE in hydrogen-containing multicomponent mixtures, which are of high interest for oil & gas applications. This step is crucial, since proper description of VLE in binary systems does not always guarantee that a model will also perform well in multicomponent mixtures.

The experimental VLE data employed for this purpose are shown in Table 8.4, along with UMR-PRU and PPR78 prediction results in terms of AARD% in bubble point pressure and AAD% in vapor phase composition. Some representative results with UMR-PRU for some ternary mixtures are also plotted in Figure 8.3. It should be noted that in Figure 8.3 some experimental tie lines are not clearly visible, because they coincide with the ones predicted by UMR-PRU.

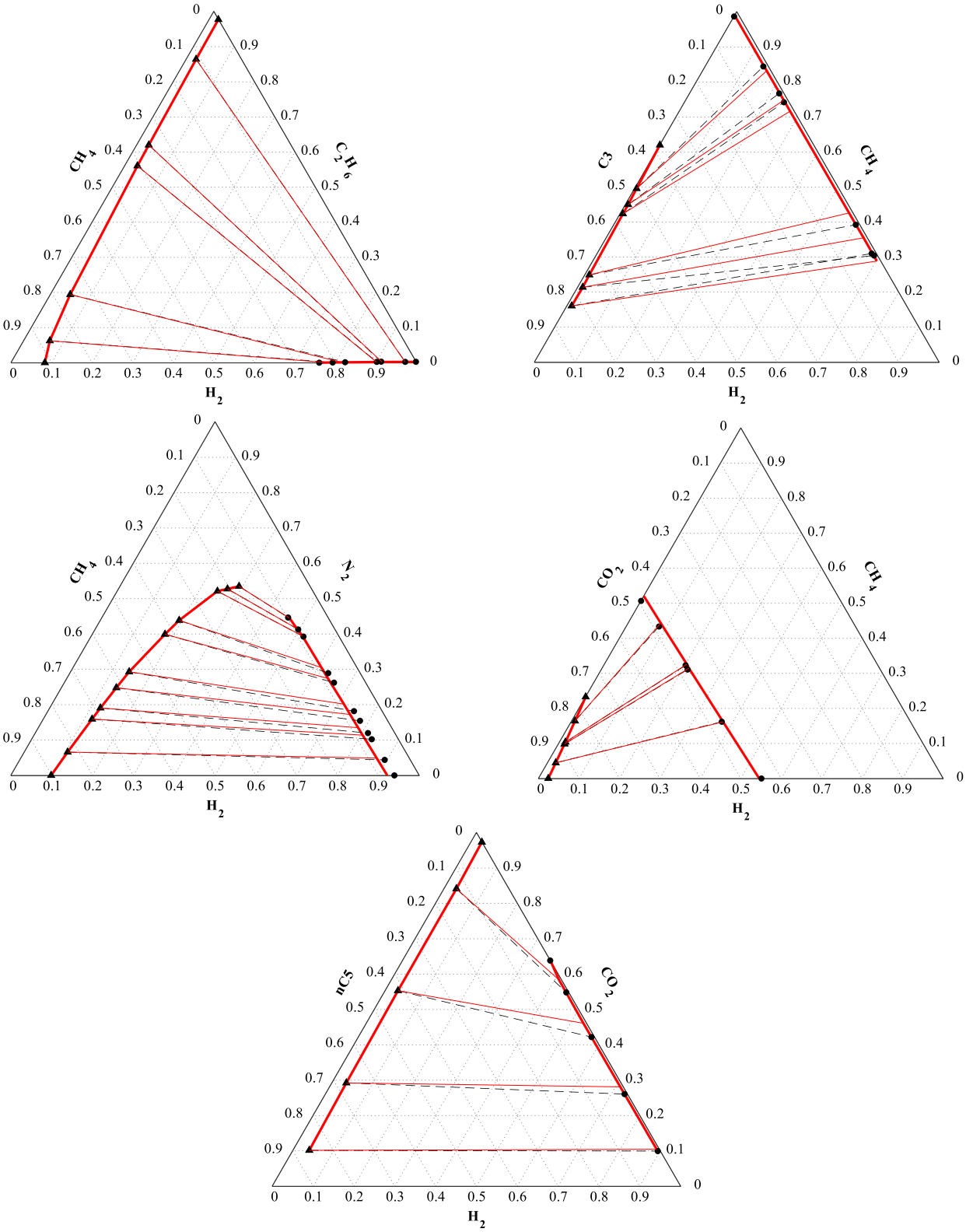

Figure 8.3. Experimental points and VLE results for 5 ternary mixtures of hydrogen: (a) $H_2/CH_4/C_2H_6$ at 144.26 K and 68.95 bar, (b) $H_2/CH_4/C3$ at 199.82 K and 34.47 bar, (c) $H_2/N_2/CH_4$ at 120 K and 100 bar, (d) $H_2/CO_2/CH_4$ at 258.15 K and 68.95 bar, (e) $H_2/CO_2/nC5$ at 273.15 K and 68.95 bar. (▲): exp. mole fractions in liquid phase; (●): exp. mole fractions in vapor phase; dashed lines: exp. tie lines; solid red lines: UMR-PRU model predictions.

Table 8.4. Experimental data and prediction results regarding hydrogen mixtures with UMR-PRU and PPR78 models.

						UMR-PRU		PPR78	
H_2 with	**Ref.**	**T range (K)**	**P range (bar)**	**NDP**	**NDy**	**AARDP%**	**AADy[a]**	**AARDP%**	**AADy**
$CH_4 + CO_2$	[119]	227.35-258.15	68.9-276.1	35	35	6.4	0.79	10.2	2.19
$CH_4 + N_2$	[118, 120]	80.0-199.8	34.5-152	72	71	12.2	2.53	16.1	2.52
$CH_4 + C_2H_6$	[118]	115.3-255.5	13.5-137.9	111	111	17.6	1.18	19.5	1.58
CH_4 + C3	[118]	144.26-255.37	34.5-69	40	38	11.8	1.92	8.0	1.88
CH_4 + tetralin	[118]	462.0-663.0	50.4-256.1	23	23	3.5	1.00	5.2	2.12
$CH_4 + C_2H_6 + N_2$	[118]	144.3-199.8	34.5-69	7	7	3.0	1.95	16.4	2.57
CO_2 + nC5	[119]	273.15-323.15	68.9-276.1	29	28	6.6	1.14	11.9	2.14
CO_2 + toluene	[121]	305-343	12.3-103.5	73	73	4.1	1.15	3.9	1.18
benzene + cyC6 + nC6	[118]	366.5-422	34.8-139.5	36	36	3.2	0.26	2.1	0.27
benzene + nC16	[122]	573.15	200	7	7	4.4	0.49	6.6	0.53
			Overall	**433**	**429**	**9.9**	**1.34**	**11.5**	**1.70**

[a] AADy = $100 \cdot \sum_{i=1}^{NC} \sum_{j=1}^{ND} \left| y_{ij}^{exp} - y_{ij}^{calc} \right| / (ND \cdot NC)$, where NC is the number of components in the mixture and ND is the number of experimental data points

It is observed that both models can accurately predict the VLE behavior of H_2 in various mixtures, with UMR-PRU yielding better results than PPR78 in the majority of the studied systems.

8.5 Conclusions

In this chapter, the UMR-PRU model was employed for studying hydrogen phase equilibria with oil & gas components. Due to the fact that hydrogen is found in supercritical state at common process conditions, a study of the attractive term of the PR EoS was conducted, in order to ensure consistency and satisfactory pure H_2 property prediction both in sub- and supercritical regions. The results indicated that the original Soave expression for the attractive term is best suited for hydrogen.

Furthermore, the UMR-PRU model was successfully extended to mixtures of hydrogen with hydrocarbons, gases (CO_2, N_2, H_2S), and polar compounds (H_2O, MeOH, MEG, TEG) by introducing a new UNIFAC group (H_2) and estimating temperature-dependent binary interaction parameters between different groups. The performance of the model in binary and multicomponent hydrogen mixtures was compared with that of another predictive model based on the PR EoS, namely PPR78. The overall results showed that both models are capable of accurate vapor-liquid equilibrium description in the studied systems, with UMR-PRU yielding the lowest deviations from the experimental data.

In conclusion, despite the quantum nature of hydrogen and the high size asymmetry encountered in its mixtures, UMR-PRU can be successfully applied in such systems due to its advanced mixing rules. The employment of UNIFAC also enables model predictions when no experimental data are available.

9. Mercury chemical & phase equilibria in natural gas

9.1 Introduction

For the proper monitoring and management of Hg levels throughout a gas processing plant, thermodynamic models are required, an important index is the solubility of elemental mercury in a fluid, i.e. the concentration above which Hg^0 is expected to drop out of the fluid as a separate pure liquid or solid phase. Knowledge of this is especially important in LNG production plants, where very low processing temperatures are involved and aluminum heat exchangers are usually employed, which are susceptible to corrosion by liquid Hg^0. Calculating the saturation concentration of Hg^0 in streams already comprised of 3 phases (e.g. vapor-liquid hydrocarbon-aqueous) can prove to be challenging, since a 4-phase PT-flash must be solved. When the stream becomes oversaturated in mercury under constant temperature and pressure, a 4^{th} pure Hg^0 liquid (or solid) phase will be formed. Most of the widely used commercial process simulators are not capable of 4-phase flash calculations, so the industry is resorting to internal proprietary tools to tackle the problem. In this chapter, the multiphase flash algorithm developed in Section 5.1.4 is employed for calculating the solubility of mercury in typical natural gas and gas condensate fluids.

Although Hg^0 is the dominant mercury form in natural gas, β-HgS solid particles can also be found in gas condensate and produced water in downstream operations [123]. Mercury sulfide can occur naturally in reservoir fluids and would be expected to be removed from them during preliminary separations, so this indicates that it may also be produced through reaction of Hg^0 with sulfur compounds present in natural gas, of which the most abundant is H_2S. It is known that mercury has a high affinity for sulfur compounds [7], so the possibility of a Hg reaction with H_2S in natural gas is investigated in the second part of this chapter. More specifically, the thermodynamics of the reaction are studied, and simultaneous chemical & phase equilibria (CPE) calculations are performed in the aforementioned natural gas and gas condensate fluids with the algorithm developed in Section 5.2.

Both algorithms employed in this chapter are coupled with the UMR-PRU model, which has been successfully extended to mixtures of mercury and hydrogen with natural gas components in the previous chapters and has proved to be the most accurate among other tested models.

9.2 Mercury solubility in typical natural gas and condensate mixtures

The multiphase flash algorithm developed in Section 5.1.4 is employed for calculating the solubility of mercury in typical natural gas and gas condensate fluids. The test fluid compositions are presented in Table 9.1. Fluids 1 to 4 contain water and are examples of systems involved in early-stage flash separations at offshore platforms. Finding the saturation concentration of mercury in these processes is challenging since a 4-phase flash must be solved. Fluid 5 resembles a typical condensate mixture that can be found in the condensate

stabilization train. Mercury solubility is expected to be higher in heavy hydrocarbons, so it is of interest to compare the results with those for the other fluids. Fluid 6 exhibits a typical composition of a fluid that can be found in cryogenic processes of an onshore processing plant. Knowledge of mercury saturation levels in streams involved in cryogenic processes is essential for avoiding Hg^0 dropout from the fluid either as pure liquid or solid, which can lead to equipment corrosion or other health, safety, and environmental (HSE) problems.

Table 9.1. Molar composition (%) and C_{7+} fraction properties of the fluids studied in this work.

Component	Fluid 1	Fluid 2	Fluid 3	Fluid 4	Fluid 5	Fluid 6
H_2O	2.6739	16.1859	5.0528	6.2202	-	-
N_2	0.6830	0.4046	0.5684	0.4700	0.0023	0.1645
CO_2	0.7806	2.3523	4.3010	4.6539	0.4561	3.4847
CH_4	80.0583	53.9253	70.5593	65.3640	2.2850	56.0970
C_2H_6	8.6958	6.6222	8.7764	8.6307	4.7830	20.0438
C3	3.4807	4.0543	4.5052	4.5563	11.5300	14.1081
iC4	0.5790	0.7407	0.7083	0.7579	3.9690	1.7055
nC4	1.0424	1.6616	1.4649	1.5481	11.3800	3.0476
iC5	0.3124	0.6231	0.4737	0.5188	5.7440	0.5141
nC5	0.3428	0.7905	0.5639	0.6120	7.0330	0.4984
nC6	0.3389	0.9800	0.5834	0.7546	9.3050	0.1877
C_{7+}	1.0123	11.6595	2.4416	5.9118	43.5172	0.1486
MW(C_{7+}) (g/mol)	109.62	181.5	118.57	129.33	127.21	91.19
C_{7+} density at 15°C (kg/m^3)	773.43	832.01	783.40	794.53	792.61	773.81

For the thermodynamic modeling with UMR-PRU, the characterization method proposed by Pedersen et al. [124-126] was used for the C_{7+} fraction. The results regarding mercury solubility in the different phases versus temperature and pressure are presented in Figure 9.1 and Figure 9.2, respectively. It should be noted that the studied temperature and pressure range was selected to reflect the conditions expected in the actual processes, in which the fluids are involved.

In Figure 9.1 it is observed that mercury solubility in all phases increases exponentially with temperature, with the liquid hydrocarbon phase exhibiting the highest Hg^0 solubility and the aqueous phase the lowest in the majority of the fluids. The only exception is Fluid 5, which shows a higher mercury solubility in the vapor phase than in the liquid hydrocarbon one. This is due to the vapor phase composition in this case, which is richer in heavy hydrocarbons than the pertinent phases in the other fluids. The lowest mercury solubilities are encountered in Fluid 6 due to the very low process temperatures. In this case, a change in the slope of the solubility curves can be observed around the melting point of mercury (234 K), which is attributed to the change in the fugacity of the pure mercury phase due to the transition from solid to liquid state.

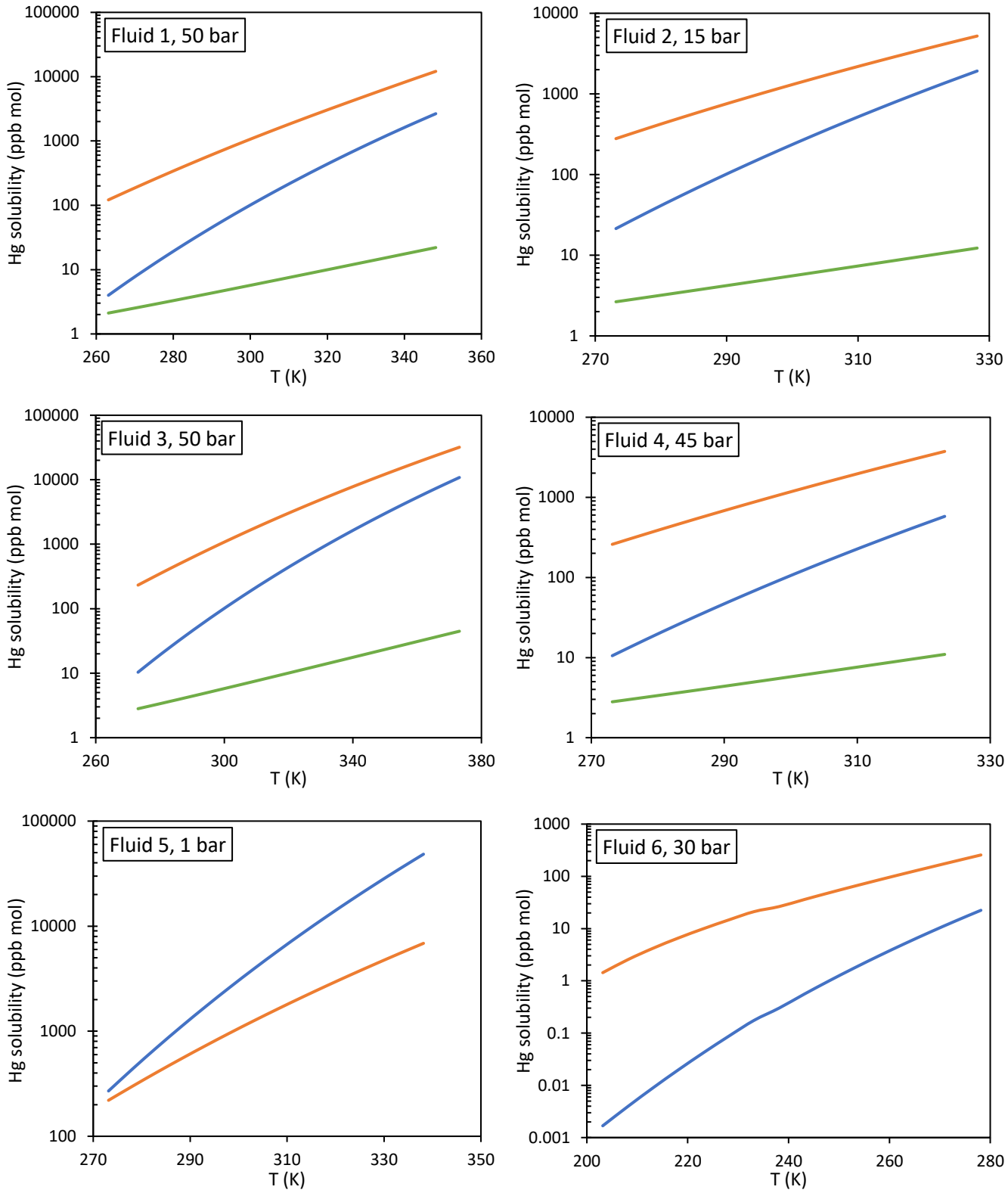

Figure 9.1. Mercury solubility vs. temperature at constant pressure with UMR-PRU. Blue line: vapor phase; Orange line: liquid phase; Green line: aqueous phase.

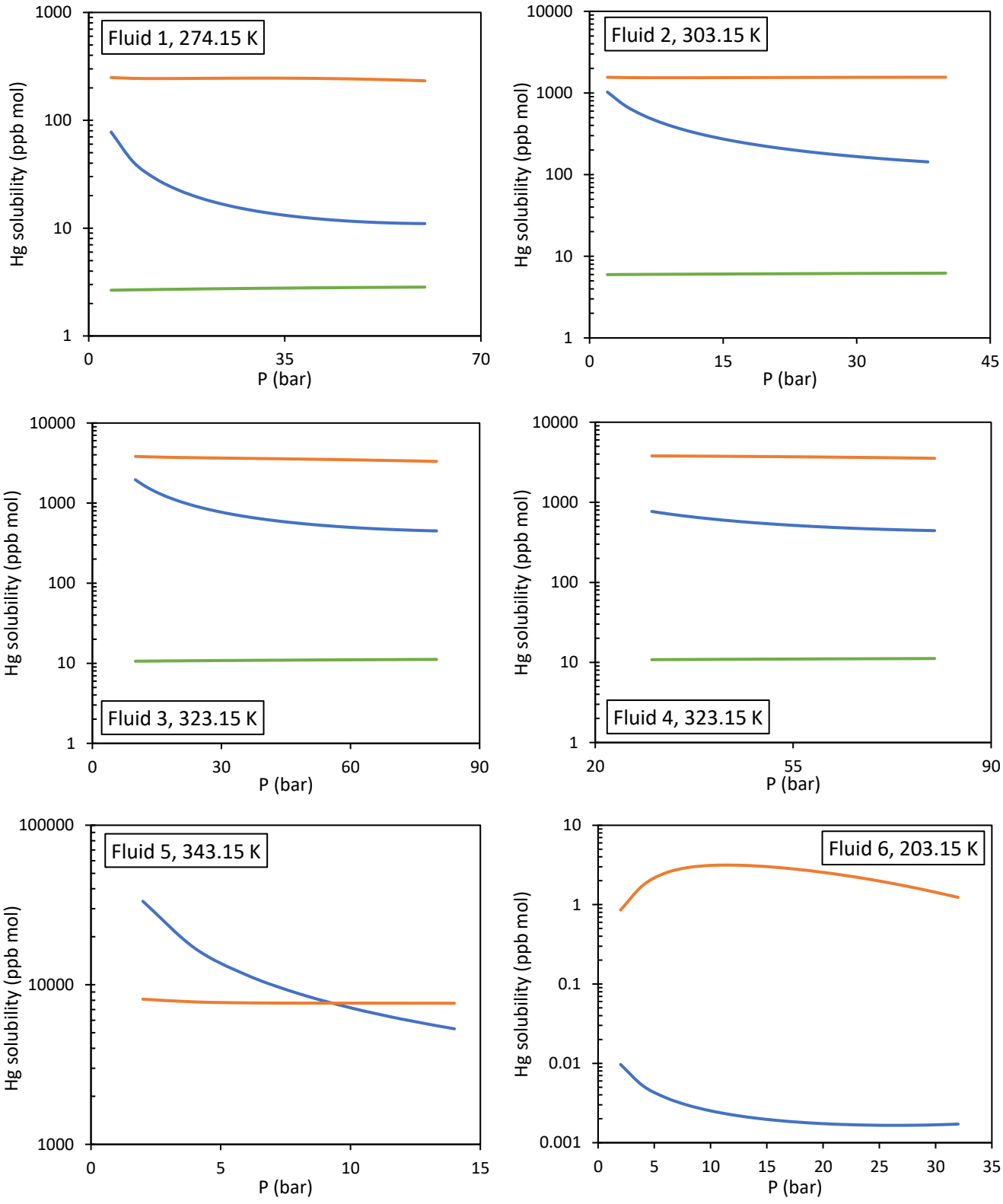

Figure 9.2. Mercury solubility vs. pressure at constant temperature with UMR-PRU. Blue line: vapor phase; Orange line: liquid phase; Green line: aqueous phase.

As shown in Figure 9.2, pressure has a minimal effect on the solubility of mercury in the liquid hydrocarbon and aqueous phases in the majority of the studied fluids. On the other hand, mercury solubility in the vapor phase appears to decrease while pressure increases, until it reaches a plateau. This can be explained by the fact that as pressure increases, the composition of heavy hydrocarbons in the vapor phase decreases, thus lowering the Hg solubility. Of great interest is the case of Fluid 5, in which a crossover of the Hg^0 solubility curves is observed around 9.5 bar. Again, this can be attributed to the composition changes in the vapor and liquid phases with pressure. In the case of Fluid 6, the vapor phase exhibits the same behavior as this in other fluids. However, mercury solubility in the liquid phase initially increases with pressure and then decreases. This is due to the composition of the liquid phase, which is rich in light hydrocarbons (C1-C2). Liquid methane and ethane are known to exhibit an increasing Hg^0 solubility with pressure [84]. As pressure increases, the liquid phase becomes richer in hydrocarbons heavier than ethane, so the C1-C2 fraction is diluted and mercury solubility decreases.

9.3 Mercury reaction with H_2S in natural gas and condensate mixtures

9.3.1 Thermodynamic analysis of the reaction

The existence of solid β-HgS particles in sediments found in condensate tanks and glycol contactors raises suspicions regarding possible Hg^0 reactions with sulfur components present in natural gas. Such mercury reactions are not covered sufficiently in the open literature, but theory suggests that Hg^0 has a high affinity for sulfur and sulfuric compounds [7]. In fact, this property is typically exploited for the removal of mercury from natural gas via adsorption beds containing metal sulfides or sulfur-impregnated activated carbon.

Since the most abundant sulfuric compound in natural gas is H_2S, a reasonable reaction that could explain the presence of β-HgS would be:

$$Hg + H_2S \Leftrightarrow \beta\text{-}HgS + H_2 \qquad \text{Eq. 9.1}$$

The reaction has not been studied experimentally in the open literature, so the phase in which it occurs and whether it reaches equilibrium or is kinetically controlled is unknown. For the purposes of this work, it is assumed that the reaction reaches equilibrium, while both cases of vapor and liquid phase reaction are examined. It should be noted that the proposed reaction is not the only one that can lead to β-HgS production, e.g. a reaction between Hg and H_2S dissociation products in the water phase could also occur.

To determine whether the reaction (Eq. 9.1) is thermodynamically feasible, the Gibbs energy of the reaction (ΔG_r^o) can be calculated from the Gibbs energy of formation of the reactants and the products presented in Table 9.2. It should be noted that the Gibbs energy of formation is different depending on the phase in which a component is present. For all components except β-HgS, the literature sources give similar values for the formation

properties, so those included in the CRC handbook [19] are presented here. Regarding the formation properties of β-HgS some discrepancies were observed in the literature sources, so all found values are included in Table 9.2.

Table 9.2. Thermodynamic properties of reaction (Eq. 9.1) components at 298.15 K and 1 atm.

Compound	State	ΔH_f^o (kJ/mol)	ΔG_f^o (kJ/mol)	Ref.
Hg	gas	61.4	31.8	[19]
	liquid	0	0	-
H_2S	gas	-20.6	-33.4	[19]
	liquid	-39.3	-26.3	This work (calculated)
β-HgS	solid	-46.7	-43.3	[127]
		-44.8	-36.8	[128]
		-53.6	-47.7	[20]
H_2	gas	0	0	-

If the reaction occurs in the gas phase, ΔG_r^o is found to range from -46.1 to -35.2 kJ/mol, depending on the literature source for the β-HgS properties. Conversely, if the reaction occurs in the liquid phase, ΔG_r^o ranges from -21.4 to -10.5 kJ/mol. Since $\Delta G_r^o < 0$ in both cases of liquid and gas phase reaction, it is shown that the reaction is feasible under ambient conditions.

With the assumption that the enthalpy of the reaction (ΔH_r^o) is temperature-independent, the equilibrium constant of the reaction at any temperature can be calculated from the integrated van 't Hoff equation:

$$lnK_{eq}(T) = lnK_{eq}(T_0) - \frac{\Delta H_r°(T_0)}{R}\left(\frac{1}{T} - \frac{1}{T_0}\right) \quad \text{Eq. 9.2}$$

where T is the temperature in K, T_0 is the reference temperature (298.15 K) and $K_{eq}(T_0)$ is the equilibrium constant of the reaction at 298.15 K, as calculated from:

$$lnK_{eq}(T_0) = -\frac{\Delta G°(T_0)}{RT_0} \quad \text{Eq. 9.3}$$

By combining Eq. 9.2 and Eq. 9.3, and performing some basic operations, a simpler equation can be derived:

$$lnK_{eq}(T) = A + B/T \quad \text{Eq. 9.4}$$

Depending on the source for the properties of β-HgS, the coefficients A and B for Eq. 9.4 are presented in Table 9.3. The resulting equilibrium constants are plotted against temperature in Figure 9.3. It is observed that at temperatures lower than 431.5 K (1/T above 2.3) the equilibrium constants for the vapor phase reaction are higher than the respective for the

liquid phase. This means that at this temperature range higher conversions are expected in the case of vapor phase reaction. From the values of B it is clear that vapor phase reaction constants have a stronger temperature dependency, which is also indicated by their steeper slopes than their liquid phase counterparts in Figure 9.3. Unfortunately, due to the lack of experimental data on the reaction, it is not possible to distinguish which equilibrium constant better reflects the reality.

Table 9.3. Constants A and B used in Eq. 9.4 for calculating the equilibrium constant of the reaction between Hg^0 and H_2S.

Name	Reaction phase	A (-)	B (K)	Ref. for *β*-HgS formation properties
KG1	gas	-19.485	11354.34	[20]
KG2	gas	-18.477	10524.42	[127]
KG3	gas	-20.332	10295.89	[128]
KL1	liquid	1723.6	2.834	[20]
KL2	liquid	897.92	3.820	[127]
KL3	liquid	661.39	2.008	[128]

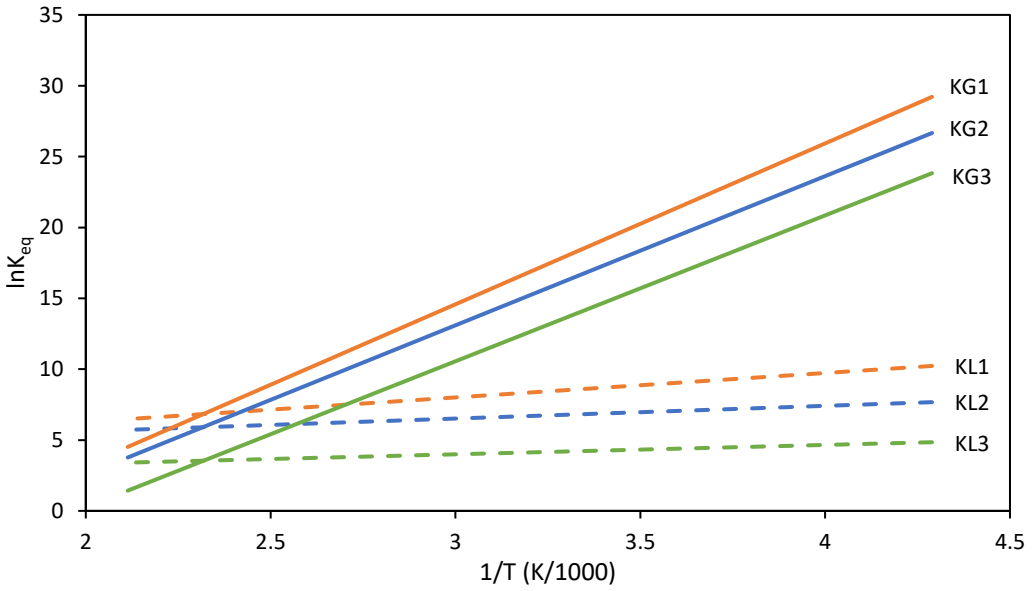

Figure 9.3. Equilibrium constant for $Hg^0 + H_2S$ reaction as function of temperature. Solid lines: vapor phase reaction; Dashed lines: liquid phase reaction.

9.3.2 CPE calculations in typical natural gas and condensate fluids

For studying the proposed reaction (Eq. 9.1) between elemental mercury and H_2S in natural gas mixtures, the same fluids as in Section 9.2 were employed. Since no information was available regarding the H_2S and Hg^0 content in the fluids, their concentrations were assumed to be 1 ppm mol and 1 ppb mol, respectively. These values are considered to be within the expected range for such fluids, and the Hg^0 concentration was selected to be below saturation. Therefore, H_2S is expected to be the reactant in excess. The initial amount of the reaction products (β-HgS and H_2) in the fluids was assumed to be zero.

To understand if the reaction proceeds and to what extent, the conversion of Hg^0 to β-HgS as percent of the initial total Hg amount was calculated as a function of temperature. Both cases of vapor or liquid phase reaction were examined by employing the pertinent reaction equilibrium constants presented in Table 9.3. Some representative results are shown in Figure 9.4 and Figure 9.5. The conversion trend with temperature was found to be the same for all examined fluids, so some typical results for Fluid 1 and Fluid 4 are presented.

In the case of vapor phase reaction, it is shown that roughly 100% conversion is achieved until a certain temperature, above which conversion reduces rapidly until it reaches zero. Therefore, below a specific temperature all mercury is expected to be in the form of β-HgS, while above another specific temperature all mercury is in the elemental form, since no reaction occurs. These temperatures depend on fluid composition and the selected equilibrium constant of the reaction. As expected, at each temperature the conversion is higher for the K_{eq} with the higher value (Figure 9.3). Unfortunately, due to the lack of experimental data it is not possible to distinguish which K_{eq} leads to results that better reflect the reality.

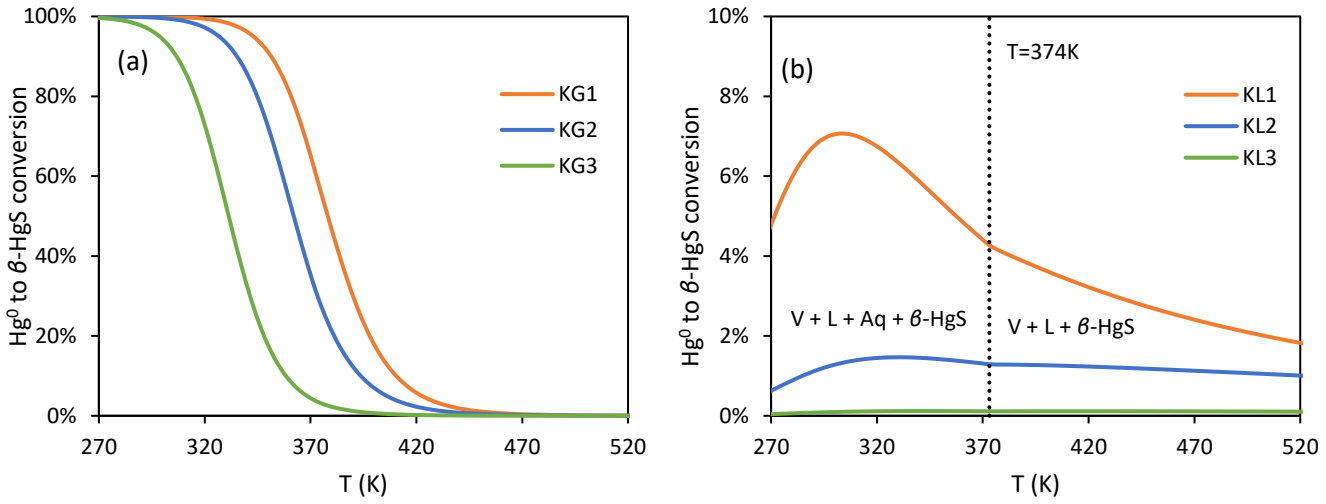

Figure 9.4. Conversion of elemental mercury to β-HgS vs. temperature for Fluid 1 at 50 bar with different reaction equilibrium constants: (a) vapor phase reaction, (b) liquid phase reaction. Solid lines: UMR-PRU model predictions; Dashed line: maximum temperature at which an aqueous phase is present.

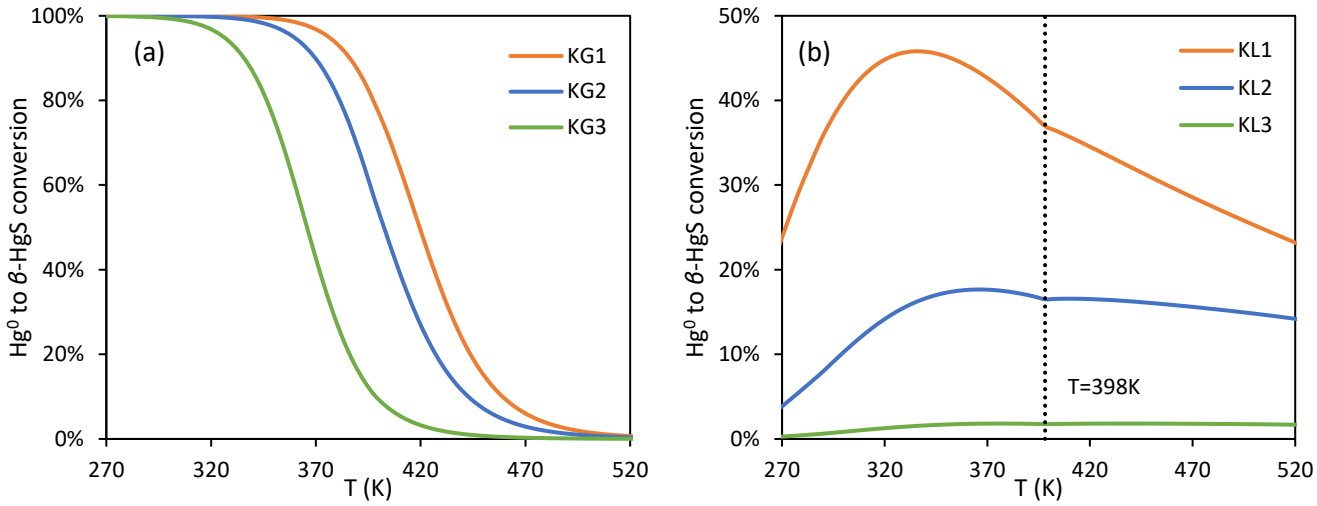

Figure 9.5. Conversion of elemental mercury to *β*-HgS vs. temperature for Fluid 4 at 45 bar with different reaction equilibrium constants: (a) vapor phase reaction, (b) liquid phase reaction. Solid lines: UMR-PRU model predictions; Dashed line: maximum temperature at which an aqueous phase is present.

In the case of liquid phase reaction, the conversion initially increases with temperature until it reaches a maximum and then decreases. Overall, the liquid phase reaction exhibits lower conversions than the vapor phase reaction, which can be explained by the comparison of equilibrium constants (Figure 9.3). A different trend of conversion with temperature can also be observed as compared to the vapor reaction, which could be attributed to the high non-ideality of the liquid phases.

More specifically, the reaction equilibrium constant is by definition equal to the product of the activities of reactants and products raised to the respective stoichiometric numbers. Since the reaction is exothermic, K_{eq} is reduced as temperature increases so the activity product must reduce as well. However, conversion depends on concentrations and not on activities. In cases where the liquid phase deviates notably from ideality, concentrations can differ significantly from activities. The effect of liquid phase non-ideality is also highlighted by the change of slope in the conversion vs. temperature charts at the maximum temperature where an aqueous phase is also present in the system. The existence of an aqueous phase appears to have an influence on conversion since it changes the distribution of components among phases.

The effect of pressure on conversion was also investigated for both cases of vapor and liquid phase reaction in Fluid 4, and the results are presented in Figure 9.6. Regarding the vapor phase reaction, it is observed that conversion increases with pressure, but the effect becomes less pronounced at higher pressures. In the case of liquid phase reaction things are not so straightforward due to the concavity of the conversion curves. However, it can be observed that a locus of maximum conversions is formed, which is also a concave function.

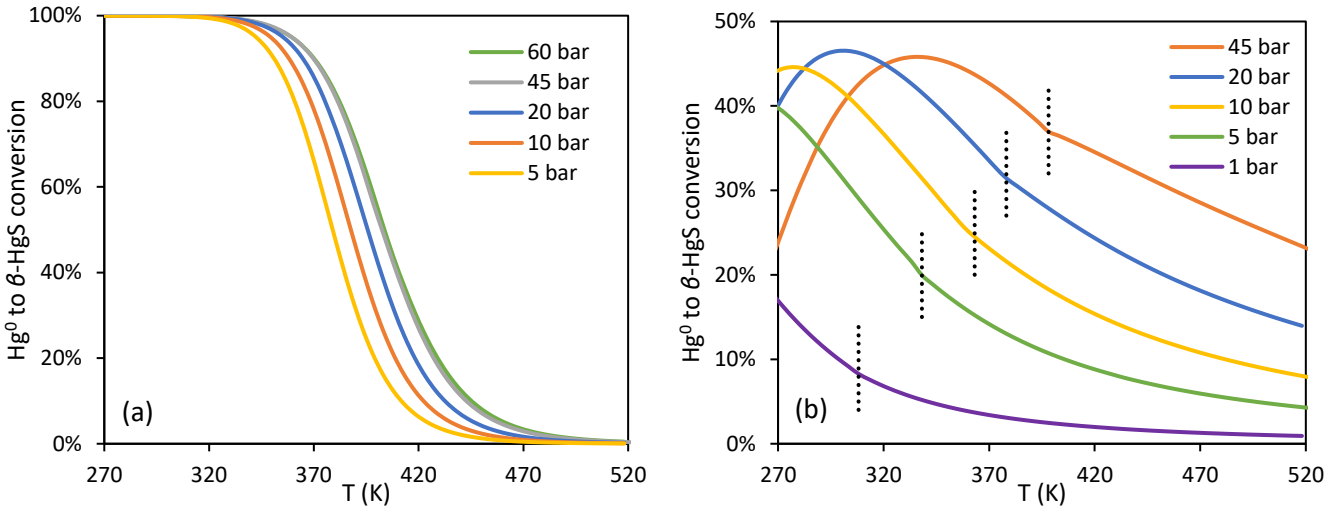

Figure 9.6. Conversion of elemental mercury to β-HgS vs. temperature for Fluid 4 at different pressures: (a) vapor phase reaction (K_{eq}=KG2), (b) liquid phase reaction (K_{eq}=KL1). Solid lines: UMR-PRU model predictions; Dashed line: maximum temperature at which an aqueous phase is present.

The practical implication of the above observations is that if the reaction occurs in the vapor phase, the conversion of Hg^0 to β-HgS is expected to be almost 100% until 320-380 K, depending on the equilibrium constant. However, elemental mercury can also be found in processes operating below these temperatures [14, 129], so it is likely that the vapor phase reaction is either hindered by kinetics or does not occur at all in reality. On the other hand, the liquid phase reaction exhibits conversions lower than 50% at the studied fluids and conditions, indicating that mercury can be present both as elemental and β-HgS. This result is in agreement with field observations [14, 129].

Another implication of the possible reaction of elemental mercury with H_2S is the increase in the initial overall mercury concentration that is required in a fluid to reach Hg^0 saturation. Since a portion of the initial Hg^0 amount in the bulk fluid is converted to HgS, more Hg^0 is required to cause saturation. If the reaction occurs in the vapor phase, it is implied that a fluid will never reach saturation at low temperatures because the conversion is 100%. However, this effect can be encountered in the case of liquid phase reaction, which exhibits lower conversions. An example is presented in Figure 9.7, where it is shown that the reaction can significantly increase the initial Hg^0 concentration that is required for reaching saturation.

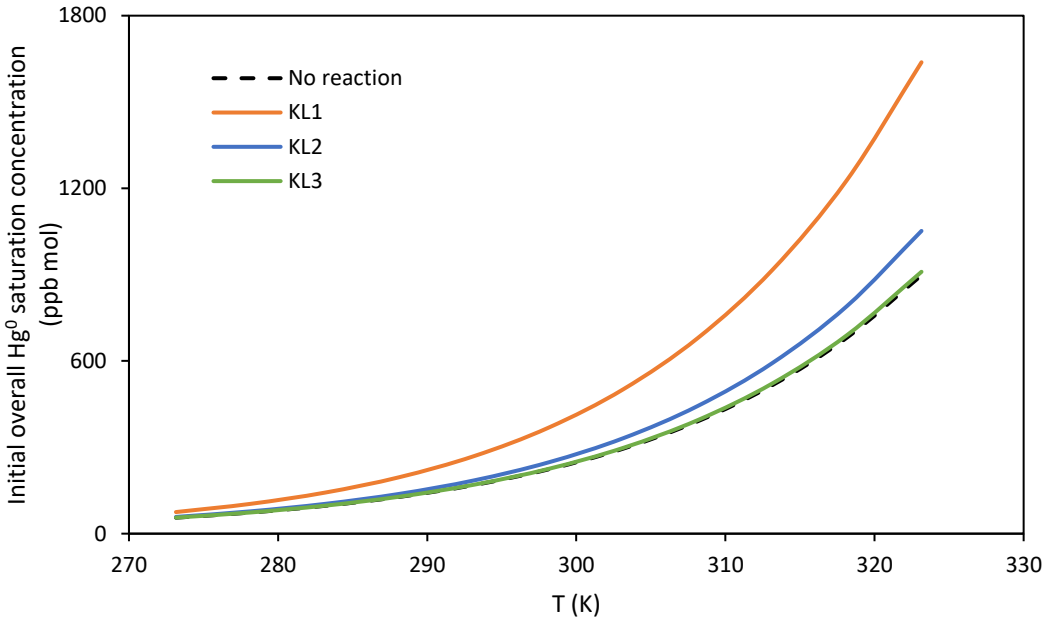

Figure 9.7. Initial overall Hg^0 concentration that is required for saturation of Fluid 4 vs. temperature assuming liquid phase reaction with different equilibrium constants (45 bar).

9.4 Conclusions

In this chapter, the multiphase flash algorithm developed in Section 5.1.4 was successfully employed for calculating the solubility of mercury in typical natural gas and condensate mixtures. The results showed that mercury solubility in the various phases increases exponentially with temperature and generally increases in the order aqueous < vapor < liquid hydrocarbon phase. The effect of pressure on mercury solubility in the different phases was also examined, and results showed a weak dependency in the liquid hydrocarbon and aqueous phases. An exception was a test fluid that can be involved in cryogenic processes, which exhibited a liquid phase rich in C1-C2 hydrocarbons. On the other hand, Hg^0 solubility in the vapor phase was found to decrease with pressure, until a plateau was reached. In any case, phase composition plays an important role and different behaviors can be observed, e.g. in fluids taken from the inlet separation process from those found in the condensate stabilization train of a gas processing plant.

The second point of focus in this chapter was the theoretical study of the reaction between elemental mercury and H_2S in natural gas, which could provide an explanation for the origin of β-HgS solid particles found in condensate tank sediments. Chemistry dictates that mercury has a high affinity for sulfur and its compounds, and H_2S is the most abundant sulfuric compound in natural gas, so a reaction between them is deemed reasonable. Both cases of vapor and liquid phase reaction were examined by calculating the pertinent equilibrium constants. Depending on the literature source for the thermodynamic properties of β-HgS, three different equilibrium constants were calculated for each case. Then, the simultaneous

chemical & phase equilibria in the same fluids were solved by employing the Gibbs energy minimization algorithm developed in Section 5.2.

In the case of vapor phase reaction, it was found that below 320-380 K all mercury is expected to be in the form of β-HgS, while above 450-500 K all mercury is in the elemental form. In the case of liquid phase reaction, conversions lower than 50% were observed at the studied conditions and conversion was found to be a concave function of temperature. The effect of pressure on conversion was also studied, and it was found that in the vapor reaction the conversion increases with pressure. Regarding the liquid reaction, it was observed that a locus of maximum conversions is formed.

Since field measurements [14, 129] indicate that elemental mercury can be found in processes below 320-380 K, it appears that either the vapor phase reaction is hindered by kinetics or it does not proceed at all in reality. Conversely, the results of the liquid phase reaction indicate that mercury can exist both in elemental form and as β-HgS at these conditions, which is more in agreement with the field data. In any case, a thorough experimental study is required to shed more light into the feasibility and the exact mechanism of the reaction.

10. Simulation of mercury distribution in an offshore natural gas processing plant

10.1 Introduction

In this chapter, the UMR-PRU thermodynamic model that has been successfully extended to mixtures of mercury with natural gas components, and applied for the study of mercury solubility in typical gases and condensates, as well as for the study of the possible reaction of mercury with H_2S in natural gas, is employed for the study of the distribution of mercury in an existing offshore natural gas processing platform. Towards this, a simplified simulation of the platform is implemented in UniSim Design R460.2 and the distribution of mercury in the various streams as calculated with UMR-PRU is compared to field measurements. For comparison, simulations are also performed with the SRK-Twu model, which was developed for mercury in Chapter 7.

10.2 Process description

The platform receives production from several natural gas reservoirs, which is inserted in the plant as two separate feeds, Feed A and Feed B. The raw gas undergoes various separations to achieve rich gas transport specifications, and is subsequently transported via pipeline to an onshore processing plant for further treatment. The produced condensate and crude oil are mixed and transported to onshore refineries via shuttle tankers. A simplified process flow diagram (PFD) of the platform is presented in Figure 10.1.

The plant feeds go through 4 parallel inlet flash separators, which operate at different conditions. An inlet flash separator, “test separator”, also receives a small amount of the feeds for performing various tests and to monitor feed composition. The gas streams from Feed A inlet separators are mixed with the gas streams from the condensate stabilization process and are led to an H_2S removal unit after passing through a scrubber. The sweet gas is mixed with the gas streams from the Feed B inlet separators and passes through two parallel glycol contactors. The produced dry gas is led to two final scrubbers while being compressed and cooled, to meet rich gas transport specifications. The condensates from the inlet separators are led to a second stage separator to further remove light components and water, and then pass through a stabilizer vessel and a stabilizer distillation column. The stabilized condensate is cooled and pumped into the export condensate tanks.

Field experimental data are available regarding elemental (Hg^0) and total (THg) mercury in some fluids, as well as H_2S and CO_2 concentrations in some streams, found in various processes on the platform.

10.3 Simulation of mercury distribution in the overall process

The first step of this study is the simulation of mercury distribution in the overall process, by implementing a simplified version of the plant in UniSim Design R460.2. Mercury distribution in TEG dehydration and TEG, MEG regeneration processes will be examined in separate simulations, as described in the following sections.

For the simplified simulation, the inlet separators, the gas treatment system (sweetening & dehydration), the 2nd stage separator, the stabilizer vessel and column were maintained, while the condensate/MEG separators and gas recompression scrubbers were disregarded. The gas sweetening and dehydration processes were represented by component splitters. The resulting process flow diagram is presented in Figure 10.1. It was assumed that 100% of H_2S and 10% of CO_2 are removed by the amine contactor, and 99.99% of water is removed by the glycol contactor (per mole basis). Since a portion of mercury is known to be removed in the sweetening and dehydration processes, it was also assumed that 9% of mercury is removed by the amine unit and 3.5% of mercury is removed by the glycol contactor, based on field campaign observations.

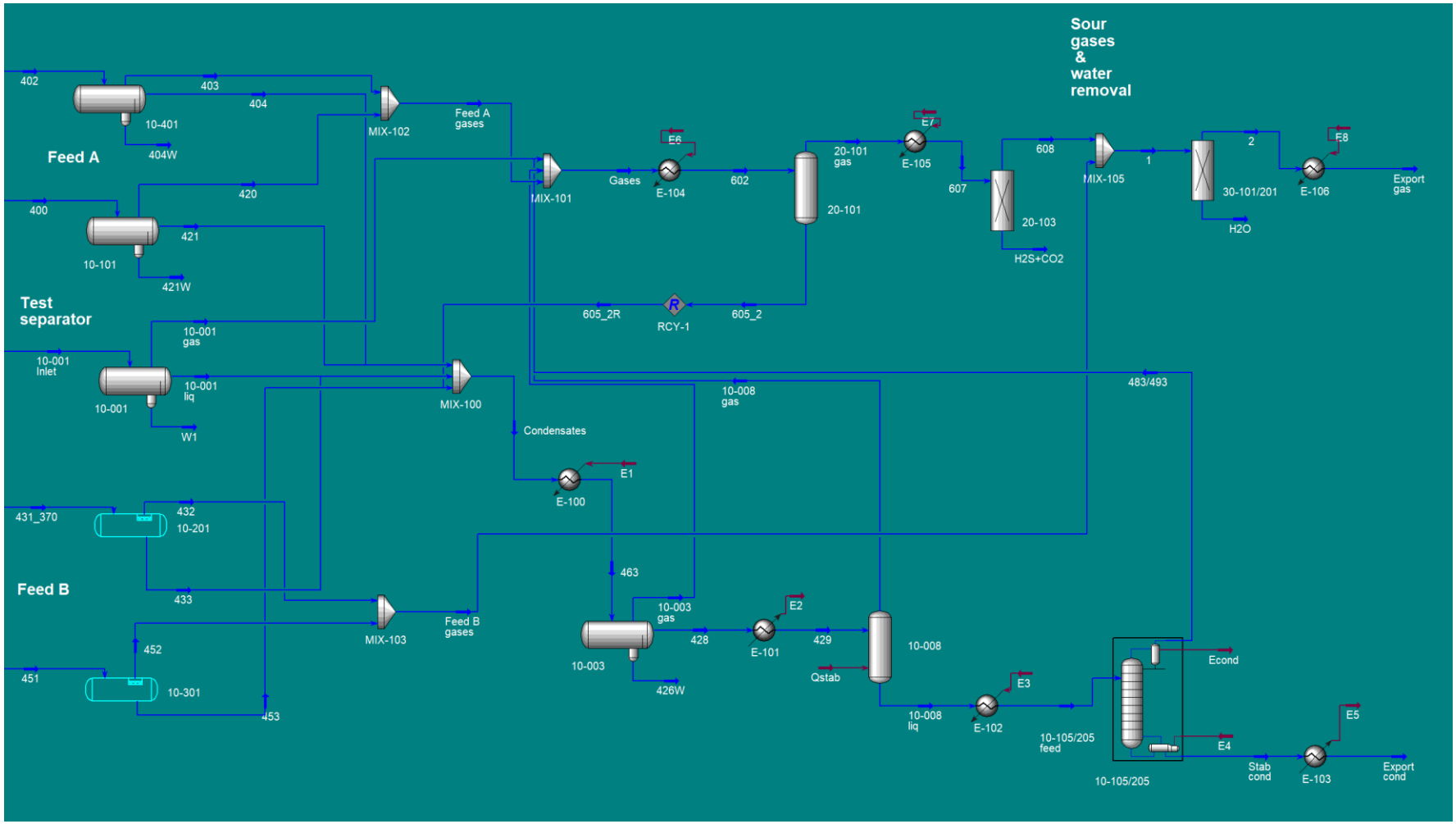

Figure 10.1. Process flow diagram of the simplified simulation of the offshore NG processing platform.

For constructing the simplified simulation, actual process data were used. These concern process conditions, flowrates, and compositions of feeds, which are directed to the inlet separators. Process conditions are shown in Table 10.1. Pseudocomponents are also used to characterize the C_{6+} fraction of the fluids, and their properties (MW, T_c, P_c, ω and density) are presented in Appendix D.

Table 10.1. Process conditions according to real process information.

Tag	Description	T (°C)	P (barg)
10-001	Test separator	51.50	45.89
10-101	Feed A inlet sep.	49.88	46.04
10-201	Feed B inlet sep.	4.08	48.93
10-301	Feed B inlet sep.	0.99	47.89
10-401	Feed A inlet sep.	29.82	14.71
10-003	2nd stage sep.	64.86	14.57
10-008	Stabilizer tank	54.92	8.52
10-105/205	Stab. column condenser	44.4	6.35
10-105/205	Stab. column reboiler	115.6	6.36
20-101	Gas treat. scrubber	24.75	45.07
20-103	Amine contactor	29.25	45.07
30-101	Glycol contactor A	26.63	44.43
30-201	Glycol contactor B	15.51	44.55

For the simulation with SRK-Twu, the L, M, N parameters for mercury and the binary interaction parameters (k_{ij}) between mercury and other components were set equal to the optimum values calculated in Chapter 7. In cases where no component-specific k_{ij}'s were available, they were calculated from the generalized correlations proposed in the same Chapter. For the k_{ij}'s between components other than mercury, the default values in UniSim R460.2 were used.

For the simulation with UMR-PRU, the CAPE-OPEN protocol was used, since UMR-PRU is not inherently available in the program. The CAPE-OPEN protocol allows for the use of an external thermodynamic model in process simulation software. The external model is inserted in the form of a fluid package that contains information about the components and their properties. All thermodynamic properties are calculated by the model externally, and the values are returned to the simulator. The simulator then performs all mass and energy balance calculations, as well as all kinds of equilibrium calculations. For the purposes of this study, a fluid package was created, which contained the same components as the SRK-Twu simulation file. The same number of pseudocomponents was also added, with the same properties (Appendix D).

10.3.1 Mercury mass balance calculations

From the field campaign measurements, the total mass balance of mercury in the plant can be constructed. Hg concentration in all outlets (export gas, condensate, produced water and vents) is known, and with information about the stream flowrates, the total amount of mercury throughout the plant can be calculated. Data regarding the actual flowrates during the field campaign period are available, which can be used for mass balance calculations. The calculated mercury mass flowrate at the plant outlets is presented in Table 10.2. A more detailed analysis is presented in Appendix D.

Table 10.2. Estimated elemental (Hg^0) and total (THg) mercury mass flowrates at plant outlets, based on field campaign measurements and actual process data (flowrates).

Stream	Hg^0 flowrate (g/d)	THg flowrate (g/d)
Export gas	354.9	354.9
Export condensate	39.5	52.3
Hg removal from TEG contactor A	24.1	24.1
Hg removal from TEG contactor B	9.8	9.8
Hg removal from amine contactor	34.1	34.1
Produced water	0	1.5
Total	**462.4**	**476.7**

In Table 10.2 it is shown that 476.7 g of mercury transit the plant every day, of which 462.7 g are elemental mercury. Assuming the production runs 24 h per day, 365 days per year, with constant flowrates, it is calculated that 174 kg of mercury transit the plant annually. Of these, 129.5 kg enter the gas transport system, 19 kg follow the export condensate, while the remaining 25.5 kg are either absorbed by process chemicals (amine, glycol) or released to the environment through vents and produced water.

Elemental mercury distribution in plant outlets is presented in Figure 10.2 as percentage of total Hg^0 exiting the plant. It is shown that the majority of mercury (76.8%) follows the export gas, while 8.5% is distributed in the export condensate. The rest amount of mercury is absorbed by process fluids or released to the environment during the amine (7.4%) and glycol (7.3%) regeneration processes. The amount of elemental mercury in produced water was found to be below the limit of detection during the field campaign.

The total mass balance of mercury can also be constructed for the test separator (10-001), since the concentration of mercury in all outlet streams is measured, and gas and condensate flowrates are known. The density of the condensate has also been measured. The results are presented in Table 10.3.

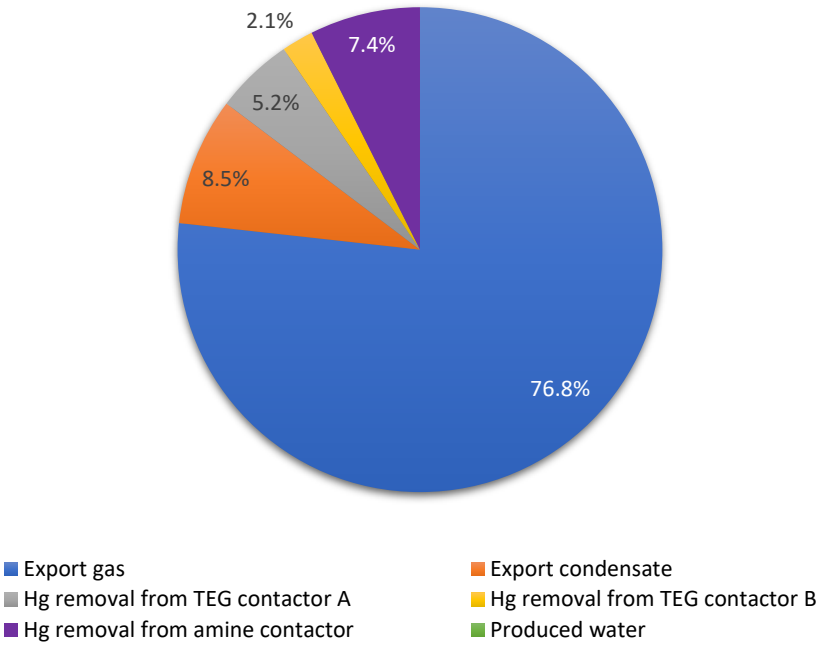

Figure 10.2. Elemental mercury distribution in plant outlets as percentage of total Hg^0 exiting the plant. The distribution is estimated based on the field campaign measurements and actual process data (flowrates).

Table 10.3. Estimated elemental (Hg^0) and total (THg) mercury mass flowrates at test separator (10-001) outlets, based on field campaign measurements and actual process data (flowrates).

Stream	Flowrate	Density (kg/m^3)	Hg^0 concentration	Hg^0 flowrate (g/d)	THg concentration	THg flowrate (g/d)
Vapor	1.18 MSm^3/d	N/A	95.2 µg/Sm^3	112.3	95.2 µg/Sm^3	112.3
Liquid	559 m^3/d	797	17.5 µg/kg	7.8	62 µg/kg	27.6
Aqueous	133 m^3/d	1062	< 0.1 µg/kg	0	1.2 µg/kg	0.17
			Total	**120.1**		**140.0**

From mass balance calculations for the test separator, it is estimated that the flowrate of elemental mercury at the outlet is 120.1 g/d, while the flowrate of total mercury is 140 g/d. By assuming zero mercury accumulation in the equipment, these flowrates lead to a concentration at the separator inlet of 12.6 and 14.6 ppb mol, for elemental and total mercury, respectively.

Regarding the stabilizer (10-008), both inlet and outlet Hg concentrations have been measured, and stream flowrates are known. The density of the inlet and outlet condensates has also been measured. The mass balance for the stabilizer is presented in Table 10.4.

Table 10.4. Estimated elemental (Hg^0) and total (THg) mercury mass flowrates at the stabilizer (10-008), based on field campaign measurements and actual process data (flowrates).

Stream	Flowrate	Density (kg/m^3)	Hg^0 concentration	Hg^0 flowrate (g/d)	THg concentration	THg flowrate (g/d)
Inlet	6814 m^3/d	643.36	2.2 µg/kg	9.6	219 µg/kg	960.1
Vapor	13230 Sm^3/d	13.84	36.2 µg/Sm^3	0.5	36.2 µg/Sm^3	0.5
Liquid	6601 m^3/d	663.77	3.8 µg/kg	16.6	16839 µg/kg	73780
			Total out	**17.1**		**73781**

The calculations for the stabilizer (10-008) show that the mass balance of elemental and total mercury is not satisfied, as significantly more mercury exits the separator than the amount that enters. The liquid samples taken from the stabilized condensate during the field campaign contained a large amount of solids, which increased the uncertainty of the measurements. For this reason, the measured mercury concentrations in the stabilizer are not deemed to be representative of the true values.

The mass balance for Feed A and Feed B inlet separators cannot be constructed, since not enough information is available, so different scenarios must be studied. By subtracting the amount of mercury that enters the test separator from the amount of mercury that exits the plant, and assuming zero mercury accumulation in the equipment, the remaining amount of mercury entering the plant can be calculated. Different scenarios are studied in this work, which are based on how this amount is distributed among Feed A and Feed B.

10.3.2 Description of the studied scenarios

For studying Hg distribution, the THg measurements are considered as basis for calculating the amount of mercury in the plant feeds. This is necessary in order for the results with and without reaction to be comparable. All mercury at the feeds is assumed to be elemental. The amount of mercury that enters the test separator is set to be 140 g/d, according to the mass balance calculations (Table 10.3). By subtracting this amount from the total amount of elemental mercury that exits the plant (Table 10.2), the remaining 336.8 g/d are distributed among Feed A and Feed B according to three scenarios: 1) Hg enters the plant only through Feed A, 2) Hg enters the plant only through Feed B, and 3) Hg enters the plant through both feeds in equal amounts. The descriptions of the scenarios are summarized in Table 10.5.

Although scenarios 1 and 2 are probably not realistic, since mercury is detected in gases coming from both feed inlet separators, they provide a perspective of the boundary conditions regarding mercury presence in the plant feeds. On the other hand, scenario 3 is a median case, which provides an intermediate estimate of the expected mercury concentration in the process fluids. By comparing the results of scenario 3 with the respective of scenarios 1 and 2, it may be possible to understand whether mercury is predominant in Feed A or Feed B.

Table 10.5. Scenarios for studying mercury distribution in the offshore NG processing platform.

Scenario	Description
1	Mercury enters the plant through test separator (140 g/d) and Feed A inlet separator 10-101 (336.8 g/d).
2	Mercury enters the plant through test separator (140 g/d) and Feed B inlet separator 10-201 (336.8 g/d).
3	Mercury enters the plant through test separator (140 g/d), Feed A inlet separator 10-101 (168.4 g/d) and Feed B inlet separator 20VA201 (168.4 g/d). The amount of mercury in Feed A and Feed B is set to be equal.

It should be noted that since there are 2 inlet separators for each feed, in scenario 1 mercury was only added in the inlet of separator 10-101 (stream "400" in Figure 10.1) which had the largest flowrate. In scenario 2, mercury was only added in the inlet of separator 10-201 (stream "431_370" in Figure 10.1), since field experience indicates that mercury levels in the other Feed B inlet separator are not significant.

10.3.3 Simulation of Hg distribution in the overall process without reaction

By assuming that mercury does not react with H_2S (or any other component), the concentration of mercury in various plant streams is calculated with UMR-PRU and SRK-Twu. The results are presented in Table 10.6 and Figure 10.3, where field measurements are also included for comparison. The distribution of mercury as percentage of the total amount entering each separator according to Scenario 3 is presented in Table 10.7 and Figure 10.4.

In the test separator (10-001), the concentration of mercury in the vapor phase as calculated with UMR-PRU and SRK-Twu is lower than the measured value. Conversely, the calculated Hg^0 concentration in the condensate is roughly 8-9 times higher than the measured value according to both models. SRK-Twu also predicts a much higher mercury concentration in the water phase, which is twice than the one predicted by UMR-PRU. Overall, both models appear to underpredict the Hg^0 concentration in the vapor phase and overpredict the Hg^0 content in the condensate phase. According to Table 10.7, the distribution of mercury in the vapor phase as calculated from the measurements is above 90%, which is significantly higher than the distributions calculated with the models. Both UMR-PRU and SRK-Twu yield a mercury distribution in the test separator of about 50%-50% in the vapor and liquid phases, respectively.

Table 10.6. Elemental mercury concentration in selected plant streams as calculated with UMR-PRU and SRK-Twu.

Description/Tag	Stream	Units	Measured (Hg^0)	Scenario 1		Scenario 2		Scenario 3	
				UMR-PRU	SRK-Twu	UMR-PRU	SRK-Twu	UMR-PRU	SRK-Twu
Feed A inlet sep. (10-101)	Inlet	ppb mol	-	3.8	3.8	0	0	1.9	1.9
Feed B inlet sep. (10-201)	Inlet	ppb mol	-	0	0	3.3	3.3	1.6	1.6
Test separator (10-001)	Inlet	ppb mol	-	14.6	14.6	14.6	14.6	14.6	14.6
Test separator (10-001)	Vapor	µg/Sm^3	**95.2**	71.5	77.3	71.5	77.3	71.5	77.3
Test separator (10-001)	Liquid	µg/kg	**17.5**	155.8	142.9	155.8	142.9	155.8	142.9
Test separator (10-001)	Water	µg/kg	**< 0.1**	1.4	2.9	1.4	2.9	1.4	2.9
Stabilizer tank (10-008)	Inlet	µg/kg	**2.2**	46.2	33.3	45.6	32.4	45.9	32.9
Stabilizer tank (10-008)	Vapor	µg/Sm^3	**36.2**	82.9	74.6	81.7	72.7	82.2	73.7
Stabilizer tank (10-008)	Liquid	µg/kg	**3.8**	46.7	33.6	46.0	32.7	46.3	33.2
Feed A inlet sep. (10-101/401)	Water	µg/kg	**< 0.1**	0.4	0.8	0	0	0.2	0.4
Amine contactor (20-103)	Inlet	µg/Sm^3	**32.9**	29.4	31.7	14.1	13.1	21.7	22.4
Glycol contactor (30-101/201)	Inlet	µg/Sm^3	**12.3**	9.9	10.7	10.5	11.4	10.2	11.1
Export gas	-	µg/Sm^3	**10.6**	9.6	10.3	10.1	11.0	9.9	10.7
Export cond.	-	µg/kg	**9.2**	31.1	24.5	30.6	23.9	30.8	24.2
Feed A gases	-	µg/Sm^3	**27.9**	23.7	25.4	0	0	11.9	12.7
Feed B gases	-	µg/Sm^3	**1.95**	0	0	9.1	11.1	4.6	5.6

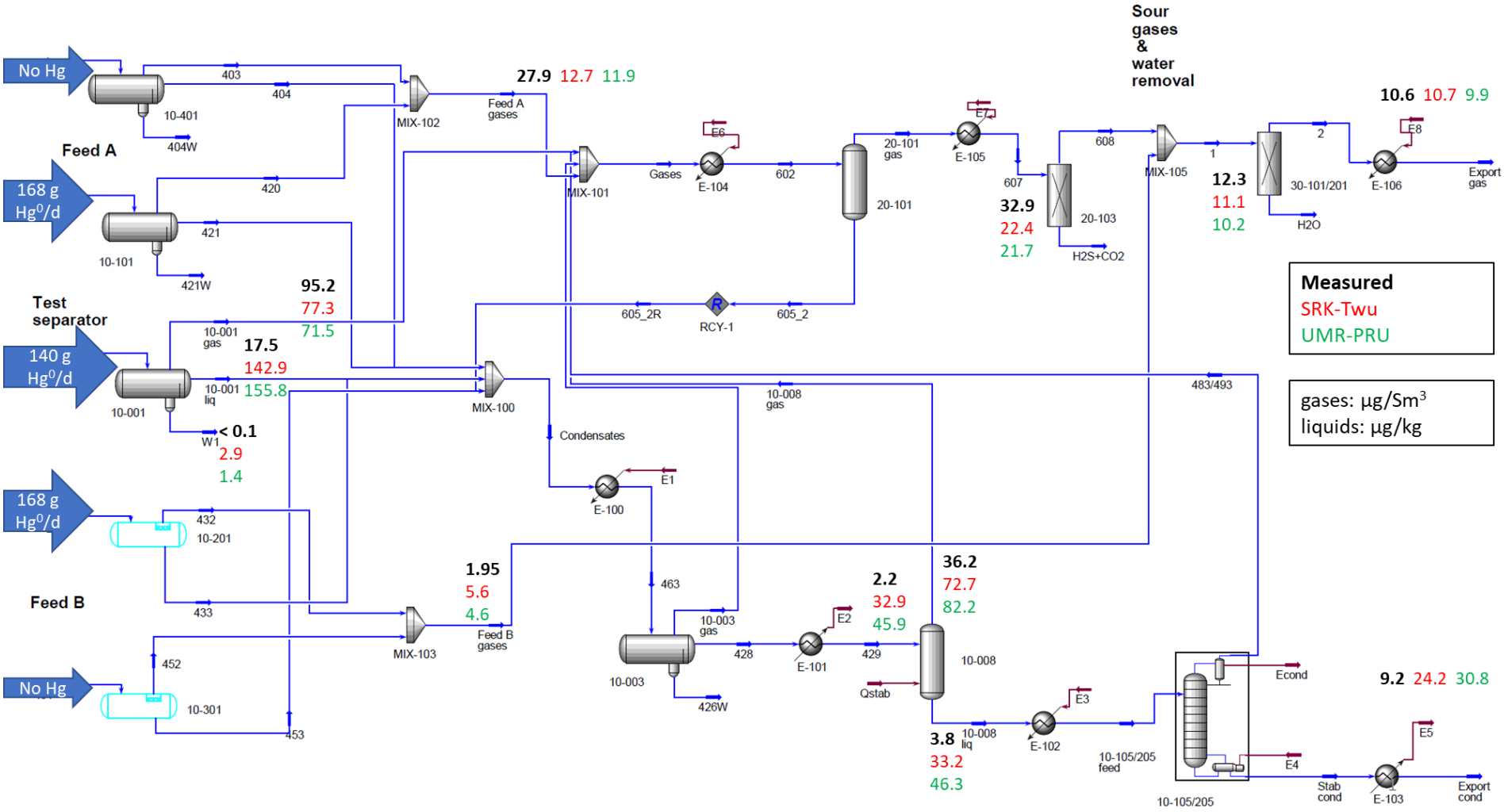

Figure 10.3. Hg^0 concentration in selected plant streams as calculated with UMR-PRU and SRK-Twu according to scenario 3 against field measurements.

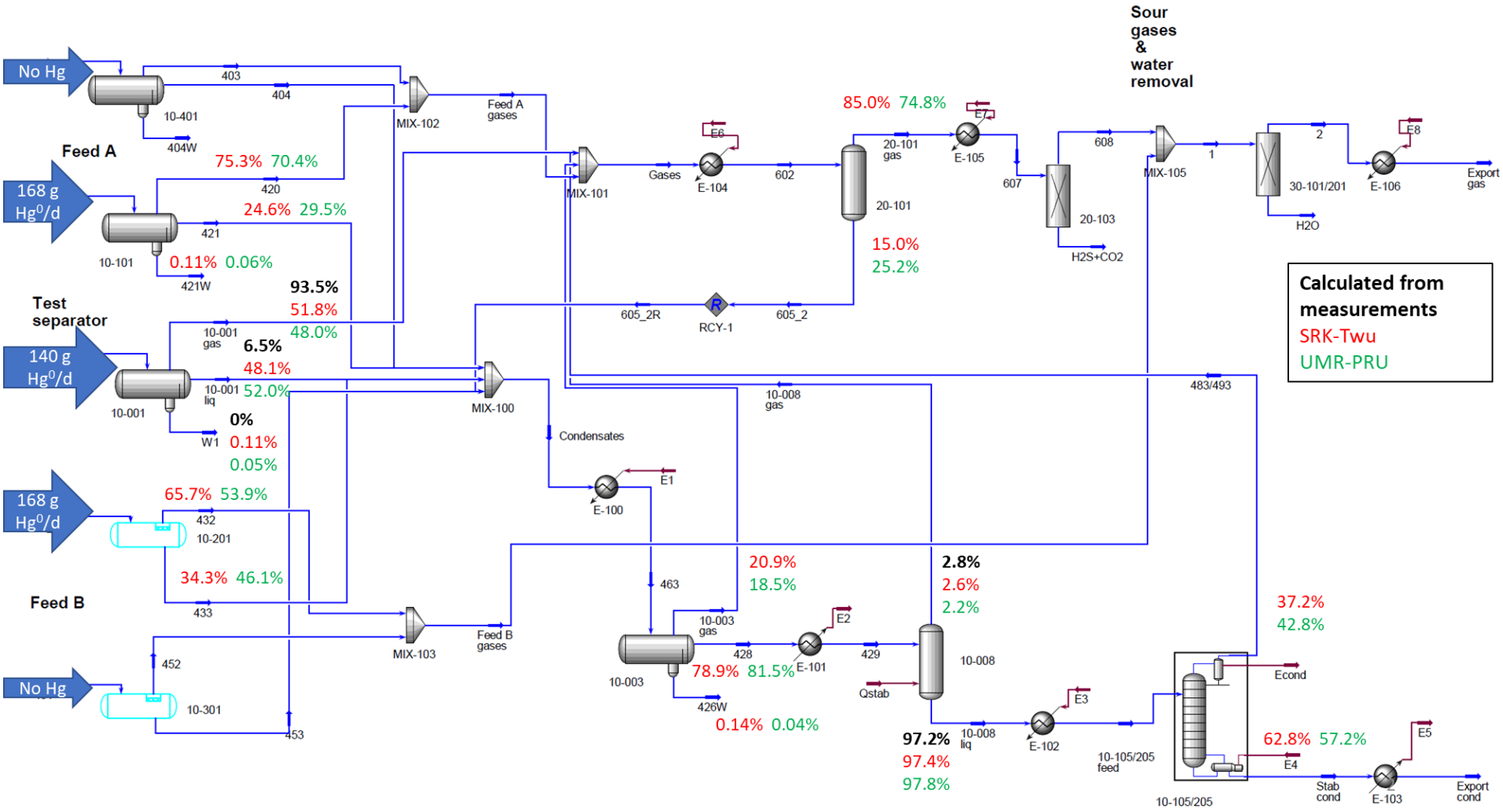

Figure 10.4. Distribution of elemental mercury with UMR-PRU and SRK-Twu as % of total amount entering each separator according to scenario 3.

Table 10.7. Distribution of elemental mercury as % of total amount entering each separator according to scenario 3.

Tag	Description	Calculated from measurements[a]			UMR-PRU			SRK-Twu		
		Vapor	Liquid	Aqueous	Vapor	Liquid	Aqueous	Vapor	Liquid	Aqueous
10-001	Test separator	93.50	6.50	0	47.97	52.02	0.05	51.77	48.12	0.11
10-101	Feed A inlet sep.	N/A	N/A	-	70.38	29.50	0.06	75.25	24.64	0.11
10-201[b]	Feed B inlet sep.	N/A	N/A	-	53.94	45.89	0.16	65.71	34.27	0
10-003	2nd stage sep.	N/A	N/A	-	18.45	81.51	0.04	20.90	78.94	0.14
10-008	Stabilizer tank	2.80	97.20	-	2.22	97.78	-	2.60	97.40	-
10-105/205	Stabilizing column	N/A	N/A	-	42.76	57.24	-	37.20	62.80	-
20-101[b]	Gas treat. scrubber	N/A	N/A	-	74.80	25.18	0.02	85.00	14.97	0.01

[a] *calculated as % of total Hg^0 amount exiting the separators*

[b] *separator is 2-phase, but a third water phase is also present according to the models*

In the condensate stabilization tank (10-008), scenarios 1-3 lead to a mercury concentration at the inlet, which is much higher than the measured value of 2.2 μg/kg, with both models. Consequently, the predicted values for Hg concentration in the vapor and liquid phases are higher than the measured values. As can be seen in Table 10.7, the distributions yielded by both models are very similar and agree with the distribution calculated from the measurements, if the outlet Hg amount is considered as basis. Taking into account the large uncertainty of the measurements in the liquid phase due to the presence of solid particles and the mass balance problems discussed in the previous section, the measured values for the stabilizer streams are not deemed suitable for evaluating the thermodynamic models.

Regarding the other separators (10-101, 10-201, 10-003) and distillation column (10-105/205), for which measurements are not available, it is observed that both models yield similar Hg^0 distributions among the different phases. The highest divergence is observed in Feed B inlet separator (10-201) and gas treatment scrubber (20-101), in which SRK-Twu predicts significantly more mercury partitioning in the gas phase. This could be explained by the higher amount of produced gas as predicted with SRK-Twu, which leads to more mercury being found in this phase due to the mass balance. In general, SRK-Twu predicts more elemental mercury partitioning in the vapor and aqueous phases, as compared to UMR-PRU.

The Hg^0 concentration in the water produced by Feed A inlet separators was found to be lower than the limit of detection during the field campaign. According to all scenarios and models, this concentration is calculated to be lower than 1 μg/kg, which essentially confirms that the mercury content there is negligible. In all scenarios, SRK-Twu yields a higher Hg content in this water stream as compared to UMR-PRU. In conjunction with the observations for the aqueous stream of the test separator, it is shown that SRK-Twu systematically overpredicts the concentration of mercury in water.

In the gases produced by Feed A inlet separators, the scenario that best matches the Hg^0 concentration is scenario 1 according to both models. On the other hand, it is shown that scenario 2 cannot reflect the reality, since it yields a higher Hg^0 concentration in Feed B inlet separator gases and zero mercury in Feed A gases. This indicates that mercury is probably predominant in Feed A well streams.

Regarding the amine contactor (20-103) inlet, scenario 1 leads to similar results with both thermodynamic models, which are also close to the measured value. When no mercury is present in Feed A (scenario 2), the calculated Hg^0 concentration at the amine contactor inlet is low. This is expected, since this stream mainly consists of gas produced by Feed A inlet separators.

For the glycol contactor (30-101/201) inlet, all scenarios with both models yield similar results, which are very close to the measured values.

All scenarios lead to similar results for Hg^0 concentration in the stabilizer (10-008) streams, in export gas and export condensate. This is expected, since these streams are formed by mixing other intermediate streams, so mercury concentration after mixing is more or less the same. The main differences are found in the gases produced by Feed A and Feed B inlet separators, and in the inlet of the amine contactor (20-103). By comparing the results according to each scenario with the measured values in these streams, it is indicated that mercury is predominant in Feed A. A calculation was made to see what Hg distribution in the feeds leads to the measured value of 1.95 μg/Sm^3 for the Feed B gases, and it was found that apart from the Hg amount that enters the test separator, the rest must be distributed roughly 80%-20% in Feed A and B, respectively.

All scenarios yield reasonable Hg concentrations in the export gas. Both UMR-PRU and SRK-Twu predict a Hg^0 content in export gas, which is very close to the measured value. However, the calculated values for the export condensate are almost two and three times higher than the measured, according to SRK-Twu and UMR-PRU, respectively. This is due to the higher calculated Hg^0 distribution in condensates as opposed to the measurements.

The overall mercury distribution in the plant as calculated with SRK-Twu and UMR-PRU according to scenario 3 is shown in Figure 10.5 and Figure 10.6, respectively. This scenario was chosen as baseline because it is a median case, which is expected to provide an average estimate of the expected mercury concentration in the process fluids.

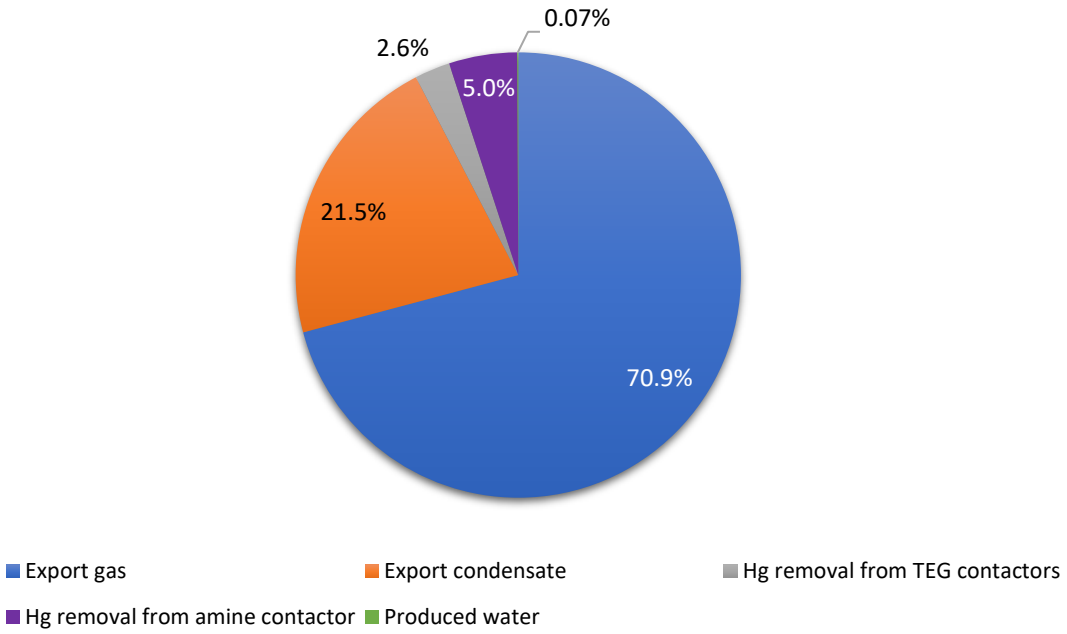

Figure 10.5. Elemental mercury distribution in plant outlets as percentage of total Hg^0 entering the plant. Calculations based on scenario 3 with SRK-Twu.

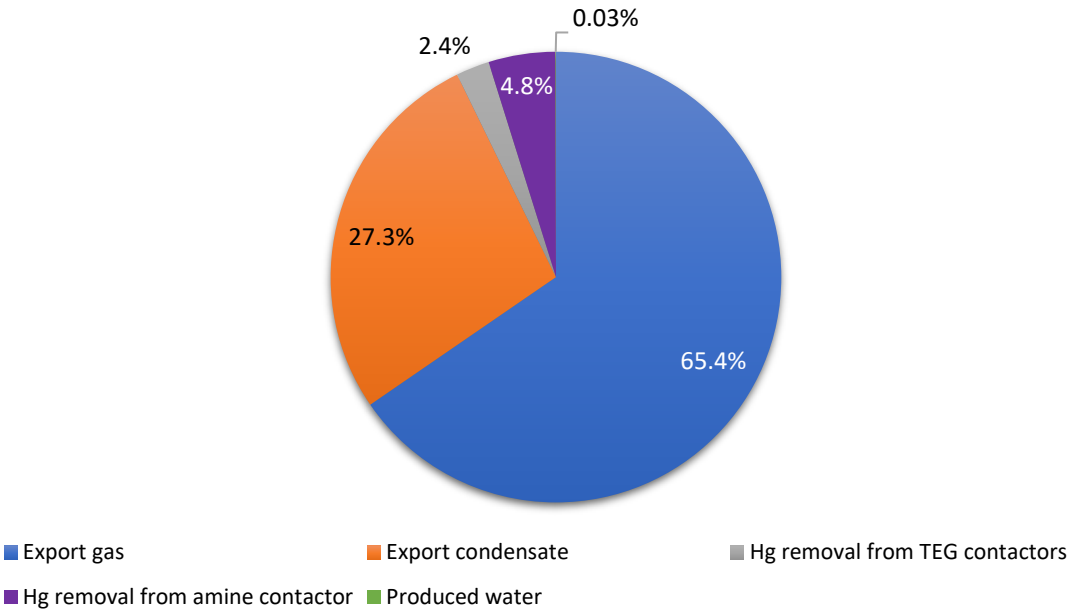

Figure 10.6. Elemental mercury distribution in plant outlets as percentage of total Hg^0 entering the plant. Calculations based on scenario 3 with UMR-PRU.

From the above figures it is observed that both models yield similar results. The models yield a Hg^0 distribution in the export gas of about 65%-70%, and in the export condensate of about 22-27%. However, both models predict less mercury partitioning in the export gas and more in the export condensate as compared to the values calculated from the mass balance (Figure 10.2). This could be explained by the higher predicted Hg concentrations in the condensates as compared to the measured values, as discussed above. In addition, the models show a lower mercury loss in the amine and glycol contactors. Finally, both models predict a very small amount of elemental mercury partitioning in the produced water, which agrees with the findings of the field campaign.

10.3.4 Investigation of the effect of fluid characterization

To understand whether the characterization method affects mercury distribution, the plant feeds were also characterized according to the method developed by Thermodynamics and Transport Phenomena Laboratory (TTPL) for UMR-PRU [69], and mercury distribution in the plant without reaction was calculated again.

For this purpose, since the plant has many different feeds, they were characterized separately and the resulting pseudocomponents were added to a single fluid package. In cases where a pseudocomponent with the same carbon number was assigned to different feeds with different properties (MW, T_c, P_c etc.), its properties in the complete fluid package (Appendix D) were set equal to the properties assigned to the feed with the highest flowrate. The simulation results with the new fluid package are presented in Table 10.8 and Table 10.9.

Table 10.8. Mercury concentration in selected plant streams as calculated with UMR-PRU and TTPL characterization method [69] (no Hg reaction considered).

Description/Tag	Stream	Units	Measured (Hg^0)	Scenario 1	Scenario 2	Scenario 3
Feed A inlet sep. (10-101)	Inlet	ppb mol	-	3.8	0	1.9
Feed B inlet sep. (10-201)	Inlet	ppb mol	-	0	3.2	1.6
Test separator (10-001)	Inlet	ppb mol	-	14.6	14.6	14.6
Test separator (10-001)	Vapor	µg/Sm^3	**95.2**	76.4	76.4	76.4
Test separator (10-001)	Liquid	µg/kg	**17.5**	145.6	145.6	145.6
Test separator (10-001)	Water	µg/kg	**< 0.1**	1.5	1.5	1.5
Stabilizer tank (10-008)	Inlet	µg/kg	**2.2**	41.6	43.1	42.4
Stabilizer tank (10-008)	Vapor	µg/Sm^3	**36.2**	81.2	84.2	82.8
Stabilizer tank (10-008)	Liquid	µg/kg	**3.8**	42.0	43.6	42.9
Feed A inlet sep. (10-101/401)	Water	µg/kg	**< 0.1**	0.4	0	0.2
Amine contactor (20-103)	Inlet	µg/Sm^3	**32.9**	30.5	14.6	22.6
Glycol contactor (30-101/201)	Inlet	µg/Sm^3	**12.3**	10.3	10.7	10.5
Export gas	-	µg/Sm^3	**10.6**	9.9	10.3	10.2
Export cond.	-	µg/kg	**9.2**	28.0	29.0	28.6
Feed A gases	-	µg/Sm^3	**27.9**	24.4	0	12.2
Feed B gases	-	µg/Sm^3	**1.95**	0	9.2	4.6

Table 10.9. Hg^0 distribution as % of total amount entering each separator according to scenario 3.

Tag	Description	Calculated from measurements[a]			UMR-PRU (TTPL characterization)		
		Vapor	Liquid	Aqueous	Vapor	Liquid	Aqueous
10-001	Test separator	93.50	6.50	0	51.45	48.49	0.05
10-101	Feed A inlet sep.	N/A	N/A	-	72.36	27.58	0.06
10-201[b]	Feed B inlet sep.	N/A	N/A	-	54.46	45.38	0.16
10-003	2nd stage sep.	N/A	N/A	-	19.32	80.64	0.04
10-008	Stabilizer tank	3.79	96.21	-	2.24	97.76	-
10-105/205	Stabilizing column	N/A	N/A	-	42.10	57.86	-
20-101[b]	Gas treat. scrubber	N/A	N/A	-	78.48	21.50	0.02

[a] *calculated as % of total Hg^0 amount exiting the separators*

[b] *separator is 2-phase, but a third water phase is also present according to the models*

By comparing the results of UMR-PRU with the different characterization methods (Table 10.6 and Table 10.8), some small differences are observed. More specifically, the TTPL method yields a slightly higher Hg^0 concentration in gases and lower in condensates, which agrees more with the measured values. The results of UMR-PRU with this characterization method are also more similar with those by SRK-Twu.

The predicted Hg^0 distribution among export gas and export condensate is presented in Figure 10.7. It is shown that UMR-PRU with the TTPL characterization method yields a higher Hg^0 distribution in the export gas. This trend is more in line with the distributions estimated from the field campaign measurements.

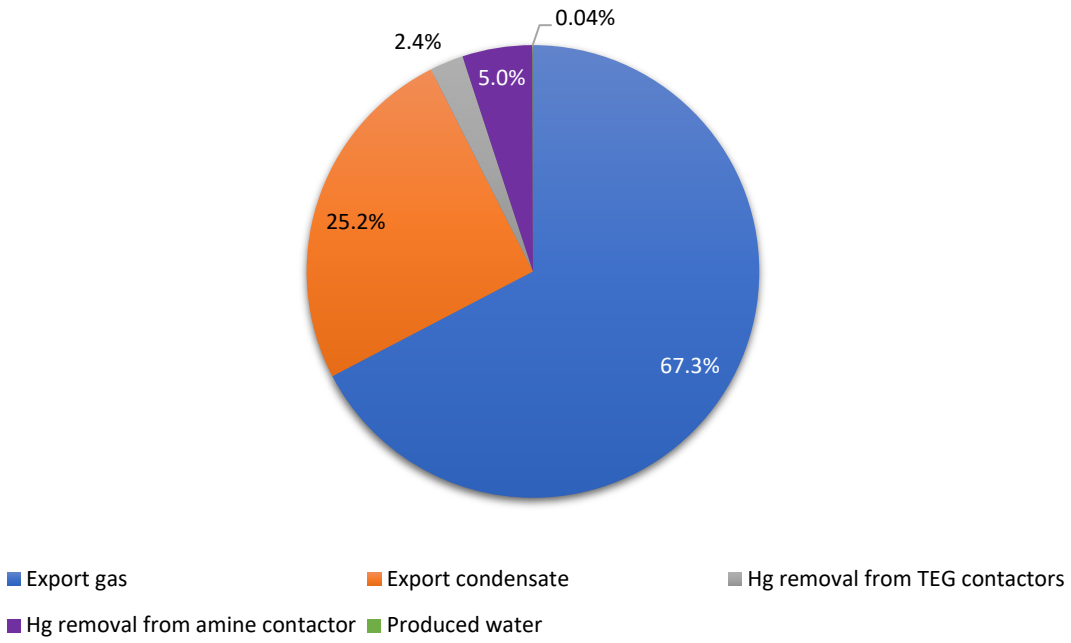

Figure 10.7. Elemental mercury distribution in plant outlets as percentage of total Hg^0 entering the plant. Calculations based on scenario 3 with UMR-PRU and TTPL characterization method [69].

10.3.5 Simulation of Hg distribution with reaction

To simulate mercury distribution in the plant with SRK-Twu while taking into account the reaction of Hg with H_2S, the same simplified simulation file was employed as described previously. The only alteration was the addition of the reaction to the fluid package, by defining the reactants and products, as well as the equilibrium constant of the reaction as a function of temperature. The same amount of mercury was assumed to enter the test separator (10-001), as the one calculated from the mass balance in Section 10.3.1. The Hg content in Feed A and B was set according to scenario 3, since it is the median case. The reaction was assumed to take place in all separators which contained mercury, except stabilization column 10-105/205.

UniSim has the capability of handling reactions within a simulation either in flash vessels or in reactor blocks. The reactions are defined when the simulation basis is set up, after the user has defined the components and the thermodynamic model that will be used for the simulation. For this purpose, there is a special tab ("Reactions" in Figure 10.8) in the Simulation Basis Manager, where the user can define the reaction type (conversion, equilibrium, kinetic etc.), the participating components and other required information, depending on the reaction type.

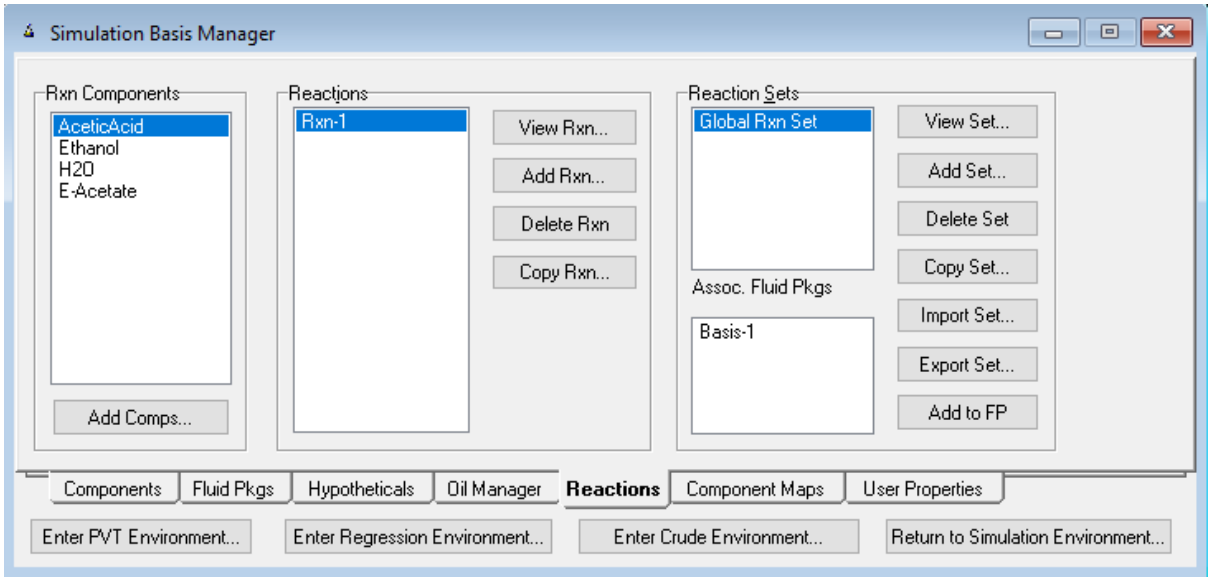

Figure 10.8. Attaching a reaction set to a fluid package in UniSim.

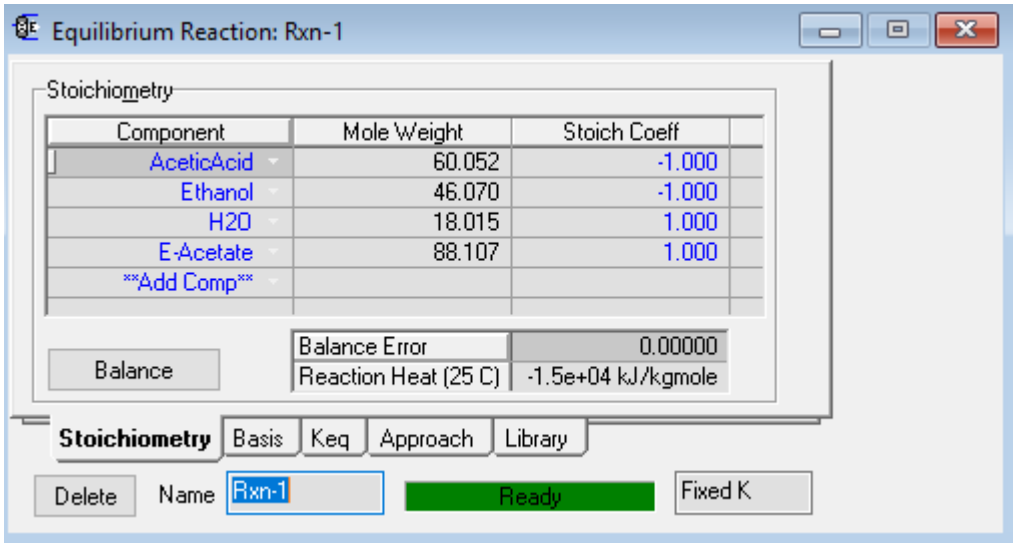

Figure 10.9. Inserting components and stoichiometric coefficients for a reaction in UniSim.

For an equilibrium reaction, such as the one studied in this work, the user must define the stoichiometric coefficients (Figure 10.9), the equilibrium constant (K_{eq}) of the reaction, the phase in which the reaction takes place (vapor, liquid, overall combined), and K_{eq} calculation

basis (e.g. activity, mole fraction etc.) (Figure 10.10). The equilibrium constant of the reaction can be calculated automatically by UniSim from internal values for Gibbs energy of formation of the components or it can be supplied by the user either as a fixed temperature-independent value or as a function of temperature.

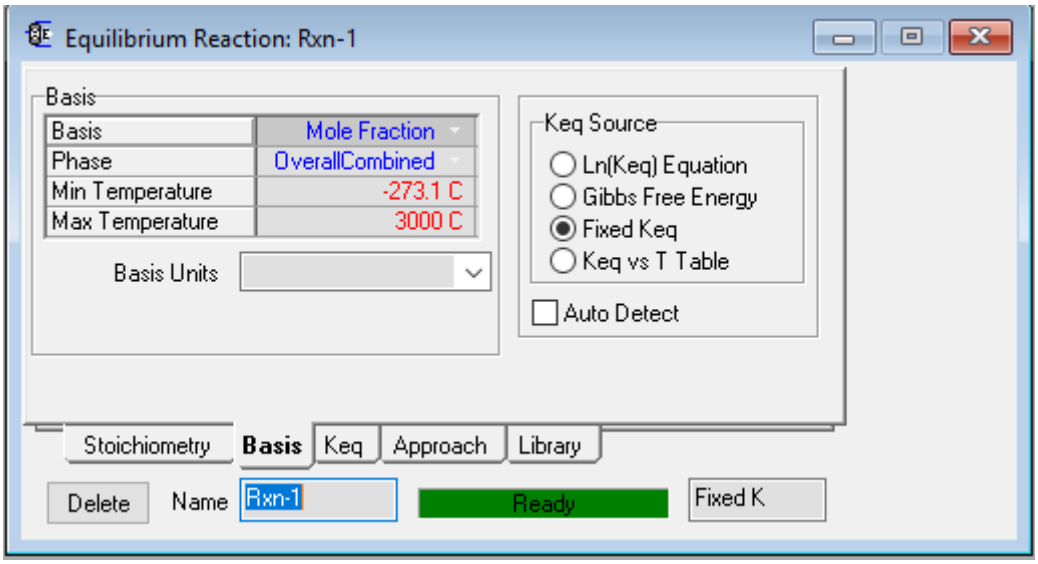

Figure 10.10. Defining calculation basis, reaction phase and equilibrium constant in UniSim.

The software documentation does not describe how UniSim solves the simultaneous chemical & phase equilibria (CPE). However, the requirement for designating the phase in which the reaction occurs implies that it uses an algorithm based on reaction extent ("law of mass action"). On the other hand, the CPE algorithm that has been developed in this work does not require a reaction phase to be specified, since the Gibbs energy is minimized for the entire system including all components and possible phases. However, the phase in which the reaction occurs plays a role in the calculation of K_{eq} from the Gibbs energies of formation.

In order to compare CPE results between UniSim and the algorithm developed in this work, some common reaction examples were studied, such as cyclohexane synthesis, acetic acid/ethanol esterification, and methanol synthesis. It was also checked how the results differ if vapor or liquid phase reaction is selected in UniSim, while keeping the same expression for K_{eq}. The results showed that when the same K_{eq} is used, the selection of vapor phase reaction leads to very similar results with the developed CPE algorithm regardless of the selected reference state for calculating K_{eq} from Gibbs energies of formation.

Mercury distribution throughout the plant while also considering the reaction between mercury and H_2S is not possible with CAPE-OPEN in UniSim Design, due to technical limitations. The problem is that HgS must be defined in the simulation as a solid component so as not to participate in the phase equilibrium. In the simulation with SRK-Twu this is done by defining HgS as a solid hypothetical component. However, this classification is not possible for a component of a CAPE-OPEN fluid package. Therefore, Hg distribution with reaction was studied individually for some separators with the CPE algorithm that has been developed in

this work. This was done in a sequential manner, by taking the flowrates and compositions from the simulation without reaction, and performing the chemical & phase equilibria calculations with the algorithm.

Preliminary simulations assuming the mercury reaction gas takes place in the gas phase with both SRK-Twu and UMR-PRU showed that almost 100% of Hg^0 is converted to HgS at the inlet separators. The resulting Hg^0 concentration in Feed A and Feed B gases exiting the inlet separators was found to be 0.05 μg/Sm^3 and 0.0003 μg/Sm^3, respectively, while in export gas it was found to be 0.002 μg/Sm^3. This is not in accordance with the field campaign measurements, since Hg^0 has been detected in much higher concentration in the gas streams. For this reason, only the results considering the reaction in the liquid hydrocarbon phase are presented in detail here.

For studying mercury distribution in the plant assuming a reaction between Hg^0 and H_2S also takes place in the liquid hydrocarbon phase, all three reaction equilibrium constants calculated in Section 9.3 were employed. Scenario 3 for mercury flowrate at plant inlets was also adopted, since it represents the median case. The results concerning Hg^0 concentrations in plant streams with SRK-Twu and UMR-PRU with K_{eq} from Robie et al. [127] (KL2 in Table 9.3) are presented in Table 10.10 and Figure 10.11. The distribution of mercury as percentage of the total amount entering each separator is presented in Table 10.11 and Figure 10.12. The results with the other equilibrium constants are presented in Appendix D.

Table 10.10. Elemental mercury concentration in selected plant streams as calculated with SRK-Twu and UMR-PRU with scenario 3 and liquid phase reaction (K_{eq} from data by Robie et al. [127]).

Description/Tag	Stream	Units	Measured (Hg^0)	SRK-Twu	UMR-PRU
Feed A inlet sep. (10-101)	Inlet	ppb mol	-	1.9	1.9
Feed B inlet sep. (10-201)	Inlet	ppb mol	-	1.6	1.6
Test separator (10-001)	Inlet	ppb mol	-	14.6	14.6
Test separator (10-001)	Vapor	μg/Sm^3	**95.2**	65.7	63.6
Test separator (10-001)	Liquid	μg/kg	**17.5**	121.4	138.5
Test separator (10-001)	Water	μg/kg	**< 0.1**	2.4	1.2
Stabilizer tank (10-008)	Inlet	μg/kg	**2.2**	28.6	42.0
Stabilizer tank (10-008)	Vapor	μg/Sm^3	**36.2**	62.7	72.5[a]
Stabilizer tank (10-008)	Liquid	μg/kg	**3.8**	28.3	43.1[a]
Feed A inlet sep. (10-101/401)	Water	μg/kg	**< 0.1**	0.3	0.2

Amine contactor (20-103)	Inlet	µg/Sm^3	**32.9**	19.3	19.3
Glycol contactor (30-101/201)	Inlet	µg/Sm^3	**12.3**	9.7	9.2
Export gas	-	µg/Sm^3	**10.6**	9.4	8.9
Export cond.	-	µg/kg	**9.2**	20.6	28.1[a]
Feed A gases	-	µg/Sm^3	**27.9**	11.1	10.8
Feed B gases	-	µg/Sm^3	**1.95**	5.1	4.3

[a] *Results with UMR-PRU for stabilizer (10-008) are not fully representative, because it is solved as isothermal.*

Table 10.11. Distribution of elemental mercury as percent of total amount entering each separator according to scenario 3 with liquid phase reaction (K_{eq} from data by Robie et al. [127]).

Tag	Description	Calculated from measurements[a]			UMR-PRU			SRK-Twu		
		Vapor	Liquid	Aqueous	Vapor	Liquid	Aqueous	Vapor	Liquid	Aqueous
10-001	Test separator	80.26	5.57	0	42.68	46.2	0.04	43.99	40.88	0.09
10-101	Feed A inlet sep.	N/A	N/A	-	64.13	26.9	0.05	65.53	21.45	0.10
10-201[b]	Feed B inlet sep.	N/A	N/A	-	50.89	43.4	0.15	60.49	31.54	0.02
10-003	2nd stage sep.	N/A	N/A	-	18.53	80.2	0.04	20.40	77.0	0.13
10-008	Stabilizer tank	N/A[c]	N/A[c]	-	3.02	96.7	-	2.60	97.05	-
10-105/205	Stabilizing column	N/A	N/A	-	44.24	55.8	-	37.20	62.78	-
20-101[b]	Gas treat. scrubber	N/A	N/A	-	74.78	25.20	0.02	85.00	14.96	0.01

[a] *calculated as % of total Hg^0 amount exiting the separators*

[b] *separator is 2-phase, but a third water phase is also present according to the models*

[c] *not possible to calculate due to high uncertainty of liquid phase measurements*

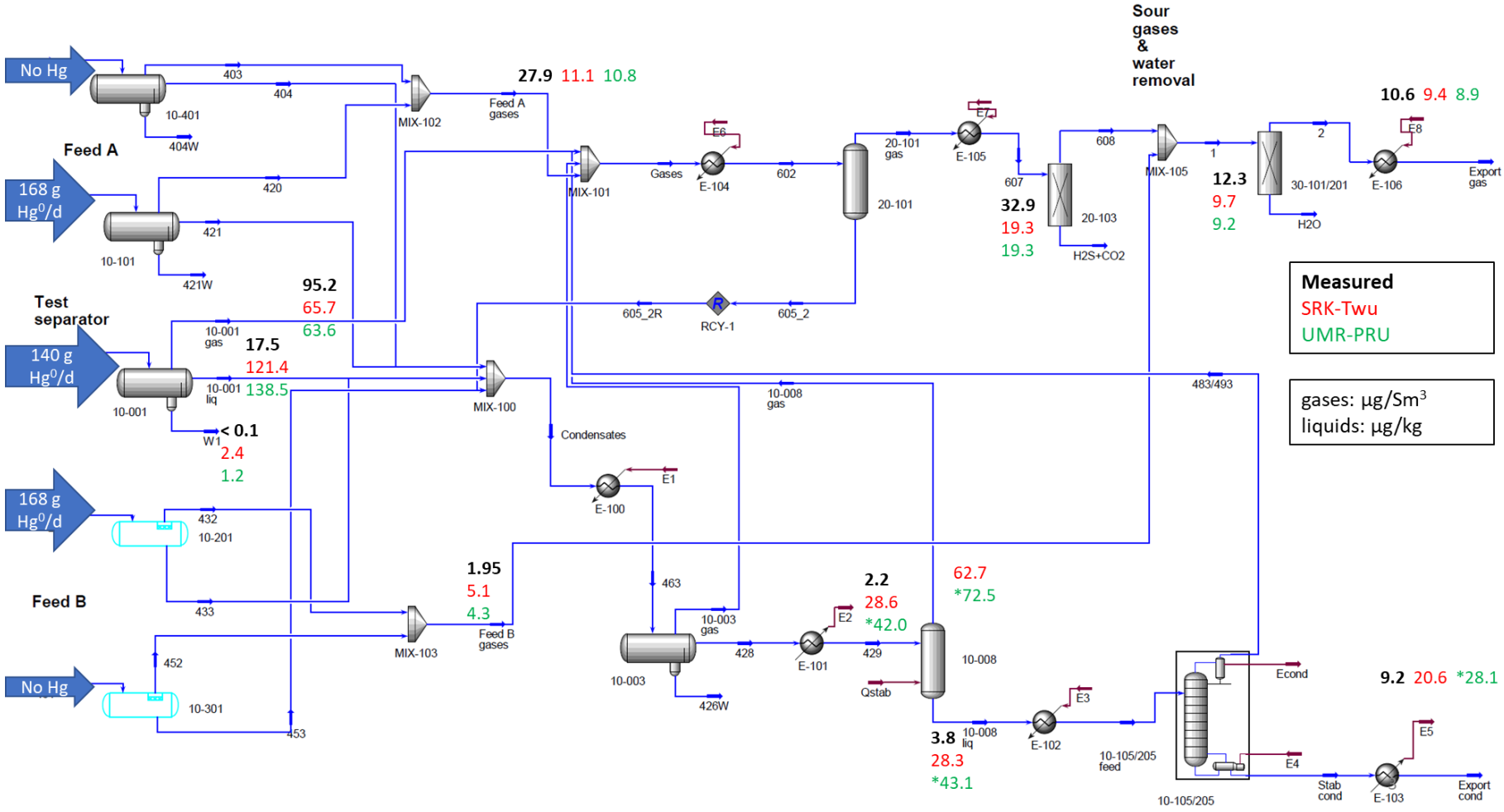

Figure 10.11. Elemental mercury concentration in selected plant streams as calculated with UMR-PRU and SRK-Twu according to scenario 3 with liquid phase reaction (K_{eq} from data by Robie et al. [127]). UMR-PRU results annotated with (*) are not fully representative, because stabilizer (10-008) is solved as isothermal.

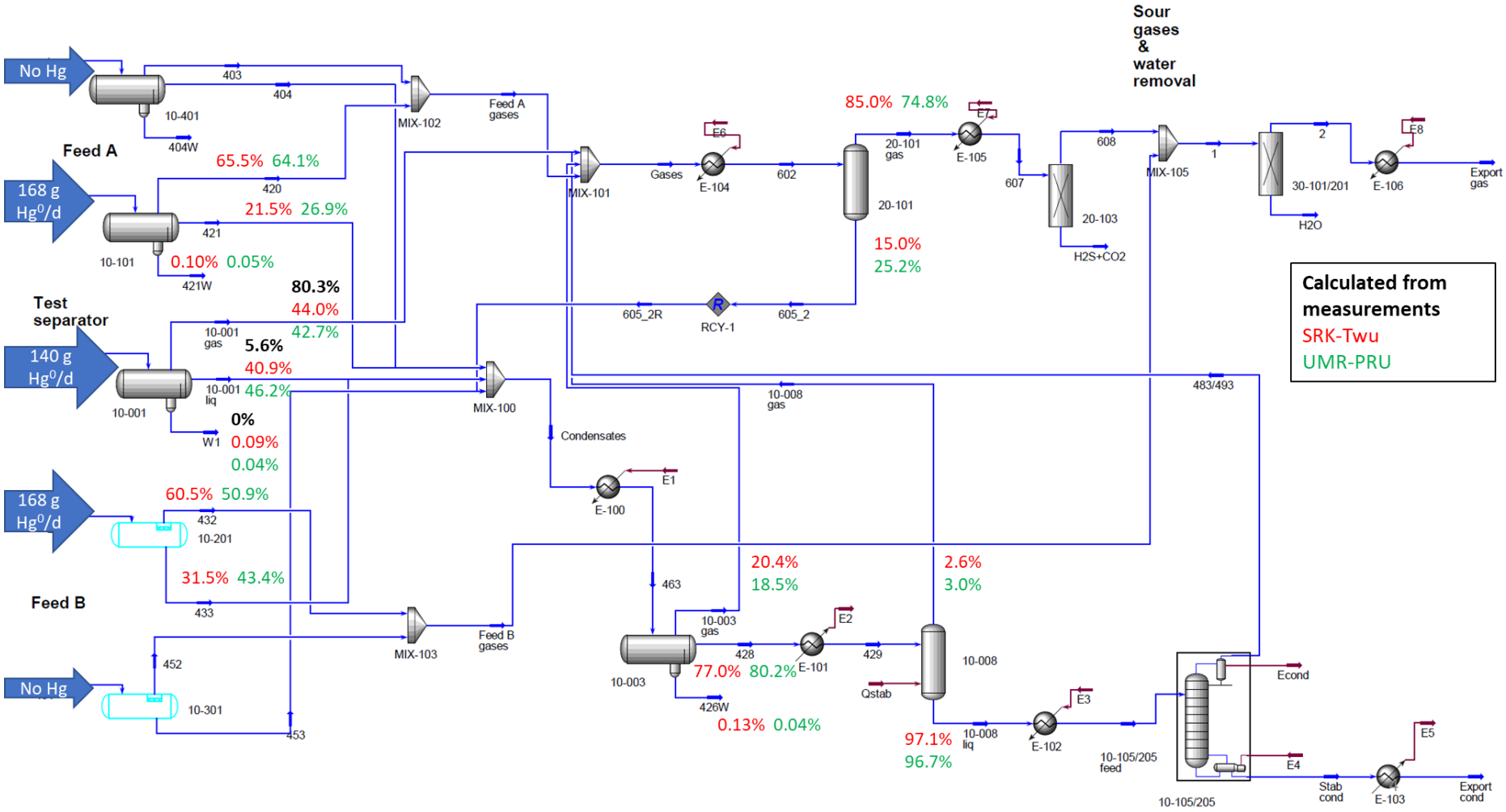

Figure 10.12. Distribution of elemental mercury with UMR-PRU and SRK-Twu as percent of total amount entering each separator according to scenario 3 with liquid phase reaction (K_{eq} from data by Robie et al. [127]).

The results with UMR-PRU were obtained by calculating the chemical & phase equilibria individually for each separator with the CPE algorithm developed in this work, and using the mass balances to calculate Hg^0 concentration in streams after mixing. A problem was encountered in the stabilizer tank (10-008), in which the inlet and outlet streams have a temperature difference of about 10°C. The developed algorithm solves the simultaneous chemical & phase equilibria in systems with constant temperature, so it cannot be directly implemented in this case. Nevertheless, CPE calculations for 10-008 were performed by assuming a constant temperature, which was taken to be equal to that of the outlets. Although the results are not fully representative because the CPE is solved as isothermal, it is observed that the yielded Hg^0 concentrations are reasonable.

As expected, due to the conversion of elemental mercury to HgS, the Hg^0 concentrations in the various streams as predicted by the models are lower than in the case where no reaction was assumed. The results with SRK-Twu are closer to the measured values in gases and liquid hydrocarbons, but it overpredicts Hg^0 content in water streams. Nevertheless, both models yield similar Hg^0 distributions in vapor and liquid phases, which are lower than the no reaction case. This is expected, since a portion of the elemental mercury is converted to HgS. It is also observed that Hg^0 distribution in the vapor phase is lower than the no reaction case, despite the reaction taking place in the liquid phase. This is due to Hg^0 being removed from the liquid phase, as it converts to HgS, which causes the phase equilibrium to shift and some Hg^0 migrating from the vapor to the liquid phase, so that finally the two phases are both in chemical and phase equilibrium. On the other hand, the elemental mercury in water phases seems to remain largely unchanged. Finally, it should be noted that Hg^0 distributions in Table 10.11 do not add up to 100%, because an amount of Hg^0 at each separator is converted to solid HgS. The remaining percent is equal to the conversion in each separator.

The Hg^0 to HgS conversion percent and the produced solid HgS amount at each separator as calculated with SRK-Twu and UMR-PRU are presented in Table 10.12. It is observed that SRK-Twu leads to higher conversions and, consequently, more solid HgS being produced, as compared with UMR-PRU. In total, SRK-Twu predicts that 70.9 g of HgS are produced per day, while UMR-PRU predicts 50.4 g/d. To understand which model is closer to reality, the produced HgS in the plant can be calculated from the difference between the total mercury measured in process fluid samples and the measured elemental mercury, by assuming that this amount is exclusively attributed to HgS and not to other mercury forms. From this difference, it is calculated that 16.6 g of HgS are being produced per day. Therefore, UMR-PRU yields an HgS production, which is closer to the expected value.

Table 10.12. Conversion percent and produced HgS amount at each separator as calculated with SRK-Twu and UMR-PRU according to scenario 3 (K_{eq} from data by Robie et al. [127]).

Tag	Description	SRK-Twu		UMR-PRU	
		Conversion (%)	Produced HgS (g/d)	Conversion (%)	Produced HgS (g/d)
10-001	Test separator	15.0	24.3	11.0	17.8
10-101	Feed A inlet sep.	12.9	25.2	8.9	17.4
10-201	Feed B inlet sep.	7.9	15.5	5.5	10.8
10-301	Feed B inlet sep.	-	-	-	-
10-401	Feed A inlet sep.	-	-	-	-
10-003	2nd stage sep.	2.5	5.3	1.2	4.0
10-008	Stabilizer tank	0.3	0.4	0.2	0.4
20-101	Gas treat. scrubber	0.06	0.2	0	0
		Total	**70.9**		**50.4**

To understand how the equilibrium constant of the reaction affects results, the produced solid HgS according to the three different equilibrium constants calculated in Chapter 9 (Table 9.3) are presented in Table 10.13 with SRK-Twu model. It is observed that the equilibrium constant from data by Perry's Handbook [128] (KL3) leads to an almost 10 times lower Hg^0 to HgS conversion as compared with the K_{eq} from data by Robie et al. [127] (KL2). On the other hand, the K_{eq} from NBS data [20] (KL1) yields an amount of produced HgS, which is much higher than the expected value of 16.6 g/d. Although the produced HgS as calculated with KL2 is closer to the expected value, the results for Hg concentrations in process fluids presented in Appendix D show that this K_{eq} provides a small improvement for model predictions regarding mercury in liquids as compared to the no reaction case. Conversely, the (KL1) leads to improved model predictions for Hg concentrations in liquids, but worse results for mercury content in process gases. Therefore, KL2 is considered to be the best compromise between Hg concentrations in streams and predicted amount of produced HgS.

The overall mercury distribution in the plant as calculated with SRK-Twu and UMR-PRU assuming liquid phase reaction and mercury inlet flows according to scenario 3 is shown in Figure 10.13 and Figure 10.14, respectively. For comparison, the Hg^0 distribution as percent of THg exiting the plant as calculated from the measurements and actual flowrates during the field campaign is presented in Figure 10.15.

Table 10.13. Conversion percent and produced HgS amount at each separator as calculated with SRK-Twu according to scenario 3 and the three different equilibrium constants calculated in Chapter 9 (Table 9.3).

Tag	Description	KL1		KL2		KL3	
		Conversion (%)	Produced HgS (g/d)	Conversion (%)	Produced HgS (g/d)	Conversion (%)	Produced HgS (g/d)
10-001	Test separator	45.7	73.7	15.0	24.3	1.4	2.2
10-101	Feed A inlet sep.	41.6	81.3	12.9	25.2	1.2	2.3
10-201	Feed B inlet sep.	38.8	75.7	7.9	15.5	0.6	1.7
10-301	Feed B inlet sep.	-	-	-	-	-	-
10-401	Feed A inlet sep.	-	-	-	-	-	-
10-003	2nd stage sep.	10.1	14.8	2.5	5.3	0.2	0.4
10-008	Stabilizer tank	1.2	1.3	0.3	0.4	0.02	0.04
20-101	Gas treat. scrubber	8.2	16.4	0.06	0.2	-	-
		Total	**263.2**		**70.9**		**6.1**

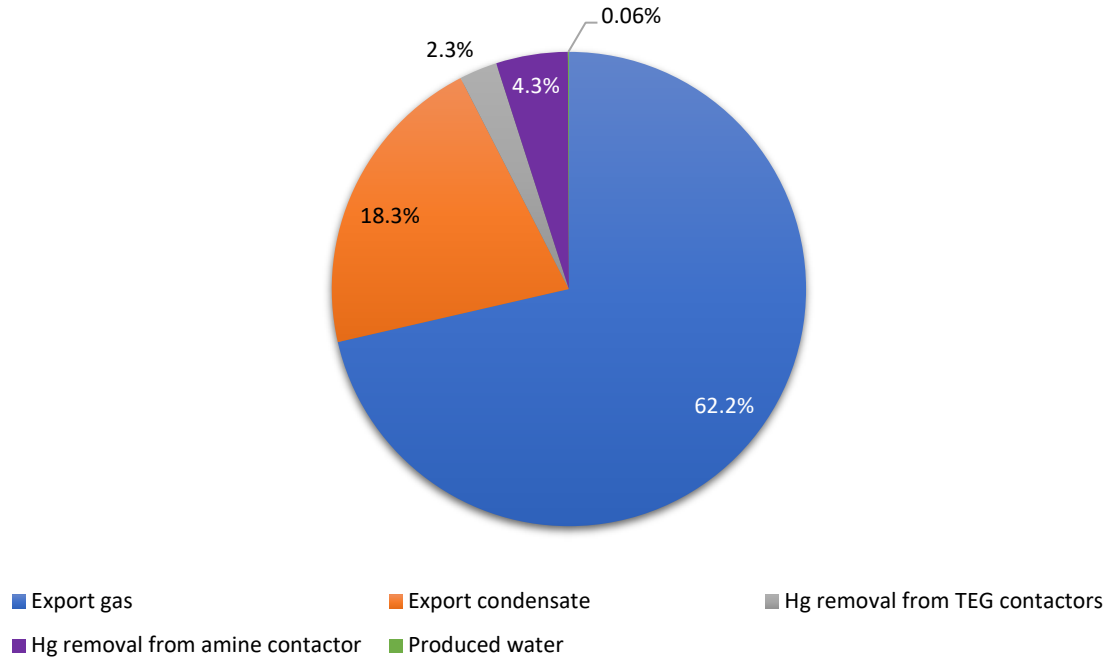

Figure 10.13. Elemental mercury distribution in plant outlets as % of total Hg^0 entering the plant. Calculations based on scenario 3 with SRK-Twu and assuming liquid phase reaction (K_{eq} from data by Robie et al. [127]).

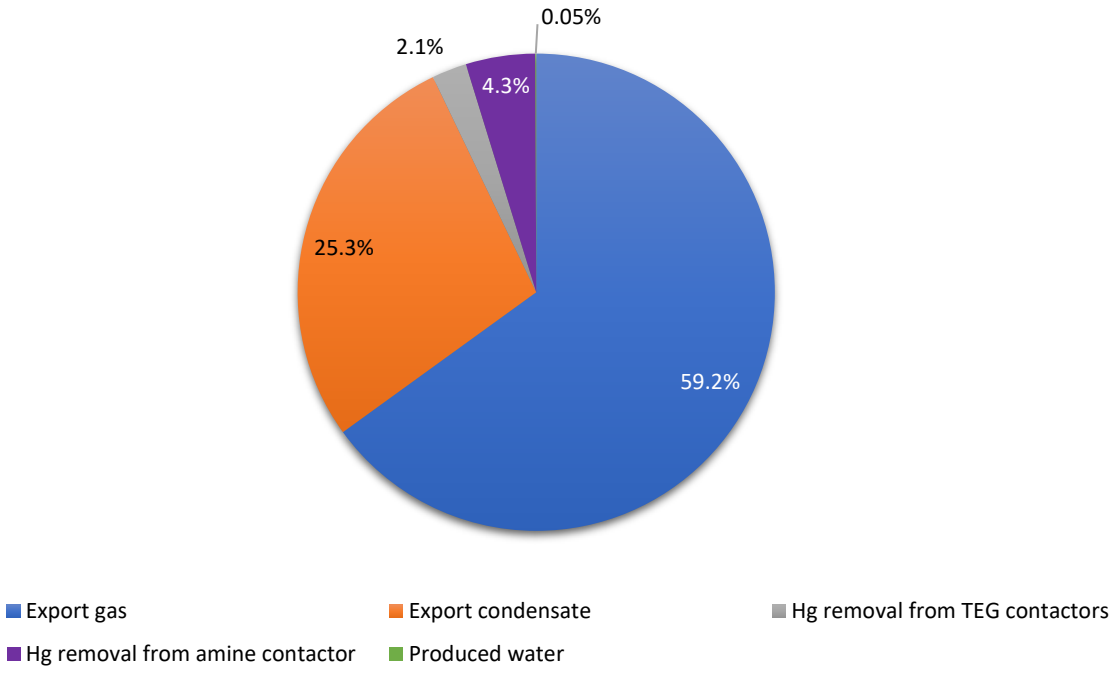

Figure 10.14. Elemental mercury distribution in plant outlets as % of total Hg^0 entering the plant. Calculations based on scenario 3 with UMR-PRU and assuming liquid phase reaction (K_{eq} from data by Robie et al. [127]).

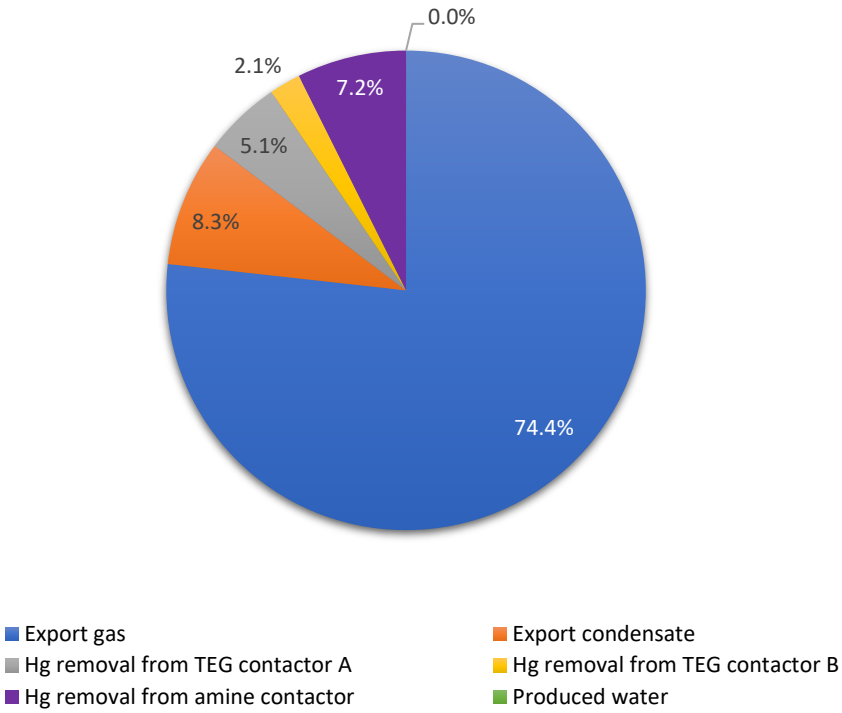

Figure 10.15. Elemental mercury distribution in plant outlets as % of THg exiting the plant. The distribution is estimated based on the field campaign measurements and actual process data (flowrates) (K_{eq} from data by Robie et al. [127]).

It is shown that both models yield similar Hg^0 distributions in all streams, except export condensate. More specifically, UMR-PRU predicts a higher distribution in export gas, which could be explained by the lower predicted Hg^0 to HgS conversions in all separators, which leads to more elemental mercury being present in all streams. In the no reaction case, it was also shown that UMR-PRU generally predicts more mercury in the liquid phase. In comparison with the distributions calculated from the measurements (Figure 10.15), both models seem to overpredict Hg^0 distribution in the export condensate and underpredict Hg^0 in the export gas.

10.4 Simulation of Hg distribution in TEG dehydration & regeneration process

10.4.1 Process description

As shown in PFD of the platform (Figure 10.16), the gases coming from the inlet separators and the condensate stabilization train are dehydrated in two parallel glycol contactors. The gases produced from Feed A inlet separators, the gases from the condensate stabilization train, and a portion of the gases from Feed B inlet separators are led to glycol contactor A. The rest amount of the Feed B gases is led to glycol contactor B.

After the gas has been dehydrated, the rich TEG is regenerated. The rich TEG passes through a flash separator to exhaust the majority of the diluted hydrocarbons. The vapor stream of

the separator is led to the flare, while the liquid product ("semi-lean" TEG) is preheated and fed to a distillation column to remove the water. The bottom product of the column is led to the top stage of a stripping column, in which stripping gas is fed at the bottom. The vapor product of the first column is used as stripping gas. The vapor product of the stripper is recycled to the first column, while the bottom product of the stripper (lean TEG) is recycled back to the glycol contactor, after being used for rich TEG pre-heating.

10.4.2 Mercury mass balance calculations

From the field campaign measurements, the actual flowrates during the field campaign, and the measured densities for lean and rich TEG, the mass balance of mercury in glycol contactor A (30-101) can be constructed, as shown in Table 10.14. It is observed that the inlet and outlet amount of Hg^0 in contactor A is almost the same. Taking into account the uncertainty of the measurements, it is deemed that the Hg^0 mass balance is satisfied.

Table 10.14. Estimated elemental mercury mass flowrates at glycol contactor A (30-101), based on field campaign measurements and actual process data (flowrates).

Stream	Flowrate	Density (kg/m³)	Hg^0 concentration	Hg^0 flowrate (g/d)
Wet gas	15.89 MSm^3/d	N/A	22.6 µg/Sm^3	359.1
Lean TEG	192 m^3/d	1124	1.7 µg/kg	0.4
			Total in	**359.5**
Dry gas	15.89 MSm^3/d	N/A	21.8 µg/Sm^3	346.4
Rich TEG	192 m^3/d	1124	28.4 µg/kg	6.1
			Total out	**352.5**

In glycol contactor B, mercury concentration in the rich TEG has not been measured, but it can be calculated from the material balance, since Hg^0 concentration in all inlets and in dry gas have been measured. The calculations presented in Table 10.15 show that 11.2 g Hg^0 must follow the rich TEG per day to satisfy the material balance. This flowrate translates to a concentration of 52 µg/kg in rich TEG.

Table 10.15. Estimated elemental mercury mass flowrates at glycol contactor B (30-201), based on field campaign measurements and actual process data (flowrates).

Stream	Flowrate (Sm^3/d)	Density (kg/m³)	Hg^0 concentration	Hg^0 flowrate (g/d)
Wet gas	18.09 MSm^3/d	N/A	1.95 µg/Sm^3	35.3
Lean TEG	192 m^3/d	1128	4.3 µg/kg	0.9
			Total in	**36.2**
Dry gas	18.09 MSm^3/d	N/A	1.38 µg/Sm^3	25.0
Rich TEG	192 m^3/d	1128	52.0[a] µg/kg	11.2[a]
			Total out	**36.2**

[a] *calculated value to satisfy the material balance*

10.4.3 Simulation of Hg distribution

To study mercury partitioning in the processes involved in TEG dehydration and regeneration, two simulations were implemented in UniSim Design R460.2 to cover both train A and B. The PFD as shown in Figure 10.16 is the same for both trains.

The composition of the gas that is led to the glycol contactor in each train was set according to field measurements. In the simulation, the gas was mixed with water until saturation. The purities of lean TEG entering the glycol contactors in train A and B were also set according to field measurements. Process conditions and stream flowrates (including TEG recirculation rate) were set according the actual process data.

For simulating the TEG regeneration process, the glycol flash drum and the 2-column setup with the overhead drum were maintained. However, during preliminary runs it was found that the overhead product from the distillation columns (30-112/212) could not be used as stripping gas at the stripping columns (30-113/213), since it was not sufficient for achieving the required lean TEG purity. Therefore, an independent stream of pure CH_4 was added to the bottom of the strippers, which served as stripping gas. The stripping gas flowrate was adjusted to achieve the known lean TEG purity (99.9% wt. in train A and 99.7% wt. in train B). The overhead product of distillation columns (30-112/212), as well as the lean TEG after regeneration were not recycled back to reduce simulation computational time and avoid convergence problems.

For studying mercury distribution in the TEG dehydration and regeneration processes, the concentration of Hg^0 in the wet gas and in lean TEG were specified in the simulation according to the field campaign measurements for soluble mercury. By fixing the amount of mercury at the process inlets, the results for the intermediate and outlet streams as calculated with the models were compared with the measurements.

In conjunction with the results for mercury distribution in the overall process, where it was found that the Hg^0 reaction with H_2S probably takes place in the liquid hydrocarbon phase and not in the vapor, no mercury reaction was considered, since the dehydration process involves gaseous hydrocarbons. The results regarding Hg^0 concentrations in train A and B are presented in Table 10.16. To verify that the simulation is representative of the real process, some process parameters, such as water content in dry gas, stripping gas rate etc. are presented in Table 10.17.

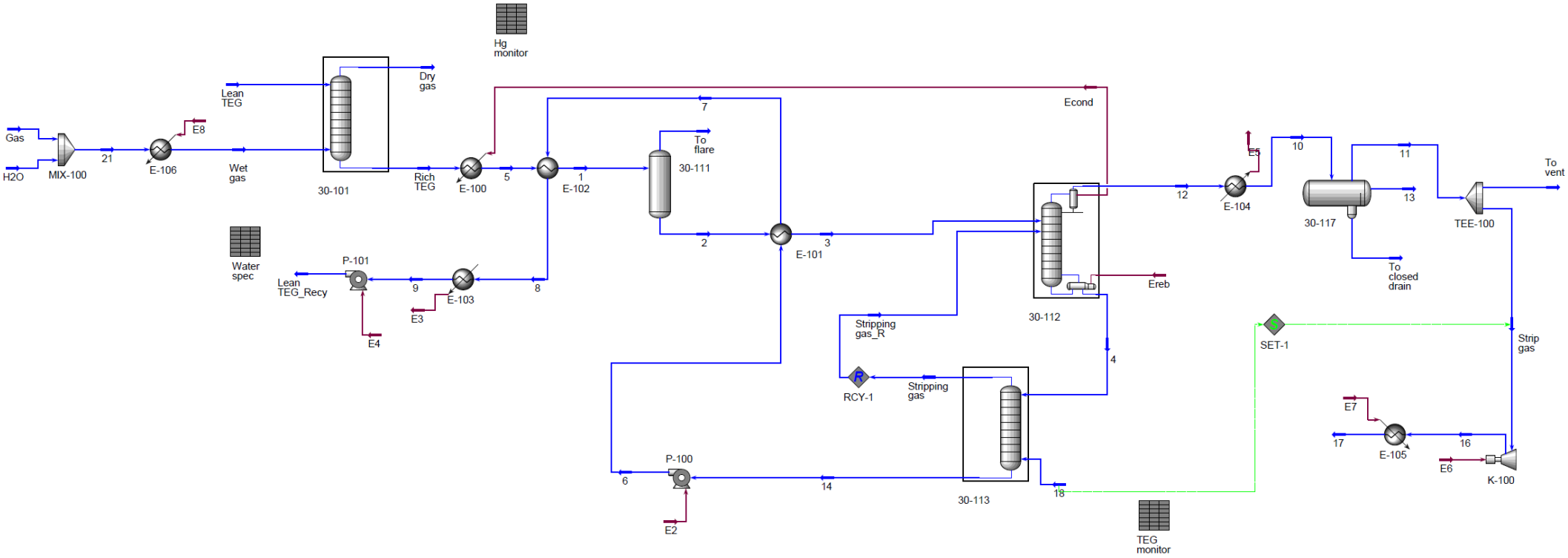

Figure 10.16. PFD of simplified TEG dehydration & regeneration unit (Train A) in UniSim.

Regarding train A, it is observed that both models yield a similar Hg^0 content in dry gas, which is very close to the measured value. However, SRK-Twu significantly underpredicts mercury concentration in rich TEG, while UMR-PRU predicts a value close to the measurement. At a first glance, in the glycol flash drum it is shown that UMR-PRU significantly overpredicts Hg^0 content both in the vapor product that is led to flare and in the semi-lean TEG, while SRK-Twu appears to agree more with the measurements. However, the Hg mass balance in the drum according to the measured concentrations is not satisfied, as presented in Table 10.18. It should be noted that the UMR-PRU simulation flowrates were used for the calculations when no actual process data were available.

Therefore, the results with UMR-PRU for train A are deemed to be the most accurate, while SRK-Twu underpredicts mercury concentration in rich and semi-lean TEG streams, and by extension in gases that are led to the vent or flare. It is also shown that the latter have very high Hg^0 concentrations, but due to their small flowrates the amount of mercury released to the environment is low.

Table 10.16. Hg^0 concentration in TEG dehydration and regeneration process streams as calculated with UMR-PRU and SRK-Twu.

			Train A			Train B		
Equipment	**Stream**	**Units**	**Measured (Hg^0)**	**UMR-PRU**	**SRK-Twu**	**Measured (Hg^0)**	**UMR-PRU**	**SRK-Twu**
Glycol contactor	Wet gas	µg/Sm³	22.6	22.6[a]	22.6[a]	1.95	1.95[a]	1.95[a]
	Lean TEG	µg/kg	1.7	1.7[a]	1.7[a]	4.3	4.3[a]	4.3[a]
	Dry gas	µg/Sm³	21.8	22.2	22.5	1.4	1.95	1.99
	Rich TEG	µg/kg	28.4	31.3	6.1	52.0[b]	4.0	0.7
Glycol flash drum	To flare	µg/Sm³	132.0	790.9	239.8	N/A	64.4	19.3
	Semi-lean TEG	µg/kg	8.7	25.5	5.9	N/A	3.7	0.7
Regen. column overhead drum	To vent	µg/Sm³	N/A	546.8	56.1	N/A	111.9	9.8
	To closed drain	µg/kg	N/A	2.1	0.1	N/A	0.4	0.01

[a] *value specified in the simulation*

[b] *calculated from mass balance*

Table 10.17. TEG dehydration and regeneration process parameters.

		Train A			Train B		
Description	**Units**	**Measured**	**UMR-PRU**	**SRK-Twu**	**Measured**	**UMR-PRU**	**SRK-Twu**
H_2O @ wet gas	ppm mol	N/A	1043	811.1	N/A	521.1	509.4
H_2O @ dry gas	ppm mol	30[a]	28.9	0.08	30[a]	9.8	0.05
Rich TEG purity	% wt.	N/A	91.3	94.5	N/A	93.9	96.0
Lean TEG purity	% wt.	99.9[b]	99.9	99.9	99.7[b]	99.7	99.7
Strip. gas rate	kmol/h	10[b]	15	41	3.6[b]	10	25.5

[a] *value specified in the simulation*

[b] *field data*

Table 10.18. Hg^0 mass balance in glycol flash drum (30-111) as calculated from field campaign measurements and UMR-PRU simulation flowrates.

Stream	Flowrate	Density (kg/m^3)	Hg^0 concentration	Hg^0 flowrate (g/d)
Inlet[a]	192 m^3/d	1124	28.4 μg/kg	6.1
Vapor	1515 Sm^3/d	N/A	132.0 μg/Sm^3	0.2
Liquid	196 m^3/d	959	8.7 μg/kg	1.7
			Total out	**1.9**

[a] *values specified in the simulation*

Regarding train B, UMR-PRU predicts that Hg^0 concentration in dry gas is the same as in wet gas, while SRK-Twu predicts a slight increase in the dry gas. Consequently, both models predict a lower Hg^0 concentration in rich TEG as compared to the expected value of 52 μg/kg, which was calculated from the mass balance. The results with UMR-PRU show a higher mercury concentration in rich TEG as compared to SRK-Twu, which also leads to higher Hg^0 content in streams involved in the regeneration part of the process. Similarly with train A, it is observed that vent and flare gases have an increased mercury concentration.

Finally, an examination of other process parameters shows that UMR-PRU yields a water content in dry gas, which is close to the normal values expected for the process. On the other hand, SRK-Twu yields an abnormally low water content in dry gas. In addition, UMR-PRU yields a stripping gas rate, which is close to the expected value, in contrast with SRK-Twu, which predicts a more than 4 times higher value. This could be explained by the limitations of cubic equations of state, such as SRK, which are encountered in polar mixtures. Conversely, UMR-PRU is capable of accurate calculations both in hydrocarbon and polar systems.

10.5 Mercury distribution in MEG regeneration process

10.5.1 Process description

MEG is injected in reservoir fluids to avoid hydrate formation. The rich MEG is separated from hydrocarbon fluids at the inlet separators and is subsequently regenerated. The rich MEG is heated and led to 2 parallel condensate/MEG separators to remove the diluted heavy hydrocarbons. The rich MEG streams are then mixed and pass through subsequent flash drums, in which the temperature is increased and the pressure is lowered to remove any remaining hydrocarbons. The semi-lean MEG is then split into 3 parallel trains, which involve MEG regeneration via vacuum distillation. The semi-lean MEG is fed at the bottom of the distillation columns, while a water stream is added at the top, which serves as a reflux to the column. The bottom product of the distillation columns is the lean MEG, while the top product is led to overhead drums, in which the water is recovered and recycled back to the columns. Finally, the vapor product of the overhead drum passes through a scrubber, which separates any remaining hydrocarbons from the water.

10.5.2 Simulation of Hg distribution

To study mercury partitioning in the MEG regeneration process, a simulation was implemented in UniSim Design R460.2. The PFD of the simulation is presented in Figure 10.17. The composition and flowrate of the fluids that are led to the inlet separators were retrieved from the simulation of the complete process (Section 10.3). MEG was also added to these streams to match the rich MEG purities according to field measurements. Process conditions were set according to actual process data.

For simulating the MEG regeneration process, the 3 parallel trains were merged into one to reduce complexity. To further reduce simulation computational time and avoid convergence problems, the water product of the distillation column overhead drum, as well as the lean MEG after regeneration were not recycled back. The reflux stream of the distillation column was assumed to be pure water, and its flowrate was adjusted to achieve the known lean MEG purity (91% wt. on average for the 3 trains).

For studying mercury distribution in the MEG regeneration process, the Hg^0 concentration at Feed B was specified in the simulation according to the scenarios studied in Section 10.3. The scenario involving mercury being present only in Feed A (scenario 1) was not studied, because only Feed B fluids are involved in MEG regeneration. It was also assumed that no reactions take place. By fixing the amount of mercury at the process inlets, the results for the intermediate and outlet streams as calculated with the models were compared with the measurements. The results of the simulations with SRK-Twu and UMR-PRU are presented in Table 10.19.

It is observed that both models yield similar results according to both scenarios. As expected, scenario 3 yields about half the concentrations of scenario 2, since the amount of mercury entering the process is also the half. Scenario 3 (mercury present in Feed A and B in equal amounts) yields an Hg^0 concentration in rich MEG which is closer to the measured value. This confirms the conclusions drawn in Section 10.3 that mercury is probably predominant in Feed A. Furthermore, all models and scenarios show that mercury concentration in lean MEG is negligible, which agrees with the findings of the field campaign.

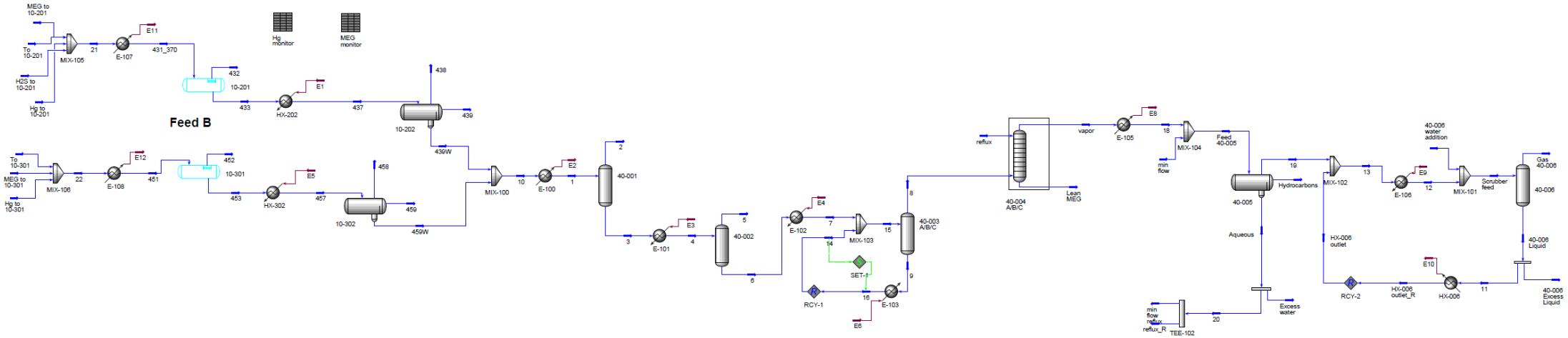

Figure 10.17. PFD of simplified MEG regeneration unit in UniSim.

Table 10.19. Hg^0 concentration in MEG regeneration process streams as calculated with SRK-Twu and UMR-PRU.

				SRK-Twu		UMR-PRU	
Tag	**Stream**	**Units**	**Measured (Hg^0)**	**Scenario 2**	**Scenario 3**	**Scenario 2**	**Scenario 3**
10-201	Feed B	ppb mol	N/A	3.30[a]	1.64[a]	3.30[a]	1.64[a]
10-202	To flare	µg/Sm^3	N/A	49.8	24.8	45.7	22.8
10-202	Rich MEG	µg/kg	0.6	5.5	2.7	4.8	2.4
10-202	Condensate	µg/kg	N/A	94.5	47.1	118.1	58.9
40-001	To flare	µg/Sm^3	N/A	51.6	25.8	46.6	23.3
40-002	To flare	µg/Sm^3	N/A	121.4	60.7	128.4	64.2
40-004 A/B/C	Vapor	µg/Sm^3	N/A	2.3	1.1	2.0	1.0
40-004 A/B/C	Lean MEG	µg/kg	< 0.1	8.1E-04	4.0E-04	4.7E-04	2.4E-04

[a] *value specified in the simulation*

10.6 Validation of the simulation

To understand how comparable are the results of the simulation of the whole plant with the field campaign measurements, it is important to verify that fluid compositions and flowrates in the simulation are representative of the real process.

10.6.1 Fluid compositions

Some process fluid samples were taken during the field campaign, which were analyzed through gas chromatography. The measured and calculated fluid compositions are presented in Figure 10.18 through Figure 10.21.

It is observed that the calculated fluid compositions are close to the measured values for the majority of fluids. The only exceptions are the inlet and outlet streams of the stabilizer tank (10-008), for which all models predict a higher C_{6+} fraction. Since mercury preferably partitions in the heavier hydrocarbons, this could explain why the calculated Hg concentration in the export condensate is higher than the measured value. On the other hand, all models predict more methane and a lower C2-C5 fraction in the vapor produced by the stabilizer tank.

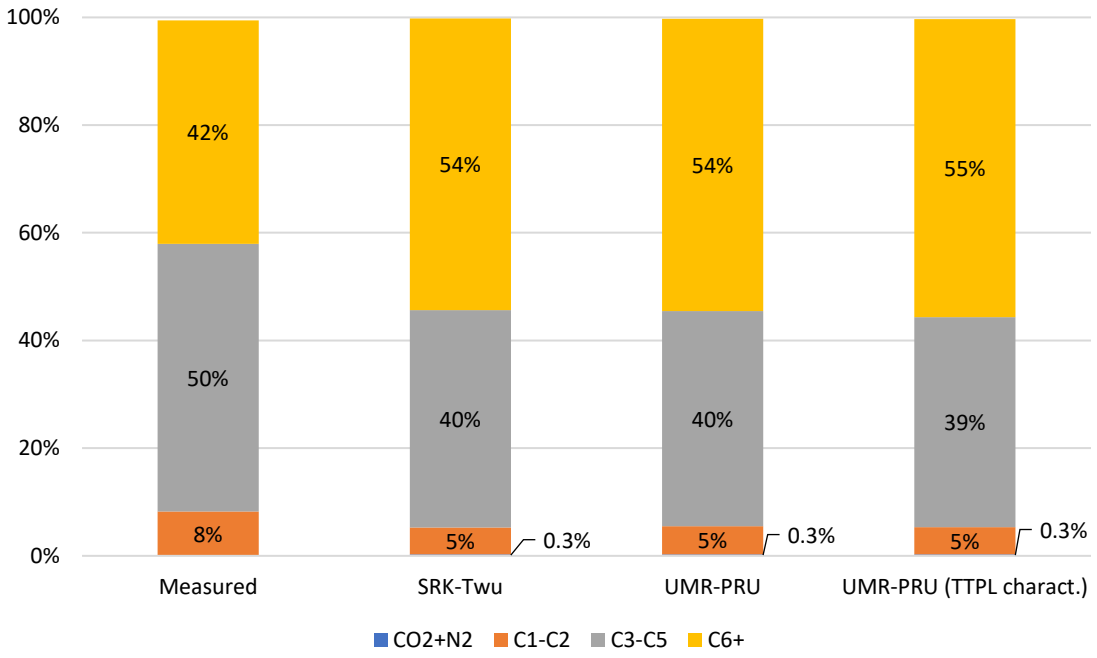

Figure 10.18. Measured and calculated composition of stabilizer (10-008) inlet.

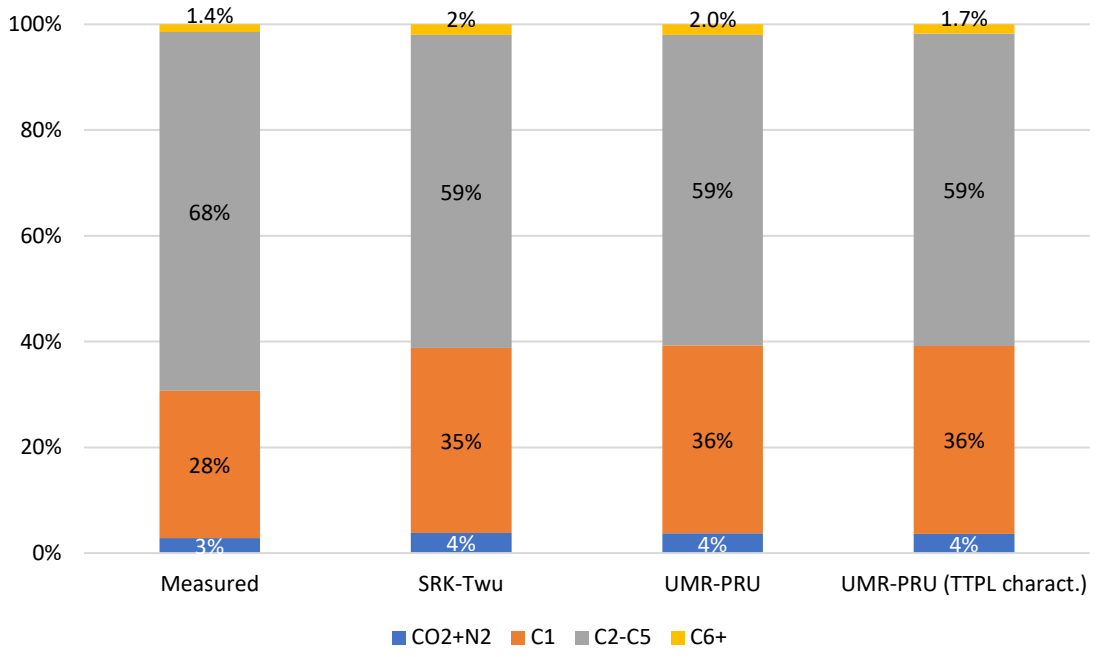

Figure 10.19. Measured and calculated composition of stabilizer (10-008) vapor outlet.

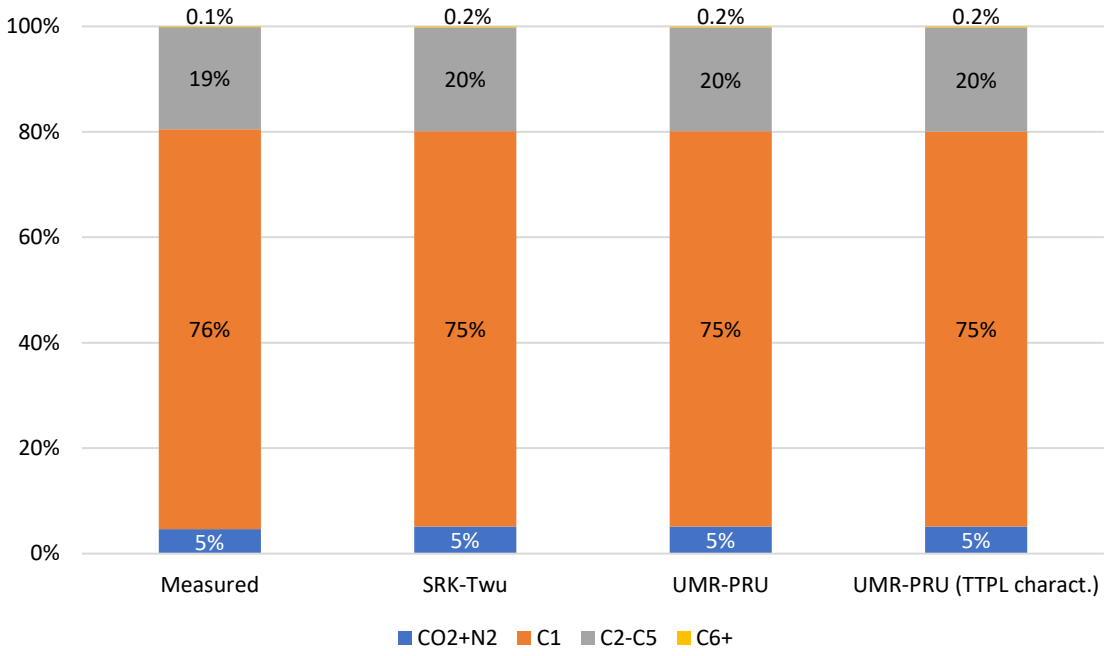

Figure 10.20. Measured and calculated composition of amine contactor (20-103) inlet.

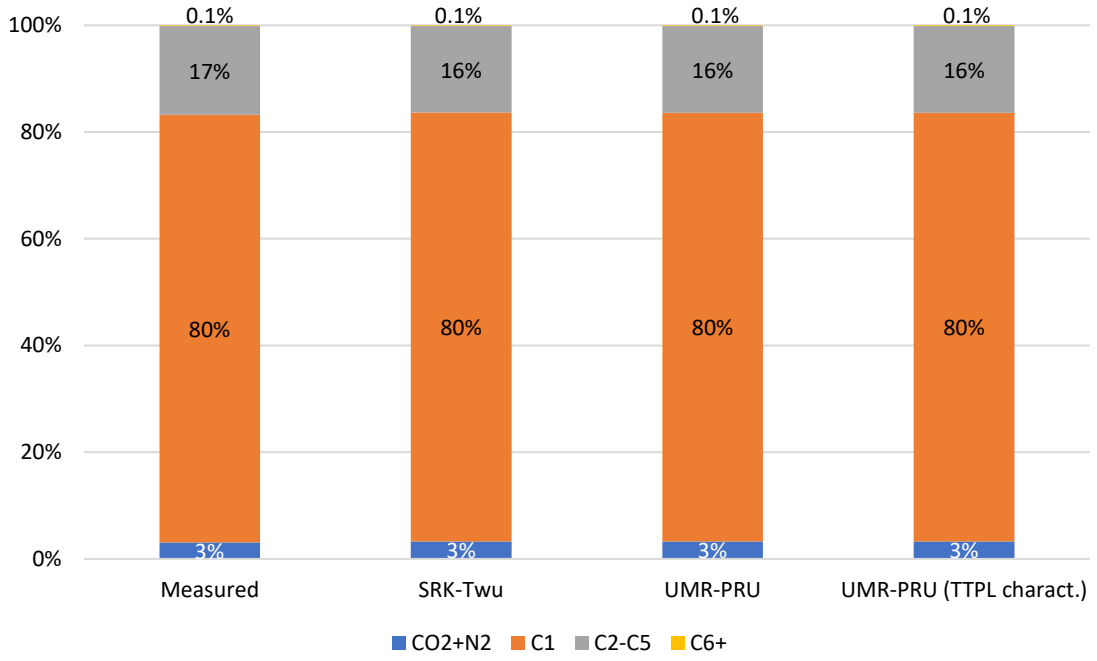

Figure 10.21. Measured and calculated composition of export gas.

10.6.2 Stream flowrates

The flowrates of gas, condensate and water streams as calculated with SRK-Twu and UMR-PRU are presented in Table 10.20 through Table 10.22. For comparison, the values from actual process data are included.

Table 10.20. Flowrates (MSm^3/d) of plant gas streams as calculated with SRK-Twu and UMR-PRU.

Tag	Description	Measured	SRK-Twu	UMR-PRU	UMR-PRU (TTPL charact.)
10-001	Test separator	1.18	0.93	0.93	0.94
10-101	Feed A inlet sep.	14.16	9.46	9.47	9.47
10-201	Feed B inlet sep.	12.70	11.53	11.51	11.52
10-301	Feed B inlet sep.	9.90	8.38	8.39	8.38
10-401	Feed A inlet sep.	0.53	0.51	0.51	0.51
10-003	2nd stage sep.	N/A	0.76	0.81	0.77
10-008	Stabilizer tank	0.013	0.059	0.063	0.057
20-101	Gas treat. scrubber	N/A	11.68	11.70	11.70
20-103	Amine contactor	11.54	11.63	11.65	11.65
30-101/201	Glycol contactor A/B	33.98	31.54	31.55	31.55
-	Export gas	33.48	31.53	31.53	31.54

Table 10.21. Flowrates (Sm^3/d) of plant condensate streams as calculated with SRK-Twu and UMR-PRU.

Tag	Description	Measured	SRK-Twu	UMR-PRU	UMR-PRU (TTPL charact.)
10-001	Test separator	559	653	655	617
10-101	Feed A inlet sep.	2716	2420	2393	2316
10-201	Feed B inlet sep.	1133	2246	2234	2175
10-301	Feed B inlet sep.	1038	1737	1669	1645
10-401	Feed A inlet sep.	1367	987	917	940
10-003	2nd stage sep.	N/A	7110	7100	6746
10-008	Stabilizer tank	6601	6937	6941	6602
20-101	Gas treat. scrubber	N/A	1338	1453	1192
-	Export condensate	5821	5720	5851	5587

Table 10.22. Flowrates (Sm^3/d) of plant water streams as calculated with SRK-Twu and UMR-PRU.

Tag	Description	Measured	SRK-Twu	UMR-PRU	UMR-PRU (TTPL charact.)
10-001	Test separator	133	50	59	59
10-101	Feed A inlet sep.	N/A	376	442	442
10-201	Feed B inlet sep.	N/A	123	145	145
10-301	Feed B inlet sep.	N/A	181	215	215
10-401	Feed A inlet sep.	N/A	92	109	109
10-003	2nd stage sep.	N/A	322	389	388
20-101	Gas treat. scrubber	N/A	30	45	44

It is shown that all models yield similar results, which are also close to the actual process data. The largest difference between model predictions and process data is observed in the flowrate of Feed A inlet separator (10-101) gas product, and in Feed B inlet separator (10-201) condensate. In addition, all models predict 50% less flowrate of the water at test separator (10-001). Nevertheless, the predicted flowrates of export gas and condensate are very similar with the measured values. Therefore, it is concluded that the simulation is representative of the real process.

10.6.3 H_2S and CO_2 in process gases

The concentrations of H_2S and CO_2 in some streams were also measured during the field campaign. It is of interest to see how the models predict their distribution, since H_2S can react with Hg, and the concentration of CO_2 provides an idea of the composition of the actual fluid measured, as compared with the fluid in the simulation.

The concentration of H_2S at the inlets of the test separator (10-001), Feed A inlet separator (10-101) and Feed B inlet separator (10-201) were set accordingly, to match the measured values in the vapor outlet of the test separator, in the vapor outlet of the gas treatment scrubber (20-101), and Feed B gases, respectively. The results with UMR-PRU and SRK-Twu are shown in Table 10.23 together with the measured values. It is observed that both models can accurately predict the concentrations of H_2S and CO_2 in the examined gases.

Table 10.23. H_2S and CO_2 concentrations in selected plant streams as calculated with UMR-PRU and SRK-Twu.

Component	Units	Tag/Description	Measured	SRK-Twu	UMR-PRU	UMR-PRU (TTPL charact.)
H_2S	µL/L	Gas treatment scrubber (20-101)	**11.6**	12.1	12.0	12.0
		Test separator (10-001)	**19.8**	19.8[a]	19.8[a]	19.8[a]
		Feed A gases	**10.9**	10.9[a]	10.9[a]	10.9[a]
		Feed B gases	**4.0**	4.0[a]	4.0[a]	4.0[a]
CO_2	% v/v	Gas treatment scrubber (20-101)	**4.0**	4.6	4.6	4.5
		Test separator (10-001)	**5.0**	5.3	5.3	5.3
		Feed B gases	**1.8**	1.8	1.8	1.8

[a] *value specified in the simulation*

10.7 Conclusions

In this chapter, the UMR-PRU model has been applied for the study of mercury distribution in an existing offshore natural gas processing platform. For comparison the SRK-Twu model was also employed, and model results were compared with field measurements regarding mercury concentration in selected streams. For the purposes of this study, simplified version of the process was implemented in UniSim Design R460.2 and the distribution of mercury in the various streams was examined. The effect of a possible reaction between mercury and H_2S was also studied. Different scenarios were considered, based on the presumed amount of mercury in the plant feeds according to mass balance calculations. Mercury partitioning in the TEG dehydration & regeneration process, as well as in MEG regeneration was examined in separate simulations.

The results for mercury distribution in the overall process can be summarized as follows:

<u>Without reaction</u>

- Both SRK-Twu and UMR-PRU yielded satisfactory results for mercury concentration in process gases, including export gas.
- Both models showed a tendency for overpredicting mercury concentration in condensates, which led to a higher Hg distribution in export condensate, as compared to the measurements.
- Both models confirmed the field campaign observations that Hg^0 concentration in water streams is very low. However, SRK-Twu generally predicts a higher mercury content in water as compared to UMR-PRU.

- Mercury distribution in flash separators was similar with both models. However, in the test separator (10-001) model predictions varied significantly from the distributions indicated by the field campaign measurements.
- High deviations between model predictions and measurements were observed in stabilizer tank (10-008) inlet and outlet streams. There is an increased uncertainty in these measurements, because of the presence of solid particles in liquid samples, so they were not deemed suitable for evaluating the models.
- The different scenarios that were studied based on which feeds carry mercury into the plant yielded similar results for Hg^0 concentration in export gas, condensate and stabilizer tank (10-008) streams. The main differences were found in the gases produced by Feed A and Feed B inlet separators, and in the inlet of the amine contactor (20-103).
- The scenarios showed that mercury is probably predominant in Feed A. The Hg distribution among Feed A and B that best matched the measurements at inlet separator gas products was about 80%-20%, respectively.
- According to the field measurements, the estimated Hg^0 distribution in export gas and export condensate is 77%-9%. The intermediate scenario of mercury being present both in feeds in equal amounts yielded an Hg^0 distribution of 71%-21% among export gas and export condensate with SRK-Twu and 65%-27% with UMR-PRU, respectively. Therefore, both models yield a similar Hg^0 distribution in export gas, which is not far from the one estimated from the campaign measurements. However, the models diverge significantly from the expected distribution in the export condensate.
- An investigation on the effect of fluid characterization method on mercury distribution was made by coupling UMR-PRU with the TTPL characterization method. It was observed that this combination yields results that are closer to the measured values and more similar with SRK-Twu. The predicted Hg^0 distribution in export gas and export condensate was 67%-25%.

<u>With reaction</u>

- The effect of a possible reaction between mercury and H_2S was studied, by assuming that it reaches equilibrium. Initially, the reaction was considered to take place in the gas phase, but the yielded Hg^0 concentrations in the gas streams were unrealistically low, when compared to the field measurements. Therefore, the reaction was assumed to take place in the liquid hydrocarbon phase.
- When the liquid phase reaction was considered, the resulting Hg^0 concentrations in gas and condensate streams was lower as compared to the no reaction case. This is expected, since an amount of elemental mercury is converted to solid HgS. The predicted Hg^0 concentrations in condensates was closer to the experimental values.
- The distribution of Hg^0 among export gas and export condensate with liquid phase reaction was found to be 62%-18% with SRK-Twu and 59%-25% with UMR-PRU,

respectively. Therefore, the calculated distributions in the export condensate are closer to the values calculated from the measurements, but deviate further in the export gas.

- UMR-PRU yields a lower conversion of Hg^0 to HgS than SRK-Twu. The results with UMR-PRU indicated that 50.4 g of HgS are produced per day, while SRK-Twu predicts 70.9 g/d. From the difference between total and soluble mercury measurements, it is estimated that 16.6 g HgS are produced per day. Therefore, UMR-PRU is closer to the expected value.
- It is unknown whether the reaction reaches equilibrium or is kinetically controlled during actual process conditions. Considering the results, it is possible that the latter is true. By comparing the results of UMR-PRU with the produced HgS amount as calculated from the measurements, it is deduced that the actual conversion is about 1/3 of the equilibrium conversion.
- The effect of different reaction equilibrium constants was also examined, and it was concluded that the K_{eq} from Robie et al. [127] is the best compromise between predicted Hg^0 concentrations in streams and produced solid HgS amount.

Regarding mercury distribution in TEG dehydration and regeneration process, the following conclusions can be drawn:

- In train A, both models yield satisfactory predictions for the Hg^0 content in dry gas, but SRK-Twu significantly underpredicts mercury concentration in rich TEG.
- Both models predict a very high Hg^0 concentration in the vapor product of the glycol flash drums, which are led to the vent, in both trains.
- In train B, both models predict a lower Hg^0 concentration in rich TEG as compared to the expected value of 52 μg/kg, which was calculated from the mass balance. The results with UMR-PRU show a higher mercury concentration in rich TEG as compared to SRK-Twu, which also leads to higher Hg^0 content in streams involved in the regeneration part of the process.
- UMR-PRU yields a water content in dry gas and a stripping gas rate, which are close to the normal values expected for the process. On the other hand, SRK-Twu yields an abnormally low water content in dry gas and a high stripping gas rate.
- Overall, UMR-PRU is deemed to be the most accurate, since it correctly predicts Hg^0 partitioning in the process and yields reasonable values for other important process parameters.

Mercury distribution in the MEG regeneration process was also studied based on the scenarios examined for the overall process, and the following observations were made:

- Scenario 3, according to which mercury is present in both feeds in equal amounts, yields an Hg^0 concentration in rich MEG which is closer to the measured value.
- All models and scenarios show that mercury concentration in lean MEG is negligible, which agrees with the findings of the field campaign.

An examination of other process parameters, such as fluid compositions and flowrates was also made to verify that simulation results are representative of the real process. A comparison between measured fluid compositions and model calculations in the simplified simulation showed that they are very similar in the majority of cases, except the inlet and outlet streams of stabilizer tank (10-008). Stream flowrates as calculated in the simplified simulation were also close to actual process data. The concentrations of CO_2 and H_2S, which were also measured in some process gases, were accurately predicted by the models. All of the above indicate that the simplified simulation is representative of the complete process.

To conclude, both UMR-PRU and SRK-Twu can predict fairly good the distribution of mercury in a gas processing plant, yielding accurate results for Hg^0 in gases, and satisfactory results for Hg^0 in condensates. If the liquid phase reaction between mercury and H_2S is also considered, UMR-PRU predicts an Hg^0 to HgS conversion which is closer to the expected value according to the field measurements. For studying mercury behavior in processes that involve polar compounds, such as TEG dehydration and MEG regeneration, UMR-PRU is the recommended model, since it yields the best results and is able to correctly describe all process parameters.

11. Phase and chemical equilibrium in systems involving non-reactive and reactive azeotropes

11.1 Introduction

In this chapter, the simultaneous chemical and phase equilibrium (CPE) algorithm developed in Section 5.2 is validated by performing calculations in complex systems involving non-reactive and reactive azeotropes, and results are compared with experimental data found in the literature.

Simultaneous chemical and phase equilibrium (CPE) calculations find application in important industrial processes, such as reactive distillation, reactive extraction, heterogeneous organic synthesis, and biofuel production. Such calculations can prove to be quite challenging in systems that involve multiple reactions taking place in multiple phases. To complicate things further, some systems can exhibit singularities, such as azeotropes or even reactive azeotropes [130]. Two common examples of such systems are methyl tert-butyl ether (MTBE) synthesis through isobutene etherification with methanol [131, 132], and isopropyl acetate synthesis via the esterification of acetic acid with isopropanol [133].

Reactive azeotropes have been studied both from a theoretical and experimental point of view since the 1980's. By definition, a system is azeotropic when its temperature and composition remain constant during isobaric boiling. In systems where reactions take place, a reactive azeotrope occurs when the rate of vaporization (or condensation) of the components is equal to the rate of the reaction. However, this does not necessarily mean that the vapor and liquid compositions are equal. Therefore, the common feature between conventional azeotropes and reactive azeotropes is that they involve a boiling state of constant composition and temperature. Doherty and his co-workers [130-137] have developed a convenient mathematical formulation of the problem by introducing transformed compositions, which at the reactive azeotrope are equal among phases. Reactive azeotropes impose restrictions on feasible product compositions during azeotropic distillation, similarly with azeotropes in conventional distillation.

In esterification and etherification reactions, where azeotropes are also involved, reactive distillation is an appealing choice for process design. Combining the chemical reaction with product separation in a single unit has several advantages: the reaction is led towards product formation, since products are constantly removed from the mixture, the formed azeotropes can be "broken" because of the reaction, and CAPEX and OPEX costs are reduced due to the requirement of fewer equipment, recycle streams etc. In the case of exothermic reactions, energy requirements are also reduced, since the heat released by the reaction is used to evaporate the liquid [138].

Nevertheless, reactive distillation is difficult to model due to the complexity of the phenomena that it entails. In order to design, operate and optimize such processes from an

equilibrium-based point of view, a robust algorithm for solving the simultaneous chemical and phase equilibria is required, coupled with an accurate thermodynamic model for describing system non-ideality. The thermodynamic modelling of the systems involved in the aforementioned esterification and etherification processes can be quite challenging due to the presence of polar and associating compounds. In addition, the models must be able to reliably predict any azeotropes that can be formed.

A comprehensive review of equilibrium data for esterification systems can be found in the paper by Toikka et al. [139]. MTBE synthesis has been extensively studied throughout the years [140-146] due to its wide use as an oxygenate fuel additive. Both systems involve polar and associating components, which render their thermodynamic modelling rather challenging, even in the absence of chemical reaction. For describing mixture non-ideality in these systems, usually activity coefficient models, such as Wilson [57], NRTL [58], UNIQUAC [59] and UNIFAC [60] are employed. In the case of acetic acid esterification, the Hayden-O'Connell second virial coefficient correlation [45] is often used in order to describe vapor phase non-ideality due to the dimerization of acetic acid.

In the context of this work, the performance of the developed CPE algorithm coupled with the aforementioned models as well as with UMR-PRU is examined. In the case of MTBE synthesis, the effect of the equilibrium constant on the CPE results is also studied. Although simultaneous chemical and phase equilibria calculations have been already addressed by other authors in the past, the field of application studied in the present paper, i.e. calculations involving reactive and non-reactive azeotropes with predictive thermodynamic models, has been little studied in the literature.

11.2 Thermodynamic modelling

The thermodynamic models employed in this chapter are the activity coefficient models UNIQUAC [59] and UNIFAC [60], as well as the EoS/G^E model UMR-PRU. All models have been extensively presented in Chapter 6, so only the modifications for the systems examined in this chapter are discussed here.

The Mathias-Copeman (MC) [50] parameters employed by UMR-PRU for polar components are presented in Appendix B. For isopropyl acetate no MC parameters were available in the literature, so they were determined by fitting pure component vapor pressure data in the temperature range 199.75 – 532 K. For this purpose, 30 pseudo-experimental data points were generated from the DIPPR database [85]. During the fitting procedure it was ensured that the MC parameters maintain alpha function consistency according to the criteria by Le Guennec et al. [55, 56]. The average absolute relative deviation (AARD) in vapor pressure was 1.26%. All other necessary pure component properties, i.e. critical temperatures, pressures and acentric factors, were retrieved from the DIPPR data compilation [85].

Two sources of interaction parameters were used for UMR-PRU between components involved in this chapter: a) UNIFAC tables [60] and b) UNIQUAC parameters. In the first case the model is referred to as UMR-UNIFAC, and in the second case as UMR-UNIQUAC.

For the UNIQUAC activity coefficient model, the binary interaction parameters were retrieved from Aspen Plus v8.8 (Appendix B). In cases where no parameters were available in Aspen Plus or the phase equilibrium results were deemed unsatisfactory, new parameters were fitted to phase equilibrium data (Appendix C).

When UNIFAC or UNIQUAC models were employed, vapor phase was considered ideal due to the low pressures involved, except from the esterification system, for which the Hayden-O'Connell method [45] was used. This was necessary in order to account for the dimerization of acetic acid in the vapor phase. The required vapor pressures of the components were calculated with an extended Antoine equation of the form:

$$lnP^s = a + \frac{b}{t} + clnt + dt^e \qquad \text{Eq. 11.1}$$

where P^s the vapor pressure in bar and t the temperature in °C. Parameters a through e in Eq. 11.1 were retrieved from Aspen Plus v8.8 (Appendix B). An exception was made for isobutene, for which parameter a of Eq. 11.1 was refitted to experimental data [147] in the range 135 – 415 K while keeping parameters b to e constant. This was deemed necessary because with the previous a parameter the normal boiling point of isobutene was underestimated and lied very close to the temperature at which the azeotrope between isobutene and methanol is formed, which prevented the activity coefficient models from predicting its presence. The resulting AARD in vapor pressure was 1.35%.

11.3 Cyclohexane synthesis

Initially, a relatively simple 2-phase system with one reaction is initially studied, and results are compared with those presented by other authors [42, 148]. This system involves the hydrogenation of benzene for the production of cyclohexane:

$$C_6H_6 + 3H_2 \Leftrightarrow C_6H_{12} \qquad \text{Eq. 11.2}$$

In accordance with other authors, the Peng-Robinson EoS without binary interaction parameters (k_{ij}) is employed for describing system non-ideality. The equilibrium constant of the reaction (K_{eq}) is calculated via the Gibbs energies of formation of the components, which are obtained from George et al. [149]. The results at 500 K and 30 atm are presented in Table 11.1. The minor differences with the results by Tsanas et al. [42] may be attributed to different pure component critical properties, while the differences with Burgos-Solórzano et al. [148] are probably due to the different sources for the chemical equilibrium constant. Therefore, it is concluded that the algorithm has been successfully implemented.

Table 11.1. CPE results in mole fractions for the cyclohexane synthesis system at 500 K and 30 atm with Peng-Robinson EoS (k_{ij} = 0, K_{eq} = 184.93).

		This work		Tsanas et al. [42]		Burgos-Solórzano et al. [148]	
Component	**Feed**	**Vapor**	**Liquid**	**Vapor**	**Liquid**	**Vapor**	**Liquid**
Benzene	0.247	4.86E-06	5.87E-06	4.45E-06	5.43E-06	4.00E-06	4.92E-06
Hydrogen	0.753	0.231	0.0196	0.238	0.0204	0.249	0.0147
Cyclohexane	0	0.769	0.980	0.762	0.980	0.751	0.985
Amount (mol)	4.05	0.133	0.916	0.132	0.918	0.148	0.902
Phase fraction		0.127	0.873	0.125	0.875	0.141	0.859

11.4 MTBE synthesis

Oxygenate fuel additives like alcohols and ethers have been extensively used since the phasing-out of lead compounds for increasing the octane number of gasoline. In contrast to alcohols, fuel ethers such as MTBE have the advantages of reducing car exhaust emissions of toxic substances (CO, volatile organic compounds, particulate matter), having lower vapor pressure, being less soluble in water, and having higher energy density [150]. MTBE is produced by the reaction of isobutene with methanol:

$$C_4H_8\ (1) + CH_3OH\ (2) \Leftrightarrow C_5H_{12}O\ (3) \qquad \text{Eq. 11.3}$$

In practice, C_4-fractions that contain isobutene are used as feedstock, which originate from refinery processes, such as steam/fluid catalytic cracking and isomerization [150]. For modelling purposes, these fractions are often represented by the inclusion of n-butane as an inert in the system. This mixture exhibits three binary azeotropes between methanol/MTBE, methanol/isobutene and methanol/n-butane.

In order to describe the phase equilibrium in the MTBE synthesis system, the UNIQUAC, UNIFAC, UMR-UNIQUAC and UMR-UNIFAC thermodynamic models are employed. The performance of the models is initially examined in the binary mixtures by performing vapor-liquid equilibrium (VLE) calculations, and the results are presented in Table 11.2.

Table 11.2. VLE results for binary and ternary mixtures involved in MTBE synthesis.

System			UNIQUAC		UNIFAC		UMR-UNIQUAC		UMR-UNIFAC	
	Ref.	ND[a]	AARDP%[b]	AADy[c]	AARDP%	AADy	AARDP%	AADy	AARDP%	AADy
MTBE/Methanol	[151]	33	0.5	0.30	8.1	4.04	6.9	3.20	8.3	3.85
MTBE/i-butene	[152]	16	3.4	1.90	5.1	2.23	2.1	0.60	3.2	0.70
MTBE/n-butane	[153]	19	3.0	-	7.4	-	1.3	-	4.6	-
MeOH/i-butene	[154]	11	2.3	0.40	5.0	0.60	6.6	1.00	8.0	1.30
MeOH/n-butane	[154, 155]	34	6.4	1.50	6.2	2.59	7.5	2.20	12.4	2.40
i-butene/n-butane	[156]	12	0.1	-	1.3	-	0.2	-	1.6	-
	Overall	**125**	**3.0**	**1.02**	**6.2**	**2.80**	**4.9**	**2.14**	**7.5**	**2.49**
MTBE/Methanol/i-butene	[157]	19	0.7	-	1.7	-	1.7	-	0.6	-

[a] ND: number of experimental data points

[b] $AARDP\% = 100/ND \sum_{i=1}^{ND} \left|P_i^{exp} - P_i^{calc}\right| / P_i^{exp}$, where P is the bubble point pressure

[c] $AADy = 100/ND \sum_{i=1}^{ND} \left|y_i^{exp} - y_i^{calc}\right|$, where y is the mole fraction of any component in the vapor phase

The results indicate that all models perform adequately, with the minimum and maximum overall deviation in bubble point pressure being 3% and 7.5% with UNIQUAC and UMR-UNIFAC, respectively. It should be noted that the results with UNIFAC, UMR-UNIQUAC and UMR-UNIFAC are pure predictions. It is also shown that existing UNIQUAC or UNIFAC parameters can be employed directly by the UMR-PRU model, without great loss in accuracy.

The models are further tested in the VLE of the ternary mixture between isobutene, methanol and MTBE without reaction. The experimental data by Vetere et al. [157] concerning vapor-liquid equilibrium at temperatures from 333.15 to 353.15 K are used as benchmark. The results are included in Table 11.2. It is observed that all models are capable of accurate bubble point pressure prediction, with the maximum deviation being below 2%. Notably, UMR-UNIFAC yields the lowest AARDP%, even though it has the highest overall deviation in the pertinent binary mixtures.

Having ensured that all models can accurately describe the phase equilibria involved in the MTBE synthesis system, the simultaneous chemical and phase equilibria are examined. A multitude of equilibrium constants of the reaction can be found in the literature [140-143, 146, 158-160] depending on temperature and the phase in which it occurs. In this work, both cases of vapor and liquid phase reaction are studied, with three different equilibrium constants in each case: two from the literature and the other one calculated from the van't Hoff equation with temperature dependent reaction enthalpy. For the vapor phase reaction, the Gibbs energies of formation of the components are obtained from Tejero et al. [160], and enthalpies of formation and heat capacities are retrieved from Lísal et al. [159]. For the liquid phase reaction, all properties are taken from Badia et al. [146]. The resulting expressions for K_{eq} are of the form:

$$K_{eq} = \exp\left[A_0 + \frac{A_1}{T} + A_2\, ln(T) + A_3 T + A_4 T^2 + A_5 T^3\right] \qquad \text{Eq. 11.4}$$

where T is the temperature in K and A_0 through A_5 parameters presented in Table 11.3.

Table 11.3. Parameters used in Eq. 11.4 for the calculation of the equilibrium constant of the MTBE synthesis reaction in the vapor and liquid phase.

Parameter	Vapor phase	Liquid phase
A_0	-11.839	1145.292
A_1	7649.331	-14727.568
A_2	-1.620	-232.778
A_3	1.339E-03	1.065
A_4	3.343E-06	1.077E-03
A_5	-3.076E-09	5.327E-07

Model results are compared with molecular simulation data by Lísal et al. [159] regarding vapor phase MTBE synthesis and experimental data by Izquierdo et al. [143] regarding liquid phase MTBE synthesis. The deviations of the examined models according to the selected K_{eq} are presented in Table 11.4 and Table 11.5. It is shown that all the examined equilibrium constants lead to similar CPE results.

Table 11.4. CPE results for vapor phase MTBE synthesis: deviations from molecular simulation data by Lísal et al. [159] (5 data points).

Model	K_{eq} source					
	Tejero et al. [160]		**Lísal et al.** [159]		**Eq. 11.4**	
	AADx[a]	**AADy**	**AADx**	**AADy**	**AADx**	**AADy**
UNIQUAC	5.44	5.71	4.06	4.63	3.96	4.62
UNIFAC	1.79	3.36	1.54	2.42	1.60	2.26
UMR-UNIQUAC	2.32	2.38	2.05	1.55	2.18	1.47
UMR-UNIFAC	2.23	2.08	2.22	1.30	2.36	1.23

[a] AADz = $100 \cdot \sum_{i=1}^{NC}\sum_{j=1}^{ND}\left|z_{ij}^{exp} - z_{ij}^{calc}\right| / (ND \cdot NC)$, where NC is the number of components in the mixture, ND is the number of experimental data points, and z is the liquid (x) or vapor (y) mole fraction

Table 11.5. CPE results for liquid phase MTBE synthesis: deviations (AADx[a]) from experimental data by Izquierdo et al.[143] (17 data points).

Model	K_{eq} source		
	Colombo et al. [140]	**Rehfinger et al.** [141]	**Eq. 11.4**
UNIQUAC	5.09	4.88	4.97
UNIFAC	5.26	5.00	5.16
UMR-UNIQUAC	5.17	4.97	5.05
UMR-UNIFAC	5.18	4.98	5.06

[a] AADx = $100 \cdot \sum_{i=1}^{NC}\sum_{j=1}^{ND}\left|x_{ij}^{exp} - x_{ij}^{calc}\right| / (ND \cdot NC)$, where NC is the number of components in the mixture, ND is the number of experimental data points, and x is the liquid mole fraction

Following the formulation by Ung and Doherty [135], the transformed compositions for the studied system can be calculated by selecting MTBE as a reference component:

$$X_1 = \frac{x_1 + x_3}{1 + x_3} \qquad \text{Eq. 11.5}$$

$$X_2 = \frac{x_2 + x_3}{1 + x_3} \qquad \text{Eq. 11.6}$$

In the case where n-butane is also included in the system as a fourth component, its transformed composition is calculated from:

$$X_4 = \frac{x_4}{1 + x_3} \qquad \text{Eq. 11.7}$$

This reformulation is convenient, because it reduces the dimensions of the system. For example, in the absence of inert n-butane, the ternary system (Eq. 11.3) can be represented by two transformed compositions that sum to unity. It should be noted that, by definition, at the reactive azeotrope X=Y for all components. In Figure 11.1 the equilibrium curves for isobutene are plotted in transformed compositions at 5 bar as calculated with UMR-UNIQUAC together with the molecular simulation data by Lísal et al. [159]. For fair comparison, the equilibrium constant is obtained from the same source.

It is observed that there is very good agreement between the molecular simulation data and the predictions by UMR-UNIQUAC. Also, as Ung and Doherty [131] have observed, a “pseudo-reactive azeotrope” is identified, which appears at an intermediate temperature between the boiling points of isobutene and methanol. According to UMR-UNIQUAC this temperature is 366.8 K. This point is characterized as a “pseudo-reactive azeotrope” because the transformed compositions in the vapor and liquid phase are not equal, as can be seen in Figure 11.2, but the X-Y curves approach very closely to the X = Y diagonal. Thus, the distillation beyond this point becomes practically unfeasible.

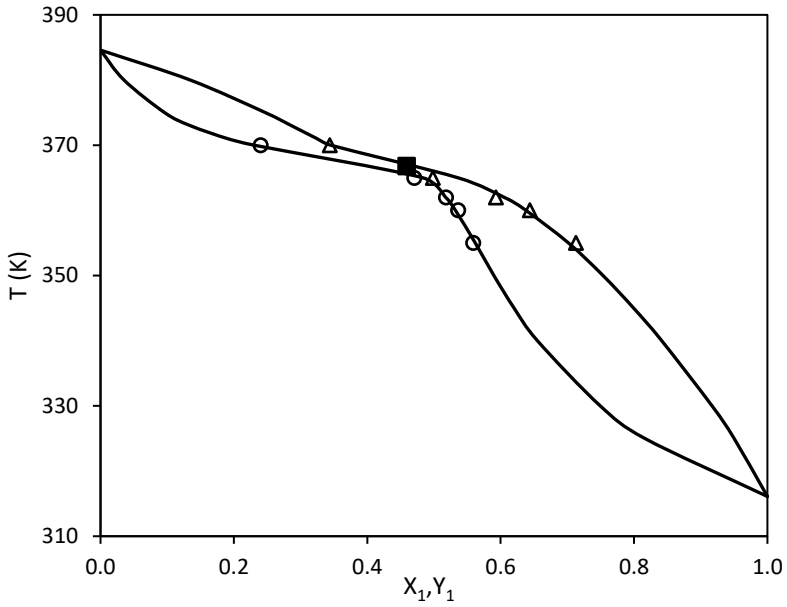

Figure 11.1. T-X-Y diagram for isobutene in MTBE synthesis system at 5 bar together with molecular simulation data points from Lísal et al. [159]. (O): transformed mole fractions in liquid phase; (△): transformed mole fractions in vapor phase; (■): pseudo-reactive azeotrope; solid lines: UMR-UNIQUAC predictions. K_{eq} from Lísal et al. [159].

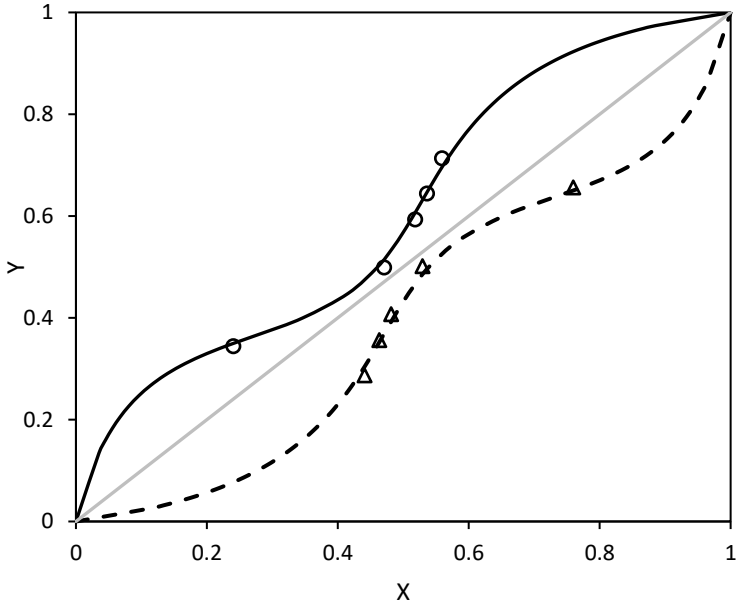

Figure 11.2. X-Y diagram for isobutene and methanol in MTBE synthesis system at 5 bar together with molecular simulation data points from Lísal et al. [159]. (O): transformed mole fractions of methanol; (△): transformed mole fractions of isobutene; solid line: UMR-UNIQUAC predictions for isobutene; dashed line: UMR-UNIQUAC predictions for methanol. K_{eq} from Lísal et al. [159].

When n-butane is included in the system as an inert component, the dimension of the solution space is increased by one. Separation feasibility of the quaternary mixture through reactive distillation can be examined by plotting residue curve maps. By using transformed compositions, these take the form of triangular charts. In Figure 11.3 and Figure 11.4 the residue curve maps of the system are plotted in transformed compositions at 1 and 7 atm by employing UMR-UNIFAC and the equilibrium constant by Tejero et al. [160].

The diagrams presented here are very similar to those by Ung and Doherty [135]. The model successfully predicts the existence of a non-reactive azeotrope between n-butane and methanol, as well as the absence of any other binary azeotropes, which disappear due to the reaction. Furthermore, at 1 atm the model identifies the presence of a reactive azeotrope on the hypotenuse of the triangle, which represents the limiting case of absence of inert.

The charts for both pressures are roughly separated into two regions (I and II) from the n-butane vertex to the reactive azeotrope. At 1 atm, in region (I) the residue curves begin at the unstable node of pure isobutene and end at the reactive azeotrope, which acts as a stable node. In region (II) the residue curves begin at the unstable node representing the non-reactive azeotrope between n-butane and methanol, pass from the reactive azeotrope, which now acts as a saddle point, and end at the stable node representing pure methanol. At the higher pressure of 7 atm the curves near the reactive azeotrope are further apart, but the tangent pinch is severe enough for the point to still qualify as a pseudo-reactive azeotrope. The above observations are in agreement with the findings by Ung and Doherty [131, 135]. Even though MTBE composition is not depicted in Figure 11.3 and Figure 11.4, during the calculations it was clear that it takes its maximum values near the reactive azeotrope. Therefore, the optimal feed composition to a reactive distillation column lies within region (I).

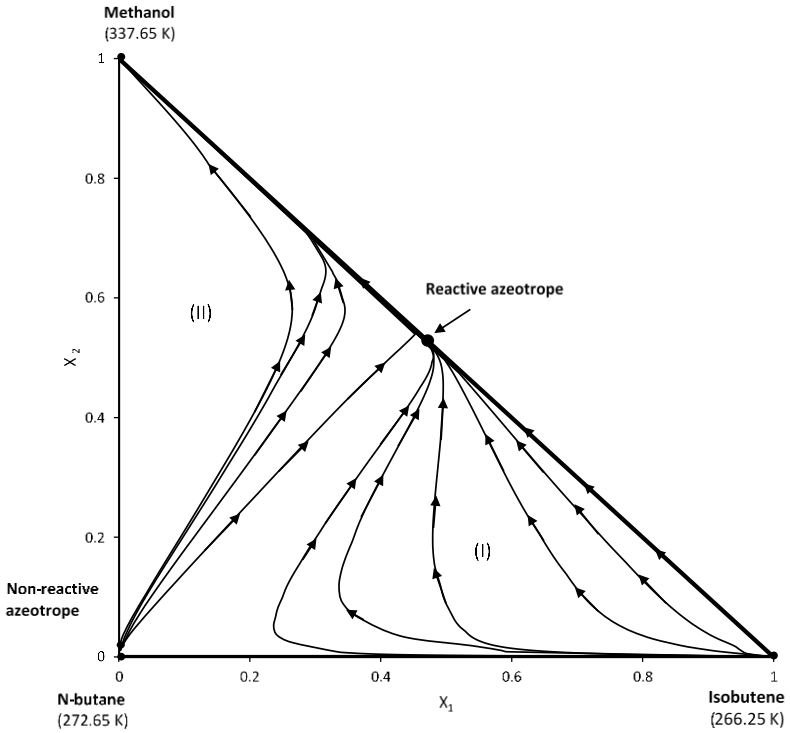

Figure 11.3. Residue curves in transformed compositions as predicted with UMR-UNIFAC for the MTBE synthesis system with n-butane present as inert at 1 atm. K_{eq} from Tejero et al. [160].

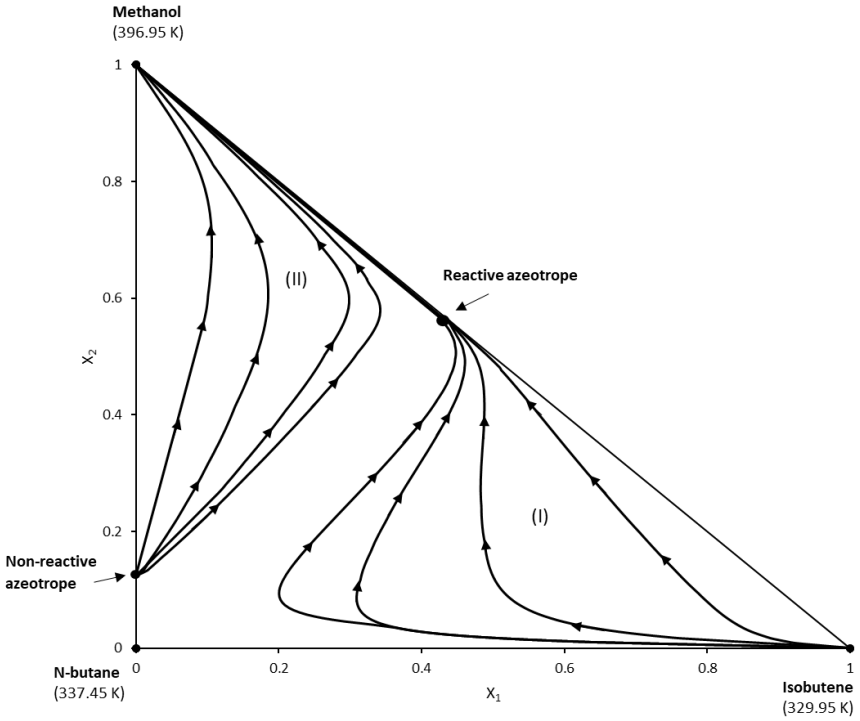

Figure 11.4 Residue curves in transformed compositions as predicted with UMR-UNIFAC for the MTBE synthesis system with n-butane present as inert at 7 atm. K_{eq} from Tejero et al. [160].

11.5 Acetic acid/isopropanol esterification

Isopropyl acetate is widely used in the chemical industry as a solvent for cellulose and resins. It can also be found in adhesives, artificial flavoring agents, perfumes and printing inks [161]. Isopropyl acetate is produced via the esterification of acetic acid with isopropanol according to the reaction:

$$CH_3COOH\ (1) + C_3H_8O\ (2) \Leftrightarrow H_2O\ (3) + C_5H_{10}O_2\ (4) \qquad \text{Eq. 11.8}$$

The mixture exhibits three binary azeotropes between isopropanol/water, isopropanol/isopropyl acetate and water/isopropyl acetate, one ternary azeotrope between isopropanol/water/isopropyl acetate, and a reactive azeotrope between all four components [133].

Due to the dimerization of acetic acid, the vapor phase cannot be approximated as ideal when an activity coefficient model is used. For this reason, the virial equation of state coupled with Hayden-O'Connell method [45] is employed together with UNIQUAC and UNIFAC models. The UMR-UNIQUAC and UMR-UNIFAC thermodynamic models are also employed, with the parameters given in Appendix B. The performance of the models is initially tested in the binary mixtures by performing bubble point calculations in all cases, except for water/isopropyl acetate which exhibits liquid-liquid equilibrium (LLE). The average deviations are presented in Table 11.6.

It is observed that all models yield satisfactory VLE results, with the virial/UNIQUAC model having the lowest and UMR-UNIFAC the highest overall deviations. Across all models, the highest deviations are observed in the mixtures involving acetic acid. This is expected due to the hydrogen bonding involved in these systems. Furthermore, despite the fact that UMR-PRU does not explicitly account for association between components, its performance is deemed adequate, even more so if one takes into account that its results are pure predictions. Concerning the LLE between water and isopropyl acetate, UNIQUAC and UNIFAC models yield accurate results for the aqueous phase composition, but describe the organic phase less accurately. On the other hand, UMR-UNIQUAC and UMR-UNIFAC accurately predict the mole fractions in the organic phase, but less so in the aqueous phase.

Table 11.6. VLE and LLE results for mixtures involved in acetic acid/isopropanol esterification.

System			virial/UNIQUAC		virial/UNIFAC		UMR-UNIQUAC		UMR-UNIFAC	
	Ref.	ND[a]	AADT[b]	AADy[c]	AADT	AADy	AADT	AADy	AADT	AADy
Acetic acid/isopropanol	[162]	19	1.00	2.90	3.32	3.43	2.33	2.95	4.42	4.60
Acetic acid/isopropyl acetate	[163, 164]	33	0.26	2.60	1.53	0.69	3.11	7.69	1.25	5.40
Acetic acid/water	[165-167]	43	0.89	1.64	0.91	2.17	1.46	0.05	1.35	3.22
Isopropanol/isopropyl acetate	[168, 169]	61	0.19	0.29	1.50	2.42	0.23	0.28	0.47	3.46
Isopropanol/water	[170, 171]	32	0.18	0.62	0.42	0.85	0.70	1.51	1.82	3.87
	Overall	**188**	**0.44**	**1.32**	**1.37**	**1.89**	**1.31**	**2.01**	**1.44**	**3.93**
Acetic acid/isopropanol/water/isopropyl acetate	[172]	44	0.75	0.74	1.99	0.85	3.65	3.59	3.62	2.17
			AADx$^{(I)}$[d]	AADx$^{(II)}$	AADx$^{(I)}$	AADx$^{(II)}$	AADx$^{(I)}$	AADx$^{(II)}$	AADx$^{(I)}$	AADx$^{(II)}$
Water/isopropyl acetate	[173-175]	11	2.11	0.15	2.95	0.14	0.23	0.96	0.23	1.00

[a] ND: number of experimental data points

[b] $AADT = 1/ND \sum_{i=1}^{ND} \left| T_i^{exp} - T_i^{calc} \right|$, where T is the bubble point temperature

[c] $AADy = 100/ND \sum_{i=1}^{ND} \left| y_i^{exp} - y_i^{calc} \right|$, where y is the mole fraction of any component in the vapor phase

[d] $AADx = 100/ND \sum_{i=1}^{ND} \left| x_i^{exp} - x_i^{calc} \right|$, where x is the mole fraction of any component in the organic (I) or aqueous (II) phase

The next step concerns model evaluation regarding the VLE of the quaternary mixture in the absence of reaction. For this purpose, the experimental data by Lee and Kuo [172] are used for performing bubble point calculations. The results (Table 11.6) indicate that virial/UNIQUAC yields the most accurate predictions with an AAD in temperature equal to 0.75 K and in vapor mole fraction equal to 0.74. Results with UMR-UNIQUAC and UMR-UNIFAC have the highest deviations from the experimental data with an AAD in temperature of about 3.6 K. Notably, UMR-UNIFAC predicts more accurately than UMR-UNIQUAC the vapor phase composition, even though both exhibit similar deviations in temperature. However, the results with UMR-PRU can be deemed adequate considering that they are predictions and the studied mixture is strongly non-ideal due to the presence of strongly polar and associating compounds.

The final step is the examination of the simultaneous chemical and phase equilibria involved in the quaternary reactive mixture. Song et al. [133] determined the composition of the reactive azeotrope by performing CPE experiments. They also generated the residue curves of the system with the NRTL [58] model and a constant value of 8.7 for the reaction equilibrium constant. They considered the association of acetic acid in the gas phase, but the exact procedure is not mentioned. The residue curve maps were drawn with the help of transformed compositions, defined as:

$$X_1 = x_1 + x_4 \quad \text{Eq. 11.9}$$

$$X_2 = x_2 + x_4 \quad \text{Eq. 11.10}$$

$$X_3 = x_3 - x_4 \quad \text{Eq. 11.11}$$

Following the same formulation and using the same K_{eq}, the residue curve maps for the system as calculated with virial/UNIQUAC and UMR-UNIQUAC are shown in Figure 11.5 and Figure 11.6. It should be noted that the binary azeotropes are omitted from these figures since they do not constitute singular points of interest. The composition of the reactive azeotrope as predicted with the models is presented in Table 11.7 together with the deviations from the experimental data by Song et al. [133].

It is observed that the plotted residue curves qualitatively match those presented by Song et al. More specifically, the reactive azeotrope acts as an unstable node lying inside the square chart representing the four-component reactive mixture. All the calculated residue curves begin at the reactive azeotrope and end at vertices representing pure components. However, the deviations between model predictions and experimental data (Table 11.7) are relatively high. Virial/UNIQUAC yields slightly better results for the compositions than UMR-UNIQUAC, but the latter predicts more accurately the temperature at which the azeotrope is formed.

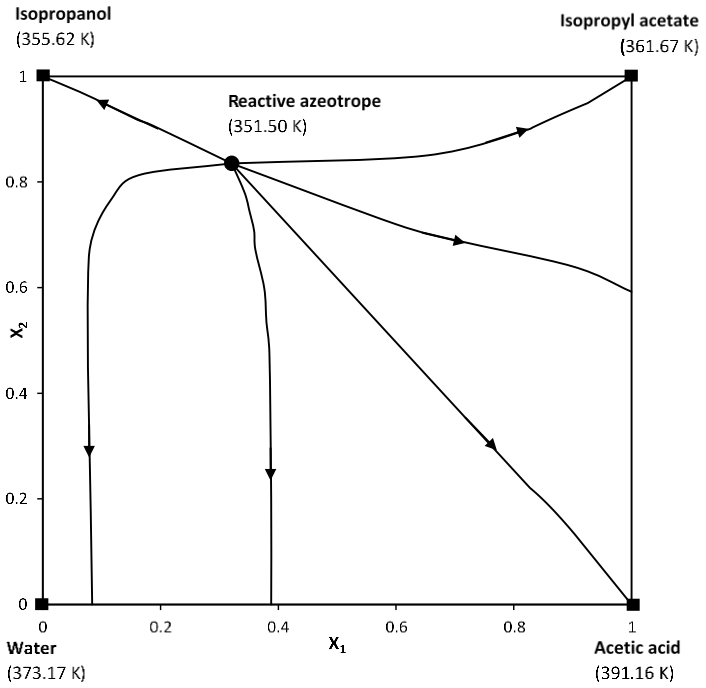

Figure 11.5. Residue curves in transformed compositions as predicted with virial/UNIQUAC for the acetic acid/isopropanol esterification system at 1 atm (K_{eq} = 8.7). The temperatures shown are those predicted by the model.

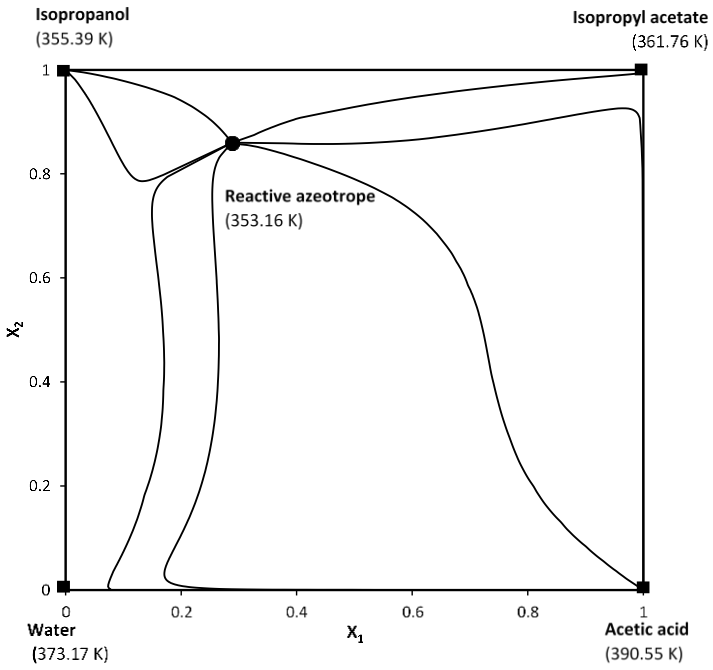

Figure 11.6. Residue curves in transformed compositions as predicted with UMR-UNIQUAC for the acetic acid/isopropanol esterification system at 1 atm (K_{eq} = 8.7). The temperatures shown are those predicted by the model.

Table 11.7. Calculated and experimental reactive azeotrope composition in the acetic acid/isopropanol esterification system at 1 atm.

	Song et al. [133] (exp. data)	Song et al. [133] (NRTL, K_{eq} = 8.7)	Mandagarán et al. [176] (NRTL, K_{eq} = 10.7)	This work (virial/UNIQUAC, K_{eq} = 8.7)	This work (UMR-UNIQUAC, K_{eq} = 8.7)
x_1	0.0540	0.0530	0.0574	0.0590	0.0478
x_2	0.5650	0.5655	0.5608	0.5730	0.6198
x_3	0.1670	0.1628	0.1608	0.1060	0.0921
x_4	0.2140	0.2187	0.2209	0.2620	0.2402
AADx [a]	-	**0.26**	**0.52**	**3.05**	**4.05**
y_1	0.0000	0.0033	0.0031	0.013	0.0076
y_2	0.4910	0.5158	0.5060	0.527	0.5778
y_3	0.2390	0.2125	0.2141	0.152	0.1335
y_4	0.2700	0.2684	0.2767	0.308	0.2811
AADy	-	**1.41**	**1.24**	**4.35**	**5.28**
X_1	0.2680	0.2717	0.2783	0.321	0.2880
X_2	0.7790	0.7842	0.7817	0.835	0.8600
T (K)	351.75	352.14	352.28	353.3	353.16
AADT [b]	-	**0.39**	**0.53**	**1.55**	**1.41**

[a] $AADz = 100/NC \sum_{i=1}^{NC} \left| z_i^{exp} - z_i^{calc} \right|$, where z the mole fraction of component i in the liquid phase (x) or the vapor phase (y) and NC is the number of components in the mixture

[b] $AADT = |T^{exp} - T^{calc}|$, where T the temperature

The results by Song et al. [133] with the NRTL model (Table 11.7) show very small deviations from their experimental data. According to the authors, the NRTL parameters for isopropanol/isopropyl acetate and water/isopropyl acetate were optimized based on the respective non-reactive azeotropes. These parameters appear to yield remarkably accurate predictions for the quaternary reactive azeotrope, but their performance regarding VLE calculations in binary and multicomponent non-reactive mixtures is unknown. Since parameter values are not mentioned by Song et al. [133], further examination into this matter is not possible.

Mandagarán et al. [176] have also performed the same study with the NRTL model. They fitted binary parameters to VLE, LLE and azeotropic experimental data, and adjusted the equilibrium constant of the reaction to the quaternary reactive azeotrope. Their results (Table 11.7) show good agreement with the experimental data, but the deviations are slightly higher than those reported by Song et al. [133].

Taking into account all of the above, the results with virial/UNIQUAC and UMR-UNIQUAC are deemed satisfactory since no parameter adjustment was made to the quaternary reactive azeotrope.

11.6 Conclusions

In this chapter, the developed CPE algorithm based on Gibbs energy minimization with Lagrange multipliers was successfully applied for performing simultaneous chemical and phase equilibria calculations in systems involving azeotropes. The algorithm was initially verified against calculations by other authors for the cyclohexane synthesis, providing similar results. Subsequently, the algorithm was applied for studying the MTBE synthesis from methanol and isobutene, as well as the synthesis of isopropyl acetate via esterification of acetic acid with isopropanol.

For the MTBE synthesis system, calculations were performed with and without n-butane present as an inert, and both vapor and liquid phase reaction cases were examined with different reaction equilibrium constants. Phase non-ideality was described with traditional activity coefficient models UNIQUAC and UNIFAC, as well as with the EoS/G^E model UMR-PRU by directly employing parameters from the first two models. It was observed that all models yielded accurate results for the VLE of binary and multicomponent mixtures. The reactive mixture was also studied and good agreement between model predictions and molecular simulation or experimental data was observed. The residue curve maps of the system in the presence of n-butane were also constructed, which helped to identify the optimum feed composition to a reactive distillation column, in order to achieve maximum MTBE concentration. The residue curves provided a good qualitative description of the system, with observations similar to these by other authors.

The same thermodynamic models were also employed for the study of acetic acid/isopropanol esterification system. Due to the presence of the acetic acid, when an activity coefficient model was used, the vapor phase was described by the virial EoS with the Hayden-O'Connell method. Model performance was initially tested in binary and multicomponent non-reactive mixtures, in which virial/UNIQUAC was found to be the most accurate. Despite not explicitly accounting for association forces, the UMR-PRU model with parameters from UNIQUAC or UNIFAC managed to yield adequate predictions. The residue curve maps of the quaternary reactive system were also constructed, giving a good qualitative description of the system. The location of the reactive azeotrope was also predicted with virial/UNIQUAC and UMR-UNIQUAC models, but with relatively high deviation from experimental data. In previous works by other authors, the location of the reactive azeotrope was calculated with higher accuracy, but at the cost of extensive parameter fitting both to equilibrium and azeotropic data, as well as an adjustment of the equilibrium constant of the reaction. Considering this, model predictions in this work are deemed satisfactory.

12. Conclusions & future work

12.1 Conclusions

Mercury is a trace component of fossil fuels, which can cause significant health, safety and environmental (HSE) problems during oil & gas processing due to its toxic and corrosive properties. The aim of this thesis was to develop thermodynamic models and algorithms that can predict the chemical & phase equilibria of mercury in natural gas. Such tools are paramount for the monitoring and proper management of mercury levels in gas processing plants, in order to mitigate the mercury-related HSE issues. They are also important in the design and optimization of mercury removal methods, in order to comply with current environmental regulations and end-user specifications.

In the first chapter of this thesis, a thorough literature review on mercury was conducted, especially with regards to oil & gas applications, in order to highlight the main problems caused by mercury during oil & gas processing. These include its toxic effects to living organisms, adsorption on equipment and corrosion mechanisms, as well as poisoning of catalysts. The dominant form of mercury in natural gas was found to be the elemental (Hg^0), however other forms can also be found in natural gas condensates, such as ionic compounds (e.g. $HgCl_2$) or solid β-HgS particles. It was also found that mercury can participate in reactions with other components of natural gas, such as sulfur compounds. A possible reaction that can explain the occurrence of β-HgS particles in process fluids is that between mercury and hydrogen sulfide, which also produces hydrogen as a by-product. In addition, the experimental techniques for determining mercury concentration in various matrices were presented, and the challenges faced by the experimenters were discussed.

In the subsequent chapters, the theoretical background of thermodynamic equilibrium was explained, and algorithms were presented for performing various types of equilibrium calculations. Furthermore, multiphase flash and simultaneous chemical & phase equilibria (CPE) algorithms were developed, with appropriate modifications for mercury systems. The algorithms are capable of handling multiple non-ideal phases, in which multiple reactions can also take place. In the case of multiphase flash calculations in mercury-saturated hydrocarbon fluids, a “free-mercury” approach was proposed in order to accelerate solution procedure. According to this, when mercury drops out from a mixture either as pure liquid or solid, the fugacity of other components in this phase is not calculated explicitly, but it is set to an arbitrary high value to ensure that the phase is pure mercury.

The UMR-PRU EoS/G^E model was then extended to mixtures of mercury with compressed gases (CO_2, N_2), hydrocarbons, water, and polar compounds that are often used during oil & gas processing, such as amines, glycols and alcohols. For comparison purposes, the widely used cubic EoS SRK and PR were also employed. The first step was to ensure that the models correctly predict the vapor pressure of pure mercury, so different functions for their attractive term were examined. For UMR-PRU and PR the Mathias-Copeman α-function was proposed, while for SRK the α-function by Twu was employed. Pertinent α-function parameters were

fitted to pure mercury experimental vapor pressure data with average absolute relative deviation (AARD) lower than 1%. Afterwards, a literature review on experimental Hg solubility measurements was conducted and the data were assessed. It was found that mercury solubility generally increases exponentially with temperature and is higher in hydrocarbons than polar solvents. The experimental data were then used to determine model interaction parameters. For the cubic EoS, generalized correlations for the binary interaction parameters were developed for hydrocarbons, while for polar compounds temperature-dependent BIPs were determined. The overall results showed that UMR-PRU yields the best results in binary hydrocarbon and polar mixtures containing mercury, while it also yields the lowest deviations in most multicomponent hydrocarbon mixtures and in all polar multicomponent mixtures.

In order to study the possible reaction between mercury and hydrogen sulfide in natural gas ($Hg^0 + H_2S \Leftrightarrow \beta$-HgS + H_2), the UMR-PRU model was extended to mixtures of hydrogen with compressed gases (CO_2, N_2), hydrocarbons, water, and polar compounds. For comparison, the PPR78 model was also employed. The ability of the model to predict pure hydrogen properties was checked, and the Soave expression for the attractive term was found to yield the best results, while also ensuring that the α-function is consistent. Model interaction parameters were determined by fitting binary vapor-liquid equilibrium data for hydrogen binary mixtures. UMR-PRU showed a lower overall deviation in bubble point pressure (8.1%) as compared to PPR78 (13.2%). UMR-PRU was also employed for predictions in multicomponent hydrogen mixtures with hydrocarbons and compressed gases, yielding very satisfactory results.

After successful model extension to mercury and hydrogen mixtures, UMR-PRU was employed for calculating mercury saturation concentration in typical hydrocarbon fluids. For this purpose, the multiphase flash algorithm that was developed in this work was employed, which can handle systems that contain up to four phases: vapor-liquid hydrocarbon-aqueous-mercury. The results showed that mercury solubility in the various phases increases exponentially with temperature and generally increases in the order aqueous < vapor < liquid hydrocarbon phase. The effect of pressure on mercury solubility in the different phases was also examined, and results showed a weak dependency in the liquid hydrocarbon and aqueous phases. An exception was the liquid phase of a fluid taken from a cryogenic heat exchanger, which was rich in C1-C2 hydrocarbons. On the other hand, Hg^0 solubility in the vapor phase was found to decrease with pressure, until a plateau is reached. In any case, phase composition was found to play an important role and different behaviors can be observed, e.g. in fluids involved in early-stage separation processes from those that can be found in the condensate stabilization train of a gas processing plant.

The second point of focus in this work was the theoretical study of the reaction between elemental mercury and H_2S in natural gas, which could provide an explanation for the origin of β-HgS solid particles found in condensate tank sediments. Chemistry dictates that mercury has a high affinity for sulfur and its compounds, and H_2S is the most abundant sulfuric compound in natural gas, so a reaction between them is deemed reasonable. Both cases of vapor and liquid phase reaction were examined by calculating the pertinent equilibrium

constants. Depending on the literature source for the thermodynamic properties of β-HgS, three different equilibrium constants were calculated for each case. Then, the simultaneous chemical & phase equilibria in the same fluids were solved by employing the Gibbs energy minimization algorithm developed in this work.

In the case of vapor phase reaction, it was found that below 320-380 K all mercury is expected to be in the form of β-HgS, while above 450-500 K all mercury is in the elemental form. In the case of liquid phase reaction, conversions lower than 50% were observed at the studied conditions and conversion was found to be a concave function of temperature. The effect of pressure on conversion was also studied, and it was found that in the vapor reaction the conversion increases with pressure. Regarding the liquid reaction, it was observed that a locus of maximum conversions is formed.

The UMR-PRU model was employed for simulating mercury distribution in an existing offshore natural gas processing platform. For comparison the SRK-Twu model was also used, and model results were compared to field measurements regarding mercury concentration in selected streams. For the purposes of this study, a simplified version of the process was implemented in UniSim Design R460.2 and the distribution of mercury in the various streams was examined. The effect of the possible reaction between mercury and H_2S was also studied. Different scenarios were considered, based on the presumed amount of mercury in the plant feeds according to mass balance calculations. Mercury partitioning in the TEG dehydration & regeneration process, as well as in MEG regeneration was also examined in separate simulations. The results in the case of no reaction showed that both models yield very good predictions regarding mercury concentrations in process gases, but overpredict Hg levels in condensate fluids. UMR-PRU was also found to yield the most accurate results for Hg distribution in aqueous streams, as well as in the processes involved in TEG dehydration & regeneration, and in MEG regeneration.

On the other hand, when the reaction was also included in the study, it was found that the models yielded better results for Hg concentration in condensates, but deviated from the measurements in gas streams. In addition, UMR-PRU predicted an amount of produced solid β-HgS, which was closer to the expected value based on the field data. Considering the uncertainty of measurements concerning Hg concentration in liquid samples due to various experimental challenges, it is deemed that UMR-PRU yields the best overall results, while it is also capable of fully describing processes involving polar compounds, such as TEG dehydration & regeneration, where classical cubic EoS perform poorly.

Finally, the developed CPE algorithm was applied to study phase and chemical equilibria in complex mixtures involving non-reactive and reactive azeotropes. Such mixtures are commonly encountered in the chemical and petroleum industry, and require advanced thermodynamic tools that can accurately predict their equilibria. Such tools are important in order to determine the feasibility of separation processes, such as reactive distillation. The CPE algorithm was applied for studying the MTBE synthesis from methanol and isobutene, as well as the synthesis of isopropyl acetate via esterification of acetic acid with isopropanol.

The algorithm was coupled with classical activity coefficient models, UNIQUAC and NRTL, as well as with UMR-PRU. The results showed that the models, as well as the algorithm, can successfully describe the chemical & phase equilibria involved in these systems, providing important information about the feasibility of separation processes.

12.2 Future work

The study of mercury implications for oil & gas processing is currently active in the scientific community, and one PhD thesis is impossible to cover this multifaceted topic, but rather act as a step towards further advancement of knowledge.

For the development of a complete thermodynamic model that can fully describe the chemical & phase equilibria of mercury in oil & gas, more experimental data must become available in the open literature. These include elemental mercury solubility measurements in hydrocarbons, for which limited data are available (e.g. nC4, iC5), as well as in polar solvents, where experimental data are extremely scarce.

In addition, further examination of the possible reactions of mercury with oil & gas components is required. In this thesis, a possible reaction between Hg^0 and H_2S was theorized, but the reaction must also be studied experimentally in order to measure its equilibrium constant and to understand if it is kinetically controlled. This reaction is not the only one that can explain the presence of β-HgS in process fluids, and further reactions must be studied, e.g. between mercury and H_2S dissociation products in water phases. Furthermore, ionic mercury forms in oil & gas (e.g. $HgCl_2$) must be further investigated both through field measurements and thermodynamic modelling.

Another important aspect of the mercury-related problems in the oil & gas industry, is mercury adsorption (or chemisorption) on piping and equipment. The development of models that can predict the amount of adsorbed mercury versus time is important for the proper monitoring and anticipation of mercury levels in the natural gas transport grid.

Finally, it would be useful to simulate mercury distribution in more gas processing plants. In this work, a study for an offshore processing platform was made, but conditions and processes across plants can vary, especially when it comes to onshore processing plants, which involve an increased number of processes. This is important, since the conclusions of this work indicated that the overall mercury distribution in a plant can vary depending on process conditions.

References

1. Bingham, M.D., *Field Detection and Implications of Mercury in Natural Gas.* SPE Production Engineering, 1990. **5**(02): p. 120-124.

2. Wilhelm, S.M., *Mercury in Petroleum and Natural Gas: Estimation of Emissions from Production, Processing, and Combustion*. 2001, United States Environmental Protection Agency.

3. Gallup, D.L., D.J. O'Rear, and R. Radford, *The behavior of mercury in water, alcohols, monoethylene glycol and triethylene glycol.* Fuel, 2017. **196**: p. 178-184.

4. Chalkidis, A., et al., *Mercury in natural gas streams: A review of materials and processes for abatement and remediation.* Journal of Hazardous Materials, 2020. **382**: p. 121036.

5. *Mercury in Europe's environment: A priority for European and global action*. 2018, European Environment Agency: Copenhagen, Denmark.

6. Dean, J.A., *Lange's Handbook of Chemistry*. 15th ed. 1999: McGraw-Hill.

7. Cotton, F.A. and G. Wilkinson, *Advanced Inorganic Chemistry*. 3rd ed. 1972: Interscience Publishers.

8. 17/4/2017]; Available from: http://www.webmineral.com.

9. Panduan, G., *Guidelines on Mercury Management in Oil & Gas Industry*, M.o.H.R. Department of Occupational Safety and Health, Malaysia, Editor. 2011.

10. Eckersley, N., *Advanced mercury removal technologies.* Hydrocarbon processing, 2010. **89**(1): p. 29-35.

11. Lynch, S.P., *Failures of Structures and Components by Metal-Induced Embrittlement.* Journal of Failure Analysis and Prevention, 2008. **8**(3): p. 259-274.

12. Carnell, P.J., V.A. Row, and R. McKenna, *A re-think of the mercury removal problem for LNG plants.* Johnson Matthey Group, USA, 2007.

13. 28/8/2020]; Available from: https://www.epa.gov/mats.

14. Ezzeldin, M.F., et al., *Mercury Speciation and Distribution in an Egyptian Natural Gas Processing Plant.* Energy & Fuels, 2016. **30**(12): p. 10236-10243.

15. Crafts, P., *Genesis Mercury Consultancy Services Presentation*. 2016.

16. Smit, C.J., H. Meijer, and E.M. Hendriks. *Mercury, the Volatile Surprise in Gas Processing*. in *Annual GPA Convention, New Orleans*. 2004.

17. Evans, M. and L. Brown, *CAPE-OPEN Models for Hg Speciation and Partitioning Flowsheet Development*. 2012, ConocoPhillips: AIChe Annual Meeting.

18. Sabri, Y.M., et al., *Mercury Migration and Speciation Study during Monoethylene Glycol Regeneration Processes.* Industrial & Engineering Chemistry Research, 2015. **54**(19): p. 5349-5355.

19. Lide, D.R. and H.V. Kehiaian, *CRC handbook of thermophysical and thermochemical data*. Vol. 1. 1994: Crc Press.

20. Wagman, D.D., *The NBS Tables of Chemical Thermodynamic Properties: Selected Values for Inorganic and C1 and C2 Organic Substances in SI Units*. 1982: American Chemical Society and the American Institute of Physics for the National Bureau of Standards.

21. Snell, J.P., W. Frech, and Y. Thomassen, *Performance improvements in the determination of mercury species in natural gas condensate using an on-line amalgamation trap or solid-phase micro-extraction with capillary gas chromatography-microwave-induced plasma atomic emission spectrometry.* Analyst, 1996. **121**(8): p. 1055-1060.

22. Wilhelm, S.M. and N. Bloom, *Mercury in petroleum.* Fuel Processing Technology, 2000. **63**(1): p. 1-27.

23. Clevenger, W.L., B.W. Smith, and J.D. Winefordner, *Trace Determination of Mercury: A Review.* Critical Reviews in Analytical Chemistry, 1997. **27**(1): p. 1-26.

24. Wilhelm, S.M., L. Liang, and D. Kirchgessner, *Identification and Properties of Mercury Species in Crude Oil.* Energy & Fuels, 2006. **20**(1): p. 180-186.

25. Bloom, N.S., *Analysis and stability of mercury speciation in petroleum hydrocarbons.* Fresenius' Journal of Analytical Chemistry, 2000. **366**(5): p. 438-443.

26. Bloom, N.S. and D.L. Gallup. *On the solubility of mercury in liquid hydrocarbons*. in *AIChE Spring Meeting and Global Congress on Process Safety*. 2010.

27. Yu, L.-P. and X.-P. Yan, *Factors affecting the stability of inorganic and methylmercury during sample storage.* TrAC Trends in Analytical Chemistry, 2003. **22**(4): p. 245-253.

28. Mokhatab, S. and W.A. Poe, *Handbook of natural gas transmission and processing*. 2006: Gulf professional publishing.

29. Kidnay, A.J., W.R. Parrish, and D.G. McCartney, *Fundamentals of natural gas processing*. 2006: CRC press.

30. *BP Statistical Review of World Energy 2020*. 2020, BP.

31. Skouras, E., *Natural Gas Processing*. 2019, Equinor: Presentation.

32. Warrag, S.E.E., et al., *Mercury Capture from Petroleum Using Deep Eutectic Solvents.* Industrial & Engineering Chemistry Research, 2018. **57**(28): p. 9222-9230.

33. Abbas, T., et al., *Mercury capture from natural gas by carbon supported ionic liquids: Synthesis, evaluation and molecular mechanism.* Fuel, 2016. **177**: p. 296-303.

34. Chalkidis, A., et al., *Regenerable α-MnO2 nanotubes for elemental mercury removal from natural gas.* Fuel Processing Technology, 2019. **193**: p. 317-327.

35. Michelsen, M.L. and J.M. Mollerup, *Thermodynamic Models: Fundamentals & Computational Aspects*. 2007, Holte, Denmark: Tie-Line Publications.

36. Bertakis, E., et al., *Measurement and thermodynamic modeling of solid–liquid–gas equilibrium of some organic compounds in the presence of CO2.* The Journal of Supercritical Fluids, 2007. **41**(2): p. 238-245.

37. Michelsen, M.L., *The isothermal flash problem. Part I. Stability.* Fluid Phase Equilibria, 1982. **9**(1): p. 1-19.

38. Michelsen, M.L., *Calculation of multiphase equilibrium.* Computers & Chemical Engineering, 1994. **18**(7): p. 545-550.

39. Tang, Y. and S. Saha, *An Efficient Method to Calculate Three-Phase Free-Water Flash for Water−Hydrocarbon Systems.* Industrial & Engineering Chemistry Research, 2003. **42**(1): p. 189-197.

40. Smith, W.R. and R.W. Missen, *Chemical reaction equilibrium analysis : Theory and Algorithms*. 1982, Wiley: New York.

41. Michelsen, M.L., *Calculation of multiphase ideal solution chemical equilibrium.* Fluid Phase Equilibria, 1989. **53**: p. 73-80.

42. Tsanas, C., E.H. Stenby, and W. Yan, *Calculation of simultaneous chemical and phase equilibrium by the method of Lagrange multipliers.* Chemical Engineering Science, 2017. **174**: p. 112-126.

43. Leal, A.M.M., D.A. Kulik, and M.O. Saar, *Enabling Gibbs energy minimization algorithms to use equilibrium constants of reactions in multiphase equilibrium calculations.* Chemical Geology, 2016. **437**: p. 170-181.

44. Tsonopoulos, C., *An empirical correlation of second virial coefficients.* AIChE Journal, 1974. **20**(2): p. 263-272.

45. Hayden, J.G. and J.P. O'Connell, *A Generalized Method for Predicting Second Virial Coefficients.* Industrial & Engineering Chemistry Process Design and Development, 1975. **14**(3): p. 209-216.

46. Kontogeorgis, G.M., et al., *Equations of state in three centuries. Are we closer to arriving to a single model for all applications?* Chemical Engineering Science: X, 2020. **7**: p. 100060.

47. Kontogeorgis, G.M., R. Privat, and J.-N. Jaubert, *Taking Another Look at the van der Waals Equation of State–Almost 150 Years Later.* Journal of Chemical & Engineering Data, 2019. **64**(11): p. 4619-4637.

48. Soave, G., *Equilibrium constants from a modified Redlich-Kwong equation of state.* Chemical Engineering Science, 1972. **27**(6): p. 1197-1203.

49. Peng, D.-Y. and D.B. Robinson, *A New Two-Constant Equation of State.* Industrial & Engineering Chemistry Fundamentals, 1976. **15**(1): p. 59-64.

50. Mathias, P.M. and T.W. Copeman, *Extension of the Peng-Robinson equation of state to complex mixtures: Evaluation of the various forms of the local composition concept.* Fluid Phase Equilibria, 1983. **13**: p. 91-108.

51. Stryjek, R. and J.H. Vera, *PRSV: An improved peng—Robinson equation of state for pure compounds and mixtures.* The Canadian Journal of Chemical Engineering, 1986. **64**(2): p. 323-333.

52. Twu, C.H., et al., *A cubic equation of state with a new alpha function and a new mixing rule.* Fluid Phase Equilibria, 1991. **69**: p. 33-50.

53. Twu, C.H., J.E. Coon, and J.R. Cunningham, *A new generalized alpha function for a cubic equation of state Part 2. Redlich-Kwong equation.* Fluid Phase Equilibria, 1995. **105**(1): p. 61-69.

54. Boston, J. and P. Mathias. *Phase equilibria in a third-generation process simulator*. in *Proceedings of the 2nd international conference on phase equilibria and fluid properties in the chemical process industries*. 1980. Deutsche Gesellschaft für Chemisches Apparatewesen Great Neck, NY.

55. Le Guennec, Y., et al., *A consistency test for α-functions of cubic equations of state.* Fluid Phase Equilibria, 2016. **427**: p. 513-538.

56. Le Guennec, Y., et al., *On the imperative need to use a consistent α-function for the prediction of pure-compound supercritical properties with a cubic equation of state.* Fluid Phase Equilibria, 2017. **445**: p. 45-53.

57. Wilson, G.M., *Vapor-Liquid Equilibrium. XI. A New Expression for the Excess Free Energy of Mixing.* Journal of the American Chemical Society, 1964. **86**(2): p. 127-130.

58. Renon, H. and J.M. Prausnitz, *Local compositions in thermodynamic excess functions for liquid mixtures.* AIChE Journal, 1968. **14**(1): p. 135-144.

59. Abrams, D.S. and J.M. Prausnitz, *Statistical thermodynamics of liquid mixtures: A new expression for the excess Gibbs energy of partly or completely miscible systems.* AIChE Journal, 1975. **21**(1): p. 116-128.

60. Fredenslund, A., R.L. Jones, and J.M. Prausnitz, *Group ‐ contribution estimation of activity coefficients in nonideal liquid mixtures.* AIChE Journal, 1975. **21**(6): p. 1086-1099.

61. Guggenheim, E.A. and R.H. Fowler, *Statistical thermodynamics of mixtures with non-zero energies of mixing.* Proceedings of the Royal Society of London. Series A. Mathematical and Physical Sciences, 1944. **183**(993): p. 213-227.

62. Kontogeorgis, G.M., et al., *An Equation of State for Associating Fluids.* Industrial & Engineering Chemistry Research, 1996. **35**(11): p. 4310-4318.

63. Wertheim, M.S., *Fluids with highly directional attractive forces. I. Statistical thermodynamics.* Journal of Statistical Physics, 1984. **35**(1): p. 19-34.

64. Chapman, W.G., et al., *New reference equation of state for associating liquids.* Industrial & Engineering Chemistry Research, 1990. **29**(8): p. 1709-1721.

65. Gross, J. and G. Sadowski, *Perturbed-Chain SAFT: An Equation of State Based on a Perturbation Theory for Chain Molecules.* Industrial & Engineering Chemistry Research, 2001. **40**(4): p. 1244-1260.

66. Voutsas, E., K. Magoulas, and D. Tassios, *Universal Mixing Rule for Cubic Equations of State Applicable to Symmetric and Asymmetric Systems: Results with the Peng−Robinson Equation of State.* Industrial & Engineering Chemistry Research, 2004. **43**(19): p. 6238-6246.

67. Michelsen, M.L., *A modified Huron-Vidal mixing rule for cubic equations of state.* Fluid Phase Equilibria, 1990. **60**(1): p. 213-219.

68. Louli, V., et al., *Measurement and prediction of dew point curves of natural gas mixtures.* Fluid Phase Equilibria, 2012. **334**: p. 1-9.

69. Novak, N., et al., *Prediction of dew points and liquid dropouts of gas condensate mixtures.* Fluid Phase Equilibria, 2018. **457**: p. 62-73.

70. Novak, N., V. Louli, and E. Voutsas, *Prediction of Vapor–Liquid Equilibrium and Thermodynamic Properties of Natural Gas and Gas Condensates.* Industrial & Engineering Chemistry Research, 2019. **58**(17): p. 7370-7388.

71. Petropoulou, E., G.D. Pappa, and E. Voutsas, *Modelling of phase equilibrium of natural gas mixtures containing associating compounds.* Fluid Phase Equilibria, 2017. **433**: p. 135-148.

72. Petropoulou, E.G. and E.C. Voutsas, *Thermodynamic Modeling and Simulation of Natural Gas Dehydration Using Triethylene Glycol with the UMR-PRU Model.* Industrial & Engineering Chemistry Research, 2018. **57**(25): p. 8584-8604.

73. Plakia, A., G. Pappa, and E. Voutsas, *Modeling of CO2 solubility in aqueous alkanolamine solutions with an extended UMR-PRU model.* Fluid Phase Equilibria, 2018. **478**: p. 134-144.

74. Plakia, A. and E. Voutsas, *Modeling of H2S, CO2 + H2S, and CH4 + CO2 Solubilities in Aqueous Monoethanolamine and Methyldiethanolamine Solutions.* Industrial & Engineering Chemistry Research, 2020. **59**(24): p. 11317-11328.

75. Hansen, H.K., et al., *Vapor-liquid equilibria by UNIFAC group contribution. 5. Revision and extension.* Industrial & Engineering Chemistry Research, 1991. **30**(10): p. 2352-2355.

76. Jaubert, J.-N. and F. Mutelet, *VLE predictions with the Peng–Robinson equation of state and temperature dependent kij calculated through a group contribution method.* Fluid Phase Equilibria, 2004. **224**(2): p. 285-304.

77. Robinson, D.B. and D.Y. Peng, *The characterization of the heptanes and heavier fractions for the GPA Peng–Robinson programs.* GPA Research Report RR-28, 1978: p. 1-36.

78. Qian, J.-W., R. Privat, and J.-N. Jaubert, *Predicting the Phase Equilibria, Critical Phenomena, and Mixing Enthalpies of Binary Aqueous Systems Containing Alkanes, Cycloalkanes, Aromatics, Alkenes, and Gases (N2, CO2, H2S, H2) with the PPR78 Equation of State.* Industrial & Engineering Chemistry Research, 2013. **52**(46): p. 16457-16490.

79. Chapoy, A., et al., *Elemental mercury partitioning in high pressure fluids part 2: Model validations and measurements in multicomponent systems.* Fluid Phase Equilibria, 2020. **523**: p. 112773.

80. Edmonds, B., R. Moorwood, and R. Szczepanski. *Mercury partitioning in natural gases and condensates*. in *GPA European Chapter Meeting, London*. 1996.

81. Khalifa, M. and L. Lue, *A group contribution method for predicting the solubility of mercury.* Fluid Phase Equilibria, 2017. **432**: p. 76-84.

82. Polishuk, I., F. Nakonechny, and N. Brauner, *Predicting phase behavior of metallic mercury in liquid and compressed gaseous hydrocarbons.* Fuel, 2016. **174**: p. 197-205.

83. Polishuk, I., A. Vilk, and M. Chorążewski, *Predicting phase behavior of metallic mercury in liquid and compressed gaseous hydrocarbons II: Further examination of CP-PC-SAFT in the light of new data.* Fuel, 2017. **203**(Supplement C): p. 686-689.

84. Chapoy, A., et al., *Elemental mercury partitioning in high pressure fluids part 1: Literature review and measurements in single components.* Fluid Phase Equilibria, 2020. **520**: p. 112660.

85. Daubert, T.E. and R.P. Danner, *Physical and thermodynamic properties of pure chemicals : data compilation*. 1994, New York: Hemisphere Pub. Corp.

86. Clever, H.L., *Mercury in Liquids, Compressed Gases, Molten Salts and Other Elements*. IUPAC Solubility Data Series. 1987, Amsterdam: Pergamon. 102-162.

87. Miedaner, M.M., A.A. Migdisov, and A.E. Williams-Jones, *Solubility of metallic mercury in octane, dodecane and toluene at temperatures between 100°C and 200°C.* Geochimica et Cosmochimica Acta, 2005. **69**(23): p. 5511-5516.

88. Marsh, K.N., et al., *Solubility of Mercury in Liquid Hydrocarbons and Hydrocarbon Mixtures.* Journal of Chemical & Engineering Data, 2016. **61**(8): p. 2805-2817.

89. Li, J., et al., *Measurement of Elemental Mercury Solubility in Natural Gas Dehydrating Solvents.* IOP Conference Series: Materials Science and Engineering, 2018. **394**: p. 022060.

90. Butala, S.J.M., G.M. Wilson, and L.V. Jasperson, *Elemental Mercury Equilibrium in Selected Saturated Hydrocarbons*. 2016, Gas Processors Association Research Report RR 224.

91. Yamada, J., et al., *Mercury solubility measurements in natural gas components at high pressure.* Fluid Phase Equilibria, 2020. **506**: p. 112342.

92. Equinor, *Internal Report*. 2014.

93. Equinor, *Internal Report*. 2019.

94. 12/2020]; Available from: https://hydrogeneurope.eu.

95. Sadus, R.J., *Influence of quantum effects on the high-pressure phase behavior of binary mixtures containing hydrogen.* The Journal of Physical Chemistry, 1992. **96**(9): p. 3855-3860.

96. Grayson, H.G. and C.W. Streed. *Vapor-liquid equilibria for high temperature, high pressure hydrogen-hydrocarbon systems*. in *6th World Petroleum Congress*. 1963. Frankfurt.

97. Chao, K.C. and J.D. Seader, *A general correlation of vapor-liquid equilibria in hydrocarbon mixtures.* AIChE Journal, 1961. **7**(4): p. 598-605.

98. Graboski, M.S. and T.E. Daubert, *A Modified Soave Equation of State for Phase Equilibrium Calculations. 3. Systems Containing Hydrogen.* Industrial & Engineering Chemistry Process Design and Development, 1979. **18**(2): p. 300-306.

99. Moysan, J.M., et al., *Prediction of the solubility of hydrogen in hydrocarbon solvents through cubic equations of state.* Chemical Engineering Science, 1983. **38**(7): p. 1085-1092.

100. Moysan, J.M., H. Paradowski, and J. Vidal, *Prediction of phase behaviour of gas-containing systems with cubic equations of state.* Chemical Engineering Science, 1986. **41**(8): p. 2069-2074.

101. El-Twaty, A.I. and J.M. Prausnitz, *Correlation of K-factors for mixtures of hydrogen and heavy hydrocarbons.* Chemical Engineering Science, 1980. **35**(8): p. 1765-1768.

102. Wang, W. and C. Zhong, *Mixing rules for hydrogen-containing systems.* Fluid Phase Equilibria, 1989. **47**(1): p. 103-114.

103. Twu, C.H., et al., *An Approach for the Application of a Cubic Equation of State to Hydrogen−Hydrocarbon Systems.* Industrial & Engineering Chemistry Research, 1996. **35**(3): p. 905-910.

104. Ahlers, J. and J. Gmehling, *Development of a Universal Group Contribution Equation of State. 2. Prediction of Vapor−Liquid Equilibria for Asymmetric Systems.* Industrial & Engineering Chemistry Research, 2002. **41**(14): p. 3489-3498.

105. Mohammed, F., et al., *Generalized binary interaction parameters for hydrogen-heavy-n-alkane systems using Peng–Robinson equation of state.* Chemical Engineering Communications, 2018. **205**(9): p. 1226-1238.

106. Le Guennec, Y., R. Privat, and J.-N. Jaubert, *Development of the translated-consistent tc-PR and tc-RK cubic equations of state for a safe and accurate prediction of volumetric, energetic and saturation properties of pure compounds in the sub- and super-critical domains.* Fluid Phase Equilibria, 2016. **429**: p. 301-312.

107. Bell, I.H., M. Satyro, and E.W. Lemmon, *Consistent Twu Parameters for More than 2500 Pure Fluids from Critically Evaluated Experimental Data.* Journal of Chemical & Engineering Data, 2018. **63**(7): p. 2402-2409.

108. Ioannidis, S. and D.E. Knox, *Vapor–liquid equilibria predictions of hydrogen–hydrocarbon mixtures with the Huron–Vidal mixing rule.* Fluid Phase Equilibria, 1999. **165**(1): p. 23-40.

109. Aguilar-Cisneros, H., et al., *Predictive method of hydrogen solubility in heavy petroleum fractions using EOS/GE and group contributions methods.* Fuel, 2018. **224**: p. 619-627.

110. Huang, H., S.I. Sandler, and H. Orbey, *Vapor-liquid equilibria of some hydrogen + hydrocarbon systems with the Wong-Sandler mixing rule.* Fluid Phase Equilibria, 1994. **96**: p. 143-153.

111. Qian, J.-W., J.-N. Jaubert, and R. Privat, *Phase equilibria in hydrogen-containing binary systems modeled with the Peng–Robinson equation of state and temperature-dependent binary interaction parameters calculated through a group-contribution method.* The Journal of Supercritical Fluids, 2013. **75**: p. 58-71.

112. Ghosh, A., W.G. Chapman, and R.N. French, *Gas solubility in hydrocarbons—a SAFT-based approach.* Fluid Phase Equilibria, 2003. **209**(2): p. 229-243.

113. Florusse, L.J., et al., *Solubility of hydrogen in heavy n-alkanes: Experiments and saft modeling.* AIChE Journal, 2003. **49**(12): p. 3260-3269.

114. Thi, C.L., et al., *Modeling Phase Equilibrium of H2 + n-Alkane and CO2 + n-Alkane Binary Mixtures Using a Group Contribution Statistical Association Fluid Theory Equation of State (GC−SAFT−EOS) with a kij Group Contribution Method.* Industrial & Engineering Chemistry Research, 2006. **45**(20): p. 6803-6810.

115. Lei, Z., et al., *H2 Solubility and Mass Transfer in Diesel: An Experimental and Modeling Study.* Energy & Fuels, 2016. **30**(8): p. 6257-6263.

116. *NIST Chemistry WebBook*. [cited 2018 June]; Available from: https://webbook.nist.gov/chemistry/.

117. Knapp, H., et al., *Vapor-Liquid Equilibria for Mixtures of Low Boiling Substances*. Chemistry Data Series. Vol. VI. 1982, Frankfurt: Dechema.

118. Young, C.L., *Hydrogen and Deuterium*. IUPAC Solubility Data Series. Vol. 5/6. 1981, Oxford, UK: Pergamon Press.

119. Freitag, N.P. and D.B. Robinson, *Equilibrium phase properties of the hydrogen—methane—carbon dioxide, hydrogen—carbon dioxide—n-pentane and hydrogen—n-pentane systems.* Fluid Phase Equilibria, 1986. **31**(2): p. 183-201.

120. Kremer, H. and H. Knapp, *Vapor-liquid equilibria in ternary mixtures of H2, N2, CO and CH4.* Fluid Phase Equilibria, 1983. **11**(3): p. 289-310.

121. Yin, J.-Z. and C.-S. Tan, *Solubility of hydrogen in toluene for the ternary system H2+CO2+toluene from 305 to 343K and 1.2 to 10.5MPa.* Fluid Phase Equilibria, 2006. **242**(2): p. 111-117.

122. Dohrn, R. and G. Brunner, *Phase equilibria in ternary and quaternary systems of hydrogen, water and hydrocarbons at elevated temperatures and pressures.* Fluid Phase Equilibria, 1986. **29**: p. 535-544.

123. Avellan, A., et al., *Speciation of Mercury in Selected Areas of the Petroleum Value Chain.* Environmental Science & Technology, 2018. **52**(3): p. 1655-1664.

124. Pedersen, K.S., A.L. Blilie, and K.K. Meisingset, *PVT calculations on petroleum reservoir fluids using measured and estimated compositional data for the plus fraction.* Industrial & Engineering Chemistry Research, 1992. **31**(5): p. 1378-1384.

125. Pedersen, K.S., P. Thomassen, and A. Fredenslund, *Thermodynamics of petroleum mixtures containing heavy hydrocarbons. 3. Efficient flash calculation procedures using the SRK equation of state.* Industrial & Engineering Chemistry Process Design and Development, 1985. **24**(4): p. 948-954.

126. Pedersen, K.S., P. Thomassen, and A. Fredenslund, *Thermodynamics of petroleum mixtures containing heavy hydrocarbons. 1. Phase envelope calculations by use of the Soave-Redlich-Kwong equation of state.* Industrial & Engineering Chemistry Process Design and Development, 1984. **23**(1): p. 163-170.

127. Robie, R.A. and B.S. Hemingway, *Thermodynamic properties of minerals and related substances at 298.15 K and 1 bar (10^5 pascals) pressure and at higher temperatures*, in *Bulletin*. 1995.

128. Don, W.G. and H.P. Robert, *Perry's Chemical Engineers' Handbook, Eighth Edition*. 8th ed. / ed. 2008, New York: McGraw-Hill Education.

129. El-Feky, A.A., et al., *Monitoring of elemental mercury in ambient air around an Egyptian natural gas processing plant.* Journal of Natural Gas Science and Engineering, 2018. **54**: p. 189-201.

130. Barbosa, D. and M.F. Doherty, *Theory of Phase Diagrams and Azeotropic Conditions for Two-Phase Reactive Systems.* Proceedings of the Royal Society of London. Series A, Mathematical and Physical Sciences, 1987. **413**(1845): p. 443-458.

131. Ung, S. and M.F. Doherty, *Vapor-liquid phase equilibrium in systems with multiple chemical reactions.* Chemical Engineering Science, 1995. **50**(1): p. 23-48.

132. Barbosa, D. and M.F. Doherty, *The simple distillation of homogeneous reactive mixtures.* Chemical Engineering Science, 1988. **43**(3): p. 541-550.

133. Song, W., et al., *Discovery of a reactive azeotrope.* Nature, 1997. **388**(6642): p. 561-563.

134. Ung, S. and M.F. Doherty, *Calculation of residue curve maps for mixtures with multiple equilibrium chemical reactions.* Industrial & Engineering Chemistry Research, 1995. **34**(10): p. 3195-3202.

135. Ung, S. and M.F. Doherty, *Necessary and sufficient conditions for reactive azeotropes in multireaction mixtures.* AIChE Journal, 1995. **41**(11): p. 2383-2392.

136. Ung, S. and M.F. Doherty, *Synthesis of Reactive Distillation Systems with Multiple Equilibrium Chemical Reactions.* Industrial & Engineering Chemistry Research, 1995. **34**(8): p. 2555-2565.

137. Ung, S. and M.F. Doherty, *Theory of phase equilibria in multireaction systems.* Chemical Engineering Science, 1995. **50**(20): p. 3201-3216.

138. Sakuth, M., D. Reusch, and R. Janowsky, *Reactive Distillation*, in *Ullmann's Encyclopedia of Industrial Chemistry*. 2008, Wiley.

139. Toikka, A.M., et al., *Vapor-liquid equilibria in systems with esterification reaction.* Theoretical Foundations of Chemical Engineering, 2009. **43**(2): p. 129-142.

140. Colombo, F., et al., *Equilibrium Constant for the Methyl Tert-Butyl Ether Liquid-Phase Synthesis Using UNIFAC.* Ind. Eng. Chem. Fundam., 1983. **22**(2): p. 219.

141. Rehfinger, A. and U. Hoffmann, *Kinetics of Methyl Tertiary Butyl Ether Liquid Phase Synthesis Catalyzed by Ion Exchange resin—I. Intrinsic Rate Expression in Liquid Phase Activities.* Chem. Eng. Sci., 1990. **45**(6): p. 1605.

142. Izquierdo, J.F., et al., *Equilibrium Constants for Methyl Tert-Butyl Ether and Ethyl Tert-Butyl Ether Liquid-Phase Syntheses Using C4 Olefinic Cut.* Ind. Eng. Chem. Res., 1994. **33**(11): p. 2830.

143. Izquierdo, J.F., et al., *Equilibrium Constants for Methyl Tert-Butyl Ether Liquid-Phase Synthesis.* J. Chem. Eng. Data, 1992. **37**(3): p. 339.

144. Zhang, T. and R. Datta, *Integral Analysis of Methyl Tert-Butyl Ether Synthesis Kinetics.* Ind. Eng. Chem. Res., 1995. **34**(3): p. 730.

145. Solà, L., et al., *Reaction Calorimetry Study of the Liquid-Phase Synthesis of Tert-Butyl Methyl Ether.* Ind. Eng. Chem. Res., 1994. **33**(11): p. 2578.

146. Badia, J.H., et al., *Thermodynamic Analysis of the Experimental Equilibria for the Liquid-Phase Etherification of Isobutene with C1 to C4 Linear Primary Alcohols.* Journal of Chemical & Engineering Data, 2016. **61**(3): p. 1054-1064.

147. Lamb, A.B. and E.E. Roper, *The Vapor Pressures of Certain Unsaturated Hydrocarbons.* Journal of the American Chemical Society, 1940. **62**(4): p. 806-814.

148. Burgos-Solórzano, G.I., J.F. Brennecke, and M.A. Stadtherr, *Validated computing approach for high-pressure chemical and multiphase equilibrium.* Fluid Phase Equilibria, 2004. **219**(2): p. 245-255.

149. George, B., et al., *Computation of Multicomponent, Multiphase Equilibrium*. Industrial & Engineering Chemistry Process Design and Development, 1976. **15**(3): p. 372-377.

150. Winterberg, M., et al., *Methyl Tert-Butyl Ether*, in *Ullmann's Encyclopedia of Industrial Chemistry*. 2010, Wiley.

151. Toghiani, R.K., H. Toghiani, and G. Venkateswarlu, *Vapor-liquid equilibria for methyl tert-butyl ether + methanol and tert-amyl methyl ether + methanol.* Fluid Phase Equilibria, 1996. **122**(1): p. 157-168.

152. Leu, A.-D. and D.B. Robinson, *Vapor−Liquid Equilibrium for Four Binary Systems.* Journal of Chemical & Engineering Data, 1999. **44**(3): p. 398-400.

153. Wilding, W.V., N.F. Giles, and L.C. Wilson, *Phase Equilibrium Measurements on Nine Binary Mixtures.* Journal of Chemical & Engineering Data, 1996. **41**(6): p. 1239-1251.

154. Churkin, V., et al., *Liquid-vapor equilibrium in C4 hydrocarbon-methanol binary systems.* Zh. Fiz. Khim, 1978. **52**(2): p. 488-489.

155. Leu, A.D. and D.B. Robinson, *Equilibrium phase properties of the n-butane-hydrogen sulfide and isobutane-hydrogen sulfide binary systems.* Journal of Chemical & Engineering Data, 1989. **34**(3): p. 315-319.

156. Martinez-Ortiz, J.A. and D.B. Manley, *Vapor pressures for the system isobutane-isobutylene-n-butane.* Journal of Chemical & Engineering Data, 1978. **23**(2): p. 165-167.

157. Vetere, A., I. Miracca, and F. Cianci, *Correlation and prediction of the vapor-liquid equilibria of the binary and ternary systems involved in MTBE synthesis.* Fluid Phase Equilibria, 1993. **90**(1): p. 189-203.

158. Parra, D., et al., *Kinetic study of mtbe liquid-phase synthesis using C4 olefinic cut.* Chemical Engineering Science, 1994. **49**(24, Part A): p. 4563-4578.

159. Lísal, M., W.R. Smith, and I. Nezbeda, *Molecular simulation of multicomponent reaction and phase equilibria in MTBE ternary system.* AIChE Journal, 2000. **46**(4): p. 866-875.

160. Tejero, J., F. Cunill, and J.F. Izquierdo, *Equilibrium constant for the methyl tert-butyl ether vapor-phase synthesis.* Industrial & Engineering Chemistry Research, 1988. **27**(2): p. 338-343.

161. Qi, W. and M.F. Malone, *Semibatch Reactive Distillation for Isopropyl Acetate Synthesis.* Industrial & Engineering Chemistry Research, 2011. **50**(3): p. 1272-1277.

162. Amezaga, A. and F. Biarge, *Equilibrio liquido vapor en sistemas binarios formados por el acido acetico y los alcoholes propilico, isopropilico, isobutilico, butilico secundario y butilico terciario a 760 mm.* Anales de Quimica, 1973. **69**: p. 587.

163. Li, X.-l., et al., *Vapor-liquid equilibria of isopropyl acetate-acetic acid-water system.* Journal of Chemical Engineering of Chinese Universities, 2006. **20**(1): p. 7.

164. Chang, W., et al., *Isobaric Vapor−Liquid Equilibria for Water + Acetic Acid + (n-Pentyl Acetate or Isopropyl Acetate).* Journal of Chemical & Engineering Data, 2005. **50**(4): p. 1129-1133.

165. Peng, Y., et al., *Thermodynamic consistency for the vapor-liquid equilibrium data of associating system.* Acta Pet. Sin.(Pet. Process.), 2009. **25**: p. 717-724.

166. Zhang, C., et al., *Investigation on isobaric vapor liquid equilibrium for acetic acid+water+(n-propyl acetate or iso-butyl acetate).* Fluid Phase Equilibria, 2011. **305**(1): p. 68-75.

167. Xie, Q., et al., *Investigation on isobaric vapor–liquid equilibrium for acetic acid+water+methyl ethyl ketone+isopropyl acetate.* Fluid Phase Equilibria, 2009. **280**(1): p. 120-128.

168. Mato, F. and E. Cepeda, *Vapor-liquid-equilibrium of binary-mixtures alcohol acetic-acid esters. 1. Systems with methanol, ethanol, normal-propanol and isopropanol.* Anales de Quimica, 1984. **80**(3): p. 338-342.

169. Andreatta, A.E., et al., *Physical properties and phase equilibria of the system isopropyl acetate+isopropanol+1-octyl-3-methyl-imidazolium bis(trifluoromethylsulfonyl)imide.* Fluid Phase Equilibria, 2010. **287**(2): p. 84-94.

170. Kojima, K., K. Ochi, and Y. Nakazawa, *Relationship between liquid activity coefficient and composition for ternary systems.* International Chemical Engineering, 1969. **9**(2): p. 342-347.

171. Li, Q., et al., *Isobaric Vapor−Liquid Equilibrium for (Propan-2-ol + Water + 1-Butyl-3-methylimidazolium Tetrafluoroborate).* Journal of Chemical & Engineering Data, 2009. **54**(9): p. 2785-2788.

172. Lee, L.-s. and M.-z. Kuo, *Phase and reaction equilibria of the acetic acid-isopropanol-isopropyl acetate-water system at 760 mmHg.* Fluid Phase Equilibria, 1996. **123**(1): p. 147-165.

173. Hlavatý, K. and J. Linek, *Liquid-liquid equilibria in four ternary acetic acid-organic solvent-water systems at 24.6 ºC.* Collection of Czechoslovak Chemical Communications, 1973. **38**(2): p. 374-378.

174. Stephenson, R. and J. Stuart, *Mutual binary solubilities: water-alcohols and water-esters.* Journal of Chemical & Engineering Data, 1986. **31**(1): p. 56-70.

175. Hong, G.-B., M.-J. Lee, and H.-m. Lin, *Liquid–liquid equilibria of ternary mixtures of water + 2-propanol with ethyl acetate, isopropyl acetate, or ethyl caproate.* Fluid Phase Equilibria, 2002. **202**(2): p. 239-252.

176. Mandagarán, B.A. and E.A. Campanella, *Correlation of vapor - liquid equilibrium data for acetic acid - isopropanol - water - isopropyl acetate mixtures.* Brazilian Journal of Chemical Engineering, 2006. **23**: p. 93-103.

Appendix A: The Hayden-O' Connell method

The Hayden-O' Connell [1] method is widely used for estimating pure component and cross second virial coefficients for simple and complex mixtures. The authors have developed generalized correlations with critical temperature and pressure, radius of gyration, dipole moment, and a parameter to describe chemical association where applicable. Different correlations are used if a compound is polar/non-polar and associating/non-associating. They have also developed mixing rules for predicting the cross coefficients.

According to the method, various contributions to the second virial coefficient (*B*) are identified:

$$B_{total} = B_{free} + (B_{metastable} + B_{bound}) + B_{chem} \quad \text{Eq. A1}$$

where subscript *free* denotes unbound molecules, *metastable* denotes metastably bound molecule pairs, *bound* physically bound pairs, and *chem* chemically bound pairs.

Each contribution to the second virial coefficient between molecule *i* and *j* is calculated as follows:

$$B_{free_{ij}} = B_{free-nonpolar_{ij}} + B_{free-polar_{ij}} \quad \text{Eq. A2}$$

$$B_{free-nonpolar_{ij}} = b_{0_{ij}}\left(0.94 - \frac{1.47}{T^{*\prime}_{ij}} - \frac{0.85}{T^{*\prime 2}_{ij}} + \frac{1.015}{T^{*\prime 3}_{ij}}\right) \quad \text{Eq. A3}$$

$$B_{free-polar_{ij}} = -b_{0_{ij}}\mu^{*\prime}_{ij}\left(0.75 - \frac{3}{T^{*\prime}_{ij}} + \frac{2.1}{T^{*\prime 2}_{ij}} + \frac{2.1}{T^{*\prime 3}_{ij}}\right) \quad \text{Eq. A4}$$

$$B_{bound_{ij}} + B_{metastable_{ij}} = b_{0_{ij}}A_{ij}exp\left(\frac{\Delta H_{ij}}{kT/\varepsilon_{ij}}\right) \quad \text{Eq. A5}$$

$$B_{chem_{ij}} = b_{0_{ij}}\exp\{\eta_{ij}[factor_{ij} - 4.27]\} \times \left\{1 - \exp\left[\frac{1500\eta_{ij}}{T}\right]\right\} \quad \text{Eq. A6}$$

where:

$$\frac{1}{T^{*\prime}_{ij}} = \frac{\varepsilon_{ij}}{kT} - 1.6\omega'_{ij} \quad \text{Eq. A7}$$

$$b_{0_{ij}} = \frac{2\pi}{3}N_0\sigma_{ij}^3 \quad \text{Eq. A8}$$

$$A_{ij} = -0.3 - 0.05\mu^*_{ij} \quad \text{Eq. A9}$$

$$\Delta H_{ij} = 1.99 + 0.2{\mu^*_{ij}}^2 \quad \text{Eq. A10}$$

$$factor_{ij} = \begin{cases} \frac{42800}{\frac{\varepsilon}{k}+22400} \text{ (in presence of organic acids)} \\ \frac{650}{\frac{\varepsilon}{k}+300} \text{ } (in\ absence\ of\ organic\ acids) \end{cases}$$ Eq. A11

For compound *i*:

$$\omega_i' = 0.006R_i' + 0.02087R_i'^2 - 0.00136R_i'^3$$ Eq. A12

$$\frac{\varepsilon_i'}{kT_{c_i}} = 0.748 + 0.91\omega_i' - \frac{0.4\eta}{2 + 20\omega_i'}$$ Eq. A13

$$\sigma_i = (2.44 - \omega')\left(\frac{T_{c_i}}{P_{c_i}}\right)^{\frac{1}{3}}$$ Eq. A14

For non-polar components:

$$\mu^* = \frac{\mu^2}{\varepsilon\sigma^3}$$ Eq. A15

For polar components:

$$n_i = 16 + 400\omega_i'$$ Eq. A16

$$C_i = 2.882 - \frac{1.882\omega_i'}{0.03 + \omega_i'}$$ Eq. A17

$$\xi_i = \frac{k\mu_i^4}{5.723 \times 10^{-8} C\varepsilon_i'\sigma_i'^6 T_{c_i}}$$ Eq. A18

$$\varepsilon_i = \varepsilon_i'\left\{1 - \frac{n_i}{n_i - 6}\xi_i\left[1 - \left(\frac{n_i}{n_i - 6} + 1\right)\frac{\xi_i}{2}\right]\right\}$$ Eq. A19

$$\sigma_i^3 = \sigma_i'^3\left[1 + \frac{3\xi_i}{n_i - 6}\right]$$ Eq. A20

Cross coefficients are calculated as follows:

$$\varepsilon_{ij} = 0.7\left(\varepsilon_i\varepsilon_j\right)^{\frac{1}{2}} + 0.6\left(\frac{1}{\varepsilon_i} + \frac{1}{\varepsilon_j}\right)$$ Eq. A21

$$\sigma_{ij} = \left(\sigma_i\sigma_j\right)^{\frac{1}{2}}$$ Eq. A22

$$\omega_{ij}' = 0.5(\omega_i' + \omega_j')$$ Eq. A23

$$\omega_{ij}' = 0.5(\omega_i' + \omega_j')$$ Eq. A24

Especially between polar/non-polar components:

$$\xi^{pn} = \frac{\mu_i^2 (\varepsilon_j)^{\frac{2}{3}} (\sigma_j)^4}{\varepsilon_{ij} (\sigma_{ij})^6} \quad \text{Eq. A25}$$

$$n = 16 + 400\omega'_{ij} \quad \text{Eq. A26}$$

$$\varepsilon_{ij}^{pn} = \varepsilon_{ij} \left[1 + \frac{\xi^{pn} n}{n-6}\right] \quad \text{Eq. A27}$$

$$\left(\sigma_{ij}^{pn}\right)^3 = \left(\sigma_{ij}\right)^3 \left[1 - \frac{3\xi^{pn}}{n-6}\right] \quad \text{Eq. A28}$$

$$\mu^{*\prime}{}_{ij} = \begin{cases} \mu_{ij}^* - 0.25, & \mu_{ij}^* \geq 0.25 \\ 0, & 0.25 > \mu_{ij}^* \geq 0.04 \\ \mu_{ij}^*, & 0.04 > \mu_{ij}^* \geq 0 \end{cases} \quad \text{Eq. A29}$$

The mixing rule for *B* is:

$$B = \sum_i \sum_j y_i y_j B_{total_{ij}} \quad \text{Eq. A30}$$

In the absence of organic acids, the fugacity coefficient of component *i* is calculated from:

$$\hat{\varphi}_i = exp\left(\left[2\sum_{j=1}^{N} y_j B_{ij} - B\right]\frac{PR}{T}\right) \quad \text{Eq. A31}$$

In the presence of organic acids, the dimerization constant can be calculated from:

$$K_p = -\frac{B_{bound} + B_{metastable} + B_{chem}}{RT} \quad \text{Eq. A32}$$

$$K_t = K_p P \, exp\frac{B_{free} P}{RT} \quad \text{Eq. A33}$$

If a is an associating compound and b a non-associating compound, then:

$$z_{\mathrm{a}} = \frac{\sqrt{1 + 4K_t y_{\mathrm{a}}(2 - y_{\mathrm{a}})} - 1}{2K_t(2 - y_{\mathrm{a}})} \quad \text{Eq. A34}$$

$$z_b = y_b \frac{1 + 4K_t(2 - y_{\mathrm{a}}) - \sqrt{1 + 4K_t y_{\mathrm{a}}(2 - y_{\mathrm{a}})}}{2K_t(2 - y_{\mathrm{a}})^2} \quad \text{Eq. A35}$$

and the fugacity coefficient of component *i* is calculated from:

$$\varphi_i = \frac{z_i}{y_i} \exp\frac{B_{i,free} P}{RT} \quad \text{Eq. A36}$$

Nomenclature

b_0: equivalent hard-sphere volume of molecules, $\frac{cm^3}{g\ mol}$

ΔH: effective enthalpy of formation of physically bound pairs, $\frac{ergs}{molecule}$

k: Boltzman constant (1.3805×10^{-16}), $\frac{ergs}{moleculeK}$

K_p: equilibrium constant for "chemical" theory of vapor nonideality, atm^{-1}

N_0: Avogadro's number (6.0225×10^{23}), $\frac{molecules}{mol}$

P: pressure, atm

T: temperature, K

R: universal gas constant (82.054), $\frac{cm^3 atm}{gmolK}$

R': mean radius of gyration, Å

$T^{*\prime}$: reduced temperature

P_c, T_c: critical pressure and temperature, respectively

y_i: vapor mole fraction of component *i*

ε, ε' : energy parameters, $\frac{ergs}{molecule}$

ξ: angle averaged polar effect for pure substances

ξ^{pn}: angle averaged polar effect for unlike polar/non-polar interactions

η: association parameter for pure interactions, solvation parameter for unlike interactions

μ: molecular dipole moment, $D\ (10^{-18} esu)$

μ^*: reduced dipole moment

σ, σ': molecular size parameters, Å

$\hat{\varphi}_i$: vapor phase fugacity coefficient of component *i*

ω': "non-polar" acentric factor

Appendix B: Model parameters

Table B1. Mathias-Copeman parameters employed for UMR-PRU model.

Compound	Ref.	c_1	c_2	c_3
Hg	This work	0.14910	-0.16520	0.14470
H_2O	[2]	0.92366	-0.37937	0.44243
MeOH	[2]	1.22400	-0.27350	-0.39823
MEG	[3]	0.91003	1.34996	-1.89002
TEG	[4]	1.55075	-0.77780	0.31779
MEA	[5]	1.88180	-3.45160	5.84090
MDEA	[6]	2.46940	-3.81470	2.87170
MTBE	[7]	0.73832	0.17566	-0.05901
Acetic acid	[7]	1.22453	-1.57640	2.41004
Isopropanol	[7]	1.18454	0.69615	0.03812
Isopropyl acetate	This work	0.84758	0.52717	-0.94506

Table B2. Extended Antoine parameters [8].

Component	*a*	*b*	*c*	*d*	*e*
Methanol	71.205	-6904.5	-8.8622	7.466E-06	2
Isobutene	66.490[a]	-4634.1	-8.8975	1.341E-05	2
MTBE	45.617	-5200.7	-5.1398	1.651E-17	6
n-butane	54.830	-4363.2	-7.0460	9.451E-06	2
Acetic acid	41.757	-6304.5	-4.2958	8.887E-18	6
Isopropanol	99.207	-9040.0	-12.676	5.538E-06	2
Water	62.136	-7258.2	-7.3037	4.165E-06	2
Isopropyl acetate	38.241	-5563.9	-3.8789	2.476E-18	6

[a] Determined in this work.

Table B3. Group volume (R_k) and area parameters (Q_k) employed by UMR-PRU.

Group	R_k	Q_k
Hg	10.598	8.739
H_2	0.4160	0.571
H_2S	1.1665	1.163
CO_2	1.2960	1.261
N_2	0.9340	0.985
CH_4	1.1290	1.124
C_2H_6	1.8022	1.696
CH_3	0.9011	0.848
CH_2	0.6744	0.540
CH	0.4469	0.228

C	0.2195	0.000
bCH_3	0.9011	0.848
cCH_2	0.6744	0.540
cCH	0.4469	0.228
cC	0.2195	0.000
ACH	0.5313	0.400
AC	0.3652	0.120
$ACCH_3$	1.2663	0.968
$ACCH_2$	1.0396	0.660
ACCH	0.8121	0.348
H_2O	0.9200	1.400
MeOH	1.4311	1.432
EtOH	2.1054	1.972
MEG	2.4088	2.248
TEG	5.5942	4.880
MEA	2.5736	2.360
MDEA	4.9441	4.268

Table B4. UNIFAC interaction parameters employed by UMR-PRU.

m	n	A_{mn} (K)	B_{mn} (-)	C_{mn} (K^{-1})	A_{nm} (K)	B_{nm} (-)	C_{nm} (K^{-})
Hg	CO_2	681.17	4.5484	0	237.93	-1.4951	0
Hg	N_2	418.60	6.2324	0	308.81	-1.8667	0
Hg	CH_4	393.82	-0.0931	0	306.29	0.1852	0
Hg	C_2H_6	-80.36	0.5104	0	579.48	-0.6852	0
Hg	CH_2	947.05	4.9112	0	200.84	-0.9092	0
Hg	bCH_2	253.49	0.4966	0	362.76	-0.1603	0
Hg	cCH_2	733.53	3.1005	0	198.74	-0.9496	0
Hg	ACH	392.95	0.1600	0	245.11	-0.4325	0
Hg	$ACCH_2$	281.25	0.1781	0	295.44	1.0930	0
Hg	H_2O	-194.37	0.4464	0	534.35	-0.9257	0
Hg	MeOH	21.18	-0.1532	0	478.01	0.3878	0
Hg	OH	973.93	3.346	0	203.34	-0.2067	0
Hg	MEG	-9.01	-0.1574	0	535.30	0.4901	0
Hg	TEG	-34.38	1.0532	0	536.25	-0.5657	0
Hg	MEA	-52.59	1.6500	0	562.95	-1.7985	0
Hg	MDEA	14.72	0.8337	0	483.64	-0.5336	0
H_2	CO_2	-53.53	-3.276	0	521.47	0.783	0
H_2	N_2	-19.32	-0.220	0	-86.71	-1.009	0
H_2	H_2S	-107.19	-7.431	0	-29.37	-8.694	0
H_2	CH_4	-82.98	-0.121	0.003020	387.15	1.291	0.000835

H_2	C_2H_6	-185.68	-2.540	-0.003163	517.10	4.375	0.015912
H_2	CH_2	186.74	-0.711	-0.000685	-8.51	-0.934	0.002376
H_2	cCH_2	-89.31	1.945	0.000857	322.35	-3.218	0.002126
H_2	ACH	8.32	1.879	-0.001080	328.04	-3.016	0.000815
H_2	$ACCH_2$	233.79	10.954	-0.013743	83.44	-4.348	0.009500
H_2	H_2O	520.94	6.421	-0.044775	1251.53	7.474	-0.019891
H_2	MeOH	234.28	26.433	0.325551	371.45	-4.112	0.028524
H_2	MEG	232.72	0.852	0	419.94	-1.103	0
H_2	TEG	305.47	-1.018	0	443.90	-0.885	0
H_2S	CO_2	126.86	0.4804	0	87.97	-0.9614	0
H_2S	N_2	359.61	-1.4872	-0.007935	311.06	0.9930	0.041210
H_2S	CH_4	277.08	-0.5438	0	62.67	-0.0552	0
H_2S	C_2H_6	117.32	0.2769	0.005079	158.23	0.1221	0.006173
H_2S	CH_2	172.13	0.4456	-0.004905	35.71	-1.7086	0.006563
H_2S	ACH	63.79	1.0166	0.020113	-80.36	-2.2150	0.000606
H_2S	$ACCH_2$	-100.58	-0.6205	0.007750	350.93	0.6347	-0.018859
H_2S	H_2O	143.28	4.0434	-0.039800	487.63	1.4599	-0.007830
CO_2	C_2H_6	92.20	-0.6847	0	110.50	-0.3805	0
CO_2	CH_2	68.56	-0.8739	-0.000080	90.68	-0.5714	0.005770
CO_2	ACH	16.20	-2.2538	0.001050	94.49	1.5570	0.007850
CO_2	$ACCH_2$	-102.70	-3.0502	0.012000	274.36	15.5931	0.012930
N_2	CH_4	-141.07	-0.8494	0	192.06	0.7909	0
N_2	C_2H_6	-157.17	-0.9411	0	308.97	1.0030	0
N_2	CO_2	-128.17	-1.6650	0	366.62	1.5300	0
N_2	CH_2	833.27	-2.5383	0.036193	-190.64	-0.9754	-0.001980
N_2	ACH	363.68	1.8010	-0.006569	37.23	-1.2050	-0.001061
N_2	$ACCH_2$	264.19	-3.6140	0.015020	122.55	0.5598	-0.003968
CH_4	CO_2	85.80	-0.1959	0	126.21	-0.4439	0
CH_4	C_2H_6	79.06	0.2497	0	-56.01	-0.1798	0
CH_4	CH_2	555.48	2.8287	-0.010592	-268.42	-1.2346	0.001094
CH_4	ACH	108.99	1.6950	0.000509	-63.53	-1.3050	0.002178
CH_4	$ACCH_2$	169.99	-3.1420	0.010180	-88.33	1.3930	-0.008429
C_2H_6	CH_2	-73.88	-0.4092	0.000065	61.45	0.1126	0.000955
C_2H_6	ACH	-104.18	0.1872	0	171.39	-0.7241	0
C_2H_6	$ACCH_2$	-240.46	-1.2151	-0.000086	674.59	2.5318	0.051615
H_2O	CH_4	642.84	5.1182	-0.013506	1439.17	-6.87672	0.018497
H_2O	C_2H_6	549.86	3.0874	-0.007000	1490.90	-3.0931	-0.005000
H_2O	CO_2	238.53	2.5382	0.001723	794.50	-4.6872	0.003950
H_2O	N_2	807.57	6.0191	-0.019880	3000.00	0	0
H_2O	CH_2	425.51	2.3347	-0.010620	1303.83	-4.3634	0.006676
H_2O	ACH	261.18	1.0780	-0.005283	820.93	-2.9670	0.002283
H_2O	$ACCH_2$	219.27	3.2111	-0.015400	1131.26	-6.6481	0.026300
H_2O	MeOH	28.66	4.096	0	-34.07	-2.069	0
H_2O	MEG	-188.03	0.0	0	66.72	0	0

H_2O	TEG	472.57	-1.4976	0	-362.51	0.3311	0
MeOH	CO_2	-81.43	0.7278	0.005110	438.59	-1.0752	0.096718
MeOH	N_2	157.38	-0.3731	0.000391	583.38	3.9399	0.000500
MeOH	CH_4	-18.94	1.0329	0.012878	839.66	-6.7000	-0.006070
MeOH	C_2H_6	156.75	1.5900	0.004300	173.38	-0.9464	0.000100
MeOH	CH_2	28.03	-1.1030	0	617.00	3.838	0
MeOH	ACH	-44.29	0.2903	0	594.40	-1.204	0
MeOH	$ACCH_2$	217.80	-4.0190	0	548.80	19.55	0
MeOH	MEG	221.00	-4.4310	0	-168.70	6.0080	0
MEG	CO_2	218.39	-5.6585	0.030200	135.72	8.4768	0.143800
MEG	N_2	500.41	3.9826	0	635.01	-6.7326	0
MEG	CH_4	286.83	0.9565	-0.009268	1279.79	-2.5213	-0.005195
MEG	C_2H_6	257.33	1.3800	0.004300	525.04	-4.3369	0.008900
MEG	CH_2	-79.67	2.1360	0	1425.00	11.500	0
MEG	ACH	155.60	-0.5324	0	266.70	1.057	0
MEG	$ACCH_2$	2127.00	-11.9000	0	1714.00	4.024	0
TEG	CO_2	-103.95	1.5947	0.004961	372.26	-4.2923	0.007164
TEG	N_2	592.37	-1.3372	0	347.58	2.6335	0
TEG	CH_4	225.27	-3.9421	0.011400	194.03	6.0149	0.037400
TEG	C_2H_6	4.06	-0.9091	0.001700	1164.88	-3.6733	0.000200
TEG	CH_2	103.84	-0.6775	0.000500	291.99	1.1706	-0.008300
TEG	ACH	-13.11	-0.8810	0	158.47	1.3927	0
TEG	$ACCH_2$	-120.77	1.9055	0	966.73	-5.4262	0
MEA	CO_2	-295.18	-2.0348	0	-2333.98	-8.2754	0
MEA	H_2O	-209.61	1.1600	0	-66.25	-0.8100	0
MDEA	CO_2	3211.84	2.1900	0	3313.90	1.8900	0
MDEA	CH_4	687.01	-0.7197	-0.008700	319.17	-6.6222	0.034260
MDEA	H_2O	-164.86	0.3899	0.011100	37.73	0.7165	-0.016900

Table B5. UNIQUAC binary interaction parameters employed for MTBE synthesis system (A'_{ij}= 0) [8].

B'_{ij} (K)	Methanol	Isobutene	MTBE	n-butane
Methanol	0	41.67	76.16	-13.16
Isobutene	-766.91	0	162.97	28.53[a]
MTBE	-431.66	-232.67	0	-148.00[a]
n-butane	-638.06	-37.68[a]	114.93[a]	0

[a] Determined in this work.

Table B6. UNIQUAC binary interaction parameters employed for acetic acid/isopropanol esterification system [8].

A'_{ij} (-)	Acetic acid	Isopropanol	Water	Isopropyl acetate
Acetic acid	0	0	0	0
Isopropanol	0	0	2.923	0
Water	0	-3.313	0	0
Isopropyl acetate	0	0	0	0
B'_{ij} (K)	**Acetic acid**	**Isopropanol**	**Water**	**Isopropyl acetate**
Acetic acid	0	284.65	-539.14[a]	188.43[a]
Isopropanol	-301.83	0	-1133.35[a]	67.34
Water	280.86[a]	1106.26[a]	0	-124.82
Isopropyl acetate	-435.17[a]	-163.54	-404.29	0

[a] Determined in this work.

Table B7. Pure component properties employed for estimating second virial coefficients for acetic acid/isopropanol esterification system via the Hayden-O' Connell method.

	Acetic acid	Isopropanol	Water	Isopropyl acetate
μ (D)	1.738801	1.660854	1.849724	1.750792
R' (Å)	2.595	2.76	0.615	3.679
T_c (K)	318.8	235.15	373.946	258.85
P_c (bar)	57.86	47.65	220.64	32.9
η	4.5	1.32	1.7	0

Table B8. Cross solvation parameters (*η*) employed for estimating second virial coefficients for acetic acid/isopropanol esterification system via the Hayden-O' Connell method.

	Acetic acid	Isopropanol	Water	Isopropyl acetate
Acetic acid	4.5	2.5	2.5	2.0
Isopropanol	2.5	1.32	1.55	1.3
Water	2.5	1.55	1.7	1.3
Isopropyl acetate	2.0	1.3	1.3	0

Appendix C: Database with experimental data

Table C1. Database with experimental Hg^0 solubilities employed for UMR-PRU parameter fitting.

Solvent	Ref.	Type	T range (K)	P range (bar)	ND[a]
CO_2	[9]	VLE/LLE	243.15-323.15	3.9-137.9	24
N_2	[9]	SC	244.35-323.18	6.9-172.8	24
CH_4	[9, 10]	SC	244.35-323.15	5.5-186.2	74
C_2H_6	[9, 10]	VLE/LLE	243.99-323.15	5.5-113.8	51
C3	[9, 11, 12]	LLE	233.15-343.15	1.0-34.5	16
nC5	[12]	LLE	233.15-323.15	1.0	4
nC6	[13]	LLE	273.15-338.15	1.0	14
nC7	[13]	LLE	273.15-313.15	1.0	9
nC8	[12-14]	LLE	233.15-473.15	1.0	17
nC10	[13]	LLE	273.15-318.15	1.0	10
nC12	[14, 15]	LLE	273.15-498.15	1.0	9
nC20	[15]	LLE	313.15-363.15	1.0	3
nC28	[15]	LLE	363.15-383.15	1.0	3
iC4	[16]	VLLE	263.15-283.15	1.1-2.2	5
2-m-C5	[15]	LLE	273.15-313.15	1.0	3
2,2-dm-C4	[13]	LLE	273.15-308.15	1.0	8
2,2,4-tm-C5	[13]	LLE	273.15-308.15	1.0	8
cyC5	[15]	LLE	273.15-303.15	1.0	4
m-cyC5	[15]	LLE	273.15-333.15	1.0	4
cyC6	[13, 15]	LLE	288.15-333.15	1.0	9
m-cyC6	[13]	LLE	273.15-308.15	1.0	8
cis-1,2-dm-cyC6	[13]	LLE	288.15-308.15	1.0	5
cis-1,4-dm-cyC6	[13]	LLE	288.15-308.15	1.0	5
trans-1,2-dm-cyC6	[13]	LLE	288.15-308.15	1.0	5
trans-1,4-dm-cyC6	[13]	LLE	288.15-308.15	1.0	5
cyC8	[15]	LLE	293.15-333.15	1.0	3
benzene	[13]	LLE	288.15-308.15	1.0	6
ethylbenzene	[15]	LLE	293.15-333.15	1.0	3
1,2,4-tm-benzene	[15]	LLE	293.15-333.15	1.0	3
isopropyl benzene	[13]	LLE	273.15-308.15	1.0	8
t-butyl benzene	[13]	LLE	273.15-313.15	1.0	9
toluene	[12, 13, 15]	LLE	233.15-419.15	1.0	21
o-xylene	[13]	LLE	273.15-308.15	1.0	8
m-xylene	[15]	LLE	293.15-333.15	1.0	3
naphthalene	[15]	LLE	363.15-383.15	1.0	3
water	[17]	LLE	273.15-373.15	1.0	8
methanol	[17]	LLE	243.15-373.15	1.0	11
ethanol	[15]	LLE	283.15-323.15	1.0	3
propanol	[15]	LLE	283.15-323.15	1.0	3
MEG	[15]	LLE	283.15-373.15	1.0	7

TEG	[15]	LLE	293.15-373.15	1.0	6
MEA	[15]	LLE	293.15-323.15	1.0	4
MDEA	[15]	LLE	293.15-323.15	1.0	4
				Total	**440**

[a] ND: Number of experimental data points.

Table C2. Database with experimental Hg^0 solubilities employed for model predictions.

Solvent	Ref.	Type	T range (K)	P range (bar)	ND[a]
CO_2	[10]	VLLE	268.15-303.15	5.5-20.7	24
N_2	[11]	Supercritical	273.15	6.9-69.3	6
CH_4	[11, 16]	Supercritical	248.15-293.15	27.6-69.0	46
nC5	[13, 16]	LLE	258.15-313.15	1.0-22.4	16
nC6	[15]	LLE	283.15-323.15	1.0	3
methanol	[13, 15, 18]	LLE	253.00-333.15	1.0	17
MEG	[18]	LLE	253.00-373.00	1.0	7
TEG	[18]	LLE	293.00-373.00	1.0	5
				Total	**121**

[a] ND: Number of experimental data points.

Table C3. Database with experimental VLE data in hydrogen systems employed for UMR-PRU parameter fitting.

H_2 with	T range (K)	P range (bar)	NDP[a]	NDy[b]	Ref.
CO_2	219.90 - 298.15	9.3 - 1718	263	245	[19-21]
N_2	63.19 - 113.00	8.44 - 572.2	138	135	[19, 21, 22]
H_2S	243.15 - 273.15	10.1 - 50.7	11	0	[21]
CH_4	90.30 - 183.12	2.2 - 1380	560	554	[19, 21, 23, 24]
C_2H_6	92.50 - 283.15	7.08 - 5595	380	371	[19, 25]
C3	172.05 - 360.93	13.79 - 551.58	116	116	[19, 21]
nC4	144.26 - 394.25	20.68 - 541.24	110	104	[19, 21]
nC5	273.15 - 463.15	3.47 - 275.9	111	30	[26, 27]
nC6	277.59 - 477.59	12.4 - 689.47	157	99	[19, 28, 29]
nC7	238.15 - 498.85	1.01 - 784.52	42	27	[19, 30-32]
nC8	248.15 - 543.15	1.01 - 173.3	77	50	[28, 30-34]
nC10	283.17 - 583.45	12.38 - 255.24	253	26	[21, 26, 28, 35-37]
nC12	344.30 - 410.90	14.2 - 132.4	24	0	[38]
nC14	328.15 - 473.15	40.5 - 304.0	12	0	[21]
nC16	298.13 - 664.05	11.51 - 253.82	186	73	[21, 35, 39]
nC20	323.20 - 573.25	9.94 - 129.1	37	10	[36, 40]
iC4	310.93 - 394.26	34.47 - 206.84	22	22	[21]
2,3-dm-C4	308.15 - 483.15	27.17 - 164.5	92	0	[26]
iC8	248.15 - 523.15	1.01 - 368.0	50	29	[21, 32]

cyC6	293.95 - 493.15	1.01 - 690.37	181	69	[21, 26, 32, 41, 42]
m-cyC6	295.00 - 295.00	69.9 - 207.8	5	0	[32]
b-cyC6	462.15 - 701.65	20.27 - 253.31	28	28	[19]
benzene	283.15 - 533.15	1.01 - 689.27	100	75	[21, 32, 43-45]
toluene	258.15 - 575.15	1.01 - 323.0	87	25	[19, 21, 28, 32, 46, 47]
m-xylene	295.00 - 593.15	19.86 - 254.4	105	27	[21, 26, 32]
p-xylene	308.15 - 573.15	26.66 - 148.75	117	0	[26]
e-benzene	295.00 - 295.00	104.4 - 173.3	3	0	[32]
1,2,4-tm-benzene	295.00 - 295.00	69.9 - 173.3	4	0	[32]
1,3,5-tm-benzene	298.15 - 513.15	49.0- 294.1	6	0	[21]
isopropylbenzene	323.00 - 373.15	7.91 - 117.0	15	0	[41, 48]
diphenylmethane	462.75 - 701.65	20.27 - 253.31	27	27	[21]
naphthalene	373.20 - 423.20	42.90 - 193.9	14	0	[44]
1-m-naphthalene	393.15 - 730.05	20.27 - 277.83	107	45	[21, 26]
phenanthrene	383.20 - 539.10	26.13 - 252.3	65	28	[39, 44, 49]
tetralin	423.15 - 662.25	17.37 - 273.3	75	62	[19, 50-52]
H_2O	273.15 - 616.48	1.01 - 1,013	126	27	[21, 53-57]
MeOH	243.15 - 413.00	10.0 - 811.0	76	5	[21]
MEG	298.15 - 373.15	19.16 - 99.9	13	0	[21]
TEG	298.15 - 373.15	19.94 - 104.1	12	0	[21]
		Total	**3807**	**2309**	

[a] NDP: Number of experimental bubble point pressures.

[b] NDy: Number of experimental vapor phase mole fractions.

Table C4. Experimental phase equilibrium data employed for model evaluation in Chapter 11.

System	Ref.	Type	ND[a]	T range (K)	P range (bar)
MTBE/MeOH	[58]	VLE	33	333.15	0.85-1.38
MTBE/i-butene	[59]	VLE	16	323.15-353.15	0.86-12.24
MTBE/nC4	[60]	VLE	19	373.17	3.60-15.18
MeOH/i-butene	[61]	VLE	11	333.14	0.55-6.31
MeOH/nC4	[61, 62]	VLE	34	273.15-373.15	0.04-17.18
i-butene/nC4	[63]	VLE	12	277.59-294.26	1.32-2.58
Acetic acid/isopropanol	[64]	VLE	19	355.55-390.85	1.013
Acetic acid/isopropyl acetate	[65, 66]	VLE	33	363.95-388.05	1.013
Acetic acid/water	[67-69]	VLE	43	373.65-388.49	1.013
Isopropanol/isopropyl acetate	[70, 71]	VLE	61	353.65-361.75	1.013
Isopropanol/water	[72, 73]	VLE	32	353.34-373.15	1.013
Water/isopropyl acetate	[74-76]	LLE	11	282.15-347.75	1.013
MTBE/MeOH/i-butene	[77]	VLE	19	333.20-353.20	3.65-11.11
Acetic acid/isopropanol/water/isopropyl acetate	[78]	VLE	44	356.45-382.65	1.013

[a] ND: Number of experimental data points.

Appendix D: Simulation data

Table D1. Pseudocomponent properties provided by offshore plant operator.

Component	MW (g/mol)	T_b (K)	T_c (K)	P_c (bar)	ω (-)
C6*	86.18	357.15	511.93	30.12	0.3038
C7*	90.96	389.75	527.12	30.46	0.3206
C8*	103.43	389.75	552.16	27.92	0.3625
C9*	117.19	415.35	576.64	25.53	0.4081
C10-C12*	145.81	460.35	620.23	21.76	0.5008
C13-C14*	181.33	544.50	667.69	18.91	0.6120
C15-C16*	212.28	574.18	704.76	17.28	0.7047
C17-C19*	248.14	605.15	744.45	15.95	0.8067
C20-C22*	289.22	637.23	786.98	14.90	0.9153
C23-C25*	330.34	666.42	827.11	14.15	1.0135
C26-C30*	384.70	701.51	877.41	13.42	1.1245
C31-C38*	471.16	751.07	952.91	12.66	1.2467
C39-C80*	662.46	842.39	1107.93	11.76	1.2260

Table D2. Pseudocomponent properties calculated via TTPL characterization method [79].

Component	MW (g/mol)	T_b (K)	T_c (K)	P_c (bar)	ω (-)
C7*	94.00	366.82	549.28	32.09	0.2883
C8*	108.00	397.73	587.79	30.28	0.3194
C9*	122.00	426.64	623.02	28.69	0.3491
C10*	136.00	453.87	655.59	27.29	0.3776
C11*	150.00	479.68	685.94	26.04	0.4051
C12*	164.00	504.28	714.42	24.93	0.4318
C13*	178.00	527.80	741.27	23.92	0.4579
C14*	192.00	550.38	766.71	23.01	0.4833
C15*	205.99	572.12	790.91	22.18	0.5082
C16*	219.99	593.11	814.01	21.42	0.5328
C17*	234.03	613.45	836.17	20.72	0.5570
C18*	257.03	645.75	870.97	19.67	0.5960
C19*	265.33	652.81	875.38	19.08	0.6154
C20*	282.60	662.34	874.61	17.40	0.6677
C22*	309.72	684.24	887.85	15.75	0.7375
C27*	373.04	726.34	905.77	12.35	0.9275
C37*	513.40	847.13	1012.23	9.99	1.2633

Table D3. Estimated elemental (Hg^0) and total (THg) mercury mass flowrates at plant outlets, based on field campaign measurements, actual process data (flowrates) and densities.

Stream	Flowrate	Density (kg/m^3)	Hg^0 conc.	Hg^0 flowrate (g/d)	THg conc.	THg flowrate (g/d)
Export gas	33.48 MSm^3/d	N/A	10.6 µg/Sm^3	354.9	10.6 µg/Sm^3	354.9
Export cond.	5821 m^3/d	737	9.2 µg/kg	39.5	12.2 µg/kg	52.3
Hg removal from TEG contactor A				24.1		24.1
Hg removal from TEG contactor B				9.8		9.8
Hg removal from amine contactor				34.1		34.1
Water from Feed A inlet separators	469.1 tn/d	N/A	<0.1	-	1.6	0.75
Water from Feed B inlet separators + test separator	357.1 tn/d	N/A	<0.1	-	2.0	0.71
			Total	**462.4**		**476.7**

Table D4. Elemental mercury concentration in selected plant streams as calculated with SRK-Twu and different equilibrium constants (Table 9.3) for the liquid phase reaction.

Description/Tag	Stream	Units	Measured (Hg^0)	KL1	KL2	KL3
Feed A inlet sep. (10-101)	Inlet	ppb mol	-	1.9	1.9	1.9
Feed B inlet sep. (10-201)	Inlet	ppb mol	-	1.6	1.6	1.6
Test separator (10-001)	Inlet	ppb mol	-	14.6	14.6	14.6
Test separator (10-001)	Vapor	µg/Sm^3	**95.2**	42.0	65.7	76.2
Test separator (10-001)	Liquid	µg/kg	**17.5**	77.7	121.4	140.9
Test separator (10-001)	Water	µg/kg	**< 0.1**	1.6	2.4	2.8
Stabilizer tank (10-008)	Inlet	µg/kg	**2.2**	17.1	28.6	33.0
Stabilizer tank (10-008)	Vapor	µg/Sm^3	**49.6**	37.3	62.7	72.6
Stabilizer tank (10-008)	Liquid	µg/kg	**3.8**	16.7	28.3	32.7
Feed A inlet sep. (10-101/401)	Water	µg/kg	**< 0.1**	0.2	0.3	0.4

Amine contactor (20-103)	Inlet	µg/Sm^3	**32.9**	11.0	19.3	22.2
Glycol contactor (30-101/201)	Inlet	µg/Sm^3	**12.3**	5.9	9.7	11.0
Export gas	-	µg/Sm^3	**10.6**	5.7	9.4	10.6
Export cond.	-	µg/kg	**9.2**	11.6	20.6	23.9
Feed A gases	-	µg/Sm^3	**27.9**	7.4	11.1	12.6
Feed B gases	-	µg/Sm^3	**1.95**	3.4	5.1	5.5

Appendix E: Publications

A. Publications in peer-reviewed scientific journals

1. V. Koulocheris, V. Louli, E. Panteli, S. Skouras, E. Voutsas, "Modelling of elemental mercury solubility in natural gas components". Fuel, 2018. **233**: p. 558-564.
2. V. Koulocheris, V. Louli, E. Panteli, S. Skouras, E. Voutsas, "Modelling of hydrogen vapor-liquid equilibrium with oil & gas components". Fluid Phase Equilibria, 2019. **494**: p. 125-134.
3. V. Koulocheris, M. Panteli, E. Petropoulou, V. Louli, E. Voutsas, "Modeling of simultaneous chemical and phase equilibria in systems involving non-reactive and reactive azeotropes". Industrial & Engineering Chemistry Research, 2020. **59** (18): p. 8836-8847.
4. V. Koulocheris, A. Plakia, V. Louli, E. Panteli E. Voutsas, "Calculating the chemical and phase equilibria of mercury in natural gas". Chemical Engineering Science, 2021. (submitted)

B. Communications in conferences

1. V. Koulocheris, V. Louli, E. Panteli, S. Skouras, E. Voutsas, "Predicting the solubility of mercury in hydrocarbons, compressed gases, water and methanol with the UMR-PRU model". 30th European Symposium on Applied Thermodynamics, Prague, Czech Republic, 10-13 June 2018. (poster)

2. Petropoulou, E., Novak, N., Koulocheris, V., Louli, V., Pappa, G., Boukouvalas, Ch., Voutsas, E., "Thermodynamic modelling and simulation of natural gas processes". National Scientific Conference of Chemical Engineering, Athens, 29-31 May 2019. (poster)

3. V. Koulocheris, V. Louli, E. Panteli, E. Voutsas, "Chemical and phase equilibria of mercury in natural gas with the UMR-PRU model". 31st European Symposium on Applied Thermodynamics, Paris, France, 4-7 July 2021. (oral presentation - accepted)

Appendix References

1. Hayden, J.G. and J.P. O'Connell, *A Generalized Method for Predicting Second Virial Coefficients.* Industrial & Engineering Chemistry Process Design and Development, 1975. **14**(3): p. 209-216.

2. Boukouvalas, C., et al., *Prediction of vapor-liquid equilibrium with the LCVM model: a linear combination of the Vidal and Michelsen mixing rules coupled with the original UNIFAC and the t-mPR equation of state.* Fluid Phase Equilibria, 1994. **92**: p. 75-106.

3. Petropoulou, E., G.D. Pappa, and E. Voutsas, *Modelling of phase equilibrium of natural gas mixtures containing associating compounds.* Fluid Phase Equilibria, 2017. **433**: p. 135-148.

4. Petropoulou, E.G. and E.C. Voutsas, *Thermodynamic Modeling and Simulation of Natural Gas Dehydration Using Triethylene Glycol with the UMR-PRU Model.* Industrial & Engineering Chemistry Research, 2018. **57**(25): p. 8584-8604.

5. Vrachnos, A., G. Kontogeorgis, and E. Voutsas, *Thermodynamic Modeling of Acidic Gas Solubility in Aqueous Solutions of MEA, MDEA and MEA−MDEA Blends.* Industrial & Engineering Chemistry Research, 2006. **45**(14): p. 5148-5154.

6. Vrachnos, A., et al., *Thermodynamics of Acid Gas−MDEA−Water Systems.* Industrial & Engineering Chemistry Research, 2004. **43**(11): p. 2798-2804.

7. Hernández-Garduza, O., et al., *Vapor pressures of pure compounds using the Peng–Robinson equation of state with three different attractive terms.* Fluid Phase Equilibria, 2002. **198**(2): p. 195-228.

8. *Aspen Plus v8.8*. 2014, Aspen Technology Inc.: Cambridge, MA.

9. Chapoy, A., et al., *Elemental mercury partitioning in high pressure fluids part 1: Literature review and measurements in single components.* Fluid Phase Equilibria, 2020. **520**: p. 112660.

10. Yamada, J., et al., *Mercury solubility measurements in natural gas components at high pressure.* Fluid Phase Equilibria, 2020. **506**: p. 112342.

11. Equinor, *Internal Report*. 2014.

12. Marsh, K.N., et al., *Solubility of Mercury in Liquid Hydrocarbons and Hydrocarbon Mixtures.* Journal of Chemical & Engineering Data, 2016. **61**(8): p. 2805-2817.

13. Clever, H.L., *Mercury in Liquids, Compressed Gases, Molten Salts and Other Elements*. IUPAC Solubility Data Series. 1987, Amsterdam: Pergamon. 102-162.

14. Miedaner, M.M., A.A. Migdisov, and A.E. Williams-Jones, *Solubility of metallic mercury in octane, dodecane and toluene at temperatures between 100°C and 200°C.* Geochimica et Cosmochimica Acta, 2005. **69**(23): p. 5511-5516.

15. Equinor, *Internal Report*. 2019.

16. Butala, S.J.M., G.M. Wilson, and L.V. Jasperson, *Elemental Mercury Equilibrium in Selected Saturated Hydrocarbons*. 2016, Gas Processors Association Research Report RR 224.

17. Gallup, D.L., D.J. O'Rear, and R. Radford, *The behavior of mercury in water, alcohols, monoethylene glycol and triethylene glycol.* Fuel, 2017. **196**: p. 178-184.

18. Li, J., et al., *Measurement of Elemental Mercury Solubility in Natural Gas Dehydrating Solvents.* IOP Conference Series: Materials Science and Engineering, 2018. **394**: p. 022060.

19. Knapp, H., et al., *Vapor-Liquid Equilibria for Mixtures of Low Boiling Substances*. Chemistry Data Series. Vol. VI. 1982, Frankfurt: Dechema.

20. Bezanehtak, K., et al., *Vapor–Liquid Equilibrium for Binary Systems of Carbon Dioxide + Methanol, Hydrogen + Methanol, and Hydrogen + Carbon Dioxide at High Pressures.* Journal of Chemical & Engineering Data, 2002. **47**(2): p. 161-168.

21. Young, C.L., *Hydrogen and Deuterium*. IUPAC Solubility Data Series. Vol. 5/6. 1981, Oxford, UK: Pergamon Press.

22. Yorizane, M., et al., *Measurement and prediction of the vapor-liquid equilibrium relation at low temperature and high pressure for the hydrogen-nitrogen system.* Kagaku Kogaku, 1971. **35**: p. 691-693.

23. Hong, J.H. and R. Kobayashi, *Vapor-liquid equilibrium study of the hydrogen-methane system at low temperatures and elevated pressures.* Journal of Chemical & Engineering Data, 1981. **26**(2): p. 127-131.

24. Hong, J.H. and R. Kobayashi, *Vapor Liquid Equilibrium Study of the H2-CH4 System at Low Temperatures and Elevated Pressures.* GPA Research Report RR-46, 1980: p. 1-25.

25. Heintz, A. and W.B. Streett, *Phase equilibriums in the hydrogen/ethane system at temperatures from 92.5 to 280.1 K and pressures to 560 MPa.* Journal of Chemical & Engineering Data, 1982. **27**(4): p. 465-469.

26. Connolly, J.F. and G.A. Kandalic, *Gas solubilities, vapor-liquid equilibria, and partial molal volumes in some hydrogen-hydrocarbon systems.* Journal of Chemical & Engineering Data, 1986. **31**(4): p. 396-406.

27. Freitag, N.P. and D.B. Robinson, *Equilibrium phase properties of the hydrogen—methane—carbon dioxide, hydrogen—carbon dioxide—n-pentane and hydrogen—n-pentane systems.* Fluid Phase Equilibria, 1986. **31**(2): p. 183-201.

28. Brunner, E., *Solubility of hydrogen in 10 organic solvents at 298.15, 323.15, and 373.15 K.* Journal of Chemical & Engineering Data, 1985. **30**(3): p. 269-273.

29. Gao, W., R.L. Robinson, and K.A.M. Gasem, *Solubilities of Hydrogen in Hexane and of Carbon Monoxide in Cyclohexane at Temperatures from 344.3 to 410.9 K and Pressures to 15 MPa.* Journal of Chemical & Engineering Data, 2001. **46**(3): p. 609-612.

30. Lachowicz, S.K., D.M. Newitt, and K.E. Weale, *The solubility of hydrogen and deuterium in n-heptane and n-octane at high pressures.* Transactions of the Faraday Society, 1955. **51**(0): p. 1198-1205.

31. Cook, M.W., D.N. Hanson, and B.J. Alder, *Solubility of Hydrogen and Deuterium in Nonpolar Solvents.* The Journal of Chemical Physics, 1957. **26**(4): p. 748-751.

32. Peramanu, S. and B.B. Pruden, *Solubility study for the purification of hydrogen from high pressure hydrocracker off-gas by an absorption-stripping process.* The Canadian Journal of Chemical Engineering, 1997. **75**(3): p. 535-543.

33. Connolly, J.F. and G.A. Kandalic, *Thermodynamic properties of solutions of hydrogen in n-octane.* The Journal of Chemical Thermodynamics, 1989. **21**(8): p. 851-858.

34. Kim, K.J., et al., *Solubility of Hydrogen in Octane, 1-Octanol, and Squalane.* Journal of Chemical & Engineering Data, 1997. **42**(1): p. 214-215.

35. Florusse, L.J., et al., *Solubility of hydrogen in heavy n-alkanes: Experiments and saft modeling.* AIChE Journal, 2003. **49**(12): p. 3260-3269.

36. Park, J., R.L. Robinson, Jr., and K.A.M. Gasem, *Solubilities of Hydrogen in Heavy Normal Paraffins at Temperatures from 323.2 to 423.2 K and Pressures to 17.4 MPa.* Journal of Chemical & Engineering Data, 1995. **40**(1): p. 241-244.

37. Schofield, B.A., Z.E. Ring, and R.W. Missen, *Solubility of hydrogen in a white oil.* The Canadian Journal of Chemical Engineering, 1992. **70**(4): p. 822-824.

38. Gao, W., R.L. Robinson, and K.A.M. Gasem, *High-Pressure Solubilities of Hydrogen, Nitrogen, and Carbon Monoxide in Dodecane from 344 to 410 K at Pressures to 13.2 MPa.* Journal of Chemical & Engineering Data, 1999. **44**(1): p. 130-132.

39. Breman, B.B., et al., *Gas-Liquid Solubilities of Carbon Monoxide, Carbon Dioxide,Hydrogen, Water, 1-Alcohols (1 .ltoreq. n .ltoreq. 6), and n-Paraffins (2 .ltoreq. n .ltoreq. 6) in Hexadecane, Octacosane, 1-Hexadecanol, Phenanthrene, and Tetraethylene Glycol at Pressures up to 5.5 MPa and Temperatures from 293 to 553 K.* Journal of Chemical & Engineering Data, 1994. **39**(4): p. 647-666.

40. Huang, S.H., et al., *Solubility of synthesis gases in heavy n-paraffins and Fischer-Tropsch wax.* Industrial & Engineering Chemistry Research, 1988. **27**(1): p. 162-169.

41. Herskowitz, M., J. Wisniak, and L. Skladman, *Hydrogen solubility in organic liquids.* Journal of Chemical & Engineering Data, 1983. **28**(2): p. 164-166.

42. Ronze, D., et al., *Hydrogen solubility in straight run gasoil.* Chemical Engineering Science, 2002. **57**(4): p. 547-553.

43. Connolly, J.F., *Thermodynamic Properties of Hydrogen in Benzene Solutions.* The Journal of Chemical Physics, 1962. **36**(11): p. 2897-2904.

44. Park, J., R.L. Robinson, and K.A.M. Gasem, *Solubilities of Hydrogen in Aromatic Hydrocarbons from 323 to 433 K and Pressures to 21.7 MPa.* Journal of Chemical & Engineering Data, 1996. **41**(1): p. 70-73.

45. Simnick, J.J., et al., *Vapor-liquid equilibrium of hydrogen/tetralin system at elevated temperatures and pressures.* AIChE Journal, 1977. **23**(4): p. 469-476.

46. Laugier, S., D. Richon, and H. Renon, *Vapor-liquid equilibriums of hydrogen-2,2,4-trimethylpentane and hydrogen-toluene systems at high pressures and temperatures.* Journal of Chemical & Engineering Data, 1980. **25**(3): p. 274-276.

47. Yin, J.-Z. and C.-S. Tan, *Solubility of hydrogen in toluene for the ternary system H2+CO2+toluene from 305 to 343K and 1.2 to 10.5MPa.* Fluid Phase Equilibria, 2006. **242**(2): p. 111-117.

48. Phiong, H.-S. and F.P. Lucien, *Solubility of Hydrogen in α-Methylstyrene and Cumene at Elevated Pressure.* Journal of Chemical & Engineering Data, 2002. **47**(3): p. 474-477.

49. Malone, P.V. and R. Kobayashi, *Light gas solubility in phenanthrene: the hydrogen—phenanthrene and methane—phenanthrene systems.* Fluid Phase Equilibria, 1990. **55**(1): p. 193-205.

50. Harrison, R.H., et al., *Solubility of hydrogen in well-defined coal liquids.* Journal of Chemical & Engineering Data, 1985. **30**(2): p. 183-189.

51. Lin, H.-M. and Y.-R. Lin, *Flow apparatus for phase equilibrium measurement at elevated temperatures.* AIChE Journal, 1990. **36**(10): p. 1597-1600.

52. Nasir, P., R.J. Martin, and R. Kobayashi, *A novel apparatus for the measurement of the phase and volumetric behavior at high temperatures and pressures and its application to study VLE in the hydrogen-tetralin system.* Fluid Phase Equilibria, 1981. **5**(3): p. 279-288.

53. Krichevsky, I.R. and J.S. Kasarnovsky, *Thermodynamical Calculations of Solubilities of Nitrogen and Hydrogen in Water at High Pressures.* Journal of the American Chemical Society, 1935. **57**(11): p. 2168-2171.

54. Kling, G. and G. Maurer, *The solubility of hydrogen in water and in 2-aminoethanol at temperatures between 323 K and 423 K and pressures up to 16 MPa.* The Journal of Chemical Thermodynamics, 1991. **23**(6): p. 531-541.

55. Setthanan, U., D.R. Morris, and D.H. Lister, *Solubilities of H2 in H2O and D2 in D2O with dissolved boric acid and lithium hydroxide.* Canadian Journal of Chemistry, 2006. **84**(1): p. 65-68.

56. DeVaney, W., et al., *High Temperature V-L-E Measurements for Substitute Gas Components.* GPA Research Report RR-30, 1978: p. 1-27.

57. Gillespie, P.C. and G. Wilson, *Vapor-Liquid Equilibrium Data on Water-Substitute Gas Components: N2-H2O, H2-H2O, CO-H2O, H2-CO-H2O, and H2S-H2O.* GPA Research Report RR-41, 1980: p. 1-34.

58. Toghiani, R.K., H. Toghiani, and G. Venkateswarlu, *Vapor-liquid equilibria for methyl tert-butyl ether + methanol and tert-amyl methyl ether + methanol.* Fluid Phase Equilibria, 1996. **122**(1): p. 157-168.

59. Leu, A.-D. and D.B. Robinson, *Vapor−Liquid Equilibrium for Four Binary Systems.* Journal of Chemical & Engineering Data, 1999. **44**(3): p. 398-400.

60. Wilding, W.V., N.F. Giles, and L.C. Wilson, *Phase Equilibrium Measurements on Nine Binary Mixtures.* Journal of Chemical & Engineering Data, 1996. **41**(6): p. 1239-1251.

61. Churkin, V., et al., *Liquid-vapor equilibrium in C4 hydrocarbon-methanol binary systems.* Zh. Fiz. Khim, 1978. **52**(2): p. 488-489.

62. Leu, A.D. and D.B. Robinson, *Equilibrium phase properties of the n-butane-hydrogen sulfide and isobutane-hydrogen sulfide binary systems.* Journal of Chemical & Engineering Data, 1989. **34**(3): p. 315-319.

63. Martinez-Ortiz, J.A. and D.B. Manley, *Vapor pressures for the system isobutane-isobutylene-n-butane.* Journal of Chemical & Engineering Data, 1978. **23**(2): p. 165-167.

64. Amezaga, A. and F. Biarge, *Equilibrio liquido vapor en sistemas binarios formados por el acido acetico y los alcoholes propilico, isopropilico, isobutilico, butilico secundario y butilico terciario a 760 mm.* Anales de Quimica, 1973. **69**: p. 587.

65. Li, X.-l., et al., *Vapor-liquid equilibria of isopropyl acetate-acetic acid-water system.* Journal of Chemical Engineering of Chinese Universities, 2006. **20**(1): p. 7.

66. Chang, W., et al., *Isobaric Vapor−Liquid Equilibria for Water + Acetic Acid + (n-Pentyl Acetate or Isopropyl Acetate).* Journal of Chemical & Engineering Data, 2005. **50**(4): p. 1129-1133.

67. Peng, Y., et al., *Thermodynamic consistency for the vapor-liquid equilibrium data of associating system.* Acta Pet. Sin.(Pet. Process.), 2009. **25**: p. 717-724.

68. Zhang, C., et al., *Investigation on isobaric vapor liquid equilibrium for acetic acid+water+(n-propyl acetate or iso-butyl acetate).* Fluid Phase Equilibria, 2011. **305**(1): p. 68-75.

69. Xie, Q., et al., *Investigation on isobaric vapor–liquid equilibrium for acetic acid+water+methyl ethyl ketone+isopropyl acetate.* Fluid Phase Equilibria, 2009. **280**(1): p. 120-128.

70. Mato, F. and E. Cepeda, *Vapor-liquid-equilibrium of binary-mixtures alcohol acetic-acid esters. 1. Systems with methanol, ethanol, normal-propanol and isopropanol.* Anales de Quimica, 1984. **80**(3): p. 338-342.

71. Andreatta, A.E., et al., *Physical properties and phase equilibria of the system isopropyl acetate+isopropanol+1-octyl-3-methyl-imidazolium bis(trifluoromethylsulfonyl)imide.* Fluid Phase Equilibria, 2010. **287**(2): p. 84-94.

72. Kojima, K., K. Ochi, and Y. Nakazawa, *Relationship between liquid activity coefficient and composition for ternary systems.* International Chemical Engineering, 1969. **9**(2): p. 342-347.

73. Li, Q., et al., *Isobaric Vapor–Liquid Equilibrium for (Propan-2-ol + Water + 1-Butyl-3-methylimidazolium Tetrafluoroborate).* Journal of Chemical & Engineering Data, 2009. **54**(9): p. 2785-2788.

74. Hlavatý, K. and J. Linek, *Liquid-liquid equilibria in four ternary acetic acid-organic solvent-water systems at 24.6 ºC.* Collection of Czechoslovak Chemical Communications, 1973. **38**(2): p. 374-378.

75. Stephenson, R. and J. Stuart, *Mutual binary solubilities: water-alcohols and water-esters.* Journal of Chemical & Engineering Data, 1986. **31**(1): p. 56-70.

76. Hong, G.-B., M.-J. Lee, and H.-m. Lin, *Liquid–liquid equilibria of ternary mixtures of water + 2-propanol with ethyl acetate, isopropyl acetate, or ethyl caproate.* Fluid Phase Equilibria, 2002. **202**(2): p. 239-252.

77. Vetere, A., I. Miracca, and F. Cianci, *Correlation and prediction of the vapor-liquid equilibria of the binary and ternary systems involved in MTBE synthesis.* Fluid Phase Equilibria, 1993. **90**(1): p. 189-203.

78. Lee, L.-s. and M.-z. Kuo, *Phase and reaction equilibria of the acetic acid-isopropanol-isopropyl acetate-water system at 760 mmHg.* Fluid Phase Equilibria, 1996. **123**(1): p. 147-165.

79. Novak, N., et al., *Prediction of dew points and liquid dropouts of gas condensate mixtures.* Fluid Phase Equilibria, 2018. **457**: p. 62-73.